



**Techniques in Dosimetry and 3-D Treatment Planning  
for  
Stereotactic Radiosurgery/Radiotherapy**

**Mostafa Heydarian**

University of Adelaide

April 1996

Thesis  
submitted in fulfilment  
of the requirements for the Degree  
of  
DOCTOR OF PHILOSOPHY  
at the  
UNIVERSITY OF ADELAIDE  
(Department of Physics and Mathematical Physics)



# Contents

<b>Title page</b>	<b>i</b>
<b>Contents</b>	<b>iii</b>
<b>Abstract</b>	<b>ix</b>
<b>Preface</b>	<b>xi</b>
<b>Statement</b>	<b>xv</b>
<b>Acknowledgements</b>	<b>xvii</b>
<b>Chapter 1. Radiotherapy Treatment Planning Dose Calculation</b>	<b>1</b>
1.1. Introduction . . . . .	1
1.2. Interactions of photon beams . . . . .	1
1.2.1. Fluence and energy fluence . . . . .	2
1.2.2. Attenuation coefficient . . . . .	2
1.2.2.1. Coherent scattering . . . . .	3
1.2.2.2. Photoelectric effect . . . . .	5
1.2.2.3. Compton effect . . . . .	5
1.2.2.4. Pair production . . . . .	6
1.2.2.5. Photonuclear reaction . . . . .	6
1.2.3. Energy transfer and energy absorption coefficients . . . . .	7
1.2.4. Radiation quantities . . . . .	7
1.2.4.1. Exposure . . . . .	7
1.2.4.2. Kerma and Terma . . . . .	8
1.2.4.3. Absorbed dose . . . . .	9
1.2.4.4. Equivalent dose and effective dose . . . . .	9
1.3. Interactions of electron beams . . . . .	10

1.3.1. Stopping power . . . . .	11
1.3.2. Scattering power . . . . .	12
1.4. Dosimetry parameters . . . . .	13
1.4.1. Depth doses . . . . .	13
1.4.2. Tissue air ratio . . . . .	16
1.4.3. Scatter air ratio . . . . .	17
1.4.4. Collimator output factors . . . . .	18
1.4.5. Tissue phantom and tissue maximum ratios . . . . .	18
1.4.6. Scatter-maximum ratio . . . . .	19
1.5. Electronic equilibrium . . . . .	19
1.6. Dose distributions . . . . .	21
1.7. Wedge filters . . . . .	22
1.7.1. Dynamic wedge . . . . .	25
1.8. Combination of radiation fields . . . . .	25
1.9. Conformal therapy . . . . .	25
1.10. Three dimensional treatment planning . . . . .	28
1.11. Three dimensional dose calculation techniques . . . . .	30
1.11.1. Effective path length method . . . . .	32
1.11.1.1. Tissue air ratio method . . . . .	33
1.11.2. Power law tissue air ratio method . . . . .	33
1.11.3. Equivalent tissue air ratio method . . . . .	34
1.11.4. The effect of electronic disequilibrium on dose calculation . . . . .	35
1.11.5. Density correction factor and <i>CT</i> numbers . . . . .	38
1.11.6. Superposition and convolution techniques . . . . .	39
1.11.7. Photon dose calculation using explicit electron transport . . . . .	41
1.11.8. Monte Carlo simulation . . . . .	42
<b>Chapter 2. Stereotactic Radiosurgery</b>	<b>45</b>
2.1. Introduction . . . . .	45
2.2. Rationale for radiosurgical treatment . . . . .	46
2.3. Gamma Knife . . . . .	47
2.4. Heavy charged particle <i>SRS</i> . . . . .	49

2.5. Linac-based <i>SRS</i> . . . . .	52
2.6. Target localization . . . . .	53
2.7. <i>SRS</i> dose calculation . . . . .	56
2.7.1. Dose calculation parameters . . . . .	57
2.7.2. Calculating the dose distribution . . . . .	57
2.8. Choice of optimum energy . . . . .	59
2.9. Dose fall off outside the target volume . . . . .	61
2.10. <i>SRS</i> quality assurance . . . . .	63
2.10.1. Probable risk analysis . . . . .	64
2.10.2. The routine <i>QA</i> . . . . .	65
2.10.3. The treatment <i>QA</i> . . . . .	65
2.10.3.1. Laser check . . . . .	66
2.11. Patient set up and target verification . . . . .	66
2.12. The accuracy of <i>SRS</i> . . . . .	67
2.12.1. Diagnostic resolution . . . . .	68
2.12.2. Linear accelerator accuracy . . . . .	68
2.12.3. The centre of the dose distribution . . . . .	69
2.13. Cost effectiveness of <i>SRS</i> . . . . .	69
2.14. Discussion and conclusion . . . . .	70
<b>Chapter 3. Evaluation of Diamond Detectors for Megavoltage Beams</b>	<b>73</b>
3.1. Introduction . . . . .	73
3.2. Theory of diamond detector response . . . . .	74
3.3. Physical properties of <i>PTW</i> diamond detectors . . . . .	76
3.3.1. Current-voltage response . . . . .	77
3.3.2. Charge collection efficiency . . . . .	79
3.3.3. Stability of detector current . . . . .	80
3.3.4. Constancy and linearity . . . . .	81
3.3.5. Directional dependence of response . . . . .	82
3.3.6. Spatial resolution . . . . .	85
3.4. Dose rate dependence . . . . .	88
3.4.1. Changing <i>FSD</i> . . . . .	89

3.4.2. Changing depth . . . . .	90
3.4.3. Changing pulse repetition frequency . . . . .	93
3.5. Evaluation of the diamond detector for photon beam measurements . . . . .	94
3.5.1. Introduction . . . . .	94
3.5.2. Output factors . . . . .	96
3.5.3. Depth dose curves . . . . .	97
3.5.4. Summary and discussion . . . . .	98
3.6. Evaluation of the diamond detector for electron beam measurements . . . . .	100
3.6.1. Introduction . . . . .	100
3.6.2. Depth dose curves . . . . .	101
3.6.3. Summary and discussion . . . . .	104
3.7. Dose rate correction . . . . .	104
3.8. Conclusion . . . . .	105
<b>Chapter 4. Monte Carlo Dose Calculation</b>	<b>109</b>
4.1. Introduction . . . . .	109
4.2. Sampling . . . . .	111
4.3. Random number generation . . . . .	113
4.4. Monte Carlo particle transport . . . . .	113
4.4.1. Photon transport . . . . .	114
4.4.2. Electron transport . . . . .	114
4.5. The <i>EGS4</i> system . . . . .	119
4.6. Dependence on electron step-size and energy cutoff parameters . . . . .	121
4.7. <i>PRESTA</i> . . . . .	122
4.8. Variance reduction techniques . . . . .	124
4.9. Reciprocity technique . . . . .	125
4.10. Benchmarking <i>EGS4</i> . . . . .	129
4.10.1. Depth doses . . . . .	129
<b>Chapter 5. Evaluation of Dosimetry Techniques in Stereotactic Radiosurgery</b>	<b>135</b>
5.1. Introduction . . . . .	135
5.2. Small field dosimetry difficulties . . . . .	137

5.2.1. Energy spectrum . . . . .	138
5.2.2. Detector response to <i>SRS</i> fields . . . . .	140
5.3. Small field dosimetry parameters and techniques . . . . .	143
5.3.1. Depth doses . . . . .	144
5.3.2. Tissue maximum ratios . . . . .	147
5.3.3. Off-axis factors . . . . .	148
5.3.4. Collimator output factors . . . . .	151
5.4. Discussion . . . . .	155

## **Chapter 6. Advances in Stereotactic Radiosurgery/Radiotherapy Treatment**

<b>Techniques</b>	<b>157</b>
6.1. Review of the existing techniques . . . . .	157
6.2. Dynamic stereotactic radiosurgery . . . . .	158
6.3. Conformal <i>SRS</i> . . . . .	160
6.4. <i>Cyberknife</i> : Image-guided <i>SRS</i> . . . . .	164
6.5. Miniature <i>x-ray</i> radiosurgery . . . . .	166
6.6. Body stereotactic radiosurgery . . . . .	166
6.7. Radiobiology of radiosurgery . . . . .	167
6.7.1. Radiobiological principles . . . . .	168
6.7.2. Dose response of <i>AVM</i> and benign lesions . . . . .	171
6.7.3. Dose response of malignancies . . . . .	173
6.8. Dose to the critical organs . . . . .	174
6.9. <i>SRS</i> limitations . . . . .	174
6.10. Stereotactic radiotherapy ( <i>SRT</i> ) . . . . .	176
6.10.1. Patient repositioning techniques . . . . .	177
6.11. Discussion and conclusion . . . . .	178

## **Chapter 7. *SRS* Treatment Planning and MC Dosimetry of Irregular Fields** 179

7.1. Introduction . . . . .	179
7.2. The validity of <i>SRS</i> treatment planning assumptions . . . . .	180
7.2.1. The effect of tissue heterogeneity on <i>SRS</i> dose calculation . . . . .	180
7.2.2. Assumptions related to the body contour . . . . .	183

7.2.3. Invariant dose profile with depth . . . . .	186
7.3. Treatment planning verification . . . . .	187
7.4. Optimum number of arcs . . . . .	193
7.5. Monte Carlo dosimetry of irregular field stereotactic radiosurgery . . . . .	198
7.5.1. Introduction . . . . .	198
7.5.2. Method . . . . .	198
7.5.3. Results . . . . .	200
7.6. Image registration and correlation . . . . .	202
7.7. Bioeffect planning . . . . .	205
7.8. Discussion and conclusion . . . . .	208
<b>Chapter 8. Discussion and Future Developments</b>	<b>211</b>
8.1. Introduction . . . . .	211
8.2. Dosimetry of <i>SRS</i> fields . . . . .	211
8.3. Treatment planning . . . . .	212
8.4. Dose delivery . . . . .	214
<b>Appendix: Publications</b>	<b>215</b>
<b>References</b>	<b>217</b>

## Abstract

The success of stereotactic radiosurgery (*SRS*) as an effective radiation technique for treating intracranial lesions is dependent on the geometric accuracy of the dose delivery. This is because in this technique a high dose (normally 10 to 30 Gy) is released by a small field, in a single-fraction, to destroy the lesion located in a generally critical region. Accurate dosimetry of *SRS* fields is difficult because of lateral electronic disequilibrium and steep dose gradients which are characteristics of these fields. Accurate dosimetry of *SRS* fields is most likely to be achieved using a high resolution tissue-equivalent detector.

Monte Carlo techniques and *PTW* diamond detectors are added to the commonly used detectors (namely silicon diodes, ionization chambers, film and thermoluminescence dosimetry) to calculate and measure *SRS* treatment planning requirements and dose distributions. Monte Carlo techniques have been confirmed as reliable references for dosimetry of *SRS* fields. Also, it will be shown that diamond detectors are potentially ideal for *SRS* and yield more accurate results than the above traditional modes of experimental dosimetry. This was demonstrated by comparing the diamond response, after correcting for dose rate dependence, with the corresponding results of the ionization chamber (for large fields) and Monte Carlo (for small fields).

Advanced techniques in stereotactic radiosurgery and radiotherapy are introduced. Using radiobiological principles it has been shown that *SRS* is appropriate for treating arteriovenous malformations and most benign lesions, while stereotactic radiotherapy (as a fractionation scheme) is highly recommended for malignancies and large tumours. Bioeffect planning as a new means for assessment of the treatment plans is introduced, by which treatment plans can be assessed according to the bioeffect distribution rather than a physical dose distribution.

A method of calculating beam data using sector-integration of Monte Carlo-generated pencil beam kernels has been proposed. This technique can be used both for circular and irregular fields, however it is more useful in calculating dosimetry parameters for irregular fields—where the shape of treatment fields is determined during planning.



## Preface

Stereotactic radiosurgery (*SRS*) is a preferred radiation technique for treating most intracranial lesions, where the lesion is surgically inaccessible or has a high risk operation. Of the most pronounced characteristics of this technique are high geometric accuracy and steep dose gradient outside the target volume. This results in sparing of normal tissue, while the target volume is given a prescribed radiation dose. Using noncoplanar multiple arc techniques results in a dose distribution which drops from 90% isodose line at the edge of the target to 50% and 20% in approximately 3 and 7 mm, respectively. In this way, the target volume receives a uniform dose while the dose to the surrounding healthy tissue is minimal. This is true only if the target volume is defined precisely, the treatment planning and dose delivery are performed accurately and the dose can be conformed with the constraints imposed. These are subject to the accuracy of diagnosis, dosimetry, treatment planning, treatment set-up and dose delivery techniques. Weakness or failure on any of these could result in treatment failure. A more interactive 3-D treatment planning system is useful for choosing the treatment parameters in order to conform the beam to the shape of the target volume, avoid critical structures and evaluate the treatment plans. This thesis is the result of work carried out to determine an appropriate technique for dosimetry of *SRS* fields and develop the treatment planning dose calculation. All work presented in this thesis has been carried out by the author (unless otherwise stated).

Chapter 1 is a review of radiation transport and some of the current treatment planning dose calculation algorithms. In this chapter advanced dose calculation techniques such as convolution, superposition and Monte Carlo are compared. Also, some of the recent dose delivery techniques such as conformal radiotherapy, tomotherapy and dynamic wedges are introduced.

In chapter 2 stereotactic radiosurgery as a modern single fraction technique in treating intracranial lesions is introduced and the rationale behind *SRS* of various lesions is discussed. In this chapter our *SRS* technique is compared with different techniques from various centres. Different aspects of the *SRS* quality assurance, as a

multidisciplinary program, are discussed. The cost effectiveness of *SRS* compared to the alternative techniques is also investigated.

Evaluation of diamond detectors for dosimetry of megavoltage radiotherapy and particularly *SRS* fields is the subject of chapter 3. Diamond detectors (because of their near tissue equivalence and small sensitive volume) are especially attractive for dosimetry in the electronic disequilibrium conditions, such as in most *SRS* fields. Dose response characteristics of these detectors are investigated. Dose rate dependence of diamond detectors is also discussed and the correction method is applied.

Monte Carlo (*MC*) dose calculation techniques are discussed in chapter 4. These techniques have been employed for benchmarking dose measurements in the presence of lateral electronic disequilibrium, after they had been validated against ionization chambers for electronic equilibrium conditions. Also, *MC* techniques are used to calculate the beam parameters such as photon and electron energy spectra for different experimental conditions. These parameters are used to quantify the energy dependence of non tissue equivalent detectors such as silicon diodes, ionization chambers and film.

Different *SRS* dosimetry techniques are evaluated in chapter 5. *MC* and diamond detectors are compared with other dosimetry techniques such as film, silicon diode and ionization chambers in an effort to determine the optimum dosimetry technique for measuring *SRS* treatment planning parameters. Special attention is paid to measuring off axis factors, due to the potential errors which could cause over- or under-estimation of the treatment volume. This is a difficult task due to the presence of lateral electronic disequilibrium across the beam for most of the *SRS* fields and the steep dose gradient, where detector convolution error is more significant. An inaccurate dose profile could result in an over-dose to the healthy tissue surrounding the target volume or an under-dose to the target—both resulting in a reduced therapeutic ratio.

Advances in *SRS* treatment and dose calculation techniques are discussed in chapter 6. This chapter shows how conventional *SRS* techniques are slowly being replaced by the newer techniques, some being capable of having the radiation beam sent from anywhere to any point of the target without using any immobilisation device, just by looking at the treatment plans in real time. Also, dose responses of arteriovenous malformations (*AVMs*) and benign lesions are compared with those of malignancies. Stereotactic

radiotherapy (*SRT*), as a preferred technique for treating the latter category and larger tumours, is also discussed.

The validity of the treatment planning assumptions such as tissue homogeneity and invariant profiles with depths are investigated in chapter 7 and deviations quantified. A method of obtaining *SRS* beam data using sector-integration of Monte Carlo-generated pencil beam kernels is proposed, which can be used both for circular and irregular fields. Image registration and fusion techniques for correcting magnetic resonance (*MR*) image distortions are presented. This enables *MRI*, as the superior soft-tissue diagnostic tool, to be used for stereotactic localization. Bioeffect planning is also introduced in this chapter. This is a new means for assessing the treatment techniques and comparing the rival plans. In this way treatment plans are assessed according to the bioeffect distribution rather than a physical dose distribution.

A list of the publications and conference presentations which the author has been involved in the course of this project is as follows:

### **Publications**

Heydarian M, Hoban P W and Beddoe A H 1996 A Comparison of Dosimetry Techniques in Stereotactic Radiosurgery. *Phys. Med. Biol.* **41** 93-110.

Hoban P W, Heydarian M, Beckham W A and Beddoe A H 1994 Dose rate dependence of a *PTW* diamond detector in the dosimetry of a 6 *MV* photon beam. *Phys. Med. Biol.* **39** 1219-29.

Heydarian M, Hoban P W, Beckham W A, Borchardt I M and Beddoe A H 1993 Evaluation of a *PTW* diamond detector for electron beam measurements. *Phys. Med. Biol.* **38** 1035-42.

## **Presentations**

Heydarian M, Hoban P W and Beddoe A H 1995 Evaluation of Diamond Detectors for Radiosurgery Dosimetry. 2nd Congress of the International Stereotactic Radiosurgery Society, Boston, USA.

Hoban P W, Heydarian M, Amies C J and Rose A 1995 Monte Carlo Dosimetry in Irregular-field Stereotactic Radiosurgery. 2nd Congress of the International Stereotactic Radiosurgery Society, Boston, USA.

Heydarian M, Hoban P W and Beddoe A H 1995 Evaluation of Diamond Detectors for Radiosurgery. 7th Asian & Oceanian Congress of Radiology, Kuala Lumpur, Malaysia.

Heydarian M, Hoban P W, Beckham W A and Beddoe A H 1994 Dosimetry of Small Field Photon Beams. World Congress on Medical Physics and Biomedical Engineering, Rio-de Janeiro, Brazil.

Heydarian M, Hoban P W, Beckham W A and Beddoe A H 1994 Dosimetry Techniques for Small Field Photon Beams. EPSM'94 Conference, Perth, Australia.

Hoban P W and Heydarian M 1994 Monte Carlo Dosimetry in Stereotactic Radiosurgery. EPSM'94 Conference, Perth, Australia.

Hoban P W and Heydarian M 1994 Monte Carlo Dosimetry in Stereotactic Radiosurgery. COSA Conference, Adelaide, Australia.

Heydarian M, Hoban P W, Beckham W A and Beddoe A H 1993 Dose Rate Dependence of Diamond Detectors in Photon Beam Dosimetry. APSEM/BECON'93 Conference, Melbourne, Australia.

Heydarian M, Hoban P W, Borchardt I M and Beddoe A H 1992 Evaluation of Diamond Detectors for Electron Beams. APSEM/BECON'92 Conference, Gold Coast, Australia.

This work contains no material which has been accepted for the award of any other degree or diploma in any university or other tertiary institution and, to the best of my knowledge and belief, contains no material previously published or written by another person, except where due reference has been made in the text.

I give consent to this copy of my thesis, when deposited in the University Library, being available for loan and photocopying.

Signed:

dated: .....9/8/96.....



## Acknowledgements

I wish to thank all people who have been involved in different aspects with this project. My original thanks go to Drs. A H Beddoe and P W Hoban who have supported me throughout the course of this project and given me valuable discussion and guidelines. Many thanks especially to Dr. Hoban for his ideas, suggestions, initiating Monte Carlo simulations and his "*red pen!*", without which this thesis would not have been as colourful. My thanks also go to Dr. J R Patterson, as my third supervisor for the last year of this project.

Thanks to my wife and wonderful daughter for their support and patience during this long term project. Very special thanks to all my friends and colleagues in the Department of Medical Physics, Royal Adelaide Hospital – without their help, discussion and friendship this work could not have been as completed.

Finally, I would like to thank the Ministry of Health and Medical Education of Iran and Shaheed Beheshti University of Medical Sciences, as without their financial support this course was not possible.





# Chapter 1

## Radiotherapy Treatment Planning Dose Calculation

### 1.1. Introduction

The current generation of diagnostic tools (*MRI*, *CT*, angiography, etc.), three dimensional treatment planning systems and radiotherapy machines are able to diagnose, plan, position, and treat a lesion with high geometric and dosimetric accuracy. It is known that successful treatment requires both a sufficiently high dose to the entire tumour to give a high tumour control probability and a low enough dose to surrounding healthy tissues to ensure that the benefit of eradication of the tumour is not outweighed by complications in healthy organ function. Accurate positioning and shaping of the radiation beams are of paramount importance in satisfying this requirement. Once this is achieved, being able to accurately predict the dose distribution due to each beam becomes essential if the benefits of high geometric precision are to be realised. Improvements in dose calculation accuracy are made by more realistically modeling the physical processes involved in photon and electron transport along with the use of faster computer hardware which enables calculations to be performed in an acceptable time.

This chapter focuses on the underlying processes in radiation transport as well as some of the treatment planning dose calculation algorithms. Dosimetry parameters and the relevant definitions are presented. Electron transport parameters have been included because the dose deposition in the medium in photon beam irradiation is by the secondary electrons set in motion by primary and scattered photons and the fact that, for the range of photon energies being used in radiotherapy, these electrons can travel significant distances before they stopped.

### 1.2. Interactions of photon beams

When a photon beam passes through a medium, part or all of its energy is transferred to the medium. Photons interact with the medium mainly by the photoelectric, Compton

or pair production processes and to a lesser extent by coherent scattering and photonuclear reactions. The probability of an interaction is determined by several factors, including the photon energy, the atomic number and electron density of the medium. These, together with other photon beam parameters will be discussed in the following sections.

### 1.2.1. Fluence and energy fluence

The photon beam fluence,  $\Phi$ , is defined as  $dN/da$ , where  $dN$  is the number of photons incident on a sphere of cross section area  $da$ . The fluence per unit time,  $\phi$ , is known as fluence rate, flux density or intensity. That is:

$$\phi = \frac{d\Phi}{dt} \quad (1-1)$$

The photon energy fluence,  $\Psi$ , is defined as  $dE_{\gamma}/da$ , where  $dE_{\gamma}$  is the sum of energies of all the photons incident on a normal area,  $da$ , that is:

$$\Psi = \frac{\sum_i dN_i (h\nu)_i}{da}, \quad (1-2)$$

where  $dN_i$  is the number of photons with energy  $(h\nu)_i$ . The energy fluence per unit time,  $\psi$  is known as energy fluence rate, energy flux density, or energy intensity:

$$\psi = \frac{d\Psi}{dt} \quad (1-3)$$

### 1.2.2. Attenuation coefficient

The linear attenuation coefficient,  $\mu$ , is the relative reduction in photon fluence in passing through unit thickness of the material, so that:

$$\frac{dI}{I} = \mu dx \quad \Rightarrow \quad I = I_0 e^{-\mu x}, \quad (1-4)$$

where  $I_0$  is the photon incident intensity and  $I$  is the photon intensity after passing through a thickness  $x$  of the material. The attenuation is due to the interaction of the

photon beams with the material. There are various types of interactions, mainly coherent scattering, photoelectric effect, Compton effect, pair production, and photonuclear reactions. The probability of each type of interaction depends on the photon energy and the medium composition, in terms of atomic number and electron density (number of electrons per  $cm^3$ ). In addition, photonuclear reactions also depend on the number of nucleons. The mass attenuation coefficient is defined as  $\frac{\mu}{\rho}$ , to eliminate the density dependence of attenuation. The mass attenuation coefficient is equal to  $\sigma \times \frac{N_A}{A}$ , where  $\sigma$  is probability of interaction with an atom (atomic cross section),  $N_A$  and  $A$  are Avogadro's number and atomic weight respectively and  $\frac{N_A}{A}$  is the number of atoms per unit mass. The total mass attenuation coefficient is thus the sum of the mass attenuation coefficients of the individual processes mentioned above, respectively:

$$\frac{\mu}{\rho} = \frac{\mu_{coh}}{\rho} + \frac{\mu_{\tau}}{\rho} + \frac{\mu_{c}}{\rho} + \frac{\mu_{\pi}}{\rho} + \frac{\mu_{phn.}}{\rho} \quad (1-5)$$

Variations of the total mass attenuation coefficients of water and lead with energy are shown in Figure 1.1. Also Figure 1.2 shows the relative contribution of the Compton, photoelectric and pair production processes to the total mass attenuation coefficient for water and bone at various photon energies. In the following sections is a brief introduction of each of these processes.

### 1.2.2.1. Coherent scattering

When a photon beam passes near an orbital electron, the electron oscillates, due to the electromagnetic nature of the photon beam. The oscillating electron reradiates a photon beam with the same frequency as the incident photon. The coherent scattering, also known as classical scattering or Rayleigh scattering, is probable for high atomic number materials and very low energy photon beams. The probability of coherent scattering is determined by the coherent scattering mass attenuation coefficient,  $\frac{\mu_{coh}}{\rho}$ . This process causes photon scattering mainly at small angles. This is not of practical importance in radiotherapy.

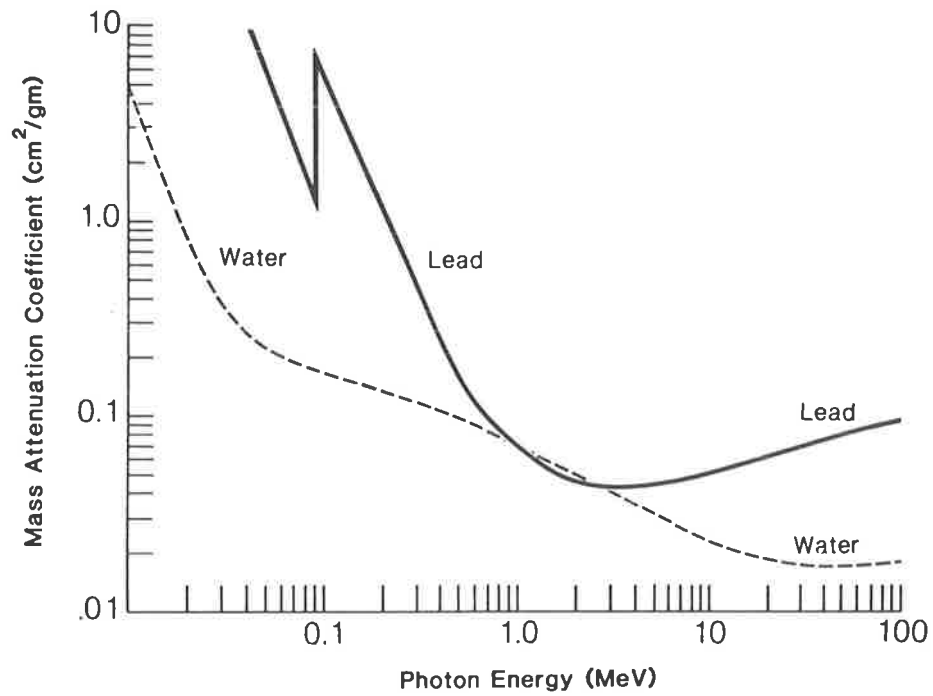


Figure 1.1. Total mass attenuation coefficient as a function of energy for water and lead (from Khan, 1994).

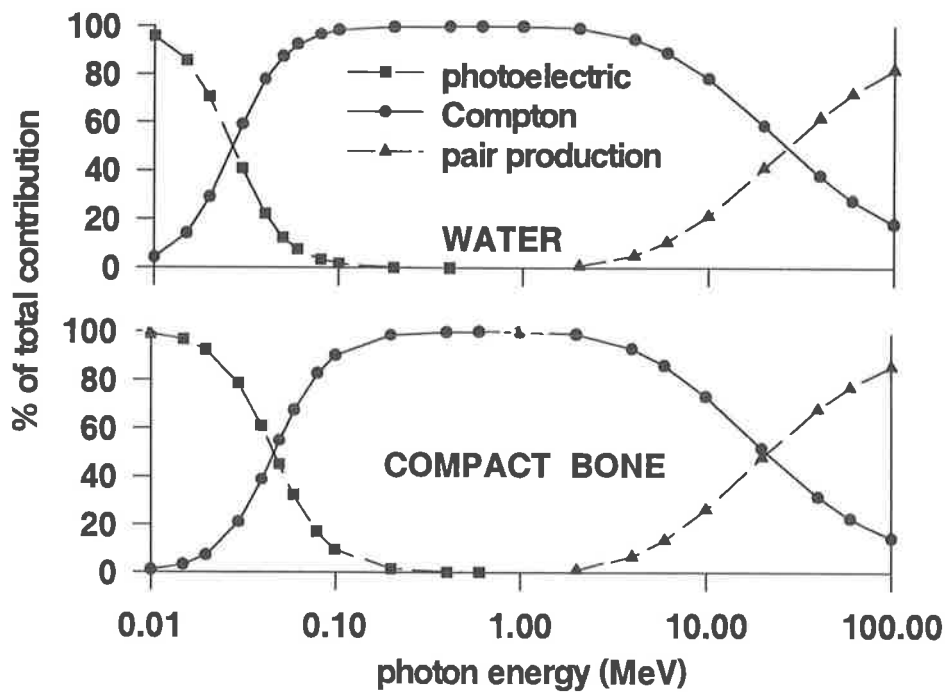


Figure 1.2. Relative contribution of different attenuation factors in the total mass attenuation coefficient (data from Hubbell, 1969).

### 1.2.2.2. Photoelectric effect

In the photoelectric effect a photon interacts with an atom in a way that transfers the whole photon energy and ejects one of the orbital electrons from the atom. The ejected electron, which is called a photoelectron, has a kinetic energy  $h\nu - E_B$ , where  $h\nu$  is the photon energy and  $E_B$  is the binding energy of the electron.

The probability of the photoelectric effect is determined by the mass photoelectric attenuation coefficient,  $\frac{\mu_{\tau}}{\rho}$ , where  $\rho$  is the density of the medium. This probability increases dramatically where the photon energy is exactly the same, or slightly more than the binding energy of an orbital electron and drops thereafter with energy approximately by a factor of energy to the power of 3. After a photoelectric interaction the orbital vacancy is refilled by an electron from outer energy levels, thereby releasing a characteristic *x-ray*.

The photoelectric cross section also depends strongly on the atomic number of the medium. The dependence of the mass photoelectric coefficient on energy and atomic number is approximately given by:

$$\frac{\mu_{\tau}}{\rho} \propto \frac{Z^3}{(h\nu)^3} \quad (1-6)$$

### 1.2.2.3. Compton effect

When a photon interacts with a free electron, the process is called Compton or incoherent scattering. The term free electron is applied when the photon energy is much more than the electron binding energy. In the Compton process, the electron with the acquired energy is emitted at an angle  $\theta$  and the reduced energy photon is scattered at an angle  $\phi$ .

The probability of the Compton effect is determined by the Compton mass attenuation coefficient,  $\frac{\mu_c}{\rho}$ . The Compton mass attenuation coefficient is independent of the atomic number of material, because the interaction is basically with free electrons.

Therefore  $\frac{\mu_c}{\rho}$  only depends on the electron density, that is the number of electrons per gram of the material ( $\propto Z/A$ ). This is almost constant for all materials, with a slight decrease with atomic number. The exception is hydrogen where electron density is more than twice that of other materials (since  $Z/A=1$  instead of  $1/2$ ).

The Compton interaction decreases almost inversely proportional to the photon energy, so that:

$$\frac{\mu_c}{\rho} \propto \frac{1}{h\nu} \quad (1-7)$$

#### 1.2.2.4. Pair production

A photon with energy more than  $1.02 \text{ MeV}$  may have a strong interaction with the electromagnetic field of a nucleus, with the photon energy transforming to an electron and a positron. The threshold energy for this phenomenon is  $1.02 \text{ MeV}$  which is equal to the rest mass energies of the produced electron-positron pair ( $2m_e c^2$ ). The photon energy in excess of this is shared between the two created particles as kinetic energy.

The probability of pair production is determined by the pair production mass attenuation coefficient,  $\frac{\mu_{\pi}}{\rho}$ . This coefficient is proportional to  $Z$  (varies with  $Z^2$  per atom, but with  $Z$  per electron or per mass) for energies less than  $20 \text{ MeV}$ . However at higher energies the degree of the proportionality decreases for higher atomic number materials, due to the screening effect by the orbital electrons (Khan, 1994). Also  $\frac{\mu_{\pi}}{\rho}$  is proportional to the logarithm of the photon energy, for energies above the threshold.

#### 1.2.2.5. Photonuclear reaction

High energy photon beams can interact directly with atomic nuclei and cause nuclear reactions. This process is known as a photonuclear reaction and results in the emission of one or more nucleons (most probably neutrons). The probability of this effect is

determined by the photonuclear reaction mass attenuation coefficient,  $\frac{\mu_{ph.n.}}{\rho}$ . The photonuclear reaction can contribute as much as 5-10% to the total attenuation coefficient between 10 and 30 *MeV*, depending on where the giant resonance with the target nuclide occurs (Hubbell, 1982).

### 1.2.3. Energy transfer and energy absorption coefficients

As a result of the photon interaction with the medium part or all its energy is transferred to electrons. The linear energy transfer coefficient,  $\mu_{tr}$ , is defined as the fraction of the energy fluence transferred per unit path length. Since some proportion of transferred energy is converted to bremsstrahlung radiation, fraction of energy fluence deposited locally (the energy absorption coefficient) is less than energy transfer coefficient. Locally, here means within the range of produced electrons which is much shorter than the range of photons. The linear energy absorption coefficient,  $\mu_{en}$ , and the linear energy transfer coefficient are related to each other by:

$$\mu_{en} = \mu_{tr}(1 - g), \quad (1-8)$$

where  $g$  is the fraction of electron energy converted to bremsstrahlung. Energy transfer and absorption coefficients are usually tabulated as the density-independent quantities  $\frac{\mu_{en}}{\rho}$  and  $\frac{\mu_{tr}}{\rho}$  where  $\rho$  is the medium density.

For dosimetry applications at energies less than a few *MeV*, it is assumed that the range of electrons set in motion is very small, however for 10 *MeV* and higher energies the electron range can be several *cm*.

### 1.2.4. Radiation quantities

#### 1.2.4.1. Exposure

Ionization produced in air by photons is measured with a quantity called exposure. Exposure,  $X$ , is defined as the absolute value of the charge (of one sign) produced per unit mass of air (ICRU, 1980), that is:

$$X = \frac{dQ}{dm} \quad (1-9)$$

The exposure unit in the system international (SI) is coulomb per kilogram (C/kg). The Roentgen,  $R$ , is the old unit of exposure, such that:  $1 R = 2.58 \times 10^{-4} C/kg \text{ air}$ .

#### 1.2.4.2. Kerma and Terma

The quantity kerma (kinetic energy released per unit mass),  $K$ , is the kinetic energy transferred to electrons from photon interactions per unit mass of the material. This can be written as:

$$K = \frac{dE_{tr}}{dm} = \Psi \left( \frac{\bar{\mu}_{tr}}{\rho} \right) \quad (1-10)$$

where  $\bar{\mu}_{tr}/\rho$  is the average mass energy transfer coefficient for the photon energy fluence ( $\Psi$ ) spectrum. The initial kerma can be divided into the collision kerma ( $K_{col}$ ) and radiation kerma ( $K_{rad}$ ), in the same way as the initial energy transfer is split, as was discussed in section 1.2.3, that is:  $K_{col} = \Psi \left( \frac{\bar{\mu}_{en}}{\rho} \right)$  and  $K_{rad} = \Psi \left( \frac{\bar{\mu}_{tr}}{\rho} - \frac{\bar{\mu}_{en}}{\rho} \right)$ . Referring to equation (1-8) it can be written as:  $K_{col} = K(1-g)$  and  $K_{rad} = Kg$ .

Terma (total energy released per unit mass),  $T$ , is a term which describes the total energy released by the primary photon beam per unit mass, including the energy of the subsequent scattered photon. Terma is defined as:

$$T = \Psi \left( \frac{\mu}{\rho} \right) \quad (1-11)$$

$\left( \frac{\mu}{\rho} \right)$  is the total mass attenuation coefficient. A good explanation of terma is the loss of energy in the primary beam, that is:  $T = -\nabla \cdot \Psi$ . Kerma and terma have the same unit as absorbed dose (see the next section), that is  $J kg^{-1}$ .

### 1.2.4.3. Absorbed dose

The quantity absorbed dose, or simply the dose is defined as:  $\lim_{dm \rightarrow 0} (dE / dm)$ , that is the energy deposited at a point per unit mass of material. The *SI* unit of absorbed dose is the Gray (*Gy*) which is defined as:

$$1 \text{ Gy} = 1 \text{ J / kg} \quad (1-12)$$

The old unit of absorbed dose is the rad, such that:  $1 \text{ rad} = 10^{-2} \text{ Gy}$ .

### 1.2.4.4. Equivalent dose and effective dose

The probability of a stochastic effect, such as the induction of cancer or of heritable defect, depends on the absorbed dose as well as the type and energy of the radiation. This is taken into account by applying a radiation weighting factor to the absorbed dose. The weighting factor depends on the radiation quality and the linear energy transfer (*LET*). The quantity "dose equivalent" is a factor which incorporates the relative biological effectiveness (*RBE*) of different radiation types. The equivalent dose is defined as the product of the absorbed dose and the *RBE* (as the radiation weighting factor), where *RBE* is the ratio of dose from a standard radiation (usually 200 *kV<sub>p</sub>* x-rays) to produce a given biological effect to the dose from the current radiation to give the same effect.

$$\text{Equivalent dose} = D \times RBE \quad (1-13)$$

The *RBE* recommended by the International Commission on Radiological Protection (*ICRP*, 1991) for different types and energies of radiations is shown in Table 1.1. The *SI* unit of the equivalent dose is sievert (*Sv*), which is equivalent to gray (*Gy*) because *RBE* is a dimensionless factor. However, the unit will be in rems if the dose is in rads. *RBE* increases with the *LET* of the particle. This is the rate at which energy is deposited along a particle track.

The above definition neither takes into account nonuniformity of the radiation exposure nor different sensitivities of various tissues. Indeed, truly uniform total body irradiation is rare, especially when dealing with radionuclides. Also it is known that some organs like the gonads and lung are more susceptible to radiation than muscles. To include

Table 1.1. Radiation weighting factors (from *ICRP*, 1991)

TYPE AND ENERGY RANGE	<i>RBE</i>
Photons, all energies	1
Electrons and muons, all energies	1
Neutrons, energy < 10 KeV	5
10 to 100 KeV	10
> 100 KeV to 2 MeV	20
> 2 MeV to 20 MeV	10
> 20 MeV	5
Protons, other than recoil protons, energy > 2 MeV	5
$\alpha$ -Particles, fission fragments, heavy nuclei	20

these factors, *ICRP* (1991) introduced the concept of the tissue weighting factor ( $W_T$ ), which represents the relative contribution of each tissue or organ to the total damage. The effective dose is the sum of all of the weighted equivalent doses in all tissues and organs, that is:

$$\text{Effective dose} = \Sigma \text{ equivalent dose} \times W_T \quad (1-14)$$

Tissue weighting factors recommended by *ICRP* are listed in Table 1.2.

### 1.3. Interactions of electron beams

Electrons interact with matter basically in two different ways: (i) collision with orbital electrons, in which an electron loses its energy by ionization or excitation, and (ii) interaction with the nucleus, where the electron either loses energy (bremsstrahlung production) or is elastically scattered with no energy loss. Because of their small mass, electrons passing through a medium suffer a great number of interactions until they lose their energy and are captured by an atom. As the result, the Bragg peak which is very noticeable for heavy charged particles (e.g., protons and alpha), is not observed for electrons because of straggling. In radiation dosimetry and radiotherapy, it is important to have accurate information about the spatial and angular distributions of electron

Table 1.2. Tissue weighting factors (Hall, 1994)

TISSUE/ORGAN	$W_T$
Gonads	0.20
Bone marrow (red)	0.12
Colon	0.12
Lung	0.12
Stomach	0.12
Bladder	0.05
Breast	0.05
Liver	0.05
Oesophagus	0.05
Thyroid	0.05
Skin	0.01
Bone surface	0.01
Remainder	0.05

beams. The average electron energy loss is determined by the mass stopping power and the change in direction of electrons can be explained by the mass scattering power. International Commission on Radiation Units and Measurements (ICRU) reports 35 and 37 (1984) contain full descriptions of these factors.

### 1.3.1. Stopping power

The electron energy loss per unit path length of the medium is called total linear stopping power,  $S_{tot}$ . The total stopping power depends on the electron energy as well as the atomic number and the electron density of the material. In order to eliminate dependence to the density, the total mass stopping power,  $(S/\rho)_{tot}$ , of a material is defined by the ICRU (1980) as  $dE/\rho dl$ , where  $dE$  is the total energy loss by the electron travelling a path length  $dl$  in the material of density  $\rho$ . The total mass stopping power can be written as:

$$(S/\rho)_{tot} = (S/\rho)_{col} + (S/\rho)_{rad}, \quad (1-15)$$

where  $(S/\rho)_{col}$  and  $(S/\rho)_{rad}$  are the collisional and radiation mass stopping powers, respectively.

The collisional stopping power is the electron energy loss due to ionization and excitation of atoms. The collisional stopping power depends on electron density and incident beam energy. Therefore, the collision stopping power is greater for low atomic number materials where  $Z/A$  is greater. The ratio of air to water stopping power is greater at lower energies. This ratio increases with depth, as the electrons slow down.

The radiative stopping power is the electron energy loss due to bremsstrahlung production. The main contribution to this is from Coulomb interaction of electron with the field of the nucleus (electron-nucleus bremsstrahlung). Also there is the Coulomb interaction with the field of the atomic electrons (electron-electron bremsstrahlung). The total mass radiation stopping power is proportional to  $Z^2 + Z\eta$ , where  $Z^2$  and  $Z\eta$  show the contributions from the electron-nuclear and the electron-electron bremsstrahlung, respectively (Seltzer and Berger, 1982).  $\eta$  varies from zero for very low energy electrons to the order of unity for electron energies more than a few  $MeV$ .

### 1.3.2. Scattering power

As mentioned in the previous section electron interactions with matter are Coulomb interactions. Therefore, electrons passing through a medium suffer multiple scattering and their directions change. The rate of scattering can be expressed using the mass scattering power,  $T/\rho$  [ $rad^2 cm^2 g^{-1}$ ]. The mass scattering power is defined as the increase in the mean square angle of scattering,  $\overline{d\theta^2}$ , per travelled distance,  $ds$ , per density,  $\rho$  (Li and Rogers, 1995), that is:

$$\frac{T}{\rho} = \frac{\overline{d\theta^2}}{\rho ds} \quad (1-16)$$

$\frac{T}{\rho}$  is sensitive to the theory used in the calculation. For many practical purposes, the angular and spatial distributions can be expressed by Gaussian functions, as defined in the Fermi-Eyges theory (Li and Rogers, 1995). The Molière multiple scattering theory has been shown much better agreement with experiment than using a Gaussian model, but at the expense of complexity.

## 1.4. Dosimetry parameters

### 1.4.1. Depth doses

As a beam is incident on a patient or a phantom (e.g., water), the absorbed dose in the medium varies with depth. The variation depends on the beam geometry, quality, and the medium composition. The percentage depth dose,  $P$ , for a  $r \times r$  square field at depth  $d$  along the central axis can be defined as:

$$P(d, r, SSD) = \frac{D(d, r, SSD)}{D(d_{max}, r, SSD)} \times 100, \quad (1-17)$$

where  $SSD$  is the radiation source to the surface distance (this is a general term which in case of  $x$ -ray source it is called focus to the surface distance,  $FSD$ ) and  $d_{max}$  is depth of maximum dose.

Figure 1.3 shows a 6  $MV$  photon depth dose curve for  $10 \times 10 \text{ cm}^2$  field at  $FSD=100 \text{ cm}$ , together with the collision kerma. As it is seen from this figure, the collision kerma is maximum at the surface and decreases with depth monotonically. However, there is an initial build-up of dose with depth and after a maximum it will gradually decrease. The build-up is due to the finite range of electrons set in motion by photon interactions and the fact that these electrons deposit their energies (on average) deeper than the site of photon interaction. This effect becomes more pronounced for high energy beams and gives them the advantage of the skin-sparing effect. The build-up region is well explained by Johns and Cunningham (1983) and Khan (1994).

Depth dose distributions depend on the beam quality and increase with energy at depths beyond  $d_{max}$ , as it is shown in Figure 1.4. The choice of radiation type and energy for an optimum treatment is made according to the tumour position and depth. For a shallow tumour electron or low energy photon beams are preferred, due to their more rapid dose fall off with depth. On the other hand, for a deep tumour, such as in the pelvis, higher energy photons are preferred. The increase in dose beyond  $d_{max}$  as beam energy increases becomes small for high energies, because there is a less than linear decrease in mass attenuation coefficient with increase in energy. Furthermore higher energy photon beams give rise to secondary electrons with larger range and the problems of electronic disequilibrium then increase. In Figure 1.4 the central axis depth dose curves for  $Co-60$ ,

4, 6, 10 and 23 *MV* photon beams and also for 15 *MeV* electrons are shown for comparison. Depth doses are for  $10 \times 10 \text{ cm}^2$  fields and  $SSD=100 \text{ cm}$ . *Co-60* depth dose for  $SSD=80 \text{ cm}$  is also included. *Co-60* depth dose curves are from Monte Carlo calculations (see chapter 4) and all others are experimental results.

In choosing radiation type and energy, it is important to notice the surface dose, depth of maximum dose, and penetration of the beam. Among radiations shown in this figure, the electron beam gives a good uniform depth dose up to 3 *cm* depth. One of the main advantages of electron beams is a very steep dose gradient in the fall off region, as is seen here, and sparing healthy tissues beyond the target. *Co-60* has a shallow  $d_{max}$  ( $=5 \text{ mm}$ ), but the penetration is not small. 4 *MV x-rays* have almost the same penetration and fall off rate as *Co*, since this property of depth dose curves is determined mainly by the mean energy of the photon beams (for the same field size), but with a  $d_{max} = 10 \text{ mm}$ . This is because the depth of maximum dose and the surface dose are determined by the maximum energy of photon beam, as well as the electron contamination. The surface dose for the *Co-60* is unexpectedly low in this figure, because the *Co* depth dose curves, as mentioned before, are results of Monte Carlo calculations and the fact that neither electron contamination nor scattered photons from the source capsule and collimator were modelled. The expected scattered photon contribution from the source capsule and collimator to the *Co-60* spectrum is about 30% (Li et al, 1995).

Depth dose distributions also depend on the *SSD* and field size. The depth dose beyond  $d_{max}$  is greater for larger *SSD* because of a lesser inverse square fall off. This is shown in Figure 1.4 for *Co-60*. Dependence on the field size is more complex. The build-up thickness ( $d_{max}$ ) is less for small size photon beams, increases to a maximum for field sizes about  $5 \times 5 \text{ cm}^2$  and then decreases for larger field sizes (Arcovito et al, 1985 and Sixel and Podgorsak, 1994). The original increase in  $d_{max}$  is due to the fact that electrons originating further from the central axis tend to deposit their energy at greater depths. This will increase  $d_{max}$  until the field is large enough such that electrons originating at the edge of the field do not reach the central axis. The reduction for larger fields is due to the electron contamination (Sixel and Podgorsak, 1993 and 1994). Depth dose beyond the build-up region, however, increases uniformly with field size due to the increase in scattered photons (whose peak in energy deposition is beyond  $d_{max}$ ).

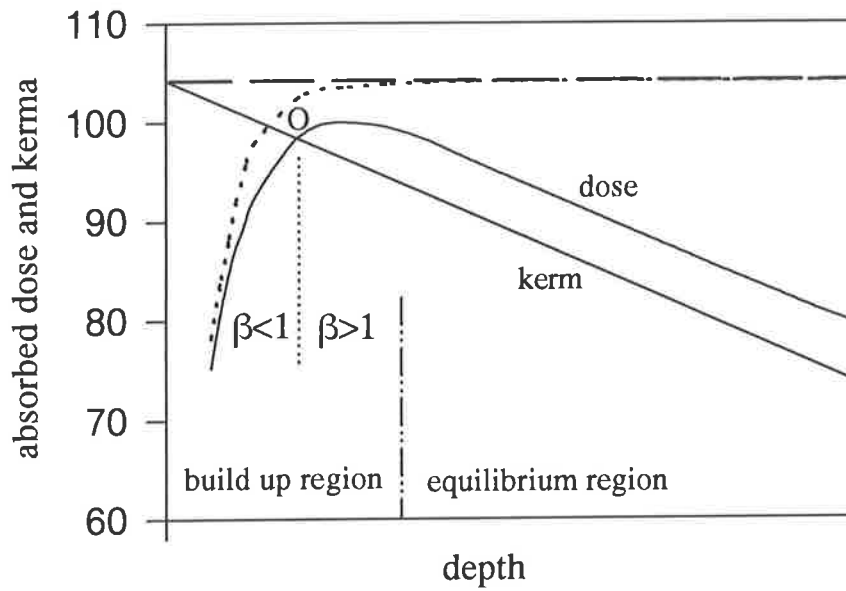


Figure 1.3. Variations of absorbed dose and kerma (relative response) with depth in water for a 6 MV photon beam.

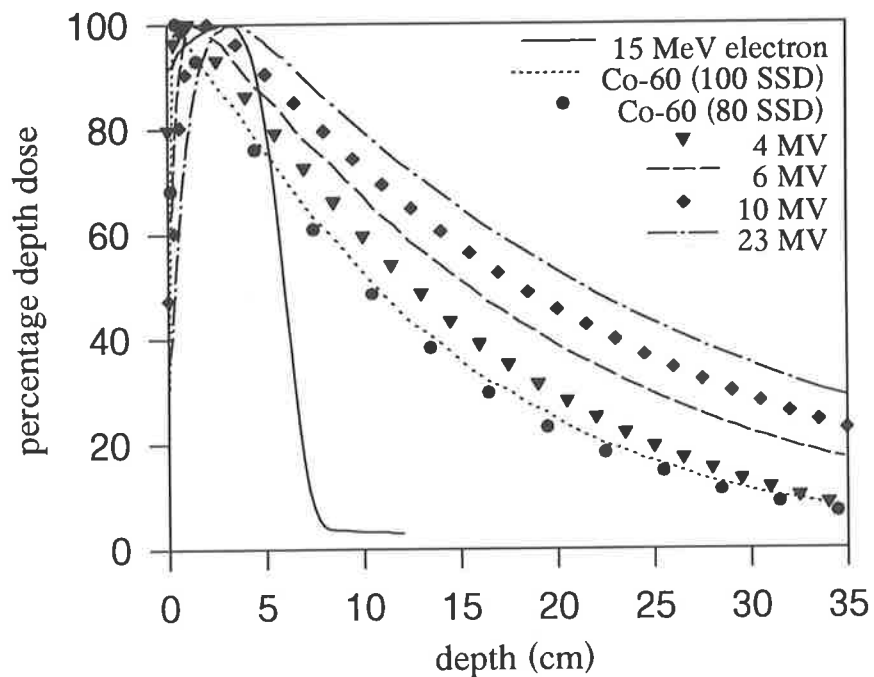


Figure 1.4. Central axis depth dose curves for  $10 \times 10 \text{ cm}^2$  fields for *Co-60*, 4, 6, 10 and 23 MV photon beams and also for 15 MeV electrons at  $SSD = 100 \text{ cm}$ . Also *Co-60* depth dose curve at  $SSD = 80 \text{ cm}$  is shown for comparison.

By increasing the nominal energy, as it is seen from Figure 1.4, the penetration and so the depth dose increases (but to a lesser extent for higher energies). In treating a 15 cm deep tumour with the *Co-60*, the percentage depth dose at the tumour site is less than 40% (the surface dose is more than twice), while the percentage depth dose for 23 MV is over 65% with a surface dose much less (about half as much). This is the advantage of higher energy beams, but with the expense of a higher exit dose as well as a wider penumbra, due to increased electron range. Also this can have regions of electronic disequilibrium for small fields or low densities which can cause difficulties in dosimetry and treatment planning. Indeed, beyond 15 MV photon energy there is not much gain, but complications regarding to increase in lateral electronic disequilibrium. This includes the interface dose nonuniformity and larger penumbra.

#### 1.4.2. Tissue air ratio

The tissue air ratio (*TAR*) is the ratio of the dose at a given point in the phantom,  $D_d$ , to the dose at the same point in air,  $D_0$ , with sufficient build-up material to provide electronic equilibrium at that point. The main property of the *TAR* is that, in contrast to the percentage depth dose, it is independent of *SSD*. Also important is that the variation of *TAR* with field size is only dependent on phantom scatter, as the collimator scatter effects are contained in both numerator and denominator. *TAR* for a given material and a beam quality depends on the depth,  $d$ , and the field size,  $r_d$ , at that depth and has almost the same variation as percentage depth dose, except that there is no inverse square effect to contribute to the dose fall off.

$$TAR(d, r_d) = \frac{D_d}{D_0} \quad (1-18)$$

The tissue air ratio at the depth of maximum dose ( $d_{max}$ ) on the central axis is called back-scatter factor (*BSF*), or peak-scatter factor (*PSF*) for *x-rays* generated above 400 kV (supplement 17, *BJR*). As expected from its name, *PSF* represents the increase in the total dose at  $d_{max}$  due to phantom scatter.

$$PSF = TAR(d_{max}) = \frac{D_{max}}{D_0}, \quad (1-19)$$

where  $D_{max}$  is the dose at  $d_{max}$  in the phantom.  $PSF$  is dependent on the irradiated volume (for a given phantom thickness only depends on the field size at  $d_{max}$ ) and the beam quality, so that it is maximum at half value layer ( $HVL$ ) of about  $0.7 \text{ mm Cu}$  and increases with field size. The relationship between  $TAR$  and percentage depth dose,  $P$ , is determined from their basic definitions so that:

$$P(d, r, SSD) = TAR(d, r_d) \frac{1}{PSF_r} \left( \frac{SSD + d_{max}}{SSD + d} \right)^2 \times 100, \quad (1-20)$$

where  $r$  and  $r_d$  are field sizes at the surface and depth  $d$ , respectively.

### 1.4.3. Scatter air ratio

Scatter air ratio ( $SAR$ ) at a point is defined as the ratio of the scattered dose to the primary dose (the dose in free space) at that point.  $SAR$ , like  $TAR$ , is independent of  $SSD$ , but depends on the depth, field size and beam quality.

The total dose at any point in phantom consists of the primary and scattered dose:  $D_{tot} = D_p + D_s$ . Dividing both sides of this equation by the dose in free space,  $D_0$ , gives:

$$\frac{D_{tot}}{D_0} = \frac{D_p}{D_0} + \frac{D_s}{D_0}, \quad (1-21)$$

where  $\frac{D_{tot}}{D_0} = TAR(d, r)$  and  $\frac{D_s}{D_0} = SAR(d, r)$  is the scatter air ratio. Also  $\frac{D_p}{D_0} = TAR(d, 0)$ ,

which is the  $TAR$  at depth  $d$  and zero field size, giving the primary dose. The tissue-air ratio is thus given in terms of the zero-area  $TAR$  and the  $SAR$  as:

$$TAR(d, r_d) = TAR(d, 0) + SAR(d, r_d) \quad (1-22)$$

This separation is especially useful in irregular beam dose calculations, where the  $SAR$  is used to account for scatter from each volume in the irradiated medium.

#### 1.4.4. Collimator output factors

Collimator total output factor ( $OF$ ) is the relationship between the dose per monitor unit for each collimator to that under calibration conditions (Holt et al, 1970).  $OF$  is defined as the ratio of the measured dose,  $R(r)$ , for field size  $r$  to that of the calibration condition,  $R(c)$ , (which for linear accelerators is normally the value for a  $10 \times 10 \text{ cm}^2$  field at  $d_{max}$  and  $FSD=100 \text{ cm}$ ).

$$OF(r) = R(r) / R(c) \quad (1-23)$$

The collimator total output factor,  $OF$  can be separated into the collimator scatter factor,  $CF$ , and the phantom scatter factor,  $PF$ , by the following formula (Khan et al, 1980; Arcovito et al, 1985 and Haider and El-Khatib, 1994):

$$OF (r) = CF (r) \times PF (r) \quad (1-24)$$

This separation is important in dose calculation (Khan et al 1980).  $CF(r)$  is the ratio of reading of the collimated beam to that of the calibration condition, when measurement is performed in air with enough build up material to provide electronic equilibrium.  $PF$  is the phantom scatter contribution at  $d_{max}$ , that is  $PSF$ .  $CF$  expresses the increase in dose with field size which occurs due to increased photon fluence and  $PF$  expresses the increase due to in-phantom scatter.

#### 1.4.5. Tissue phantom and tissue maximum ratios

The tissue phantom ratio ( $TPR$ ) is the ratio of the dose at a given point in phantom to the dose at the same point at a reference depth (usually  $5 \text{ cm}$ ). If the reference depth is at depth  $d_{max}$ , the ratio is called tissue maximum ratio ( $TMR$ ).  $TMR$ , like  $TPR$  and  $TAR$ , is independent of  $SSD$  and does not suffer from inverse square variation of the beam. The relationship between  $TMR$  and percentage depth dose,  $P$ , is as follows:

$$TMR (d, r_d) = \left( \frac{P(d, r, FSD)}{100} \right) \left( \frac{FSD + d}{FSD + d_{max}} \right)^2 \left( \frac{PF(r_{d_{max}})}{PF(r_d)} \right), \quad (1-25)$$

where  $r$  is the field size at the surface,  $r_d = r \cdot \left(\frac{FSD+d}{FSD}\right)$  and  $r_{d_{max}} = r \cdot \left(\frac{FSD+d_{max}}{FSD}\right)$ . Also

$TMR$  and  $TAR$  are interrelated by the following equation:

$$TMR(d, r_d) = \frac{TAR(d, r_d)}{PSF(r_d)}, \quad (1-26)$$

where  $r_d$  is the field size at depth  $d$ .

#### 1.4.6. Scatter-maximum ratio

Scatter-maximum ratio ( $SMR$ ) is the ratio of the scattered dose at a point in a phantom to the primary dose at the same point at  $d_{max}$ .  $SMR$  has the same property as  $SAR$ , except it is more applicable in higher energy beams.  $SMR$  is useful in scatter dose calculations, especially in irregular field dosimetry (Khan, 1994) and is related to the  $TMR$  by:

$$SMR(d, r_d) = TMR(d, r_d) \left( \frac{PF(r_d)}{PF(0)} \right) - TMR(d, 0) \quad (1-27),$$

where  $PF(0)$  is the extrapolated phantom scatter correction factor for zero area field size and  $TMR(d, 0)$  is the extrapolated value of  $TMR(d, r)$  for  $r = 0$ . The current definition of  $SMR$  (Khan et al, 1980) is not zero for all field sizes at  $d_{max}$ , unlike the old definition which was simply  $SMR(d, r_d) = TMR(d, r_d) - TMR(d, 0)$ .

#### 1.5. Electronic equilibrium

Electronic equilibrium exists when primary dose is equal to collision kerma; that is, when energy transferred to charged particles in a small mass (excluding that which will be converted to bremsstrahlung) is equal to the energy deposited in that mass. Because of the significant range of charged particles in megavoltage photon beam irradiation, this occurs only at a single depth (point "O" in Figure 1.3). Since charged particles predominantly travel in the forward direction, and kerma is decreasing with depth (due to attenuation of the photon beam), dose is greater than collision kerma for depths

greater than that where collision kerma equals dose (point  $O$ ). Transient electron equilibrium is then said to exist.

Secondary electrons have a maximum range,  $R$ , in the forward direction which is almost the same as  $d_{max}$ . Lateral electronic equilibrium exists at a point in the beam, if the distance of that point to the nearest beam edge or medium boundary is more than the maximum lateral range of electrons,  $R_{lat}$ . Similarly, the lateral electronic equilibrium exists at the central axis if the beam diameter is greater than or equal to  $2R_{lat}$ , as shown in Figures 1.5(a) and (b). In this figure, beams are shown as shaded area with parallel lines representing photon beams. In Figure 1.5(c), however, the beam diameter is less than  $2R_{lat}$  and hence there is electronic disequilibrium at the central axis of this beam. In this case there is a lack of secondary electrons at the central axis which could have originated from regions outside the beam boundaries (within distance  $R_{lat}$  from central axis). These regions are shown within grid lines in this figure.  $R_{lat}$  increases with photon energy and a reduced medium density.

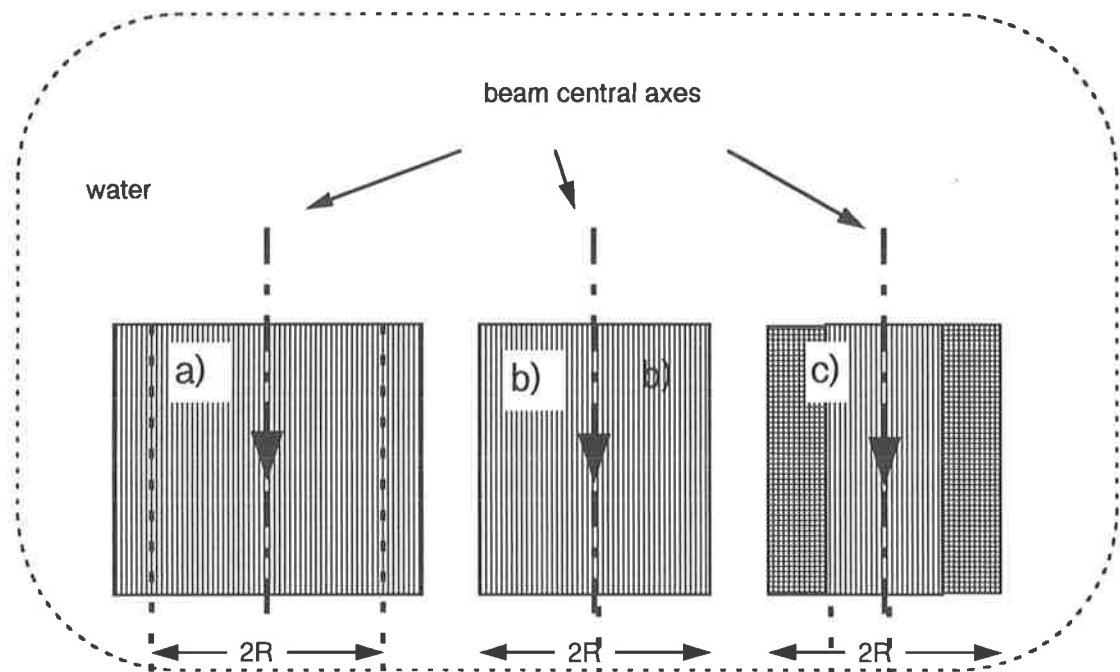


Figure 1.5. Lateral electronic equilibrium at the central axis of a beam exists when the beam diameter is (a) greater than or (b) equal to  $2R_{lat}$ , and does not exist when the beam diameter is smaller than  $2R_{lat}$  (c).

The effects of photon energy and medium density on the lateral electronic equilibrium are shown in Figure 1.6. In this figure ratios of total dose to collision kerma at the

central axis are shown for different beam diameters for *Co-60*, 6 *MV* and 23 *MV* photon beams. These results were obtained with Monte Carlo simulations, using the reciprocity technique (see chapter 4 of this thesis for more detail). The ratios are at 5 *cm* depth in water for the parallel photon beams. As is seen from this figure, for very small field sizes the ratios are less than 1, due to lateral electronic disequilibrium. The ratio increases with the beam diameter and reaches unity when the beam diameter reaches  $2R_{lat}$  of the relevant beam. It is seen from this figure that the lateral electronic equilibrium for *Co-60*, 6 *MV* and 23 *MV* photon beams establish at 6, 30 and 80 *mm* beam diameters, respectively. The effect of medium density is also shown in this figure, when the *Co-60* simulation was performed in a medium of water composition but of density  $0.25 \text{ g/cm}^3$ . Lateral electronic equilibrium is in this case reached at 25 *mm* beam diameter, in agreement with the density scaling theorem (O'Connor, 1957), for a given beam quality:

$$\rho_1 R_{lat(1)} = \rho_2 R_{lat(2)}, \quad (1-28)$$

where  $\rho_1$ ,  $\rho_2$ ,  $R_{lat(1)}$  and  $R_{lat(2)}$  are media densities and the maxima lateral electron ranges in those media, respectively.

## 1.6. Dose distributions

Central axis depth dose distributions (discussed in section 1.4), are not sufficient for dose characterisation in a three dimensional volume. The dose variation across the field, that is in a plane perpendicular to the beam central axis, is best determined by beam profiles. Figure 1.7 shows the beam profile for a 23 *MV* photon beam,  $40 \times 40 \text{ cm}^2$  field size, measured at depth  $d_{max}$ , at the isocenter level, that is at 100 *cm* source axis distance (*SAD*). Dose profiles are usually normalised to 100% at central axis and the beam width is defined as the profile width at 50%. In general physics this is known as the full width at the half maximum (*FWHM*) of the beam.

The dose at any depth is normally maximum at central axis of the beam, except for some linear accelerator beams in which the maximum dose is near beam edges (called horns) and the minimum dose is at the central axis (called dip), as it is seen from Figure 1.7. These are created by the flattening filter, and lead to a uniform dose across the

beam (flat profile) at greater depths (normally 10 *cm* deep). Horns (and dips) disappear with depth because (i) there is a larger increase in scattered dose at central axis than at the edge, (ii) near the beam edges, the beam is softer (due to flattening filter being thinner), and (iii) the beam attenuation with depth is more for beams which are further away from central axis, due to their obliqueness. As it is seen from Figure 1.7, near the edges of the beam, that is in the penumbra region, the dose drops very rapidly. The penumbra width is defined as the distance between two specified dose levels, normally 90%-10% or 80%-20%. A small penumbra is best to ensure dose is conformed to the target volume. The penumbra is due to both the finite source size (the geometric penumbra) and, mainly, the lateral range of secondary electrons in the medium. The geometric penumbra depends on the source size, distance from the source, and source to the collimator distance. Penumbra width generally increases with beam energy due to the increased secondary electron range.

Isodose curves are another way of visualising the dose distribution. An isodose curve is a line passing through points of equal dose. A family of isodose curves with different dose values for a given beam is called an isodose chart. Figure 1.8(a) shows an isodose chart (from the General Electric *RT Plan* system) for a 6 *MV* photon beam, 10×10 *cm*<sup>2</sup> field and *SSD*=100 *cm*, with dose increments of 10%. The isodose normalisation is performed either at depth of maximum dose on the central axis or at the isocenter. These correspond to treatment at a constant *SSD* and isocentric therapy, respectively. Isodose charts are normally in a plane containing the beam central axis (as in this figure) or perpendicular to that, but they can be in any other plane, depending on the region of interest. Isodose charts are very important in assessing treatment planning process in visualisation of the dose conformability around the lesion and the dose to the healthy tissues, especially critical organs. This becomes more important when a complex combination of techniques are used, such as in stereotactic radiosurgery (*SRS*).

### 1.7. Wedge filters

Isodose distributions can be modified by placing special filters or blocks in the way of a beam. Wedge filters are commonly used for this purpose. These are wedge-shaped absorbers, normally made of a dense material such as lead or steel. Passing through

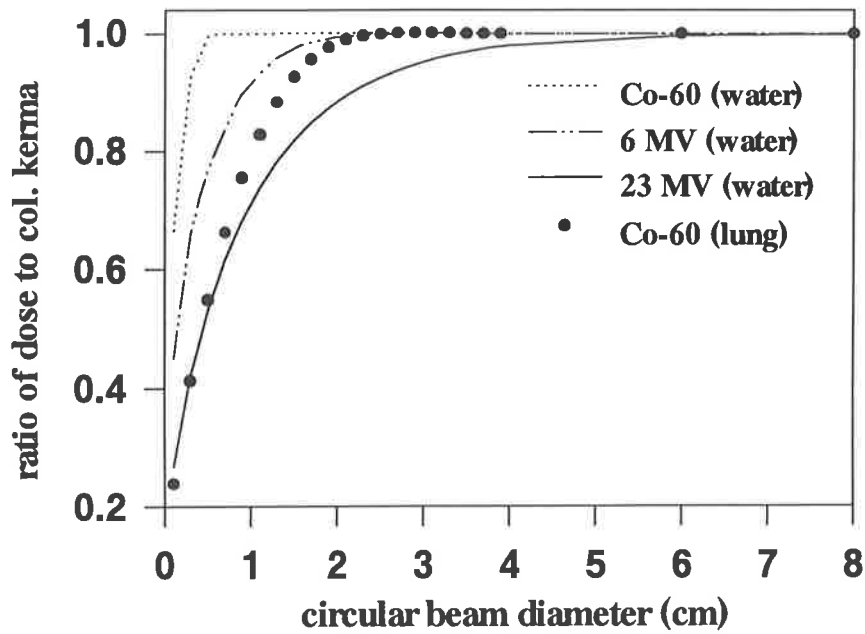


Figure 1.6. Ratios of total dose to collision kerma at the central axis are shown for different parallel beam diameters for *Co-60*, 6 and 23 MV photon beams. Lateral electronic equilibrium achievement at the central axis depends on the photon energy. The effect of medium density on this achievement is shown for *Co-60* beam in the lung ( $\rho = 0.25$ ).

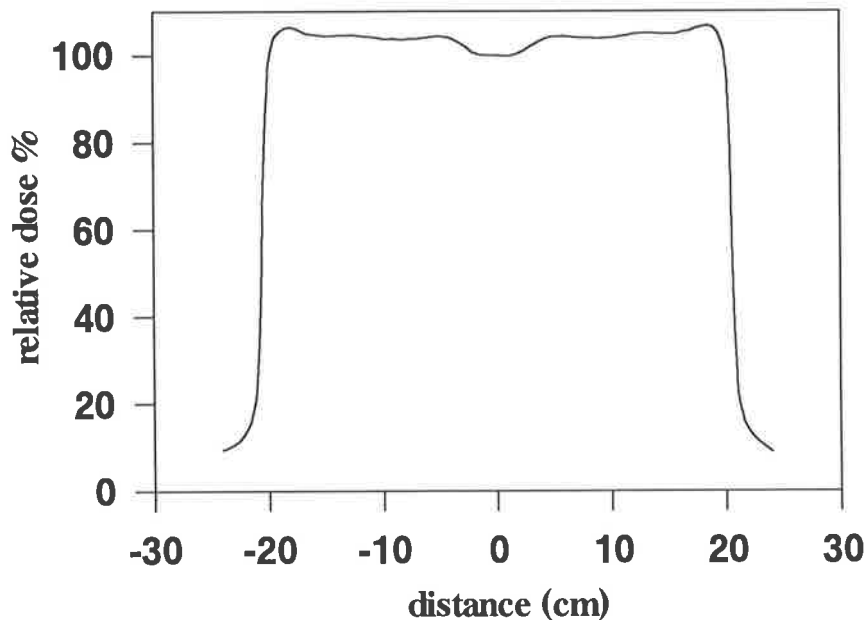


Figure 1.7. Beam profile measured at depth  $d_{\max}$  for a 23 MV photon beam,  $40 \times 40 \text{ cm}^2$  field size, at the isocenter level ( $SAD = 100$ ).

different thickness of a wedge filter, the beam will have a differential attenuation across the field, resulting in a tilt in the isodose curves, as shown in Figure 1.8(b). The wedge angle is sometimes (especially for *Co-60* and lower energy photon beams) defined as the tilt angle of the 50% isodose curve at the central axis. For high energy photon beams, however, because of the greater depth of 50% dose, the above definition is not very efficient. The wedge angle in this case can be defined as the tilt angle of an isodose line at a specific depth on the central axis. The wedge (transmission) factor is defined as the ratio of the dose with wedge to the dose without wedge (open field) at a depth beyond  $d_{max}$  on the central axis of the beam.

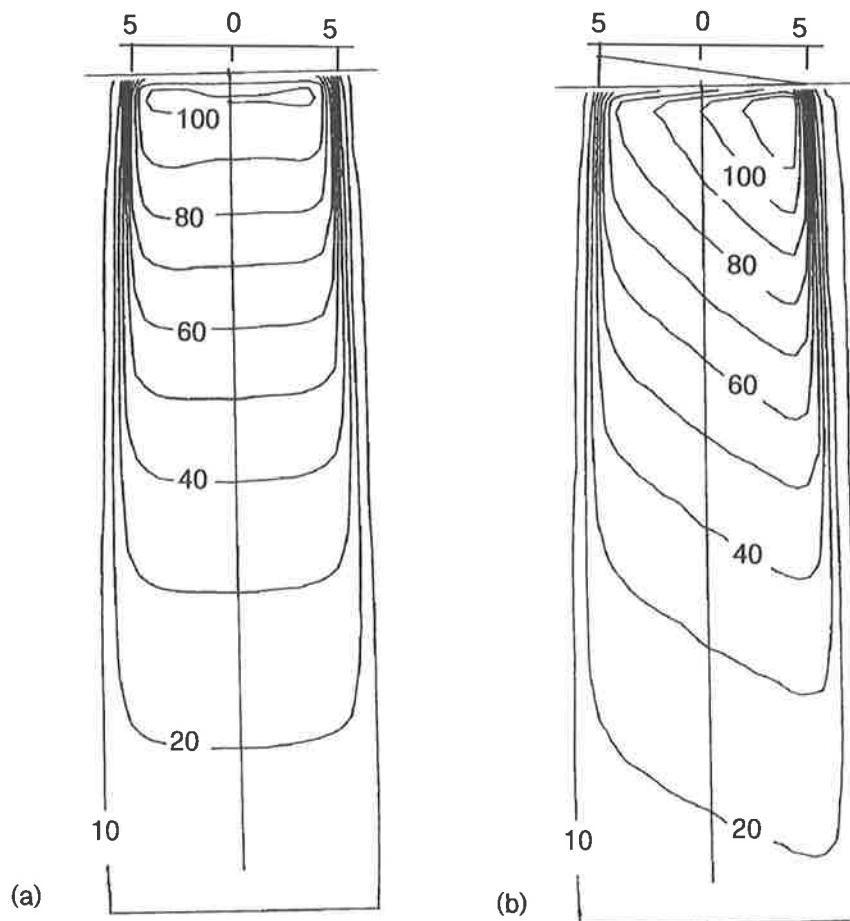


Figure 1.8. Isodose charts in a plane containing central axis for a 6 MV photon beam,  $10 \times 10 \text{ cm}^2$  field and  $SSD=100 \text{ cm}$ , (a) for an open field and (b) the effect of a  $45^\circ$  wedge on that.

### 1.7.1. Dynamic wedge

In linear accelerators with computer controlled asymmetric jaws, it is possible to create the effect of a wedge by moving one or two jaws while the beam is on. The dose profile can be made the same as using conventional wedges and or can be a desirable customised dose distribution. The idea first was applied by Leavitt et al (1990). Dynamically wedged fields are slightly more penetrating than the equivalent open fields (Thomas and Foster, 1995), although there is not the beam hardening effect as is the case for conventional wedges. This is caused by the dose gradient effect (Kalend et al, 1990) and for a 60° degree dynamic wedge is in the order of 2% of the dose at 25 cm depth, for a 10×10 cm<sup>2</sup> field, 6 MV photon beam and becomes negligible for 15° dynamic wedge. The dose gradient effect is found by above authors to be due to the differences in scattered radiations from within the phantom of wedged and open fields. Dynamic wedging and the related algorithms give good agreement with measurements, in terms of depth doses, profiles and the wedge factors. Also, the method is fast enough for routine treatment planning (Thomas and Foster, 1995).

### 1.8. Combination of radiation fields

In radiotherapy generally a combination of two or more fields is used in order to have a uniform dose across the tumour and also to spare the skin and have an acceptably low dose to the surrounding normal tissues. Different combinations of open and wedge fields with either static or rotation therapy may be used, depending on the tumour size, depth, and position relative to other organs (especially critical organs). Superficial tumours are the exception where normally a single beam is used. Figure 1.9 shows a combination of an anterior open field and two lateral wedge beams to cover the target using a 4 MV photon beam.

### 1.9. Conformal therapy

It is a long time since Takahashi et al (1961) suggested conformation radiotherapy as a way to match exactly the high-dose region in the target volume and the prescribed target contour. However, it has been only in the last few years, with more powerful

computers for treatment planning and computer-driven treatment delivery systems such as multi-leaf collimators (*MLCs*) and on-line verification systems, that this has become possible. The degree of conformability depends on the diagnostic tools ability to differentiate true anatomical tumour from surrounding healthy tissues, as well as the accuracy of the treatment planning and delivery systems.

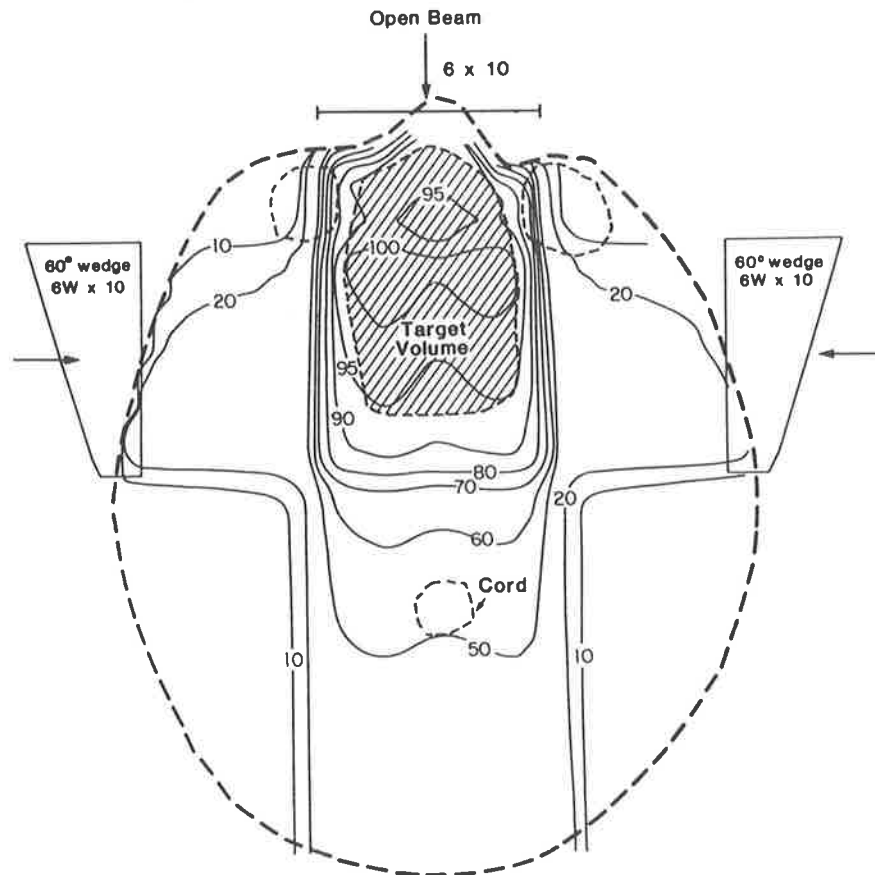


Figure 1.9. Combination of an anterior open field and two lateral wedge fields using 4 *MV* photon beam (from Khan, 1994).

The similarity between performing computed tomography (*CT*) and conformation therapy has been mentioned in the last few years (Brahme, 1988; Webb, 1989; Carol, 1992 and Holmes and Mackie, 1994). This similarity is shown in Figure 1.10 and the reason why the method is known as “*tomotherapy*” or “*inverse radiotherapy*”. *CT* delivers a spatially uniform radiation exposure at the skin surface, measuring the spatially non-uniform attenuation of the exit beam, while in tomotherapy (or intensity modulation radiotherapy) a spatially non-uniform radiation exposure is delivered to the

skin surface to create a uniform dose distribution across the target (Carol, 1992) or to obtain a biologically optimal dose distribution (Holmes and Mackie, 1994). The method for a true 3-D conformal therapy requires variable intensity modulation across a dynamic geometrically shaped beam.

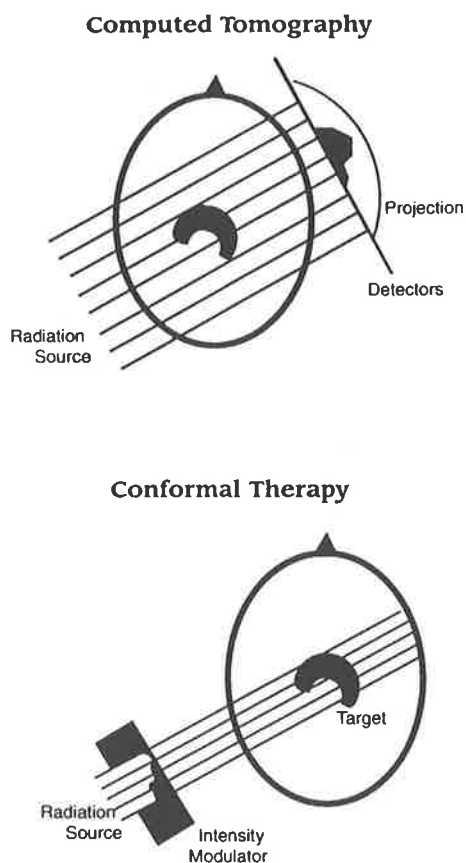


Figure 1.10. Intensity modulation radiation therapy compared to *CT* (from Carol, 1992).

A better analogy is with *SPECT*, where the distribution of a radionuclide within the patient is determined by “backprojecting” the photon intensity profiles outside the patient. In inverse planning, a desired dose distribution within the patient (analogous to the radionuclide distribution) is “projected” to obtain the required beam intensity profiles. As mentioned before, the goal of 3-D treatment planning is to conform a high radiation dose to the shape of the tumour contour while keeping the integral dose to the surrounding tissues as low as possible. As a result, the local tumour control improves while the radiation toxicity is reduced; this will consequently enhance the long-term survival in principle. Figure 1.11(a) shows a treatment plan example where a C-shaped

lesion, partially wraps around a circular critical structure. Intensity modulated arc therapy is used in this case to conform the dose to the target. The delivery dose distribution is shown in Figure 1.11(b). As it is seen from this figure a good degree of conformability has been achieved in this example, as an extreme case.

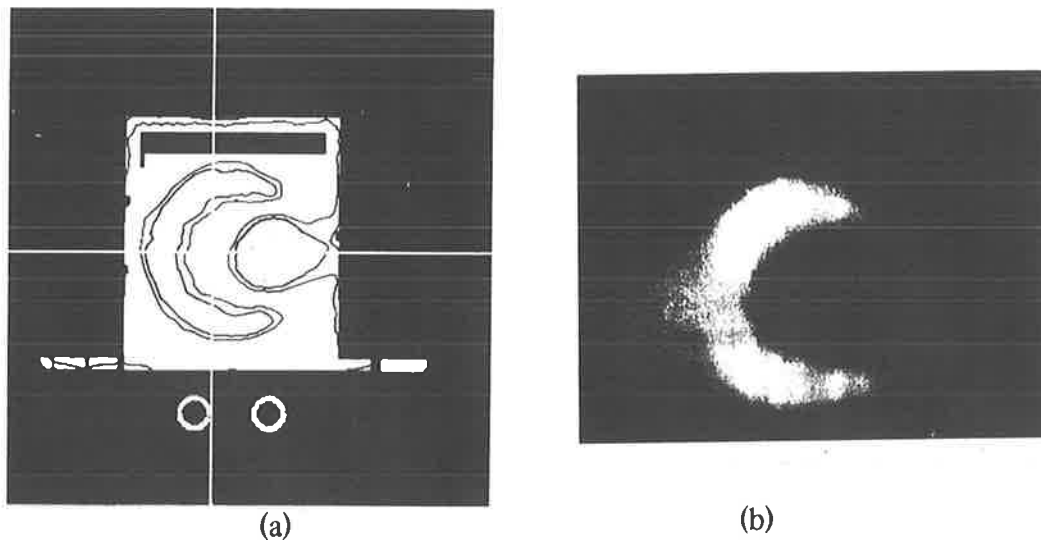


Figure 1.11. (a) A treatment plan example for the intensity modulated arc therapy. The inner and outer isodose contours are 90% and 80% on the C-shaped target, 10% and 20% on the circular critical structure, respectively. (b) Delivered dose distribution for the treatment plan as a grey scale, with the high-dose area as the light regions (Yu, 1995).

### 1.10. Three dimensional treatment planning

Depth dose distributions, discussed in previous sections, are normally measured in a water phantom which is homogeneous and has a flat surface and the beam is incident perpendicularly on the surface. A patient body, of course, is neither homogeneous nor flat. The treatment planning task is to calculate dose distributions in regions of interest within the patient, normally using measurements made in a standard water phantom. Patient data, including tissue inhomogeneities (in terms of electron densities) and contour curvature are required for this calculation.

In the Target treatment planning system, which is used in the Radiation Oncology department at the Royal Adelaide Hospital, photon beam data is stored at 17 equally spaced data points along the central axis (*CAX*). The *CAX* numbers 1 and 17 are at depths  $d_{max}$  and a user-defined depth (i.e. 30-40 cm), respectively. Also, off axis factors

(profile data) are stored on 47 divergent grid lines at five different depths corresponding to *CAX* numbers 1, 5, 9, 13 and 17, as is shown in Figure 1.12.

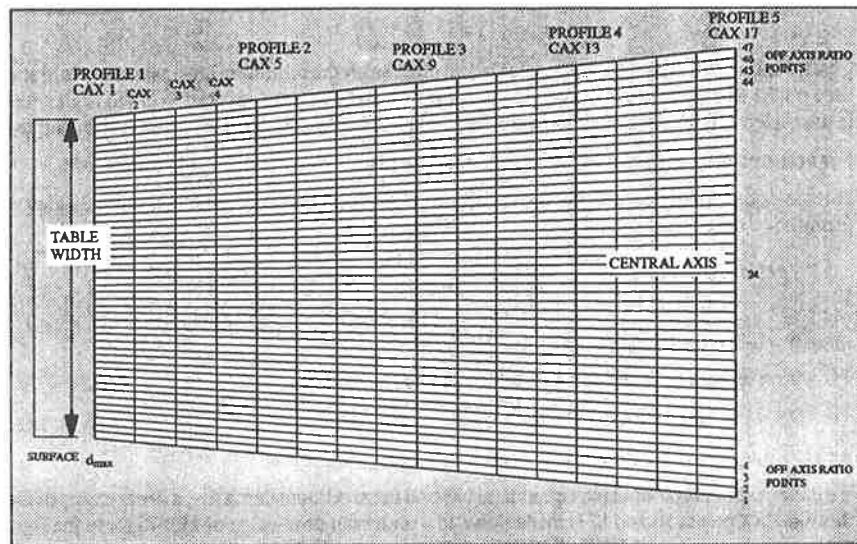


Figure 1.12. Photon beam data storage grid at different depths and off axis distances (from GE Medical System).

Before storage, the treatment planning software converts the percentage depth doses at the measurement *SSD* to infinite *SSD* data (*CAX* values), using the following formula:

$$CAX(r, d) = P(\infty, r, d) = P(SSD, r, d) \times \left( \frac{SSD + d}{SSD + d_{max}} \right)^2, \quad (1-29)$$

where  $r$  is the field size at the surface and  $P(\infty, r, d)$  is the percentage depth dose at depth  $d$  and infinite *SSD*. For dose calculation at a point at depth  $x$  in the build-up region, the system makes a linear interpolation between a user-defined surface dose value and the dose at  $d_{max}$  for a modified depth  $x'$  below the surface which is given by:

$$x' = d_{max} - \frac{(d_{max} - x)^3}{(d_{max})^2} \quad (1-30)$$

This gives an acceptably accurate result. Off axis factors are measured at the five different depths mentioned above and profiles at any other depth are obtained by linear interpolation of those profiles. Profiles must be entered for open and wedge fields, and each profile is normalised to 1 at the central axis. In addition to above data, the

following information is required for each beam by the system in order to create a photon beam file:  $SSD$ ;  $d_{max}$ ; dose rate at this  $SSD$  ( $cGy/MU$  for those machines which operate with monitor unit instead of time settings); half life, in years for radioactive source machines;  $CAX$  separation (mm);  $ISO-SSD$  (this difference is required if the isocentric distance is different from standard  $SSD$ ); dose at the skin surface,  $D_s$ ;  $PSF$  (or  $BSF$ ); wedge No.; and Table width at  $SSD$ .

Patient data is provided by  $CT$ -Scans and patient  $3-D$  anatomy is reconstructed from individual transverse scans. The distance between  $CT$  slices should be sufficiently small to provide accurate reconstruction. Depending on the tumour size and position and also the complexity of the tumour site,  $CT$  slices with 2 to 10 mm separation are taken. In the planning process, delineation of target and critical organs has to be done on each slice for the  $3-D$  reconstruction of these structures. This is a time consuming process, but features like automatic contouring can be helpful in this regard. Apart from this an extensive and a high-tech computing calculation is required for  $3-D$  treatment planning dose calculation which may not be realistic and cost effective for routine radiotherapy. However, the cost can be justified if the procedure significantly improves the tumour control probability. Certainly the case where high geometric and dosimetric precision is required, as in stereotactic radiosurgery ( $SRS$ ) for treatment of brain tumours. This procedure will be discussed in coming chapters as a major part of this thesis. The treatment of these tumours by  $SRS$  has greatly benefited by  $3-D$  treatment planning.

### **1.11. Three dimensional dose calculation techniques**

Treatment planning dose calculation for the patient is performed by applying correction factors to the water phantom data to account for tissue inhomogeneities and body contours. The presence of inhomogeneities will affect the dose distribution in different ways, depending on the photon energy and field size. For orthovoltage and lower energy  $x$ -rays the photoelectric process has an important effect and dose to the bony structures (high atomic number) is higher than in surrounding soft tissues. In megavoltage beams however, the Compton effect is the dominant interaction where the attenuation of the beam in a tissue depends on the electron density (number of electrons

per  $cm^3$ ). In this case the inhomogeneity correction is performed by incorporating the electron density of the appropriate tissue relative to water. Different dose calculation techniques are used for inhomogeneity corrections, in which electron densities (relative to water) are generally found from the relevant  $CT$  numbers. The inhomogeneity correction can be applied in two different ways. Firstly, the “bulk” method in which an inhomogeneity region such as lung can be outlined and a density is assigned to the outlined region and a density correction factor is then calculated (ie., correction to dose). Secondly, the “pixel-by-pixel” method, where the  $CT$  number of each pixel (and hence the relevant electron density of that pixel) is used for all tissue inhomogeneities along the path of the radiation beam.

The bulk method is used where the  $CT$  data is not available, can not be utilised, or when a quicker dose calculation is desirable. The density of the outlined region in this model may be entered manually or if  $CT$  data is available may be obtained automatically. In the latter case the average  $CT$  number for the entire region of interest is found and converted to a density. In the pixel-by-pixel correction method there is no need for outlining an anatomical region. Instead, correction for all variations in tissue inhomogeneities is performed by calculating the equivalent thickness of each pixel automatically.

Figure 1.13 shows a simple geometry of a semi-infinite inhomogeneity of a thickness  $d_2$  with a relative electron density  $\rho_e = 0.25$  (e.g., lung) which is surrounded by two semi-infinite layers of water ( $\rho_e = 1$ ). The dose calculation point,  $P$ , distances from the lower and upper levels of the inhomogeneity are  $d_3$  and  $d_2 + d_3$ , respectively. The dose at point  $P$  at depth  $d = d_1 + d_2 + d_3$  on the central axis of the beam is to be found using different dose calculation techniques in the following sections and results compared.

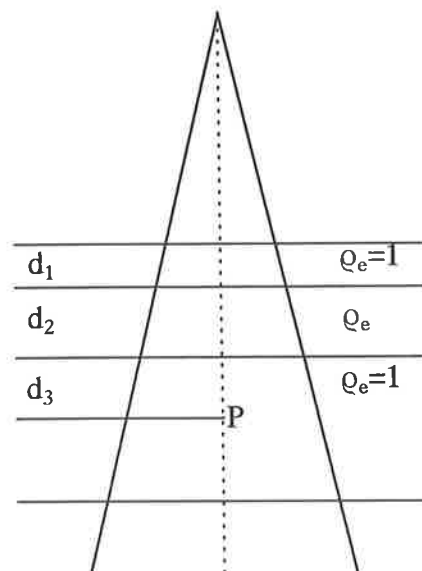


Figure 1.13. Water-cork-water semi-infinite slabs as a simple inhomogeneity model for dose calculation.

### 1.11.1. Effective path length method

Effective path length (*EPL*) method simulates the effect of inhomogeneities by replacing them with an effective thickness of water. The effective thickness of a set of layers,  $d'$ , is calculated from:

$$d' = \sum_i d_i \rho_i, \quad (1-31)$$

where  $d_i$  is the thickness of the layer number  $i$  with the electron density  $\rho_i$  relative to water. The effective path length of point  $P$  in the simple inhomogeneity configuration shown in Figure 1.13, for  $d_1=2$  cm,  $d_2=4$  cm,  $d_3=3$  cm (physical depth 9 cm) is:

$$d' = 2 \times 1 + 4 \times 0.25 + 3 \times 1 = 6 \text{ cm}$$

The effective depth is used to obtain the *CAX* value at point  $P$  and therefore the correction factor is derived from the ratio of the *CAX* at depth  $d'$  to that at the actual depth ( $d$ ), as if the entire phantom was water equivalent:

$$CF = \frac{CAX(d')}{CAX(d)} \quad (1-32)$$

Combining equation (1-29) with the above equation gives the correction factor which is known as the effective *SSD* method:

$$CF = \frac{P(SSD, r_o, d')}{P(SSD, r_o, d)} \left( \frac{SSD + d'}{SSD + d} \right)^2, \quad (1-33)$$

where  $r_o$  is the field size at the surface. The *EPL* method is a simple-first-order correction method which accounts for the change in primary photon fluence and field size. However, in this method the position (relative to the calculation point,  $P$ ), size of the inhomogeneity and so the scatter contribution are not taken into account.

### 1.11.1.1. Tissue air ratio method

The dose distribution in a heterogeneous medium can be approximated by the *TAR* method. The dose at point *P* in Figure 1.13 can be calculated by taking the ratios of *TARs* for the effective depth to the physical depth, both for the physical field size.

$$CF = \frac{TAR(d', r_d)}{TAR(d, r_d)}, \quad (1-34)$$

where  $r_d$  is the field size at depth  $d$  and the equivalent water depth,  $d'$ , is equal to *EPL* in previous section. This method is essentially the same as the *EPL* method and does not include position of inhomogeneity and scatter contribution.

### 1.11.2. Power law tissue air ratio method

Power law *TAR* method which was developed by Batho (1964), takes into account the position of inhomogeneities, but not their lateral shape. The correction factor at point *P* in Figure 1.13, using Batho method is:

$$CF = \left[ \frac{TAR(d_2 + d_3, r_d)}{TAR(d_3, r_d)} \right]^{\rho_2 - 1}, \quad (1-35)$$

where  $\rho_2$  is the electron density (number of electrons per  $cm^3$ ) of the second layer (e.g., lung) relative to water. This method accounts for the fact that the effect of an inhomogeneity depends on its position. For example a layer of low density material above a dose calculation point will increase the dose, but the increase will be larger when the inhomogeneity is further away from the calculation point: this is because the reduction in scattered dose reaching *P*, caused by the low density inhomogeneity, is less in this case.

Sontag and Cunningham (1977) have modified the Batho correction so that a correction inside the inhomogeneity can be calculated:

$$CF = \left[ \frac{TAR(d_3, r_d)^{\rho_3 - \rho_2}}{TAR(d_2 + d_3, r_d)^{1 - \rho_2}} \right], \quad (1-36)$$

where  $\rho_3$  is the electron density of medium where point  $P$  lies and  $d_3$  is its depth within that medium. Also  $\rho_2$  is the electron density of the overlying medium, and  $d_2 + d_3$  is the depth below the upper surface of it.

### 1.11.3. Equivalent tissue air ratio method

The correction factor discussed in Equation (1-34) does not correctly predict the scatter contribution to the dose calculation, because the position of inhomogeneity is not included. Sontag and Cunningham (1978) introduced the equivalent tissue-air ratio (*ETAR*) method which accounts for this contribution by including an effective field size as well as an effective depth in the ratio of *TARs*. In this method the absorbed dose in an inhomogeneous medium can be related to the absorbed dose in a unit-density phantom by the following correction factor:

$$CF = \frac{TAR(d', r')}{TAR(d, r_d)}, \quad (1-37)$$

where  $d'$  and  $d$  are the water equivalent and actual depth, respectively and  $r_d$  is the field size at depth  $d$ . The parameter  $r' = r_d \tilde{\rho}$  is the effective field size, where  $\tilde{\rho}$  is the weighted electron density of the irradiated medium. The weighted electron density  $\tilde{\rho}$  can be determined by the following formula (Woo et al, 1990):

$$\tilde{\rho} = \frac{\sum_i \sum_j \sum_k \rho_{ijk} W_{ijk}}{\sum_i \sum_j \sum_k W_{ijk}}, \quad (1-38)$$

where  $\rho_{ijk}$  is the electron density of scattering element relative to water. Also  $W_{ijk}$  is the weighting factor accounting for contribution of the  $(i, j, k)$  element to the scatter dose at the point of calculation.  $W_{ijk}$  is given by:

$$W_{ijk} = P_{ijk} + S_{ijk}, \quad (1-39)$$

where  $P_{ijk}$  and  $S_{ijk}$  account for the primary and scatter fluence contributions to the element  $(i, j, k)$ , respectively. The *ETAR* method uses *CT* data for this calculation and is more accurate than the power law method because it takes into account the lateral

extent of heterogeneities, however it requires extensive computation time mainly due to the calculation of  $\tilde{q}$ .

Tables of *TARs* for a homogeneous medium (water) can be easily determined from direct measurement or calculation. Therefore, the effective tissue air ratio in the inhomogeneous medium,  $TAR(d',r')$ , can be obtained from these tables. The correction factor *CF*, then is found using equation (1-37). However, *ETAR* gives the wrong result for conditions of electronic disequilibrium (Metcalf et al, 1993), because  $TAR(d',r')$  is too large. As a result the dose calculation in a low density material (such as lung) is over-estimated by this technique. The effect of lateral electronic disequilibrium on dose calculation will be discussed in the following section.

#### 1.11.4. The effect of electronic disequilibrium on dose calculation

Lateral electronic disequilibrium and its dependence on photon energy and medium density were discussed in section 1.5. In the dose calculation models, which have been mentioned in the previous sections, it was assumed that electronic equilibrium exists at the point of dose calculation. Therefore, dose calculation in regions of non-equilibrium is not accurate. As was mentioned in section 1.5, for higher energy photon beams and also lower density materials, electronic disequilibrium becomes more important. This will cause an overestimate of dose for low density materials where electronic disequilibrium exists.

The above situation can be explained from Figure 1.14 (from Hoban, 1991). In this figure the dose calculation point, *P*, is on the central axis for two different conditions, that is when lateral electronic equilibrium (a) exists and (b) does not exist on the central axis of the beam. The primary dose at *P* is the dose deposition in this point by secondary electrons, originated from primary photon interactions. The volumes from which primary photon (i.e., photon that had not interacted before) interactions give rise to a primary dose at *P* are shown as shaded area. The scattered dose could be from outside of this area. From the *TAR* curves in this figure, it is seen that in case (a) the zero area *TAR* gives the correct primary component of the *TAR* (shaded column in the graph). However, using the zero area *TAR* in case (b) will over-estimate the primary

component of the  $TAR$  by  $\Delta P$ . Therefore, in dose calculation using sector integration (differential  $SAR$ ) method, where

$$TAR(d,r) = TAR(d,0) + \sum_i SAR(d,r_i), \quad (1-40)$$

the error from using  $TAR(d,0)$  will be  $\Delta P$ . This problem has been addressed by Woo et al (1990), where they used Monte Carlo generated data for the primary component (extended data), instead of measured zero area  $TAR$  (original data). The effect of electronic disequilibrium on dose calculation is shown in Figure 1.15.

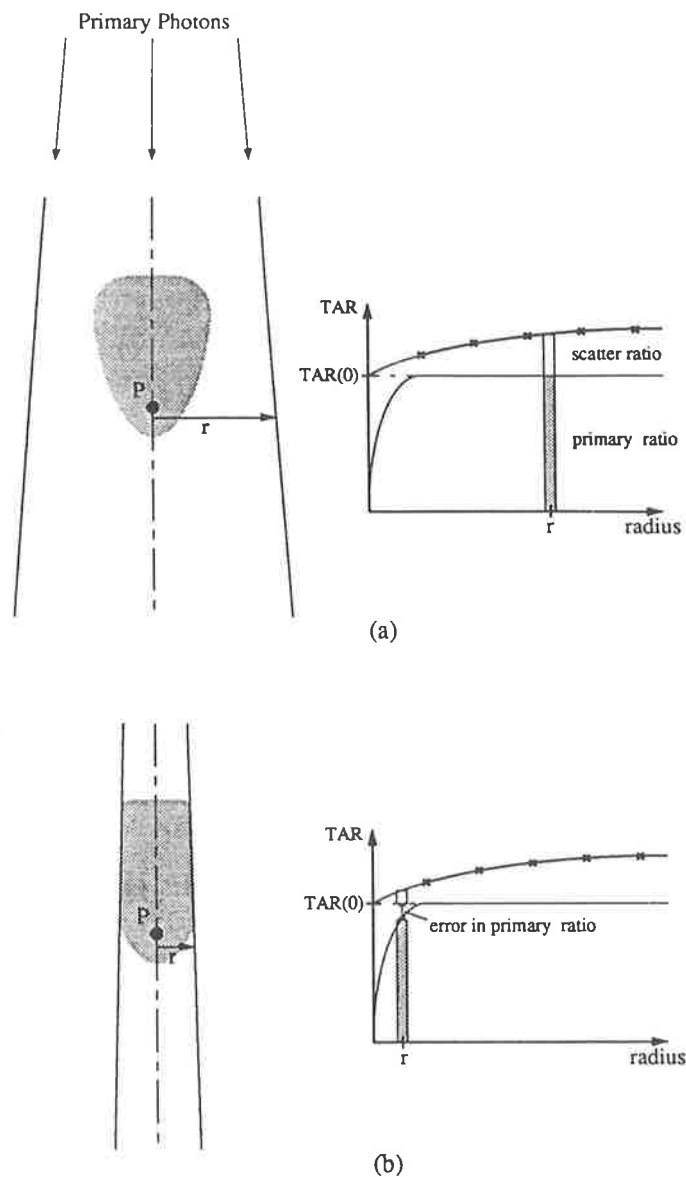


Figure 1.14. Calculation of central axis dose using standard  $ETAR$  model (with zero area  $TAR$ ), when lateral electronic equilibrium exist (a) and does not exist (b) at point  $P$  (from Hoban, 1991).

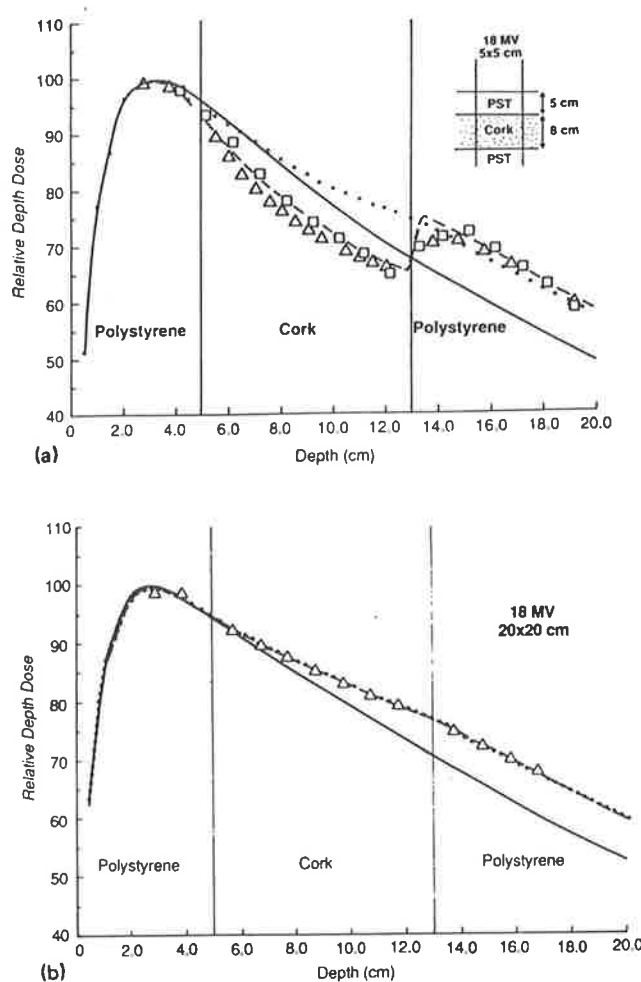


Figure 1.15. Comparison of the calculated and measured central axis depth dose curves in a polystyrene–cork–polystyrene phantom for an 18 MV photon beam for (a)  $5 \times 5 \text{ cm}^2$  and (b)  $10 \times 10 \text{ cm}^2$  fields when lateral electronic equilibrium exist and does not exist, respectively (from Woo et al, 1990), as the result of configurations shown in Figure 1.14. The solid curve is measured data for the homogeneous polystyrene phantom, but all other curves are for polystyrene-cork-polystyrene phantom. The triangle curves are measured data, dotted and dashed curves are calculation using the equivalent  $TAR$  with the original data and the new extended data respectively, and square curve is calculation using Monte Carlo.

In this figure the depth dose in a homogeneous medium (polystyrene) is compared with the depth dose in polystyrene-cork-polystyrene phantom. Polystyrene and cork have densities  $1.0$  and  $0.25 \text{ g/cm}^3$ , respectively. The comparison is for an 18 MV photon beam for (a)  $5 \times 5 \text{ cm}^2$  and (b)  $20 \times 20 \text{ cm}^2$  field at  $SSD=97 \text{ cm}$ . In both cases the dose beyond the cork slab is higher than in the homogeneous medium, because of the lower attenuation in the cork. For the same reason the dose inside the cork slab becomes increasingly higher than in the homogeneous medium, for the  $20 \times 20 \text{ cm}^2$  field.

The same result is obtained for  $5 \times 5 \text{ cm}^2$  field, if the dose calculation is performed using *ETAR* method (with the original *TAR* data). In this case, as it is seen from Figure 1.15(a), the dose calculation shows a large difference (up to 10%) from the measured data. However, when the extended data is used for this field size, the disagreement between calculated and measured data is reduced to less than 2% in the most part of the curve. Also Haidar and El-Khatib (1995) using differential scatter integration have modified the primary and scatter dose model by introducing an electron perturbation factor for dose calculation in electronic disequilibrium regions.

#### 1.11.5. Density correction factor and *CT* numbers

All dose calculation techniques, discussed in sections 1.11.1 to 1.11.3, use electron densities derived from *CT* numbers. In this way the linear attenuation coefficients, measured by *CT*, are converted to  $\rho$ . Strictly speaking, the ratios of the linear attenuation coefficients of the relevant tissues to those of water should be used, instead. However, because these coefficients are energy dependent and are not easily determined, the relevant electron densities are used.

Using relative electron density rather than relative attenuation coefficient is acceptable because the Compton scattering cross section, which is the dominant interaction type for the most radiotherapy energy ranges, is proportional to the electron density of the medium. The Compton scattering is still predominant at the *x-ray* energies used in the *CT* scanners, but the photoelectric effect can't be ignored. Therefore, the relationship between  $\mu$  and  $\rho$  is different for *MV* than *CT* energies. The latter effect has an increasing contribution for lower energies, especially for high atomic number structures like bone. The photoelectric effect, unlike Compton scattering, has a strong relationship with the atomic number and therefore there is not a simple relationship between attenuation coefficients of the beams in the *CT* energy ranges and megavoltage energies. Conversion between attenuations in the two energy ranges is very difficult and requires the effective atomic number and effective electron density.

The relationship between *CT* number and the relative electron density may be determined by scanning various materials with known electron densities. The

relationship between *CT* numbers (Hounsfield Units) and electron density relative to water ( $3.333 \times 10^{23} \text{ cm}^{-3}$ ) and the values for various biological tissues are shown in Table 1.3.

Table 1.3. The relationship between *CT* numbers and the density correction factors (from Target treatment planning system).

Material	<i>CT</i> numbers	Relative electron density
Air	-1000	0
	-820	0.14
	-780	0.17
	-740	0.20
	-700	0.25
Lung	-650 (-673 to -620)	0.31
	-590	0.37
	-520	0.45
	-410	0.56
	-290	0.69
	-180	0.81
	-105	0.90
	-70 (-90 to -55)	0.93
Fat	-40	0.96
	0 (-19 to 20)	1.00
Water	40	1.04
	100 (71 to 139)	1.11
Muscle	180	1.09
	400	1.20
	740 (571 to 870)	1.32
Bone	1000	1.45
	1200	1.70

#### 1.11.6. Superposition and convolution techniques

The convolution/superposition techniques have been developed particularly for dose calculation in electronic disequilibrium conditions in high energy photon beams. This method was first introduced by Dean (1980) and developed by Mackie et al (1985) and also Boyer and Mok (1985), Ahnesjo (1989) and Yu et al (1995). Using the convolution techniques in treatment planning dose calculation is an increasingly viable alternative to the above mentioned methods. This is due to the increasing availability of faster computers and commercial convolution algorithms. In these techniques, from the

knowledge of the photon fluence, the total energy released per unit mass (terma) is found and convolved with the energy deposition kernels (*EDKs*) to obtain the dose distribution. These kernels are also called dose spread arrays, point spread function or differential pencil beams.

The convolution can be performed for any arbitrary geometry and is referred to as superposition for an inhomogeneous medium, by replacing the invariant kernel with a variable kernel. Using the convolution technique the dose deposition at a point is calculated from the following formula:

$$D(r) = \iiint_{r'} T(r') K(r-r') d^3 r', \quad (1-41)$$

where  $r'$  and  $r$  are the photon interaction site and the dose calculation site respectively,  $T(r')$  is the terma at  $r'$  and  $K(r-r')$  is the energy deposition kernel, describing the energy deposition about the primary interaction site. In these techniques, *EDKs* are usually calculated using Monte Carlo methods. If the *EDK* does not vary with position, the dose calculation can be performed using Fourier transform techniques which are considerably faster. However, with a variable *EDK* (as a result of the presence of inhomogeneities) the Fourier transform is not valid and the dose calculation is performed in a real-space superposition technique.

Superposition techniques are able to model situations of electronic disequilibrium such as occurs in the lung region for small fields. This is at the expense of a large computation time and requires knowledge of beam characteristics, including the beam spectrum, in order to correctly calculate terma and *EDKs*. The effect of beam hardening with depth on the polyenergetic energy deposition kernels (*PEDKs*) has been discussed by Metcalfe et al (1990), Papanikolaou et al (1993) and Hoban et al (1994). Also comparisons of depth dose calculations in lung phantom (polystyrene -cork- polystyrene slab) using superposition, *MC* and experiment for the condition of electronic disequilibrium have shown generally good agreement between them (Hoban, 1991).

### 1.11.7. Photon dose calculation using explicit electron transport

In the convolution/superposition methods which were discussed in previous section, dose distribution from interaction points are usually calculated using pre-generated *EDKs*. Inhomogeneity effects in these methods are generally handled by using the average density between the interaction and calculation (energy deposition) sites. The validity of the density scaling approach for low-density inhomogeneities of similar atomic number has been investigated by Woo et al (1990) and also Woo and Cunningham (1992). Lack of an explicit electron transport near the inhomogeneities of different atomic composition can cause a dose difference as much as 10% at points close to inhomogeneity (Yu et al, 1995).

Keall and Hoban (1995), from this department, have incorporated Fermi-Eyges electron-scattering theory into the primary dose calculation for *x-ray* radiotherapy using the convolution method. In this work they have accounted for the density distribution between the interaction and deposition sites. This results in a better agreement with MC, compared to a conventional convolution method. The effect is more evident for a higher degree of lateral electronic disequilibrium. Moreover, the presence of an inhomogeneity with different atomic composition (different scattering and stopping powers) will cause a different secondary electron transport compared to the presence of an inhomogeneity with the same atomic composition, but only different density. The magnitude of perturbation strongly depends on the proximity of the dose calculation point to the inhomogeneity and its atomic composition.

Since O'Connor's density scaling theorem only applies to inhomogeneities with different electron densities, for inhomogeneities with different atomic compositions it is expected to give errors. Yu et al (1995), by incorporating explicit transport of the secondary electrons with Fermi-Eyges theory, as part of photon dose calculation, have reduced this error. This has been done for the primary dose component only, since this is affected most by secondary electron transport. In this model the scattered photon component, which has small contribution to the total dose for photon energies of 10 MV or higher, is calculated using previous *EDK* methods to reduce unnecessary computation time.

### 1.11.8. Monte Carlo simulation

Monte Carlo (*MC*) modelling is a direct dose calculation technique which uses explicit radiation transport to simulate the physical situation (see chapter 4). Apart from statistical fluctuations caused by insufficient particle histories, there is no limitation on the accuracy of simulation, providing that radiation transport modelled adequately (Murray, 1991). *MC* techniques can be employed to solve dosimetric problems of clinical interest, in particular where simpler methods are known to be inaccurate.

In the last few years the use of Monte Carlo techniques in radiotherapy physics has increased dramatically, due to the rapid development of computer technology, in terms of speed and cost, as well as the availability of user-friendly *MC* packages such as *EGS4* (Rogers and Bielajew, 1990). In *MC* simulation, using the probability relationships of the discrete events and a high-quality random number generator, events in radiation transport can be predicted with the correct probability. The track length between interaction points for each particle, the type of an interaction at each such point, the choice of energy and direction following a scattering interaction, and the possible products as the result of an interaction all can be determined by sampling processes.

*MC* is a very powerful dose calculation technique, but its direct application in the treatment planning dose calculation at the moment is unreasonable because of the great computation time which is required. However, with the rapid increase in computer power, this very important application could be practical in the next few years. Some current *MC* applications in radiotherapy are: benchmarking other treatment planning techniques, calculating dose at presence of lateral electronic disequilibrium, calculating beam characteristics for *Co-60* machines and linear accelerators, and generation *EDKs* for the convolution/superposition approach. In Table 1.4 a comparison between above treatment planning dose calculation algorithms as well as their features is presented.

Table 1.4. Features of various treatment planning algorithms (from Murray, 1991).

Algorithm	Method accounts for:					Complexity/ Speed
	Photon path length	Field size	<u>Inhomogeneity</u> position	shape	Electronic disequilibrium	
Equivalent pathlength	✓	—	—	—	—	very simple/ very fast
Effective <i>SSD</i>	✓	✓	—	—	—	simple/fast
Ratio of <i>TARs</i>	✓	✓	—	—	—	very simple/ very fast
Power law <i>TAR</i>	✓	✓	✓	—	—	simple/fast
<i>ETAR</i>	✓	✓	✓	✓	—	complex/slow
Volume integration of <i>dSARs</i>	✓	✓	✓	✓	—	complex/slow
Convolution/ Superposition	✓	✓	✓	✓	✓	simple/ very slow
Monte Carlo	✓	✓	✓	✓	✓	very complex/ extremely slow



## Chapter 2

### Stereotactic Radiosurgery

#### 2.1. Introduction

Stereotactic radiosurgery (*SRS*) is a radiation treatment technique which combines stereotactic apparatus and energetic radiation beams to treat intracranial lesions. Stereotactic methods enable highly conformal delivery of dose to a well-defined target volume with maximal sparing of adjacent normal tissue (Killoran et al, 1996). In *SRS* a single high dose (normally 10 to 30 *Gy*), in a small radiation field (typically 5 to 40 *mm* in diameter) is given to a stereotactically defined target volume to destroy the selected lesion. Also, stereotactic radiotherapy (*SRT*) is a similar technique to *SRS*, but for multiple fraction treatment. In *SRT* the high accuracy of *SRS* is combined with the radiobiological advantages of fractionation to treat tumours where a single high dose would cause intolerable damage to healthy tissue (*SRT* is also performed where the lesion is too large to have a single dose).

*SRS* was first developed by Leksell in the late 1940s to destroy dysfunctional loci in the brain using orthovoltage *x-rays* (Schell et al, 1995). *SRS* was performed later using heavy charged particles produced in cyclotrons, taking advantages of the Bragg peak dose distributions of these particles (Larsson et al, 1958; Lawrence et al, 1962; Kjellberg et al, 1968 and 1983). In 1968 Leksell developed the Gamma unit (Gamma Knife) for *SRS* using multiple converging cobalt beams. Also, Larsson et al (1974) have proposed linac-based radiosurgery as an alternative to above systems, but practicaly treatment using this technique has only started in the last decade. Some of the important considerations for dose delivery in *SRS* are (Podgorsak et al, 1990): (i) high spatial and numerical accuracy of dose delivery to the target; (ii) steep dose fall-off outside the target volume; (iii) low dose to critical organs (such as the brain stem, optic nerves and tracks); (iv) low or minimal scatter and leakage dose to radiosensitive organs (such as thyroid, breast, gonads, etc.); (v) knowledge of dose inside the target volume; and (vi) cost effectiveness.

The advantages of linac-based radiosurgery are the choice of the *x-ray* energy, more collimator sizes, high dose rates and therefore reduction in treatment time, no source decay problems, greater source to isocentre distance, and availability and cheaper cost (Arcovito et al, 1985). One of the biggest advantages of the linear accelerator over Gamma unit is its ability to do beam shaping and conformal *SRS* (see chapter 6). On the other hand, excellent geometrical accuracy and taking advantages of the Bragg peak in case of heavy charged particles are advantages of Gamma Knife and heavy charged particle systems, respectively (Podgorsak et al, 1988). Both heavy charged particle and Gamma unit techniques have shown their effectiveness in treating several thousand patients and long term follow-up results have proven their usefulness in treating certain brain diseases (Pike et al, 1987 and Podgorsak et al, 1988). In the following sections the rationale for *SRS* is discussed and different *SRS* techniques are introduced and their relative advantages discussed.

## **2.2. Rational for radiosurgical treatment**

Radiosurgery has been used to treat a variety of benign and malignant lesions as well as functional disorders, including chronic pain and movement disorders due either to Parkinson's disease or other disorders (Young et al, 1996). Arteriovenous malformations (*AVMs*) and acoustic neuromas are the principal non-malignant lesions treated with *SRS*.

*AVMs* consist of a nidus of abnormal vessels, often interlaced within a matrix of glial cells. *AVMs* lack a normal capillary bed and local blood flow through them is increased of the expense of the adjacent parenchyma. The adjacent tissues are generally assumed to be dysfunctional and hence suffer minimal additional neurological deficit from the radiation damage. This, together with the dose-response characteristics of *AVMs* (see section 6.7.2), is the main reason why *AVMs* are frequently referred for *SRS*, especially when surgically inaccessible, eg when it is located in the speech area or in the brain stem. The obliteration rate for small *AVMs* is about 86% at the end of 2 years with a low complication rate (Friedman, 1995 and Hirai et al, 1995). However, there are difficulties in treating large *AVMs* due to the large volume of normal tissue irradiated. There is a dose limitation with a low obliteration rate (Friedman, 1995). The reaction of the adjacent brain is dose and volume dependent. Other benign lesions which are

treated using *SRS* include most types of meningiomas and pituitary adenomas, acoustic neuroma and Nelson's syndrome.

*SRS* of primary malignant intracranial lesions as a sole treatment modality has less justification where tumour cells are known to extend beyond the borders visible on *CT* or *MRI*. *SRS* in this case can be used as a high-dose boost in conjunction with the standard external radiotherapy. This will improve the local control probability (Fuller et al, 1992 and Gannett et al, 1995) and it is very important indeed due to the great number of patients involved (as many as 50% of patients dying from cancer have brain metastases at autopsy; Flickinger et al, 1994).

The cost effectiveness of *SRS* is presented in section 2.13. It is shown that using whole brain radiotherapy (*WBRT*)-*SRS* combination is more effective (improved local control) than *WBRT* and *WBRT*-surgery combination. The other advantage is that *SRS* can be performed almost regardless of tumour location in the brain. In *SRS* of intracranial lesions, developing radiation necrosis in long-term survivors has to be considered as well. The dose which tended to cause radiation necrosis two years after *SRS* was found by De Salles et al (1995) to be more than 1800 *cGy*.

### 2.3. Gamma Knife

*SRS* with the so called "Gamma Knife" was introduced by Leksell in 1968. Figure 2.1 shows a picture of a current model of the Gamma Knife unit. The Gamma Knife is a dedicated radioisotope *SRS* unit in which 201 Cobalt-60 sources are distributed on spherical segments around the central beam in  $\pm 48^\circ$  arc along the long axis and  $\pm 80^\circ$  arc along the transverse axis of the treatment couch (Wu et al, 1990). A schematic diagram of the cross-sectional view of the Gamma Knife system is shown in Figure 2.2. All 201 beam channels are focused to a single point at the center of the radiation unit (in a focal distance of 40.3 *cm*) with a dose rate of about 200 *Gy/min*. Each of the Cobalt sources has a nominal activity of  $1.1 \times 10^6$  *MBq* (30 *Ci*) and consists of 20 pellets, each 1 *mm* in diameter and height, stacked on top of each other. The central axis of the 201 beams intersect at the focus with a mechanical precision of  $\pm 0.3$  *mm*.

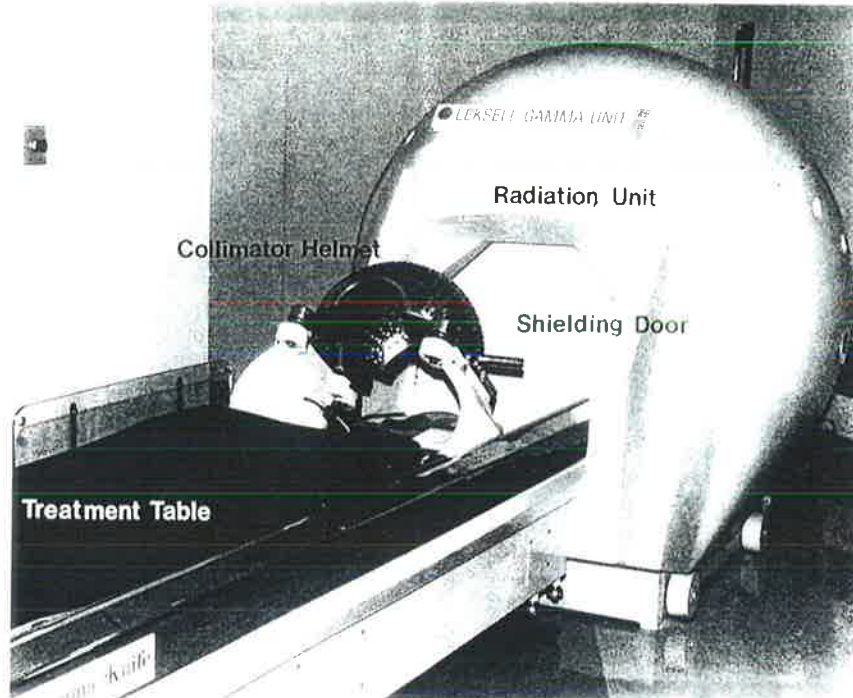


Figure 2.1. A current model of the Gamma Knife unit with the shielding door closed, a collimator helmet and the treatment table (from Wu et al, 1990).

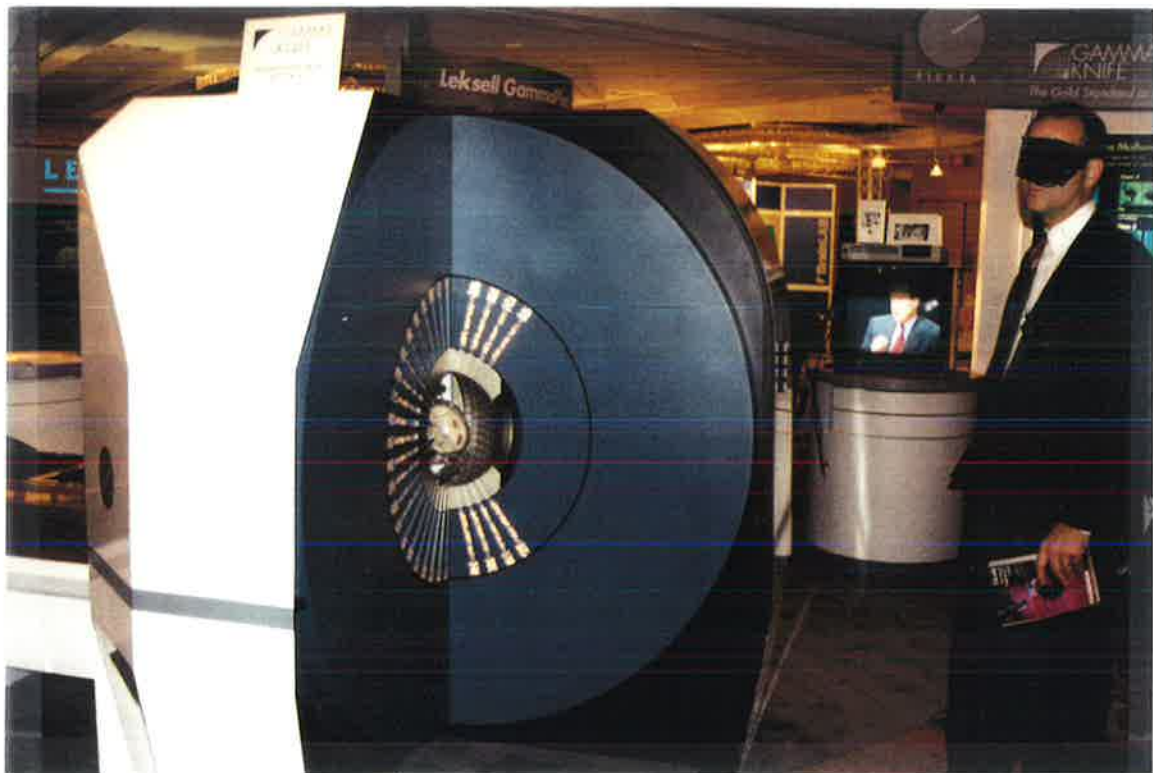


Figure 2.2. A cross-sectional view of the Gamma Knife system, showing the radiation sources, a collimator helmet and the beam channels focused to a single point at the isocentre.

The Gamma Knife unit collimation is accomplished with one of four helmets. Each helmet is 6 *cm* thick with an inner radius of 16.5 *cm* and 201 channels are drilled in each of them. Removable, 6 *cm* thick collimators with circular apertures are used to produce 4, 8, 14, or 18 *mm* diameter fields at the focus. The aperture of individual collimators can be plugged to prevent irradiation of critical structures or to alter the isodose shape. The relative helmets output factors, measured with a diode detector and *TLDs*, are 0.821, 0.950, 0.978 and 1.000 for the above collimators respectively (Wu et al, 1990). These values are normalised to 1 for the 18 *mm* collimator helmet and are very close to the corresponding collimator output factors for a single beam geometry. The maximum variation of 3.5% occurs for the 4 *mm* collimator.

#### **2.4. Heavy charged particle SRS**

The advantages of using heavy charged particles in radiotherapy in delivering a high dose to the tumour while sparing normal tissues has been appreciated since the late 1940s (Schell et al, 1995). Investigation has shown that proton, deuteron and helium ion beams can be used effectively in treatment of selected human brain disorders (Lyman et al, 1986). A 184-inch Synchrocyclotron at the University of California, Berkeley was used for biological studies in 1948 and for treatment of patients in 1954, using proton or deuteron beams. Initial stereotactic helium-ion irradiation was performed in 1958 at the Lawrence Berkeley Laboratory (*LBL*)(Levy et al, 1995). However, the current *SRS* design was developed in 1980 at the Donner Laboratory and *LBL* (Lyman et al, 1986 and 1989). Heavy charged particle beams offer a number of unique advantages in treatment of intracranial targets. The characteristics of 230 *MeV* helium ion beam of the 184-inch Synchrocyclotron at *LBL* are: (i) uniform field between 10 and 40 *mm* in diameter; (ii) penetration range between 40 and 140 *mm* and the ability to shift the Bragg peak; (iii) sharply defined lateral and distal borders (minimal scattering), and (iv) dose rate greater than 2 *Gy/min* (Lyman et al, 1986). Figure 2.3(a) shows the helium ion beam delivery line at *LBL* along with the Irradiation Stereotactic Apparatus for Humans (*ISAH*), which is a patient-positioning device for heavy-charged-particle therapy. In Figure 2.3(b) a scaled diagram of the system is shown. Because of the large SSD and the collimation system, the beam entering the skull is almost parallel. The 230 *MeV* helium ion beam range in water is 316 *mm*,

which is greater than the maximum required for intracranial targets. The beam range is shortened by the energy degrader, consisting of 153 *mm* polyethylene followed by 3.4 *mm* of copper (Lyman et al, 1986). Further degradation is performed for individual patients with an appropriate thickness of polyethylene added to the fixed degrader to achieve the required residual range.

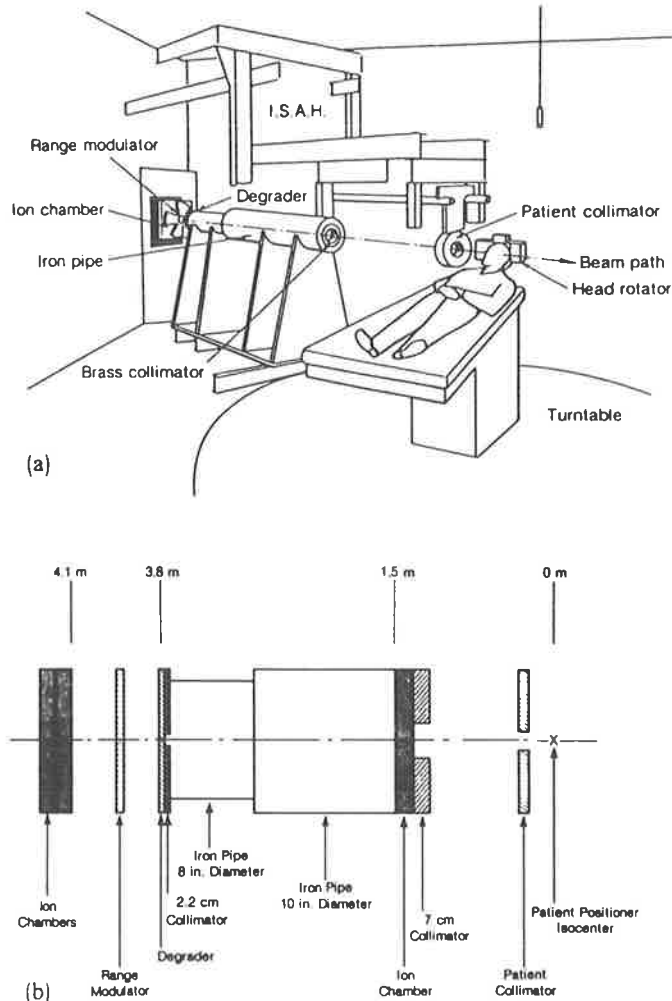


Figure 2.3. (a) The helium ion beam delivery line at *LBL* along with the *ISAH* and (b) a scaled diagram of the system (from Lyman et al, 1986).

Figure 2.4(a) shows depth dose measurements of the 230 *MeV* helium ion beam with the maximum range to the Bragg peak of 145 *mm* in water. As it is seen from this figure, the peak-to-plato dose ratio is over 3. The distal border (the dose gradient beyond the Bragg peak) from 90% of the maximum to 10% is 6 *mm*. That is the beam stops at the distal edge of the target. This is a big advantage and means that the integral

dose is reduced by approximately a factor of two, compared to photon beam therapy. Figure 2.4(b) shows the depth dose distributions of the beam with the stopping region broadened by 21.6 mm, using the range modulator fan.

In treatment using heavy charged particles, inhomogeneities (bone and air) need to be compensated for very accurately. This is performed using *CT* scans by converting photon equivalent thickness to the charged particle equivalent thickness during planning. Therefore, the treatment planning process is much more difficult than in linac-based or Gamma Knife *SRS* and might take one or two days.

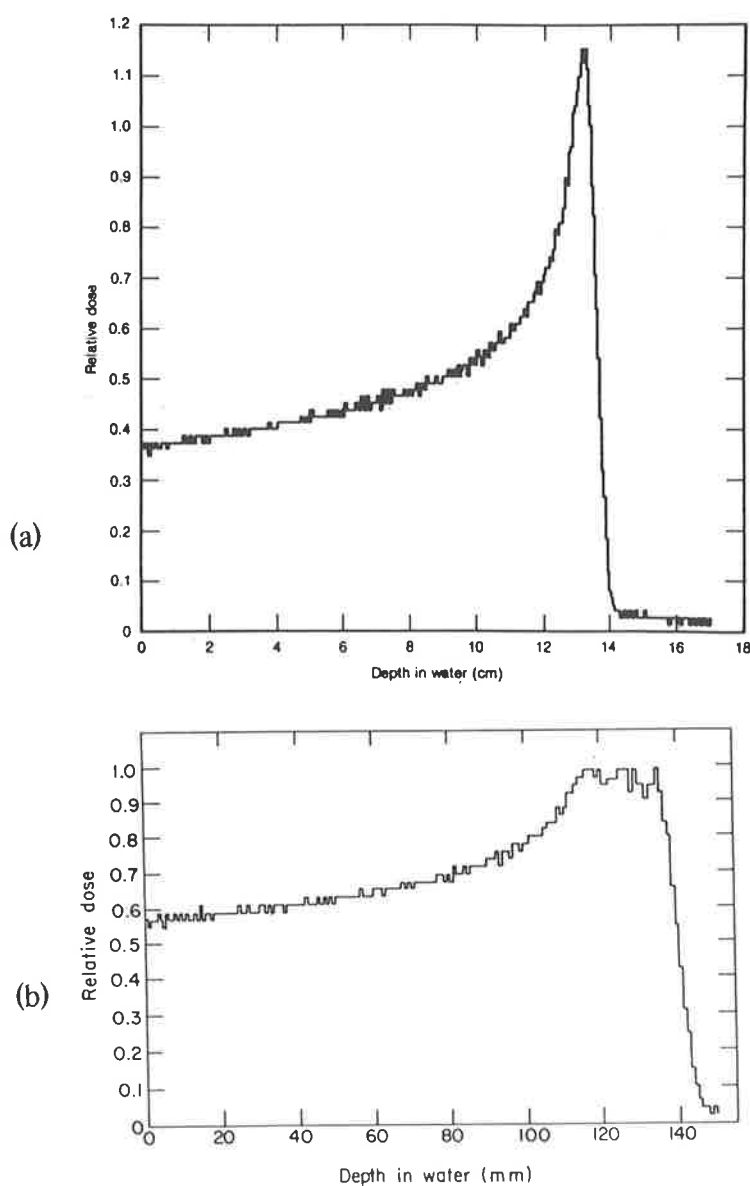


Figure 2.4. (a) Depth dose measurements of the 230 MeV helium ion beam at the 184-in Synchrocyclotron, with the maximum range to the Bragg peak of 145 mm in water and (b) the depth dose distributions of the beam in Figure 2.4.(a) with the stopping region broadened by 21.6 mm, using the range modulator fan (from Lyman et al, 1986).

The beam shaping ability of the heavy charged particles eliminates the requirements for using multiple isocentres. In this case apart from saving time required for additional set up, the non-uniformity of dose distributions (hot and cold spots) which are inevitable in multiple isocentre treatment in conventional *SRS* are avoided. Moreover, the relative risk of *SRS* with heavy-charged particles is in principle much less than with photon beams due to the Bragg peak and a better beam shaping ability, which becomes very important for large target volumes.

### 2.5. Linac-based *SRS*

Until the last decade stereotactic radiosurgery was limited to a few centers, due to the high cost of cyclotrons and Gamma units and also the related technical difficulties. Although the use of the linear accelerator in *SRS* was proposed by Larsson in 1974, the first report on clinical linac-based *SRS* was published in 1984 by Betti and Derechinsky. The main advantages of using linear accelerators in *SRS* are the lower cost and availability as well as the ability to conform the beam to the target volume. The requirement is good mechanical accuracy of the linac. The three principle mechanical axes (gantry, turntable, and collimator), as is shown in Figure 2.5, intersect at a common point (the isocentre) and should remain stable during all rotations.

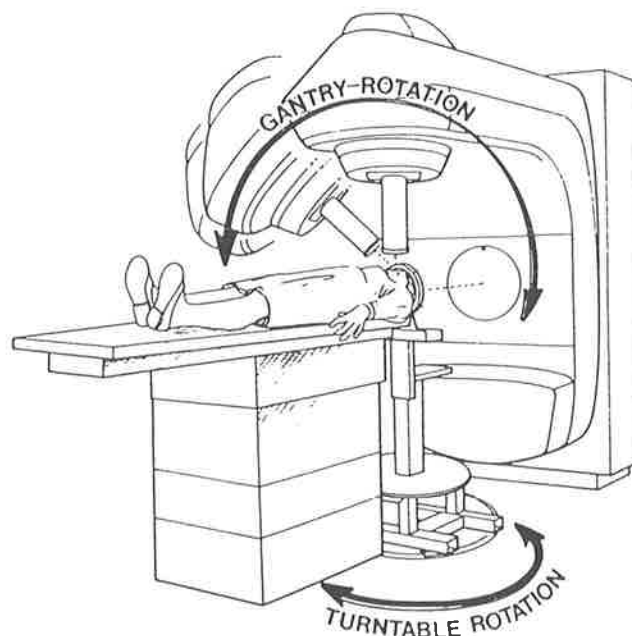


Figure 2.5. The three principle mechanical axes in linear accelerator (gantry, turntable, and collimator) intersect at a common point (isocentre) and should remain stable during all rotations (from Lutz et al, 1988).

Podgorsak et al (1990) and several other authors have shown the adequacy of linac-based multiple arcs and dynamic rotation *SRS* in fulfilling the required criteria for *SRS* as a practical alternative to the Gamma-Knife unit. Minor modifications are required to make a linear accelerator suitable for *SRS*. In order to use the existing Siemens *KD-2* linear accelerator at the Royal Adelaide Hospital (*RAH*) for *SRS* a collimator face plate, *SRS* collimators, and a couch mount adaptor were required. There are commonly two linac-based systems available: pedestal- and couch-mounted frame techniques. The pedestal or floor stand is mounted to the couch floor plate to support the patient head ring, while the patient's body is supported by the couch, as is shown in Figure 2.5. In couch-mounted frame systems, the head ring is fixed to the couch using an adaptor. The floor stand generally offers better frame stability, but providing that the couch mounting adaptor is rigid and the couch has a good mechanical accuracy, the latter can offer acceptable stability. Moreover, using the couch mounted system is more convenient and provides more arcing options, since the gantry is able to go under the couch. Also, this system is considerably safer than the floor-stand mounting since the patients head and body are both on the couch, avoiding problems with inadvertent vertical couch motions.

The *SRS* collimator diameter which are used in the *RAH* system range from 5 mm to 23 mm, corresponding to 8.9 and 41 mm field diameters at the isocentre. The conventional collimating system in a linear accelerator jaws is not suitable, because the jaws produce rectangular beams whose dose gradient is not as sharp as circular beams in the beam delivery in *SRS*. The collimator central axis must be aligned with the line connecting the radiation source to the isocentre. The treatment in our department is performed conventionally using 6 non-coplanar converging arcs, each gantry arc is 140° and corresponds to one of 6 table angles which are 30° apart. However, different combinations of arcs and table angles are possible, depending on the lesion shape, site and the position relative to critical organs.

## 2.6. Target localization

Stereotactic coordinates are defined by the stereotactic head ring (see Figure 2.6) and provide the basis for target localization. To calculate stereotactic coordinates in an axial *CT*, scans are taken with four *CT* localizer plates (see Figure 2.7(a)) attached to

the head ring. The localizing wires (fiducials) in these plates are used as reference points to calculate the coordinate transformation from the *CT* system into the stereotactic system, as is shown in Figure 2.7(b). The stereotactic coordinates of any point in the *CT* scan can then be calculated as follows. The  $z$  coordinate of the point ( $Z_T$ ) is determined from the distance between fiducial markers in each *CT* localizer plate. The  $x$  and  $y$  coordinates ( $X_T$  and  $Y_T$ ) are distances from the connecting lines between the middle fiducials on the frontal and lateral localizers, respectively. The tumour localization is performed by enhancement on *CT*, magnetic resonance imaging (*MRI*), magnetic resonance angiography (*MRA*), or angiography. The *CT* slice that best locates the lesion is selected by the neurosurgeon and then the target center is digitised. The stereotactic coordinates of this point are computed automatically as explained before. *MRI* localizer plates have the same fiducial geometries as those for the *CT* scans.

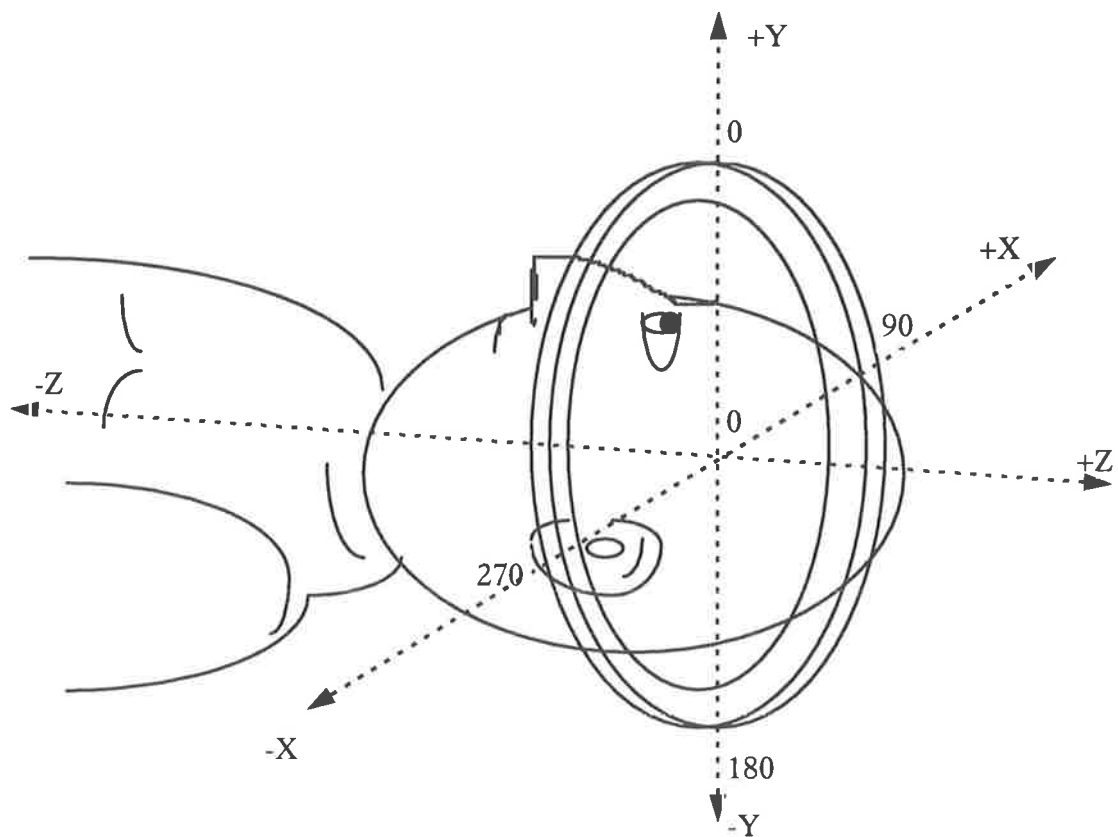


Figure 2.6. Definition of the stereotactic coordinate system, with respect to the stereotactic head ring.

Radiosurgery treatment planning of *AVMs* normally is performed using angiography. These lesions normally do not show up in a *CT* scan and the stereotactic coordinates are

found from the angiograms (see below). Nidus boundaries are drawn on angiograms. Using *MRI* or *MRA* could be a very useful adjunct to angiography (especially for nidus larger than 2 cm) for the target definition and often gives additional information and permits sparing of critical normal brain tissues (Sneed et al, 1995). Localization by *MRI* or *MRA* scans have to be corrected for image distortions if they are to be used to give accurate stereotactic coordinates (see chapter 7). The target coordinates for *AVMs* are normally determined by digitising two pairs of orthogonal angiograms (AP and lateral). Four *x-ray* localizer plates have to be attached to the head ring before angiography is performed. Each plate has 4 landmarks in a square pattern, as is shown in Figure 2.8(a), which form a reference for the stereotactic coordinate system.

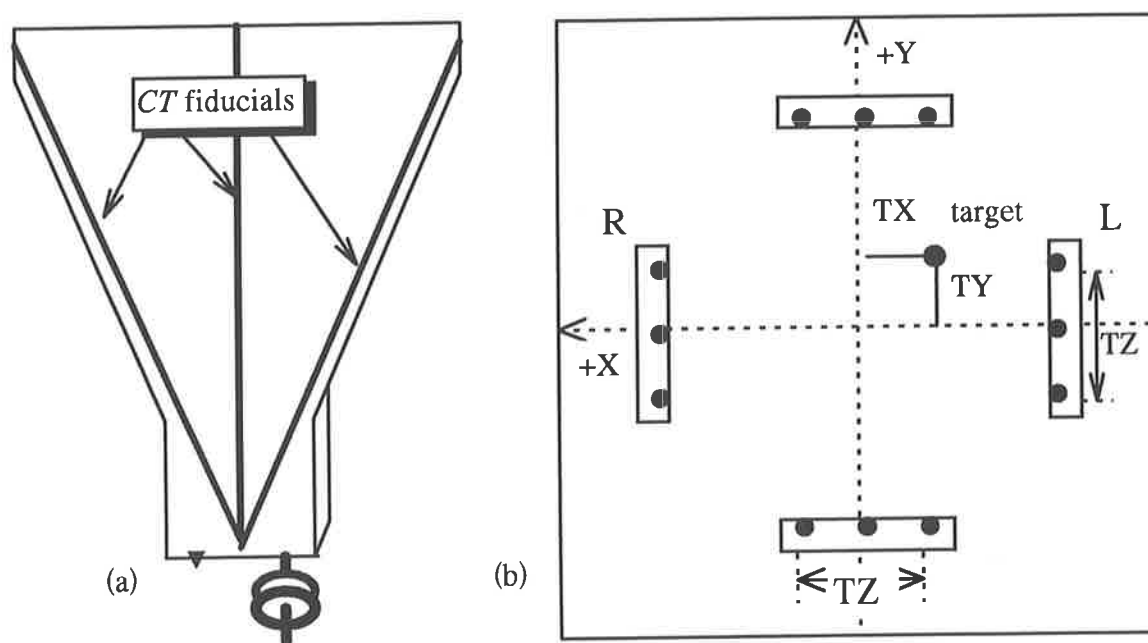


Figure 2.7. (a) *CT* localizer plate and (b) fiducial markers as they appear in the transverse *CT* to calculate the coordinate transformation from the *CT* system into the stereotactic system.

When the two films are fixed on the digitiser tablet, fiducial markers and the centre of the target on each film are digitised in a specific order corresponding to the cursor position on the computer laptop (see Figure 2.8 (b) and (a)). From this digitisation, stereotactic coordinates of the center of the target (*x-ray* focus) are calculated by constructing two rays in stereotactic space which are directed from the *x-ray* source through the target point onto the film (the intersection of the rays defines the target coordinates). Also, the target magnification is calculated from the real and projected

positions of the digitised points. In the next step stereotactic coordinates of the centre of the target and also the lesion size are entered into the *CT* scan transformation for dose calculation.

## 2.7. *SRS* dose calculation

The treatment planning dose calculation in our *SRS* system (Fischer/Leibinger) is based on measured data. However, as part of the author's project, Monte Carlo (*MC*) techniques were employed to calculate the beam data for *SRS* treatment planning requirements and use them as references for the measured data (after checking *MC* against ionization chamber dosimetry at field sizes where the latter is appropriate and accurate.

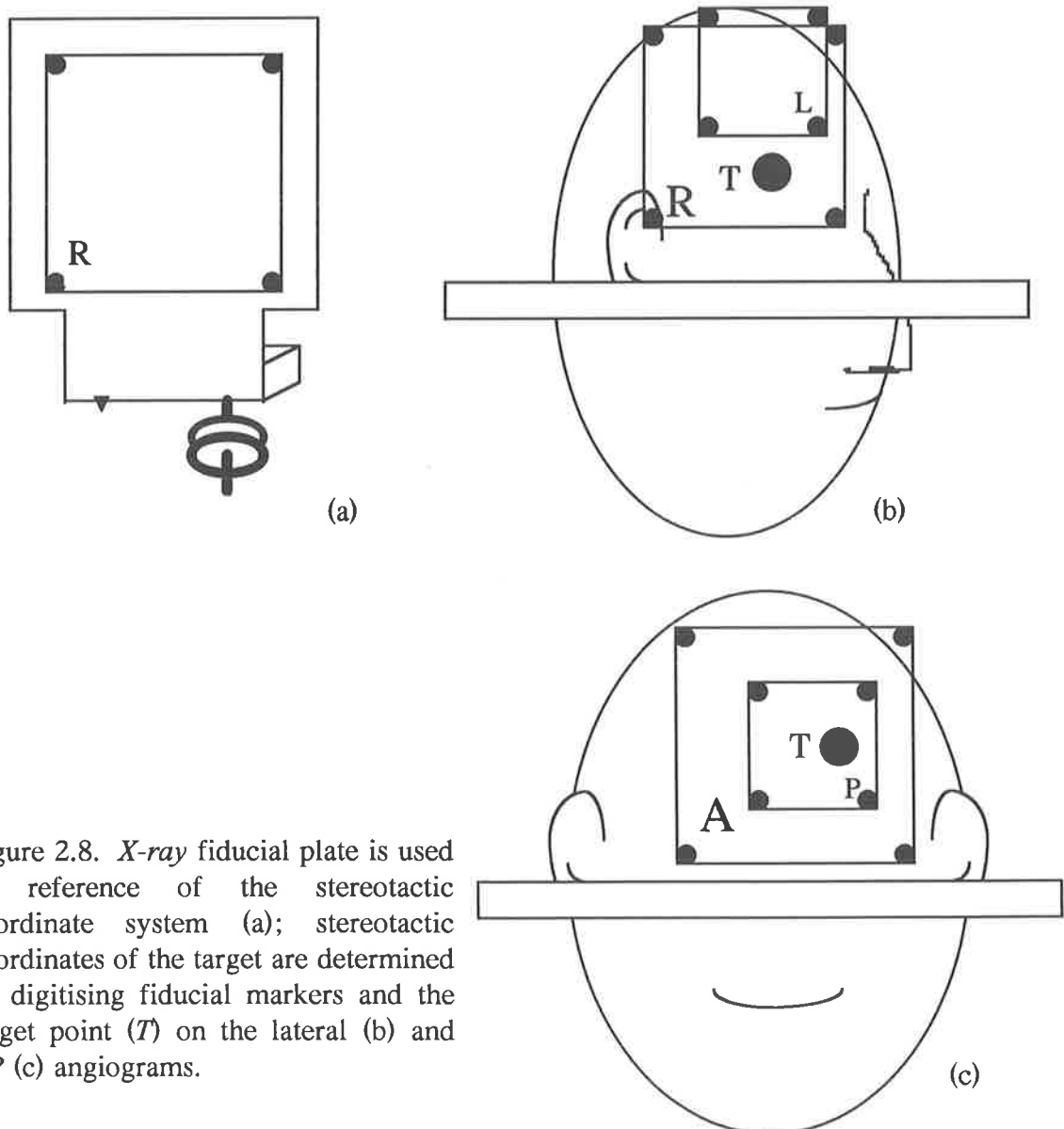


Figure 2.8. *X-ray* fiducial plate is used as reference of the stereotactic coordinate system (a); stereotactic coordinates of the target are determined by digitising fiducial markers and the target point (*T*) on the lateral (b) and *AP* (c) angiograms.

This is because the dosimetry of small *SRS* fields, where lateral electronic disequilibrium exists, is not very accurate, especially when detector is large relative to field dimensions and/ or is not tissue equivalent. This will be discussed in details in chapters 4 and 5.

The dose calculation in our *SRS* system, like in other *SRS* dose calculation algorithms, is a compromise between accuracy and calculation time. Use of only the external outline of the head to define the irradiated medium speeds the dose calculation process. However, the dose calculation is only applicable for convergent beam irradiations with several arcs and small circular fields. To the knowledge of the author, there are no inhomogeneity corrections available in commercially existing *SRS* software. In chapter 7 the validity of this assumption will be considered. Also the fact that *SRS* deals only with small fields eliminates the correction which otherwise is required for beams incident on sloped skin surface.

### 2.7.1. Dose calculation parameters

The required dosimetric parameters for the system are tissue-maximum ratios (*TMRs*) and off-axis factors (*OAFs*) at the isocentre for each collimator. *TMRs* are stored as calibrated tissue-maximum ratios (*CTMRs*), which are the ratios of *TMRs* measured at the isocentre to that of the calibration conditions. This is the equivalent of:

$$CTMR = TMR \times OF, \quad (2-1)$$

where *OF* is the total collimator output factor (see chapter 1). Also, *OAFs* have been measured at the isocentre level at 6 *cm* depth. For more information about *SRS* dose calculation parameters refer to chapter 5.

### 2.7.2. Calculating the dose distribution

Different radiotherapy dose calculation techniques have been discussed in the previous chapter. The dose calculation for *SRS* is rather simple because as mentioned before there are no corrections for inhomogeneity and body contour. The dose at point *P* relative to dose under the calibration conditions, for a single static field,  $DS_{(P)}$  (dimensionless), with the geometry shown in Figure 2.9 is calculated from:

$$DS_{(P)}(d, r, r', FSD) = \left( \frac{FAD}{FAD + d'} \right)^2 \times CTMR_{(d)}(d, r) \times OAF(r') \quad (2-2)$$

where  $r$  is field size at isocentre,  $d$  is depth of  $P$ ,  $FAD$  is the focus-axis distance,  $d' = (d + FSD) - FAD$ , and  $r'$  and  $r''$  are off axis distances of  $P$  at depths  $d-d'$  (isocentre) and  $d$  respectively. Reminding that the Fischer *SRS* system requires a unique *OAF* for all depths for each collimator. This *OAF* has been measured at the isocenter for an average target depth (6 cm). For each gantry arc there are very many beam entry points, but for speeding the process, the dose calculation is performed for a few entry points (normally 8 in our system), which are found from outline points derived from a *CT* scan.

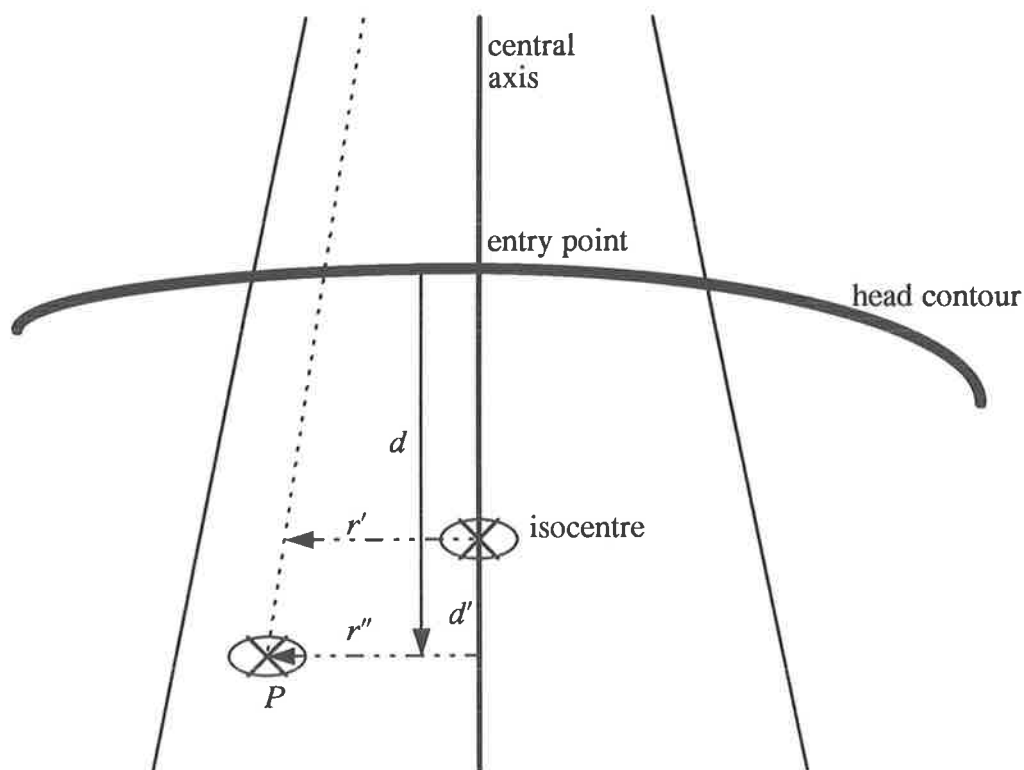


Figure 2.9. A simple geometry for *SRS* dose calculation at point  $P$  for a single static field.

The total dose at point  $P$ ,  $D_{(P)}$ , is the sum of single fields simulating the number of arcs,  $m$ , and the number of entry points,  $n$ , for each arc of gantry rotation:

$$D_{(P)}(r) = \left( \frac{1}{n \times m} \right) \times MU \times D_{MU} \times \sum_m \sum_n DS_{(P)} \quad (2-3)$$

$MU$  is the total number of monitor units and  $D_{MU}$  is the dose per  $MU$  ( $cGy/MU$ ) for the calibration conditions. The above equation gives the total dose at any arbitrary point.

The target dose ( $D_T$ ), that is the dose released at the isocentre, is readily calculated from:

$$D_T = MU \times D_{MU} \times (\text{average CTMR at the isocentre}) \quad (2-4)$$

## 2.8. Choice of optimum energy

Choosing an optimum energy in *SRS* is one of the important factors contributing to an optimum dose distribution in different ways. The energy should be high enough to deposit a reasonable dose at average tumour depths (6-8 cm). Meanwhile, a very high energy beam would have a high dose beyond the target as well as a high exit dose. Also the secondary electron range increases with photon energy. This means that a higher energy photon beam has a somewhat larger penumbra, which is not very desirable for dose conformity and sparing healthy tissues. This is particularly important when a critical organ like the brain stem is in vicinity of the target volume. The dose distribution for different energies in the target volume and also outside the target can be best described by dose volume histograms (*DVHs*) and /or by comparing isodose levels.

The effect of beam energy on *DVHs* for a five arc *SRS* technique is shown in figure 2.10. A 2.5 cm diameter spherical target was covered by 90% isodose level for each energy. The beam diameters (as measured at the 50% levels for a single beam at isocenter) required for this coverage were 2.85 cm for 5 MV, 3.0 cm for 8 MV and 3.1 cm for 16 MV photon energies. The differences in the beam diameters are due to the increase in penumbra width for higher energies, due to increased secondary electron range. This immediately suggests that lower energies will be more suitable as a field with a smaller *FWHM* (but the same 90% width) is satisfactory to give the required coverage of the tumour. In this case more healthy tissue will be spared.

From this figure, it is seen that the dose uniformity inside the target volume is marginally better for higher energies, with a minimal clinical importance in most of the cases. However, the dose outside the target volume is less for the 5 *MV* energy photons.

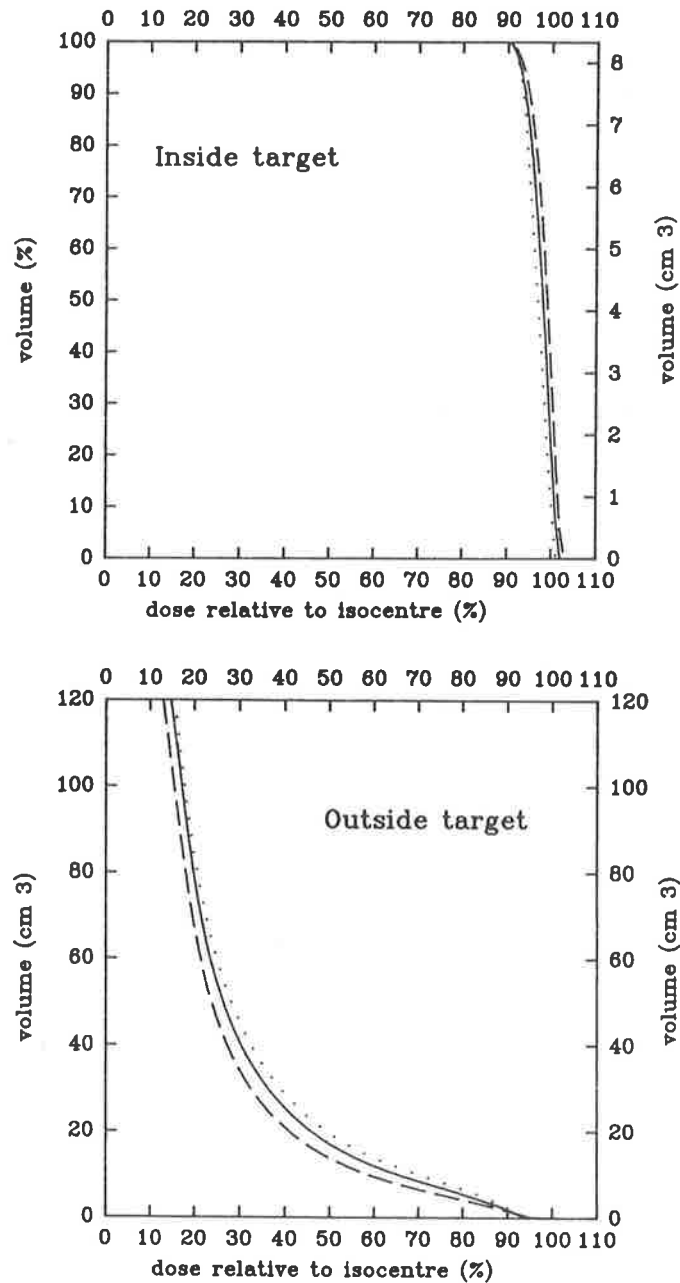


Figure 2.10. Dose volume histograms for a five arc *SRS* technique in treating a 2.5 *cm* diameter spherical target volume using 5 (dashed lines), 8 (solid lines) and 16 (dotted lines) *MV x-rays* (From Thomas, 1994).

Chierego et al (1988) defined a ratio to describe sparing healthy tissues around the target volume as follows:

$$A = \frac{90\% \text{ isodose area}}{40\% \text{ isodose area} - 90\% \text{ isodose area}} \quad (2-5)$$

In fact, the more the ratio  $A$ , the greater the dose gradient and the better dose conformity. The variation of “ $A$ ” with energy is shown in Figure 2.11 for  $Co-60$  and also for 4, 6, 10, and 18  $MV$  photon beams. The maximum value for  $A$  and so the optimum energy was found by above authors to be between 4-6  $MV$  photon energies. This is consistent with  $DVH$  shown in figure 2.10.

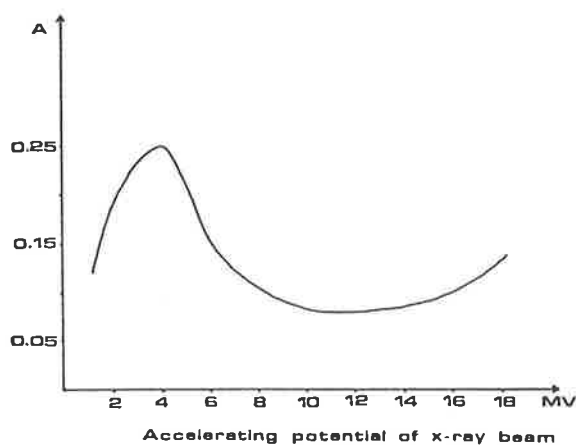


Figure 2.11. Variation of the ratio “ $A$ ” with energy for  $Co-60$  and also for 4, 6, 10, and 18  $MV$  photon beams. This inversely indicates the critical dose received by healthy tissue (from Chiarego et al, 1988).

## 2.9. Dose fall off outside the target volume

One of the most important characteristics of  $SRS$  is the steep dose gradient outside the target volume. The technique is ideal if the critical organs are avoided and there is an isotropic dose fall off anywhere else. To achieve this purpose in linear accelerators, multiple arcs, based on the treatment couch and gantry rotations, are employed. Circular tertiary collimators are generally used (except in the case of conformal therapy with multileaf collimators and other collimating systems which will be discussed in chapter 6) to give a sharper penumbra and high dose regions which are spherical, to conform the shape of most tumours.

Dose fall-off characteristics outside the target volume were considered for four different target sizes positioned in the midbrain with 100% dose at the isocenter. Targets were spheres of 9.2, 12, 23, and 37  $mm$  in diameter, which they were encompassed by 90%

isodose lines, using the existent 7, 9, 15 and 23 mm (drilled size) *SRS* collimators. Our routine *SRS* 6 arc technique was used for this purpose. To consider the dose distribution around the targets, the maximum and minimum distances for the dose to fall off from 90% (at the edge of the targets) to 50%, 20% and 10% were measured and the results are shown in Table 2.1. As it is seen from this table, the penumbra width increases with the field size. This puts even more pressure on *SRS* of larger targets, as is discussed in chapter 7. Also, the dose distributions resulted from different techniques from various Gamma-Knife unit and Linac-based *SRS* centres in treating 1 cm diameter targets (data from Pike et al, 1990), together with similar results for a 9.2 mm diameter target using our 6 arc technique, are presented in Table 2.2 for comparison. The photon energy used in the centres mentioned in Table 2.2 is 10 MV, except for our center which is 6 MV.

Table 2.1. The maximum and minimum distances for the dose to fall off from 90% at the edge of various spherical targets to 50%, 20% and 10%.

Target size (mm)	Minimum distance (mm)			Maximum distance (mm)		
	90%-50%	90%-20%	90%-10%	90%-50%	90%-20%	90%-10%
9.2	2.6	6.4	9.9	3.5	7.2	12.4
12	3.5	7.5	11.9	4	8.6	15.5
23	4	11.6	17.4	4.6	13.3	26.7
37	5.2	15.3	24	5.8	19	38.6

The dose distribution outside the target volume for different techniques at various *SRS* centres is shown in Figure 2.12. The most isotropic dose distribution, as it is seen from this figure and also Table 2.2, could be achieved with a  $4\pi$  distribution of beam entry points. This is not of course practical because of the patient geometry but gives very sharp penumbra as seen. The source distribution in Gamma-Knife units is over an angular segment of  $160^\circ \times 96^\circ$  in the new generation of these systems. Generally, the closer the minimum and maximum values are, the better the dose distribution is and so better sparing of normal tissues is obtained. As it is seen from Figure 2.12, the Adelaide technique gives better dose distribution than others, especially at 90%-20%

and 90%-10%. This is due to using 6 MV photon rather than 10 MV and also a smaller target volume (9.2 as opposed to 10 mm).

Table 2.2. The maximum and minimum distances for the dose to fall off from 90% at the edge of a 10 mm (9.2 mm for Adelaide) diameter targets to 50%, 20% and 10%.

Technique	Minimum distance (mm)			Maximum distance (mm)		
	90%-50%	90%-20%	90%-10%	90%-50%	90%-20%	90%-10%
4 $\pi$ geometry	2.5	6	10.5	2.5	6	10.5
Single plane (transverse)	2	3.5	4	3.5	14.5	33.5
Boston (4 arcs)	2.5	5.5	8	3.5	8.5	19.5
Adelaide (6 arcs)	2.8	6.7	10.5	3.6	7.6	13.3
Heidelberg (11 arcs)	2.5	5	8	3	8	14.5
MacGill (dynamic)	2	4	4.5	3	9	20
Gamma unit (Sheffield)	2	3.5	4	4	11	22.5

Dose volume histograms are another useful method to show the dose distribution both inside and outside the target volume. In this way the ability of a technique in releasing a uniform dose across the target and in sparing normal tissues is shown graphically. This method can be used to compare different treatment techniques and select the more appropriate technique, as it was shown in Figure 2.10.

### 2.10. SRS quality assurance

As mentioned before, SRS is a high precision radiation treatment technique in which a large dose is delivered in a single fraction. The dose is high enough to destroy the lesion. The dose deposition in this technique is highly focal with a sharp gradient (10-15% per mm) near the edge of the field. Therefore, accurate targeting and dose shaping are of paramount importance and require an extensive quality assurance (QA) program.

Quality assurance in *SRS* is necessarily a multidisciplinary program, not only for radiation oncology but also for radiology and neurosurgery (Schell and Kooy, 1994).

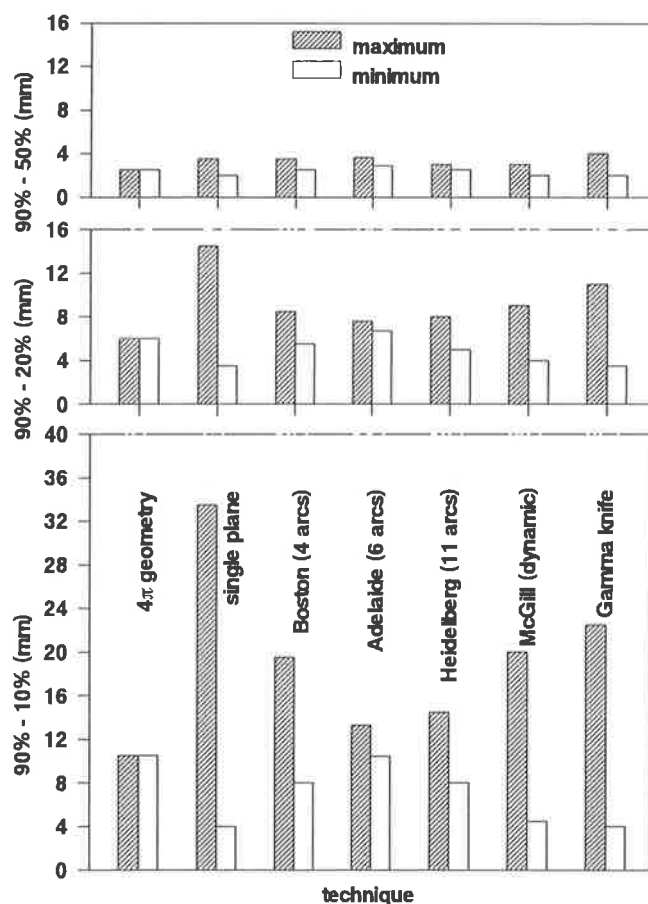


Figure 2.12. The dose distribution outside a 10 mm (9.2 mm for Adelaide) diameter target volume, as the maximum and minimum distances for the dose to fall off from 90% at the edge of the target to 50%, 20% and 10%.

Medical Physics *QA* programs apply to three stages according to the American Association of Physicists in Medicine (*AAPM*) report No. 54 (1995), which are (i) probable risk analysis (*PRA*); (ii) the routine *QA* tests; and (iii) the *QA* for each treatment.

### 2.10.1. Probable risk analysis

The *PRA* is necessary for designing individual systems and implementing new techniques. This includes a wide variety of procedures which involve patient safety, target localization, head ring movements, verification of mechanical tolerance etc. Proper interlocks have to be imposed to prevent any collision and unnecessary

movements during treatment. This is sometimes of vital importance, for example in the pedestal mounting techniques proper interlocks and even mechanical locks are used to ensure that the treatment couch does not have any vertical movement during treatment. Also of very high priorities are setting the secondary collimators (jaws) to the required size (in our system  $7 \times 7 \text{ cm}^2$ ) and checking that the tertiary (*SRS*) collimator is the right size and that the coordinates on the head ring localizer are correct.

### 2.10.2. The routine *QA*

The routine *QA* program includes those generally related to the following steps:

- (i) the stereotactic frame and localizer, including periodic checking of the localization process for a target of known coordinates. In the target localization by *CT*, thin enough slices through the target have to be used to minimise the localization error.
- (ii) the therapy machine, which includes dose calibration, checking stability of all rotational axes of gantry, couch and collimator.
- (iii) the diagnostic machines, including testing the *CT* couch-attachment device and proper alignment of the *SRS* head ring with the diagnostic machines. Also *CT* scan should be taken from below the lesion to the top of the skull to determine beam entry points to the skull, which are required for the dose calculation,
- (iv) the software, including verification of dose calculation, image transformation and digitiser linearity.

### 2.10.3. The treatment *QA*

Due to the characteristics of *SRS* as a single fraction high dose technique and the related complexities, the *QA* program must provide a treatment procedure checklist. The checklist should include the treatment step sequences, in order to minimise the risk of any maladministration that might affect patient's safety. Laser alignment check and its agreement with the beam, the required tertiary collimator size, jaw setting, anti-collision interlocks and couch disabled (in case of pedestal mounting), patient set up, target coordinates check on the target positioner frame and their alignment with lasers,

and proper attachment of angiography fiducials to the head ring (for port film verification) are examples of this kind.

### **2.10.3.1. Laser check**

In a couch mount technique as in our department, the accuracy is derived from the laser system. The laser system includes two cross wall lasers and a cross ceiling laser. During routine *QA* these lasers are aligned to the isocentre of the linear accelerator. Also, before each treatment a set of films is taken for various couch and gantry angles to confirm the agreement between lasers and the radiation isocentres.

A verification film is sandwiched between two layers of perspex and placed horizontally on the couch with the needle hole adjusted to the ceiling cross lasers. The film is exposed at the couch angles  $0^\circ$  and  $270^\circ$  at gantry angle  $90^\circ$  using a 2 mm stereotactic collimator. A second film is positioned vertically with the needle hole adjusted to the ceiling cross laser at the isocentre and the film is exposed at gantry angles  $0^\circ$  and  $90^\circ$  through the 2 mm collimator. Films are punctured through the needle hole at the isocentre and also through a second hole at an off axis point as an orientation reference, after each set of the test. After development, if the agreement is better than 1 mm the system is ready for the patient set up.

### **2.11. Patient set up and target verification**

The patient set up will proceed using the treatment protocol. Special attention required to ensure that the patient head ring has not moved between its initial placement and treatment (Tsai et al, 1991). The patient lies on the couch in the supine position with the head ring aligned and is firmly fixed to the couch-mount docking device. The target positioner frame (see Figure 2.13) is firmly attached to the patient head ring and is calibrated with respect to the stereotactic coordinate system. Then the verniers on the target localization frame are shifted to the target coordinates along *x*, *y* and *z* axes and fixed at those positions. At this stage imaginary lines connecting opposite pairs of the adjusted cross hairs on the positioner frame pass through the centre of the target. The couch is shifted so that the laser beams fall exactly on the adjusted cross hairs. Now the

centre of the target must be at the isocentre. At this stage the laser positions on the head ring are marked and the target positioner frame is detached.

The target position verification is performed using orthogonal port films with four angiographic fiducial plates embedded in the head ring. Lateral and AP port films are taken, each with a double exposure, once when the appropriate *SRS* collimator is on and the second time with a large open field (eg.  $40 \times 40 \text{ cm}^2$ ). After development, films are placed on the digitiser light box and the fiducial markers and centre of the *SRS* collimator projections are digitised. In this way the stereotactic coordinates of the centre of the collimated beam (isocentre) are derived. If the agreement between the stereotactic coordinates of the target and the isocentre is better than 1 mm, the patient irradiation is initiated, otherwise the set up process will be repeated.

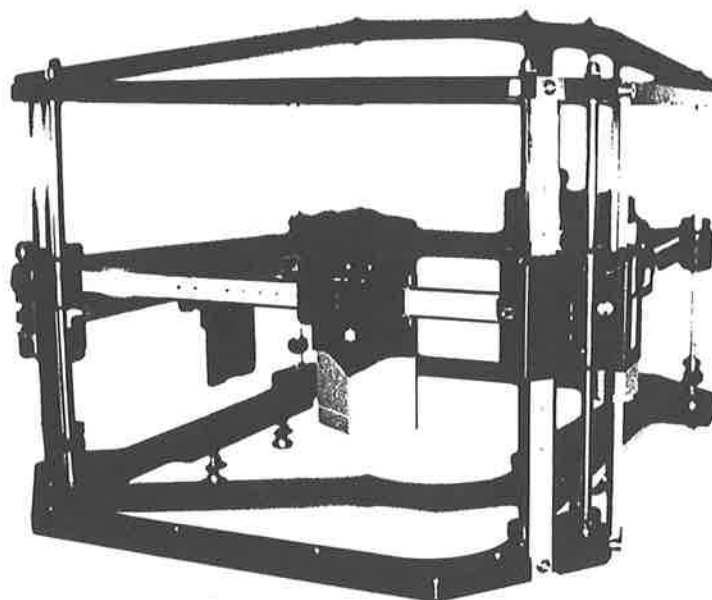


Figure 2.13. The target positioner frame.

### 2.12. The accuracy of *SRS*

The overall accuracy of *SRS* is a combined effect of the technical limitations of the diagnostic device, digitisation device, frame and treatment units, dosimetry, and dose calculation technique. The accuracy is also affected by the current knowledge of the neurological abnormality and its radiation response (Schell et al, 1995). The

uncertainty of the target alignment with the isocentre is less with the Gamma-Knife unit (0.2-0.4 *mm*) than for linear accelerator (about 1.0 *mm*) (Wu et al, 1990). However, our clinical experience (with linear accelerator) shows a mean accuracy of 0.5 *mm*, as far as the setup in the previous section is concerned. Of course, the overall accuracy depends on many factors, including the *CT* resolution and the gantry walk-out during rotation, assuming the clinical decision in outlining the lesion and determining its centre is accurate.

### **2.12.1. Diagnostic resolution**

The definition of a lesion with *CT* and or angiography (in the case of an *AVM*) depends on the contrast and resolution of the image. However, this is greatly reduced by the microscopic extent of the lesion. This is especially true for certain brain tumours and it is caused by the invasive nature of malignancies. For example, from a study on glioblastoma multiforme tumours in 11 patients, the autopsy results have confirmed that in 9 cases the tumour extended beyond a 1 *cm* margin around the contrast enhanced areas (Halperin et al, 1989 and Larson, 1994). The pixel dimensions in a *CT* image of 30 to 40 *cm* and a 512 × 512 matrix is about 0.7 *mm* and the slice separation is minimum 1-2 *mm*. Therefore, the uncertainty of an object location is more than 1.5-2 *mm*.

### **2.12.2. Linear accelerator accuracy**

A linear accelerator is acceptable for *SRS* if it has stable mechanical and radiation isocentres. The mechanical isocentre of the gantry and couch were determined using the isocentre pointer and a target point, respectively. In this way the mechanical stability of the isocentre was determined and lasers were adjusted to that point.

The isocentre of the couch can also be found by attaching the 2 *mm* diameter stereotactic collimator to the collimator holder plate. A verification film was placed horizontally on the couch at the laser cross at the isocentre. Then film was irradiated at various couch angles, while the gantry was at 90°. The isocentre was marked on the film with a needle hole. This resulted in star shape tracks of the beams, with a center at the needle hole for a perfect isocentric movement. The radiation isocentre was

measured with the verification film in vertical orientation (parallel to the gantry rotation plane) with the needle hole at the cross laser isocentre. The film was irradiated at various gantry angles. The result was similar to the previous case and the irradiation isocentre, which in a perfect condition should be at the needle hole. The deviations from the needle hole for above measurements were measured and if not acceptable, lasers adjusted to give a minimum deviation.

### **2.12.3. The centre of the dose distribution**

The centre of the dose distribution was determined for multiple arcs, in a situation similar to the treatment. A verification film was placed within a humanoid head phantom and a 3 mm needle as the target was entered through the film. The head ring was connected to the phantom and a complete set of CT scan (with CT fiducials in place) with a 2 mm slice separation was performed from below the target to the top of the skull. After treatment planning and determination of SRS coordinates, the target was positioned in the cross lasers at the isocentre. Port film verifications showed the setup accuracy to be better than 0.5 mm. After this, the target was irradiated with 6 arcs as a routine treatment course. The processed film was scanned and the centre of isodose curves showed an agreement better than 1 mm with the pinmark on the film.

### **2.13. Cost effectiveness of SRS**

As many as 50% of patients dying from cancer have shown brain metastases in autopsy series (Flickinger et al, 1994). The lack of effectiveness of radiotherapy alone to control brain metastases has been the reason to perform both tumour resection and post operation whole brain radiotherapy (WBRT). This has significantly improved medial survival and decreased local failure. Actual tumour control rates achieved at 70 weeks were 57% with surgery plus WBRT vs 13% with WBRT alone (Flickinger et al, 1994). Despite such reports, surgery (S) is not acceptable or not offered to many patients, due to the tumour location or patient's poor medical condition. In addition, some patients refuse surgery to avoid the potential morbidity and hospital stay. SRS plus WBRT is an alternative which resolve some of problems associated with the former combination.

The cost effectiveness of above treatment schedules for treatment of single brain metastases was considered by several researchers (Sperduto and Hall, 1995; Rutigliano et al, 1995; and Noyes et al, 1996). Sperduto and Hall (1995) have considered the cost-effectiveness of alternative treatments for a single brain metastasis. They have compared (i) whole brain radiation therapy (*WBRT*), (ii) surgical resection plus *WBRT*, and (iii) *WBRT* plus *SRS*. The reported average local controls are 48-75%, 78-80%, and 82-99% and the average total charges \$3536, \$36172, and \$17127 for the cases (i) to (iii), respectively. Noyes et al (1995) in a similar study have compared the cost effectiveness and outcome of *SRS+WBRT* and *S+WBRT* in similar group of patients (113 vs 54 patients, respectively). These authors have shown that clinical outcome with *SRS* is better than that of surgical resection, with a median survival 56 vs 40 weeks. Other advantages of *SRS* compared to craniotomy include shorter hospital stay, lower morbidity, no surgical mortality, and reduced cost (Flickinger et al, 1994).

#### **2.14. Discussion and conclusion**

*SRS* is a high precision radiation treatment technique in which a large dose is delivered in a single fraction. The dose deposition in this technique is highly focal with a sharp gradient near the edge of the field. Therefore, accurate targeting and dose shaping are of paramount importance and require an accurate dosimetry technique as well as an extensive quality assurance program. It was shown that the optimum *x-ray* energy for *SRS* is 4-6 *MV*, which in this case a better dose conformality and a better sparing of normal tissue are achieved. Using heavy-charged particle systems is generally better in this regard, however the higher cost and nonavailability of those systems are prohibiting factors. By comparing to the other techniques at different *SRS* centres, it was shown that the dose distribution of our 6 arc technique is more uniform. This is mainly due to the 6 *MV* photon energy which is used in our system, rather than a 10 *MV* for others.

It was shown that the biggest advantage of using linear accelerator over Gamma unit is the ability of beam shaping and conformal *SRS*. The other advantage is that there are more choice of collimator sizes in linear accelerators than Gamma Knife units. Due to this fact the target dose is prescribed to a lower percentage of the maximum dose in the Gamma Knife system. This would cause dose nonuniformity (hot spots) within the target which is not desirable, especially in certain types of tumours in which normal

tissues are embedded (see chapter 6). Gamma Knife units, however, have better geometric accuracy. It was shown that using *SRS* is more cost effective than other alternative techniques.



## Chapter 3

# Evaluation of Diamond Detectors for Megavoltage Beams

### 3.1. Introduction

The most commonly used detectors for megavoltage photon and electron beam measurements are the ionization chamber, the silicon diode and film. All have a limited range of applicability which is dictated by their design and the intrinsic properties of their respective detector elements. This investigation has been carried out as part of work to determine the best detector for use in stereotactic radiosurgery (SRS) as well as in conjunction with a project aimed at improving electron pencil beam dose calculations around small inhomogeneities, where in both cases high-resolution dosimetry is required.

The ionization chamber is able to measure dose distributions very accurately for regions where the dose is not varying rapidly. The relatively large sensitive volume of most chambers however, means that a significant spatial averaging, or smoothing, of the true dose distribution occurs. In addition, the low density ionization chamber will cause over-estimation of the penumbra width (Dawson et al, 1986). Ionization chambers are therefore not suitable when high spatial resolution is required, such as in accurate measurement of the penumbra region in conventional radiotherapy (Dawson et al, 1986) or in dosimetry of stereotactic radiosurgery beams.

Silicon diode detectors have the advantage of a small sensitive volume and thus have a high spatial resolution. A significant disadvantage in principle however, is the non water (tissue)-equivalence of the silicon. Because of the high atomic number of silicon ( $Z=14$ ), silicon diodes have energy dependent collision mass stopping power and mass energy absorption coefficient ratios relative to water ( $\bar{Z}=7.4$ ). In particular, the diode detector has high photoelectric absorption at low energies, and so over responds to lower energy scattered photons. For this reason diode detectors used for photon

dosimetry are constructed with a shield at the base of the sensitive element to screen out low energy back-scattered radiation.

Film has the advantage of simplicity in relative dosimetry and high spatial resolution but again the energy dependence, due to the high atomic number of the emulsion material (silver bromide,  $\bar{Z}=41$ ), gives different collision mass stopping power and different mass energy absorption coefficient ratios relative to water. Also differences in individual films and in developing conditions make them unsuitable for absolute dosimetry.

Diamond detectors are in principle attractive for high-resolution megavoltage photon and electron beam measurements because of their small size and near tissue-equivalence. Other advantages of diamond detectors include high sensitivity, low leakage current (Kozlov et al, 1975) and a high resistance to radiation damage (Planskoy, 1980). All experimental work discussed in this chapter was carried out by the author (unless otherwise stated).

### 3.2. Theory of diamond detector response

Diamond detectors can be considered as resistive elements (Burgemeister, 1981), where for a given bias voltage, current is zero with no radiation and increases almost linearly with dose rate. Also, for a given dose rate, current is proportional to bias voltage—this is in contrast to ionization chambers, where if the operating bias voltage is high enough to prevent recombination, any further increase in voltage does not significantly increase current (until multiplication stage). Importantly, it is the presence of metastable states (traps), provided by impurities in the crystal, which allows conductivity to vary linearly with dose rate (see next paragraph). The basic theory behind radiation-induced conduction in insulators, and an explanation for the observed dose rate dependence, is given below. For a more complete explanation of the theory, see Fowler (1966).

As a result of ionization, free electrons are produced which are collected at the anode if they do not first recombine with a vacant hole. The conductivity,  $\sigma$ , is proportional to the rate of free electron production,  $f$ , and the recombination time  $\tau$ :

$$\sigma \propto f\tau \quad (3-1)$$

The product  $f\tau$  is the equilibrium number of free electrons in existence,  $n$ . If there are no traps,  $n$  is also the number of vacant holes. Since recombination time is inversely proportional to the number of vacant holes,  $\tau \propto 1/n$ . It then follows that  $n \propto f^{1/2}$  and  $\tau \propto f^{-1/2}$ , so  $\sigma \propto f^{1/2}$ . Now since  $f$  is proportional to dose rate  $D$ ,

$$\sigma \propto D^{1/2} \quad (3-2)$$

A pure diamond crystal is thus not a dosimeter which gives a linear dose rate response as the increase in number of vacant holes with dose rate, and consequent decrease in recombination time, causes the current to be proportional to the square root of the dose rate.

If impurities are added, and hence traps introduced, the number of vacant holes existing at equilibrium is the number of free electrons,  $n$ , plus the number of electrons in traps,  $m$ . Note that  $m$  increases with dose rate but much more slowly than  $n$ . The recombination time,  $\tau$ , is now proportional to  $1/(m+n)$ . If  $m \gg n$  (as is the case at low dose rates),  $\tau$  is then approximately independent of  $n$  and therefore of dose rate. From equation (3-1), it is obvious that conductivity in a diamond crystal with sufficient traps is almost proportional to dose rate (since  $\tau$  is almost constant).

A general relationship of conductivity to dose rate for radiation induced conductors is given by Fowler (1966) as:

$$\sigma \propto D^{\Delta} \quad (3-3)$$

where:

$\Delta = 0.5$  if there are no traps (the same as in equation 3-2).

$\Delta \approx 1$  for low dose rates ( $m \gg n$ ) when a uniform and or quasi-uniform distribution of traps is present.

As dose rate increases,  $n$  becomes more significant compared to  $m$  and thus  $\tau$  decreases. This causes  $\Delta$  to reduce, until ultimately, when the dose rate is so high that traps are unimportant ( $n \gg m$ ),  $\Delta$  again becomes 0.5. Because of this reduction in  $\Delta$ , it is expected that there will be a sub-linear dose rate response as dose within a radiation pulse is increased.

As well as a sublinear increase in response as instantaneous dose rate is increased (by changing dose per pulse), a decrease in the integrated current as the pulse frequency is increased is expected. This is because of the fact that some electrons remain in traps after each pulse has finished, leaving corresponding vacant holes (Fowler, 1966). Thus, a small current (which decreases as traps empty) continues to flow between pulses. Furthermore, if the trap proportion increases with absorbed dose, a reduction in response is expected until an equilibrium trap population is reached.

It is important to note that the response of a diamond detector is critically dependent on the likelihood of electrons reaching the anode before they recombine. This likelihood will increase as (i) the distance between electrodes is reduced and (ii) the bias voltage is increased (until the maximum drift velocity is reached). From theory (Kozlov et al, 1975), it is predicted that for complete charge collection the detector thickness must be less than 1.0 mm. Konorova and Kozlov (1971) have found this thickness experimentally to be 0.2-0.3 mm. *PTW* diamond detectors used in this work are 0.33 and 0.25 mm thick.

### 3.3. Physical properties of *PTW* diamond detectors

Diamond crystals suitable for dosimetry are of type IIa (Kozlov et al, 1975), meaning that they are almost transparent to ultra-violet light. The degree of transparency increases with a reduction in the concentration of nitrogen impurities, which provides a basis for choosing crystals with a low nitrogen concentration. *PTW* diamond detectors investigated in this work are stated to have a nitrogen concentration of less than  $10^{19} \text{ cm}^{-3}$ . The effect of an increasing nitrogen concentration is to increase the number of traps, increasing  $m$  (see 3.2) and thus reducing  $\tau$  and making it less dose rate dependence. Too much nitrogen can lead to excessive loss of signal however, due to the reduction in  $\tau$ .

The radiation sensitive region of the diamond detector is a low-impurity natural diamond plate of thickness 0.33 mm and volume  $14 \text{ mm}^3$ , sealed in a cylindrical polystyrene housing of diameter 7.3 mm. Bias is applied through 0.05–0.6  $\mu\text{m}$  gold contacts and 50  $\mu\text{m}$  silvered copper wire. The surface of the diamond detector is 1.0 mm beneath the end of the housing. In Figure 3.1 is a comparison of the longitudinal

cross sections of the diamond and diode detectors. Also the physical and operating parameters of the diamond detector are given in Table 3.1. However, in most of the experimental works only diamond detectors with smaller sensitive volume were used (unless otherwise stated).

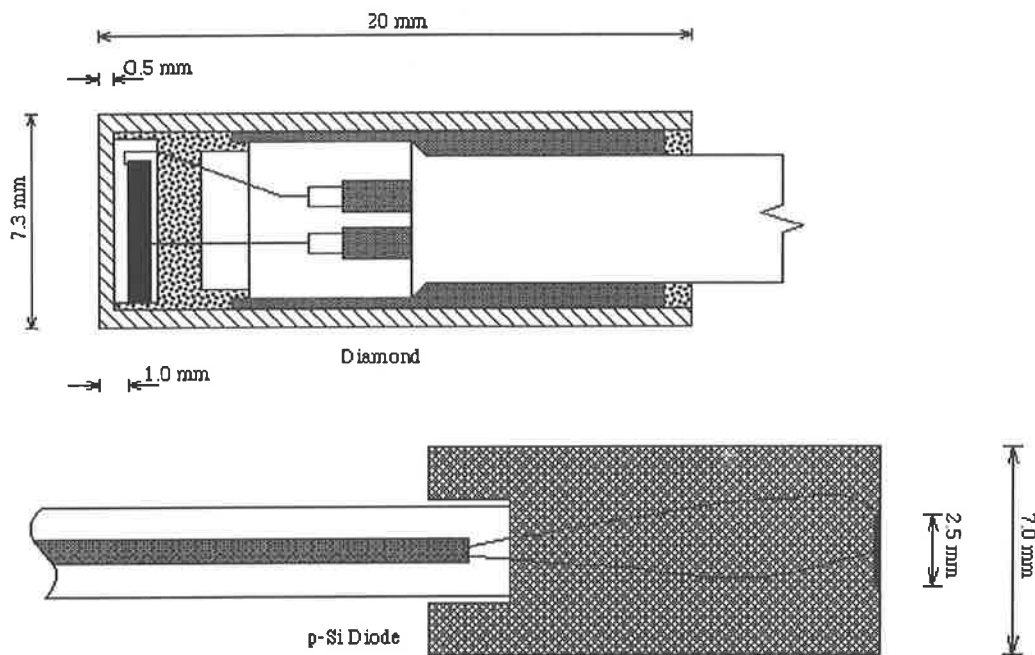


Figure 3.1. Longitudinal cross sections of the diamond and diode detectors.

### 3.3.1. Current-voltage response

Because of the rapid rate of electron-hole recombination, a very high bias voltage is required for complete charge collection to occur. Canali et al (1979) report that for a 0.15 mm thick detector, complete charge collection occurs for applied electric fields greater than  $10^4$  V/cm. In comparison, the *PTW* detector tested in this work is 0.33 mm thick and the recommended operating voltage is 100 V ( $3 \times 10^3$  V/cm). It is therefore expected that the *PTW* detector does not operate with complete charge collection. The current was measured using a Nuclear Enterprises 2570 electrometer (with bias supplied externally) for bias voltages of 20 to 200 V, at a dose rate of 2.0 Gy/min and is shown in Figure 3.2. The plotted current is the charge collected for a dose of 1.0 Gy divided by the irradiation time of 30 s. Detector current is approximately 50 times that

**Table 3.1.** Physical parameters of diamond detectors (as supplied by *PTW*) for diamond detectors No. 1 and No. 2, respectively.

Main impurities	Nitrogen and Boron ( $<10^{19}$ atoms $cm^{-3}$ )
Sensitive volume	1.4 and 1.6 $mm^3$
Sensitive area	4.3 and 6.2 $mm^2$
Thickness of sensitive volume	0.33 and 0.25 $mm$
Operating bias	+100V ( $\pm 1\%$ )
Dark current	$<10^{-12}$ A
Sensitivity to $^{60}\text{Co}$ radiation	$1.75 \times 10^{-7}$ and $1.97 \times 10^{-7}$ C/Gy
Pre-irradiation dose	2-5 Gy

of a Scanditronix *RK* ionization chamber as a consequence of a solid sensitive volume. It is obvious from Figure 3.2 that charge collection is incomplete up to at least 200 V. It also appears that the rate of increase in current with voltage decreases up to approximately 100 V, whereafter the rate of increase is approximately constant. This is consistent with the electron mobility  $\mu$  (velocity per electric field strength) reducing at high field strengths and with the reduced number of charges available to be collected (Kozlov et al, 1975 and Canali et al, 1979).

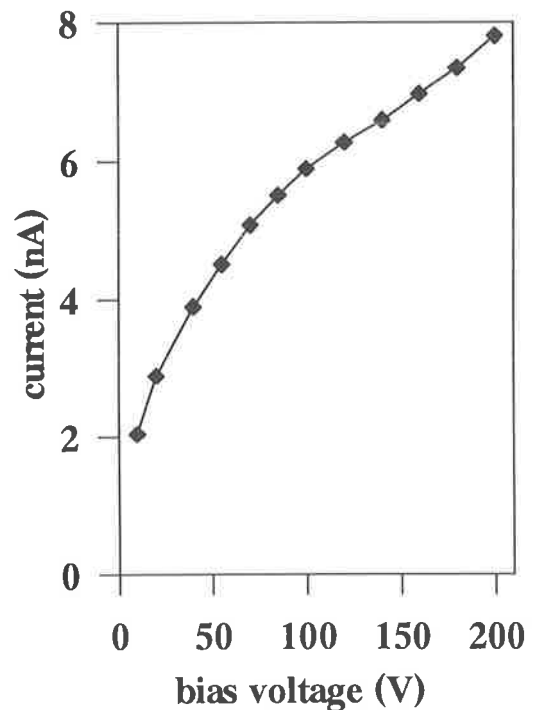


Figure 3.2. Average diamond detector current (nA) versus bias voltage for a dose rate of 2 Gy/min.

The electron mobility at room temperature is stated by Kozlov et al (1975) to be  $2000 \text{ cm}^2/\text{V}$  and by Canali et al (1979) to be  $2400 \text{ cm}^2/\text{V}$ . The maximum electron drift velocities given by these authors is  $10^7 \text{ cm/s}$  and  $1.5 \times 10^7 \text{ cm/s}$ , respectively and both state that this maximum occurs at  $10^4 \text{ V/cm}$ .

### 3.3.2. Charge collection efficiency

The charge collection efficiency is the ratio of detector current to the rate at which charge is produced in ionizations. This ratio is also known as the gain factor (Fowler, 1966). The rate of charge production in the crystal is readily calculated from knowledge of the dose rate,  $D$  density,  $\rho$  and volume,  $V$  of the sensitive element and the energy  $w$  required to produce an ion pair:

$$\frac{dQ}{dt} = \frac{DVe\rho}{w} \quad (3-4)$$

The density of diamond is  $3.5 \text{ g/cm}^3$ , the volume of the crystal is  $1.4 \times 10^{-3} \text{ cm}^3$  (see Table 1) and  $w$  is approximately  $16 \text{ eV}$  (Kozlov et al, 1977) so at a dose rate of  $2.0 \text{ Gy/min}$  ( $3.3 \times 10^{-5} \text{ J/g/s}$ ) the charge production rate is  $1.0 \times 10^{-8} \text{ C/s}$ . From Figure 3.2, the detector current at  $2.0 \text{ Gy/min}$ , with a bias of  $100 \text{ V}$ , is  $5.8 \times 10^{-9} \text{ A}$ , which gives a gain factor of 0.58.

The gain factor is less than unity because the recombination time is less than the transit time required for an electron to pass from one electrode to the other. Note that the transit time is equal to the maximum time required for a free electron to be collected. The gain factor in equilibrium is in fact equal to the ratio of recombination to transit time (Fowler, 1966). The transit time is simply the thickness of the detector,  $L$  divided by the electron velocity,  $\mu(V/L)$  and is thus equal to  $4.5 \times 10^{-9} \text{ s}$ . Using the gain factor found above, the recombination time for a dose rate of  $2.0 \text{ Gy/min}$  and a bias of  $100 \text{ V}$  is  $2.6 \times 10^{-9} \text{ s}$ . This value is close to those obtained by Planskoy (1980) for  $0.1 \text{ cm}$  thick detectors operating at a bias of  $150 \text{ V}$  ( $1.5 \times 10^3 \text{ V/cm}$ ) with a dose rate of  $1 \text{ Gy/min}$ . The values obtained for the detectors with the longest recombination time tested by that author were  $3.7 \times 10^{-9} \text{ s}$  and  $1.35 \times 10^{-9} \text{ s}$ . Note that recombination time is approximately

$10^3$  times less than the duration of a linear accelerator pulse, hence an equilibrium number of free electrons during a pulse can be assumed. Konorova (1966) showed that the upper limit for recombination time is  $10^{-8}$  s (decreasing with increasing nitrogen concentration) and that it is  $10^{-9}$  to  $10^{-8}$  s if the nitrogen impurity is less than  $10^{19} \text{ cm}^{-3}$ .

By equating the transit time to the recombination time and solving for  $L$ , a detector thickness at which complete charge collection would be expected at 100 V bias can be obtained. Since recombination time is inversely proportional to electron velocity (Fowler, 1966) and hence to electric field strength, it is proportional to detector thickness for a constant bias voltage. This means that the recombination time for a thickness  $L$  (in cm) is different by a factor  $L/0.033$  from that obtained above. The thickness for complete charge collection is thus obtained from the equality:

$$\frac{L^2}{V\mu} = 2.63 \times 10^{-9} \frac{L}{0.033}, \quad (3-5)$$

giving  $L = 0.019 \text{ cm}$ . Note that if the reduction in recombination time as field strength increases is ignored, a value of 0.025 is obtained.

Complete charge collection may be possible for a thickness of 0.033 cm by continuing to increase the bias voltage (thereby reducing transit time), although since recombination time is inversely proportional to electron velocity (and hence to bias voltage) when there is a large trap population (Fowler, 1966), this may be difficult to achieve. Furthermore, electron mobility, and hence the increase in rapidity of charge collection with field strength, decreases at high voltages (Canali et al, 1979).

### 3.3.3. Stability of detector current

The response of the *PTW* diamond detector was found to initially decrease with absorbed dose. This is attributed to the reduction in the electric field caused by increasing polarisation as traps fill (Kozlov et al, 1975). The reduction in recombination time as the number of vacant holes increases is also likely to contribute to this decrease. So that an equilibrium trap population is established before

measurements are made, it is necessary to pre-irradiate the detector with the operating bias voltage applied. The pre-irradiation dose recommended by *PTW* is 2.0-5.0 Gy.

With a bias of 100 V, the detector was irradiated at a dose rate of 2.0 Gy/min in 1.0 Gy steps until a steady charge reading was obtained. Prior to this, the detector had not been used for approximately three weeks. A stable reading was obtained when a dose of approximately 15 Gy had been delivered, after an exponential drop in response of approximately 10%. In comparison, Plansky (1980) reports a steady current after a dose of 15-20 Gy in a  $^{60}\text{Co}$  beam, with a decrease in that time of 10-15%. The detectors used in that work however did not exhibit such a drop in response unless they had not been used for several months. The detector was again exposed to successive doses of 1.0 Gy after it had been unused for only one day. A steady reading was established in this case after 3.0 Gy had been delivered, indicating that the traps had only partially emptied in a day. On the first of these two days, the bias was increased to 200 V after a stable reading was achieved at 100 V. An exponential reduction in charge collected was observed in successive 0.5 Gy irradiations, with the reading dropping by approximately 5% over 4 Gy. This indicates that an increase in the equilibrium trap population occurs as bias voltage is increased, with a consequent increase in the degree of polarisation until equilibrium is established. Consistent with this is the fact that when the bias is again decreased to 100 V, the response increases by approximately 10% over 10 Gy, indicating a reduction in the equilibrium trap population from that at 200 V. Analysing the response of the diamond detector has shown that (for the same irradiation condition) the equilibrium trap population is the same when a certain bias voltage is used. This is shown in Figure 3.3 as the result of the first day of these two days experiment. In this figure it is shown that the diamond equilibrium response when the bias had been increased from 0 V (before irradiation) to 100 V has approached the same value as when it was reduced from 200 V to 100 V.

#### 3.3.4. Constancy and linearity

If a detector is to be used for absolute dosimetry it is important that the detector has the same response for any specific dose, regardless of the radiation history of the detector and other contributing factors. The constancy of response of the diamond detector was

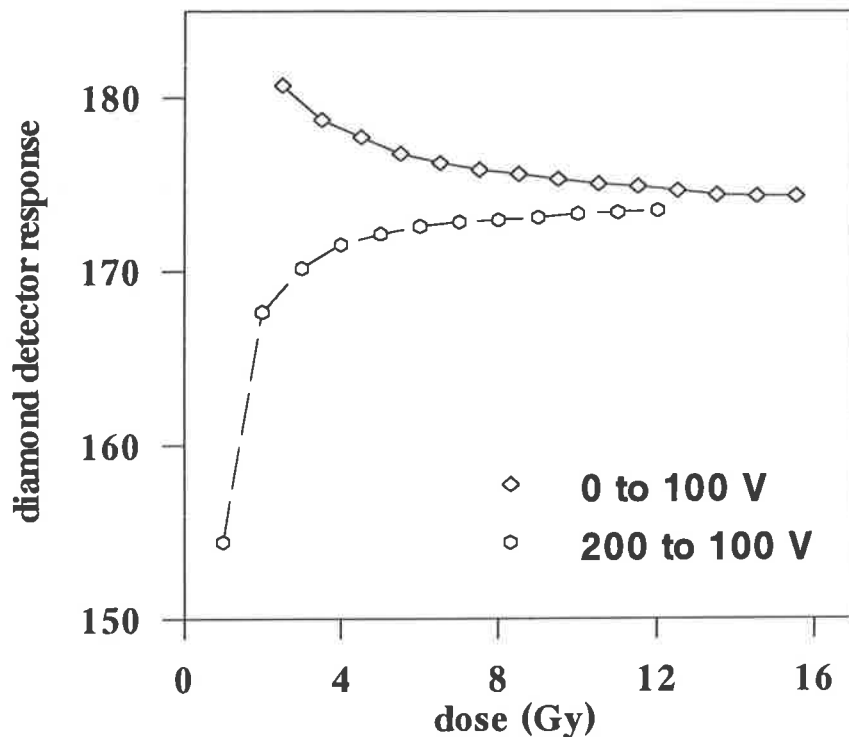


Figure 3.3. The diamond detector responses to different dose when the bias had been increased from 0 V (before irradiation) to 100 V has approached an equilibrium as when it was reduced from 200 V to 100 V.

investigated by the author over a period of 3 months. Each time after enough pre-irradiation had been delivered to achieve stable reading, the detector response for a dose of 0.5 Gy (at 2.0 Gy/min) was recorded by a Nuclear Enterprises 2570 Farmer electrometer. The experiment was performed for a 6 MV photon beam, 10x10 cm<sup>2</sup> field size, FSD=100 cm and the detector at  $d_{max}$ =14 mm. The reading at a bias of 100 V was found to have a standard deviation of only 0.67%.

The diamond detector linearity of response to dose was considered for a dose range of 10 to 110 cGy. The experiment was performed with 6 MV photon beams, FSD=100 cm, 10x10 cm<sup>2</sup> field size and the detector at 14 mm depth in solid water. The linearity with dose was better than 1% (standard deviation less than 0.67%).

### 3.3.5. Directional dependence of response

When performing dose profile measurements for both electron and photon beams, the obliqueness of electrons on the detector increases with off-axis distance, so the directional response of the detector is important. Directional response is also important

in depth dose measurements because the angular distribution of electrons broadens with depth as the abundance of scattered photons increases.

Polyethylene cylinders were drilled laterally so that the sensitive volumes of the diamond and the electron diode (unshielded) detectors could be positioned on the cylinder axis. With the axis of the cylinder at the isocentre of the linear accelerator, as illustrated in Figure 3.4, detector response versus gantry angle could be obtained. Response for 6 and 15 *MeV* electron beams was measured using cylinders of radius 14 and 33 *mm* respectively, so that the measurement depth corresponded to  $d_{max}$  in each case (Heydarian et al, 1993). A 5.0 *cm* diameter beam was used so as to minimise irradiation of the detector cable. Electrometer readings for each detector were taken for angles from 0° to approximately 130° (restricted by collision of the applicator with the detector stem) and averaged with readings at symmetrical angles about 0°.

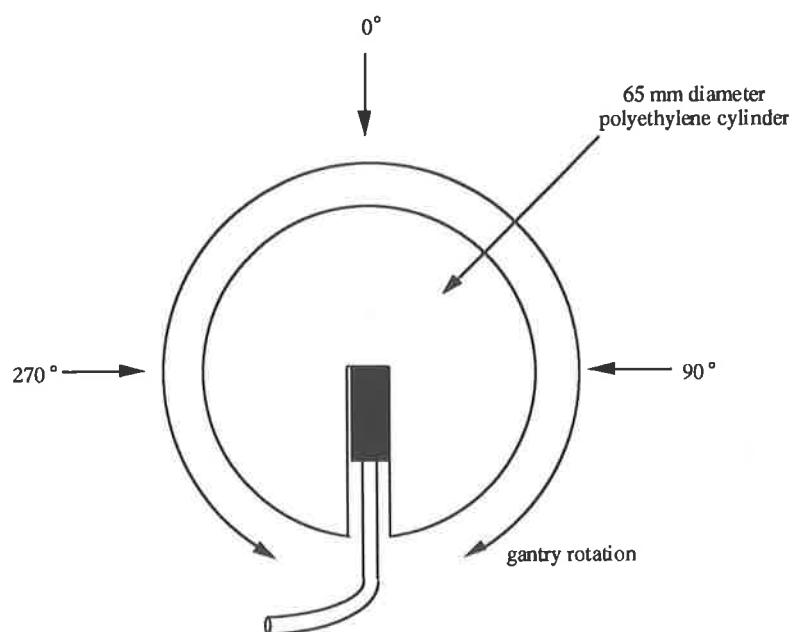


Figure 3.4. Configuration for directional response measurements, where the sensitive volume of the diamond and diode detectors is at the centre of the polyethylene cylinder at the isocentre (from Heydarian et al, 1993).

6 *MeV* results are shown in Figure 3.5a, where the readings at 0° are normalised to 100%. It can be seen that the minimum (at approximately 100°) in the diode detector response curve (12%) is less than that for the diamond (8%), while the maxima (at approximately 50°) are equal (2%) (Heydarian et al, 1993). Results for a 15 *MeV* beam are shown in Figure 3.5b where again the minimum in the diode response is less than that of the diamond. Note that for both detectors, the curves are flatter at 15 *MeV* than

at 6 MeV. The variation in response with incident direction is probably due to changing interface effects (Rikner, 1983), where a varying degree of delta-ray equilibrium is reached within the sensitive volumes (ICRU 1972).

Diamond detector directional dependence of response for photon beams have been investigated by several authors and comparisons made with the corresponding results of diode detectors (Rikner, 1983 and Rustgi, 1995). The diamond detector response has been shown to remain nearly uniform for cobalt 60 beam for angles up to 135° while the response of a p-type diode photon (shielded) detector drops to 82% at 90° and 73% at 135° relative to the 0° orientation, that is beam parallel to the detector stem (Rustgi, 1995). It has been shown by this author that the diamond detector has insignificant directional dependence for 6 and 18 MV x-ray beams for angles up to ±135°. For these energies the diamond response increases up to 2% as the incident photon direction moves away from 0°. The diode detector response drops continuously to 78% and 85% at 90° relative the value at 0° for the 6 and 18 MV x-ray beams, respectively.

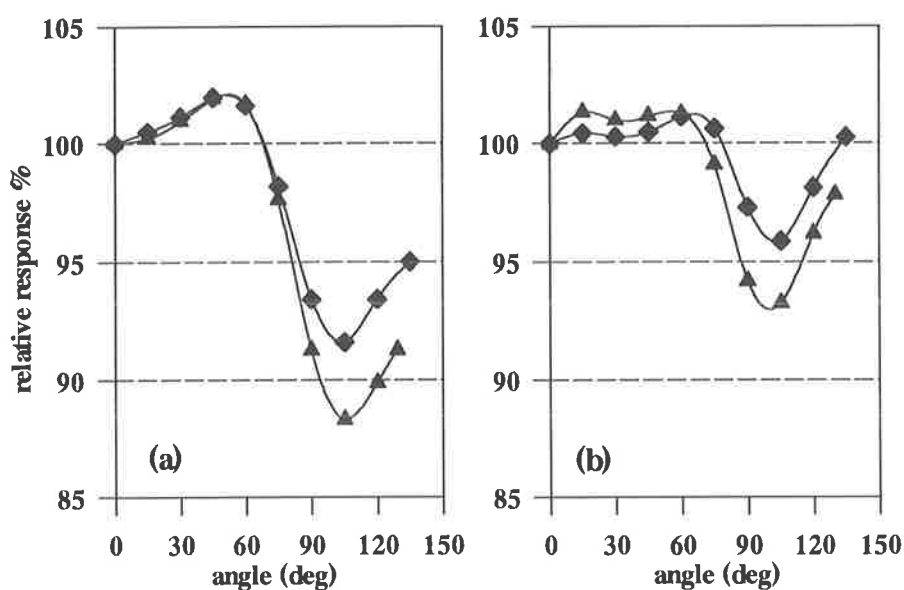


Figure 3.5. Directional response of the diamond and diode detectors for (a) 6 MeV and (b) 15 MeV electron beams, with the configuration shown in Figure 3.4 (from Heydarian et al, 1993).

It can be seen that the silicon diode photon detector has more directional dependence than the silicon diode electron detector. This is caused by the shield of the diode photon detector. The back of the sensitive region of the detector is covered with a

tungsten/epoxy layer to prevent the low energy back-scattered photons reaching to the detector. This is intended to compensate for the increased response of the high atomic number of the detector material to low energy photons. This is particularly important in low energy beams and reduces the over-response to the low energy back-scatter photons which increase with depth.

### 3.3.6. Spatial resolution

The main reason for using a diamond detector rather than an ionization chamber is the higher spatial resolution made possible by the smaller sensitive volume. The resolution of the diamond detector, compared with the ionization chamber and diode, is investigated here. 15 MeV profile curves were recorded at 10 mm deep in water, beneath a 2 mm wide slit in a 12 mm thick cerrobend applicator insert. The configuration used is shown in Figure 3.6. The diamond and diode detectors were orientated both parallel and perpendicular to the beam axis as shown, while the ion chamber axis was perpendicular to the page. Comparison was also made with film dosimetry, using Kodak X-Omat V film and a PTW digital film image processing system (FIPS) with a resolution of about 0.1 mm. Full width at half maximum (FWHM) of each curve is used here as a measure of detector resolution. This distance is the minimum separation of the centres of two slits of this kind such that the detector could resolve two peaks in the dose profile. The height on the profile curve at which the width is measured is the mean of the baseline and peak levels, where the non-zero baseline is due to bremsstrahlung dose. Profile curves measured with each detector and with film are shown in Figure 3.7, where the diamond and diode were both used in the parallel orientation. Note that the curves are not symmetric due to the fact that the slit is not quite perpendicular to the scan axis. As detector resolution increases, and hence less spatial averaging of the dose occurs in the peak region, the range of readings between the baseline and the peak, for a narrow beam like that of above configuration is increased. This has the effect of increasing the dose level at which the FWHM is measured, thus reducing it. It is probably this phenomenon which is the main factor determining the FWHM.

The FWHMs found here give an indication of the ability of the detector to give an accurate measurement of penumbral width. In a more precise consideration, one can

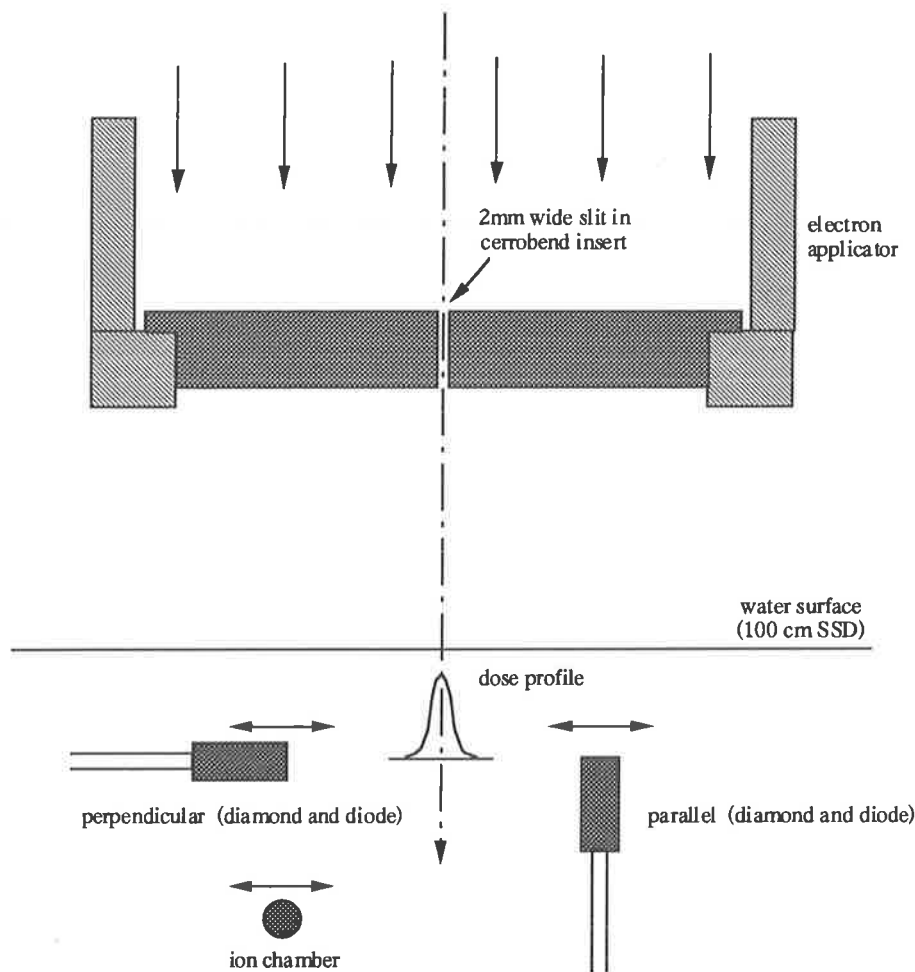


Figure 3.6. Configuration for profile measurements at 10 mm deep in water beneath a 2 mm wide slit in a 12 mm thick cerrobend applicator insert. Orientations of each detector during scans are as shown (from Heydarian et al, 1993).

define detector resolution as the detector ability to resolve the penumbral region. In this case because of the steep dose gradient and presence of electronic disequilibrium, in addition of the detector finite size, other detector characteristics are involved. For example the high density material of the diode detector and the housing will lead to an under-estimation of the penumbra width. This is due to the reduced electron range in the high density materials of the diode and the housing and will be discussed, together with other contributing factors, in more detail in chapter 5.

The *FWHMs* of the curves in Figure 3.7, as well as those for the diamond and diode in the perpendicular orientation, are given in Table 3.2. The sensitive widths of the diamond detector (as supplied by *PTW*) and those of the ion chamber and diode detectors (*Scanditronix* products guide) are also given in this table. Note that the *FWHM* of the diode (parallel orientation) curve is slightly smaller than that of the

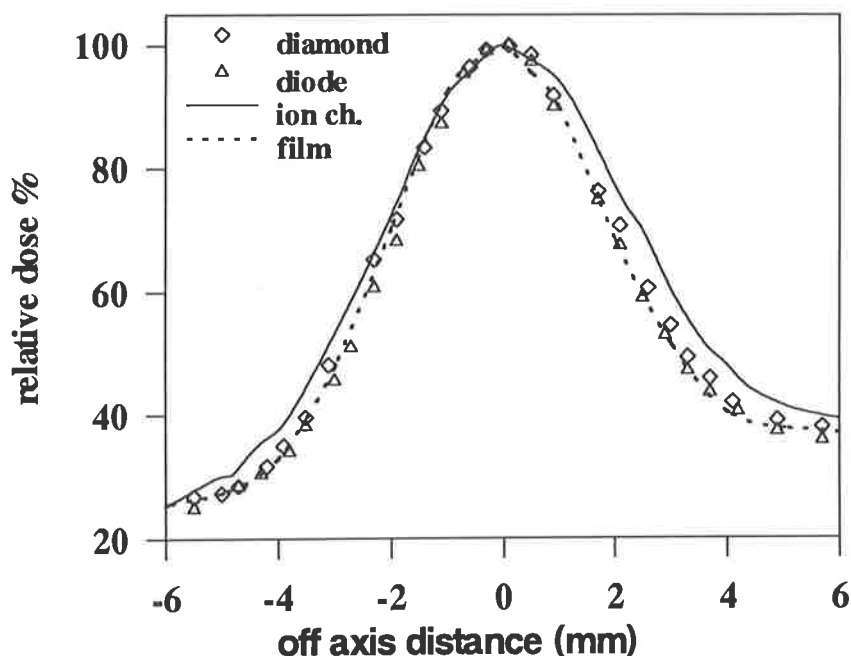


Figure 3.7. 15 MeV profile curves beneath the 2 mm slit, as measured with the diamond and diode detectors, film and ionization chamber.

diamond (parallel orientation) curve, even though its sensitive width is supposedly greater. This suggests that the sensitive width of the diode is effectively less than that of the diamond, mainly due to the reduced electron range in the high density materials of diode and the housing. Both diamond and diode show much better resolution than the ionization chamber, as expected from a comparison of the sensitive widths. The film result, although produced with a pixel-based image processing system (*FIPS*), does not show significantly better resolution than the diode. The most resolution is obtained with the diode in the perpendicular orientation since minimal spatial averaging of the true dose profile occurs. This is partly due to the reduced electron range in the high density diode detector, as mentioned before. The resolution of the diamond detector in the perpendicular orientation is also better than that of either detector in the parallel orientation. It should be pointed out, however, that since the directional response of both detectors, especially the diode varies sharply near  $90^\circ$  (see Figure 3.5), profile curves measured with the detectors in the perpendicular orientation could be affected by changes in the mean incident electron direction which occurs in the penumbral region. The most reliable configuration for high resolution profile measurements may therefore be a diode used in the parallel orientation and or a diamond in the perpendicular orientation.

**Table 3.2.** Profile widths (*FWHM*), for a 15 MeV electron beam in the configuration shown in Figure 3.6, as measured by diamond, diode, ion chamber and film (from Heydarian et al, 1993).

Detector type	Sensitive volume ( $mm^3$ )	Detector orientation	Detector width ( $mm$ )	<i>FWHM</i> ( $mm$ )
Diamond	1.4	parallel	2.1	4.9
		perpendicular	0.33	4.6
Diode	0.3	parallel	2.5	4.7
		perpendicular	0.06	4.3
Ion chamber	120	perpendicular	4.0	5.4
Film	—	perpendicular	—	4.7

Diamond detector spatial resolution for photon beams has been investigated by several authors and comparisons made with the corresponding results of diode detector and ionization chamber (Khrunov, 1990 and Rustgi, 1995). The diamond detector has a spatial resolution comparable to that of the diode detector and superior to ionization chambers, as is expectable from their relative dimensions. Rustgi has shown that the diamond and the diode detectors exhibit similar spatial resolution with the latter being slightly better. The resolution in this case was defined as the 90%-10% dose level penumbra widths. Resolutions were shown for  $1 \times 20$  and  $3 \times 20$   $cm^2$  field sizes of a 6 MV photon beam to be 0.54, 0.57, and 0.78 and 0.67, 0.73, and 0.97 mm for the diode and the diamond detectors and a  $0.14$   $cm^3$  ionization chamber, respectively.

### 3.4. Dose rate dependence

The expected sublinearity of diamond detector response with dose rate (see section 3.2) was investigated by (i) varying the dose per pulse of linear accelerators and (ii) varying the frequency of pulses. The effect of the dose rate dependence on a depth dose curve was also addressed. Dose per pulse was changed by varying (i) focus to surface distance (*FSD*) and (ii) depth. Pulse rate was varied by changing the pulse repetition frequency (*PRF*) of the linac.

### 3.4.1. Changing *FSD*

The dose rate for a 6 *MV* photon beam was varied from 0.98 to 4.77 *Gy/min* at a depth of 5 *cm* in solid water, by changing the *FSD* from 140 to 60 *cm*. The field size was kept constant at 20×20 *cm*<sup>2</sup> at isocentre (*FAD*=100 *cm*). These dose rates were established using the Farmer ionization chamber readings at each *FSD*. The measured pulse repetition frequency (*PRF*) corresponding to 200 *MU/min* was 206 pulses per second, which means that the variation in dose per pulse over this range is 0.079 *mGy* to 0.386 *mGy*. Measured pulse duration was 3.24 ms, so instantaneous dose rate (dose rate during a pulse) varied between 24.5 *Gy/min* and 119.3 *Gy/min*.

Readings were taken with the *RK* ionization chamber, diode and diamond, as well as the Farmer ionization chamber. Readings at each *FSD* were divided by the Farmer reading and these ratios normalised to 100% at an average dose rate of 0.98 *Gy/min*. Results are plotted in Figure 3.8, where it is seen that the relative response of the diamond appears to be the same as the ionization chamber for dose rates up to approximately 1.5 *Gy/min* and then decreases steadily as dose rate increases. As expected, the *RK* curve in Figure 3.8 remains close to unity. Interestingly, in contrast to the findings of Rikner (1983), the diode shows a relatively large over-response as dose rate increases.

The under-response of the diamond detector with respect to the ionization chamber as dose rate increases is expected from the inverse relationship of recombination time to the population of vacant holes. The number of holes is equal to the sum of the equilibrium density of free electrons *n* and the equilibrium density of electrons in traps *m* (Fowler, 1966). Since conductivity in equilibrium is proportional to recombination time, the increase in both *m* and *n* which occurs with dose rate will cause a sublinear increase in conductivity with dose rate. Since in general *m* >> *n* and the proportional increase in *m* with dose rate is much less than *n*, conductivity is not strongly dependent on dose rate (Fowler, 1966) but is nonetheless significant.

Detector current (normalised to that at the lowest dose rate) as a function of dose rate (normalised to the lowest dose rate) as *FSD* is changed is plotted in Figure 3.9(a). A line representing linearity of current to dose rate is shown for comparison. The relationship of conductivity to dose rate for radiation induced conductors was given in

equation (3-3) as  $\sigma \propto D^\Delta$ . The value of  $\Delta$  is near unity for the case  $m \gg n$ , where  $m+n$  is almost constant, and approaches 0.5 for the case  $n \gg m$  (as in the case of a pure crystal). As current is proportional to conductivity for a given bias, the normalised current and dose rate are related by  $i_{norm} = (D_{norm})^\Delta$ . A plot of  $\log(i_{norm})$  against  $\log(D_{norm})$  should thus yield a straight line with slope  $\Delta$ . Such a plot is shown in Figure 3.9(b), where a line of slope 0.98 is fitted to the points. The fit is very good indicating that the relationship in equation (3-3) indeed applies. As noted by Planskoy (1980), theory predicts that the value of  $\Delta$  will decrease with increasing dose rate. A second order polynomial fit to the points in Figure 3.9(b) gives a curve with slope  $0.99 - 0.02 \log(D_{norm})$ , indicating that  $\Delta$  is slightly less than unity and decreases by approximately 2% per decade increase in dose rate. In work by Planskoy (1980), mean values of  $\Delta$  for three different detectors were ascertained to be 0.91, 0.96 and 0.98. Furthermore, for the detector with a mean  $\Delta$  of 0.91,  $\Delta$  was shown to vary between 0.92 and 0.89 as dose rate was increased.

### 3.4.2. Changing depth

As with a variation in *FSD*, depth variation alters the dose rate by changing the dose per accelerator pulse. The sublinearity of response of the diamond detector should manifest itself in a percentage depth dose curve by giving a falloff which is too shallow, appearing to give an over-response as depth increases. Depth dose measurements in a  $10 \times 10 \text{ cm}^2$ ,  $100 \text{ cm FSD}$ ,  $6 \text{ MV}$  photon beam were made using the diamond and diode detectors, as well as the *RK* ionization chamber. Curves were obtained first using a Scanditronix computerized water tank data acquisition system (*RFA-7*) and then with the Farmer and a *PTW Unidos* (20007) electrometers for depths to  $35 \text{ cm}$ . In all cases, background current was subtracted. The dose rate varies from  $0.35$  to  $2.0 \text{ Gy/min}$  between  $35 \text{ cm}$  deep and  $d_{max}$ . Results are shown in Figure 3.10, where the diode detector's depth dose curve is in better agreement with that of the *RK* ionization chamber (using *RFA-7*) than is the diamond detector curve. Electrometer measurements were made at  $d_{max}$  ( $1.4 \text{ cm}$ ),  $10$ ,  $20$ ,  $30$  and  $35 \text{ cm}$  deep. In all cases results were consistent with the two electrometers, within the reading accuracy. The electrometer results are also shown in Figure 3.10. There was found to be close agreement between the *RFA-7* and electrometers for the diamond and diode, but the *RK* chamber gave higher

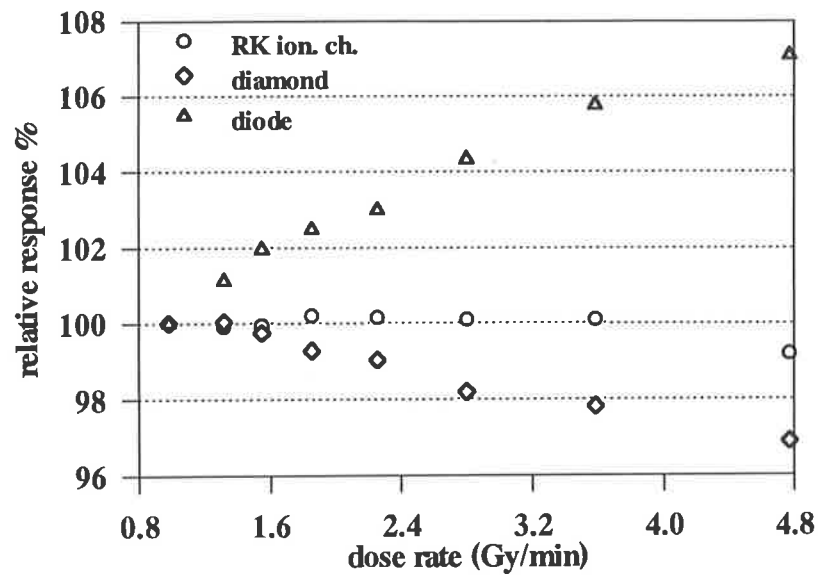


Figure 3.8. Dose rate responses of *RK* ionization chamber, diode and diamond relative to the Farmer ionization chamber. The dose rate for a 6 MV photon beam was varied from 0.98 to 4.77 Gy/min at a depth of 5 cm in solid water, by changing the *FSD* from 140 to 60 cm.

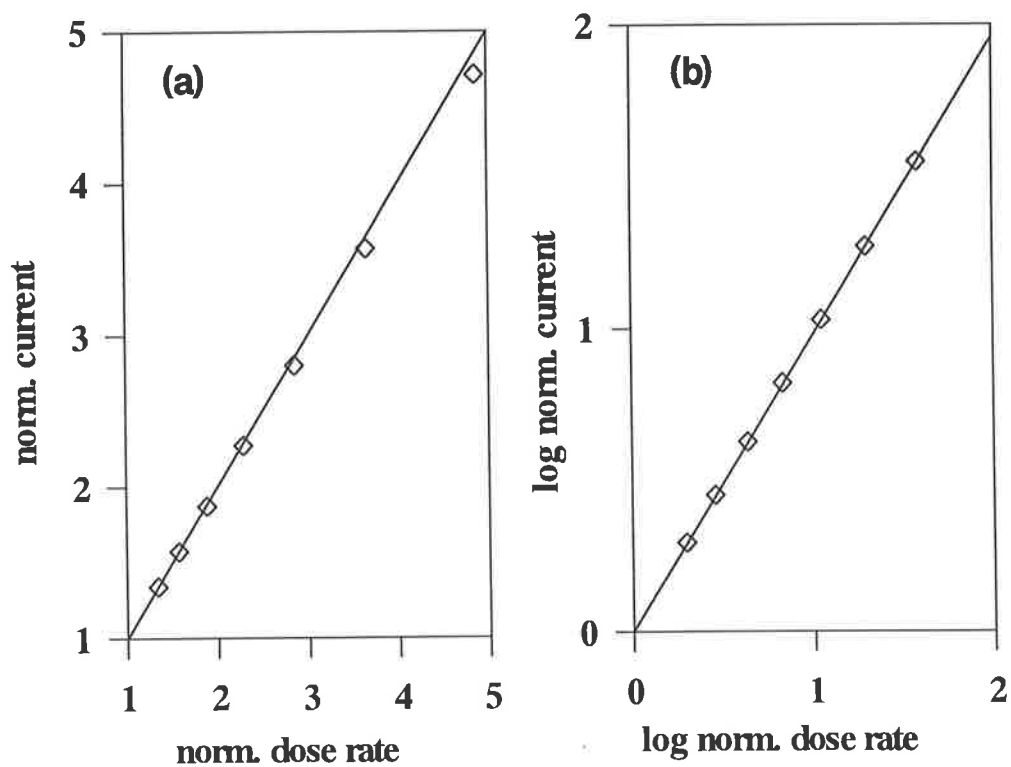


Figure 3.9. (a) Average diamond detector current (normalised to that for a dose rate of 0.98 Gy/min) as a function of dose rate (normalised to 0.98 Gy/min) as *FSD* is changed from 140 to 60 cm. A line representing linearity of current to dose rate is included for comparison. (b) *log-log* plot of the points in (a).

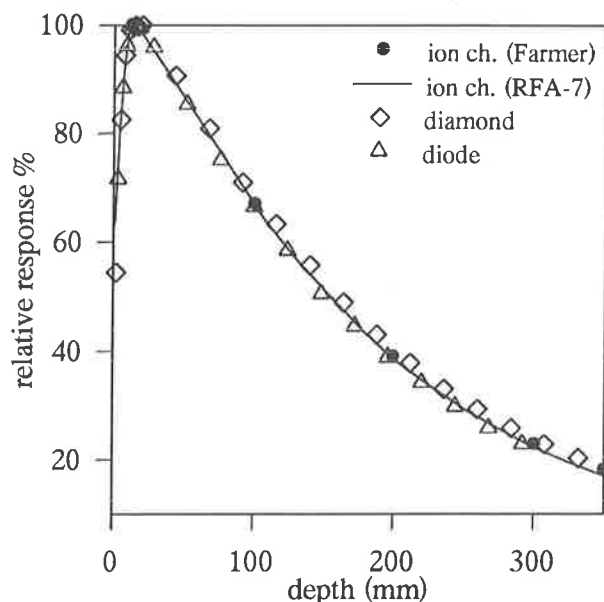


Figure 3.10. Percentage depth doses for a  $10 \times 10 \text{ cm}^2$ ,  $100 \text{ cm FSD}$ ,  $6 \text{ MV}$  photon beam, measured in the water tank using the *RFA-7* system with the diamond and diode detectors, as well as the *RK* ionization chamber. The *RK* response, measured with the Farmer electrometer is also shown.

readings when electrometers were used — putting the *RFA-7* response for the *RK* ion chamber under question. For example, at  $30 \text{ cm}$  deep, percentage depth doses measured using the *RFA-7* were 23.8% for the diamond and 22.2% for the *RK* chamber (1.6% absolute difference, 7.2% relative difference); when the Farmer electrometer was used, the corresponding values were 23.7% and 22.8% (0.9% absolute difference, 3.9% relative difference). It thus appears that the difference between depth doses measured with the diamond detector and *RK* ionization chamber is exaggerated by the *RFA-7* system but is nonetheless still evident. Another consequence of the elevated reading of the *RK* chamber when the Farmer electrometer is used is that the diode then has an under-response with depth of about the same magnitude as the over-response of the diamond detector. Note that the steep falloff rate of the diode curve is consistent with the results in section 3.4.1: any increase in response with depth due to low energy photons is outweighed by the super-linearity of response with dose rate.

If the normalised diamond detector current is plotted against normalised dose rate, using values obtained from the Farmer electrometer readings, a similar sublinearity to that in Figure 3.9(a) is seen. The slope of a line of best fit to a log-log plot of current versus dose rate is  $\Delta=0.98$ , in agreement with Figure 3.9(b). A second order fit gives a

line with slope  $0.98-0.01\log(D_{norm})$ , again indicating some decrease in  $\Delta$  with dose rate (Hoban et al, 1994).

### 3.4.3. Changing pulse repetition frequency

By varying the pulse repetition frequency (*PRF*) of a Varian 6/100 linear accelerator, the mean dose rate is changed while dose per pulse remains constant. The diamond detector was placed at  $d_{max}$  in a  $10\times 10\text{ cm}^2$ ,  $100\text{ cm FSD}$ ,  $6\text{ MV}$  photon beam and irradiated with  $100\text{ MU}$  at *PRF*s corresponding to 50, 100 and  $200\text{ MU/min}$ . The associated dose rates were 0.5, 1.0 and  $2.0\text{ Gy/min}$ . *PRF* at  $2.0\text{ Gy/min}$  was 150 pulses per second, giving a dose per pulse of  $0.22\text{ mGy}$ . Note that this pulse frequency is different to that mentioned for the same dose rate in section 3.4.1 because a different accelerator was used. Readings were taken with the Farmer electrometer, with integrated dark current over the time of irradiation subtracted. The decrease in reading at  $1.0\text{ Gy/min}$  from that at  $0.5\text{ Gy/min}$  was 2.5% and a further decrease of 1.8% occurred between 1.0 and  $2.0\text{ Gy/min}$ , giving a total decrease of 4.3%. By comparison with the previous section, the under-response in the diamond reading is 3.9% when the depth is changed from  $30\text{ cm}$  to  $d_{max}$ , thereby changing the dose rate from 0.46 to  $2.0\text{ Gy min}$ . Since a similar dose rate dependence exists whether the change is in dose per pulse or pulse frequency, the dependence appears to be on average rather than instantaneous dose rate. This implies that it is the increase with dose rate in the trap population,  $m$ , rather than in the number of free electrons,  $n$ , which is important.

In the case of varying *PRF*, a further effect, known as amplified conduction, may be significant. Amplified conduction occurs when vacant holes exist, leaving a conduction path for electrons to pass from one electrode to the other (Fowler, 1966). This can give rise to a gain factor greater than unity, since additional current to that due to ionizations may flow. For example, gain factors of  $10^3-10^4$  have been observed for *CdS* detectors. If even a small current flows between radiation pulses, the total integrated current for a given dose will increase as the *PRF* is decreased, effectively giving a drop in response with increasing dose rate. The fact that the degree of sub-linearity in the diamond detector response is similar when *PRF*, *FSD*, or depth is changed however, suggests

that amplified conduction is not very significant (since amplified conduction is only a factor for variations in *PRF*).

A further consideration in the cause of the dose rate dependence is polarisation. It is known that the population of electrons in traps (and hence polarisation) increases with dose rate (Fowler, 1966) and that polarisation reduces the electric field strength. This may also be a factor in the sublinearity of current with dose rate.

### **3.5. Evaluation of the diamond detector for photon beam measurements**

#### **3.5.1. Introduction**

A significant advantage of the diamond detector over using diodes, apart from its tissue equivalence, is that only one diamond detector is needed for both electron and photon measurements, whereas separate shielded and unshielded diodes are required for photon and electron beam measurements, respectively. The diamond detector should provide an advantage in obtaining photon beam dosimetry parameters because carbon is more closely tissue-equivalence than silicon. This has been verified for  $^{60}\text{Co}$  beams (Khrunov et al, 1990; Vatnitsky and Järvinen, 1993 and Rustgi, 1995) and for 6 and 18 *MV* photon beams (Rustgi, 1995). Although the effect of the high atomic number of silicon will reduce for higher energies where photo-electric interactions become less significant, it will appear again (to a lesser extent) at an increasing energy, because of the pair production effect. Figure 3.11 shows variations in the ratios of mass energy absorption coefficients of carbon, silicon, silver bromide, and air to water with energy for the photon energy range of 0.002 to 20 *MV*. As it is seen from this figure the mass energy absorption coefficients of air and carbon to that of water are constant for energies higher than 0.2 *MeV* and have little variations for lower energies. Also it can be seen that the corresponding ratios for silicon and silver bromide have large variation for low energies, due to their large photoelectric cross sections. As such, the change in response of film and diode when energy is changing does not necessarily show the true variation in absorbed dose to water. Change of photon energy with field size and depth are examples of conditions where an energy-dependent detector could lead to an inaccurate result, even for relative dosimetry.

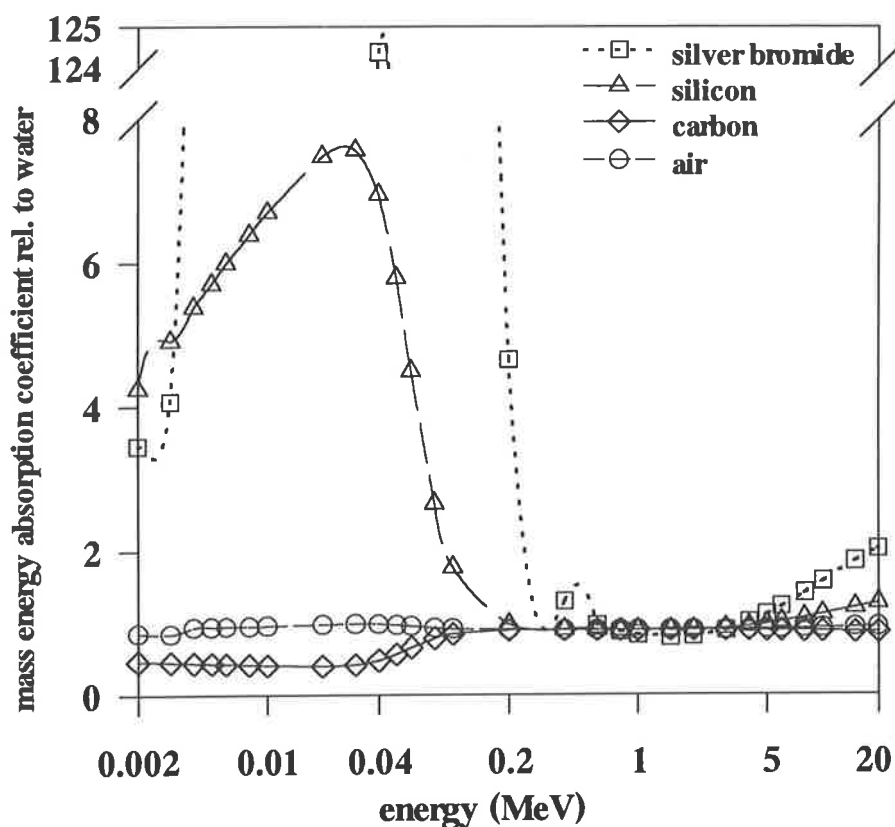


Figure 3.11. variations in the ratios of mass energy absorption coefficients of carbon, silicon, silver bromide, and air to water with energy for the photon energy range of 0.002 to 20 *MeV*.

Ionization chambers on the other hand are energy independent in photon beam dosimetry, because their responses are basically due to the electrons originated outside the air cavity and electrons energy spectrum is almost constant with depth. Problems with ionization chamber dosimetry appear however when high spatial resolution is required. Ionization chambers (because of the low density of air) have relatively large sizes otherwise their output would be too small. As such ionization chambers are not suitable for the conditions where lateral electronic equilibrium does not exist, such as in accurate dosimetry of the penumbra region and for general dosimetry of small stereotactic radiosurgery (*SRS*) beams. Moreover, the presence of the low density air cavity in a region of disequilibrium alters the electron fluence and thus gives a wrong result for the dose to water.

In this section the diamond detector response to photon beams for different experimental conditions is investigated and results are compared with the corresponding results of the diode detector and ionization chamber. A further

investigation has been carried out into the use of the diamond detector for dosimetry of small-diameter radiosurgery beams where resolution is particularly important. The result of that investigation and comparisons with the results of other techniques, including Monte Carlo (*EGS4*), is presented in chapter 5.

### 3.5.2. Output factors

Collimator output factor (*OF*) is the ratio of the dose per monitor unit for a collimator to that of the calibration conditions (10×10 field, 100 cm *FSD*) (Holt et al, 1970). In order to evaluate the diamond detector response to different field sizes, *OFs* have been compared with the corresponding results of the *RK* ionization chamber. The measurement was performed for field sizes 0.5×0.5 to 40×40 cm<sup>2</sup> in water using the *RFA-7* water tank for a 6 MV photon beam, *FSD*=100 cm, detector at  $d_{max}$ . The diamond detector was positioned with the detector stem parallel to the beam central axis and the ionization chamber in its normal orientation (stem perpendicular to the central axis). The effective point of measurement of each detector was positioned at the center of the field at  $d_{max}$ , and then the detector response to the same number of *MUs* was recorded by the Farmer electrometer. The center of the field was found each time using profiles orthogonal to the beam central axis (at *x* and *y* directions).

Figure 3.12 shows *OFs* for different field sizes measured with the diamond detector and the ionization chamber, normalized to unity for the 10×10 cm<sup>2</sup> field. As seen from this figure there is very good agreement between the diamond detector and ionization chamber results, for field sizes equal and or larger than 3×3 cm<sup>2</sup>. For field sizes smaller than 3×3 cm<sup>2</sup> the ionization chamber response is lower than the diamond detector (see insert): this is due to the reduction in electron fluence caused by the presence of the air cavity in a region of disequilibrium. In this situation the Bragg-Gray conditions are not met (Johns and Cunningham, 1983). In particular, the presence of the low density ionization chamber will increase the degree of the lateral electronic disequilibrium (for more information see chapter 5. On the other hand the diamond detector causes minimal perturbation of the electron fluence due to the small size and near unit density.

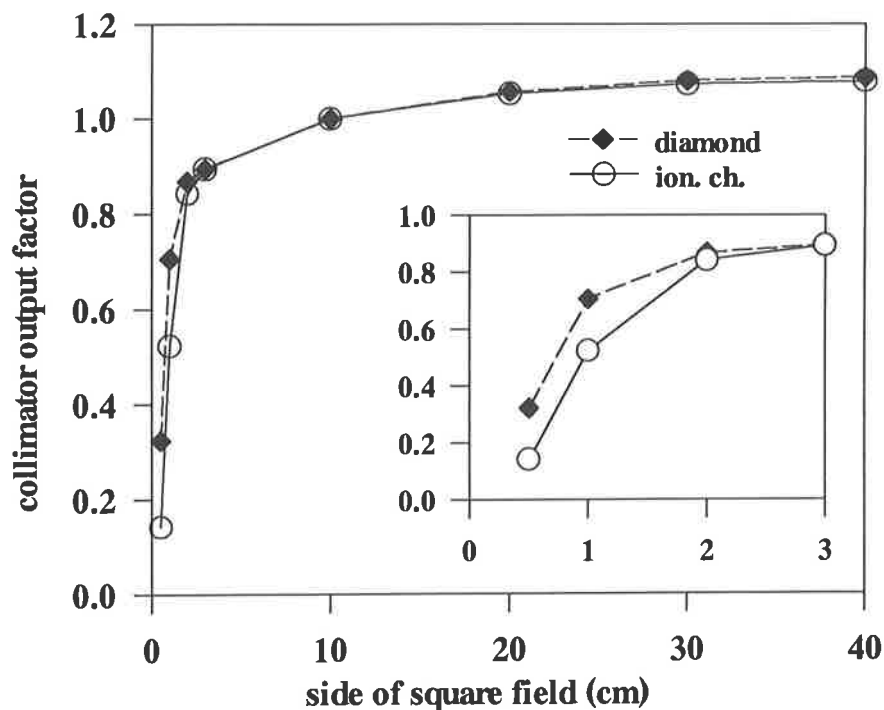


Figure 3.12. Collimator output factors for different field sizes measured with the diamond detector and the ionization chamber, normalized to unity for the  $10 \times 10 \text{ cm}^2$  field.

### 3.5.3. Depth dose curves

Central-axis depth dose curves in water were measured for  $10 \times 10 \text{ cm}^2$  fields of 6 MV photon beam, at 100 cm FSD. Comparisons between the diamond, the photon (shielded) diode, and the RK ionization chamber results are shown in Figures 3.10. The diamond and diode were both orientated parallel to the beam central axis and the ionization chamber in its normal orientation, stem perpendicular to the central axis. The effective point of measurement for the diamond and diode is 1.0 mm and 0.6 mm beneath the end of the detector housings, respectively. From Figure 3.10 it is seen that the ionization chamber and diode agree moderately well, but the diamond detector curve has a significantly shallower falloff. This shallow curve is as expected from the dose rate dependence of the diamond detector discussed in section 3.4. Also, the ionization chamber curve is slightly below its position when measured using the Farmer or the PTW electrometers (see section 3.4.2), so the true over-estimation of dose at depth is not as large as indicated by the comparison with RFA-7 curve. Depth doses measured with the detectors using the Farmer electrometer have shown that diamond and diode curves have the same deviation from ionization chamber, as it is seen from Figure 3.10. Figure 3.13 shows

6 MV photon depth dose curves for a  $0.5 \times 0.5 \text{ cm}^2$  field, measured with the diamond, diode, and ionization chamber in the water tank.

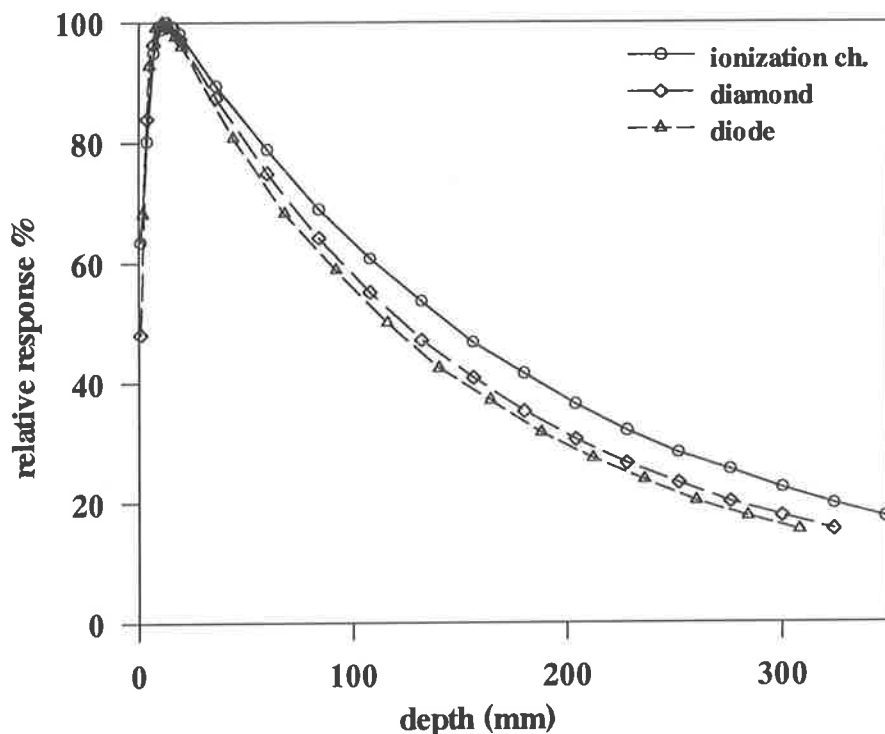


Figure 3.13. 6 MV photon depth dose curves for a  $0.5 \times 0.5 \text{ cm}^2$  field and  $FSD=100 \text{ cm}$ , measured with the diamond, diode, and ionization chamber in the water tank.

As it is seen, diamond and diode depth dose curves are relatively at the same position as for the  $10 \times 10 \text{ cm}^2$  field, but ionization chamber response has changed significantly. Further experiments have shown that this deviation starts from field sizes smaller than  $3 \times 3 \text{ cm}^2$  (at this conditions) and increases with decreasing field size. This is due to the large sensitive volume of the ionization chamber and the fact that a larger proportion of the chamber is exposed with depth as the beam diverges.

#### 3.5.4. Summary and discussion

It has been shown that the *PTW* diamond detector approximates a radiosensitive resistor (Burgemeister, 1981), where (i) current varies almost linearly with bias voltage and (ii) for a bias of 100 V, current is only slightly sublinear with dose rate. The detector operates with incomplete charge collection due to the electron-hole recombination time being shorter than the transit time for electrons to pass from one electrode to the other.

At a bias of 100 V, the recombination and transit times have been found to be approximately  $2.6 \times 10^{-9}$  s and  $4.5 \times 10^{-9}$  s respectively. The ratio of these figures gives the gain factor of the detector (the proportion of ionization charge that is collected). Calculations show that a reduction in detector thickness from 0.33 to 0.19 mm should give complete charge collection for a bias of 100 V.

When the detector had not been used for several weeks, charge readings for successive doses of 0.5 Gy were shown to drop by approximately 10% until a dose of 15 Gy had been delivered. This is attributed to (i) polarisation effects, where electrons in traps give rise to an electric field of opposite sign to that due to the bias voltage and (ii) an increase in the equilibrium trap population (causing a reduction in recombination time). When bias voltage is increased, current initially drops with dose delivered, indicating that the equilibrium number of electrons in traps is increased with bias voltage, and thereby increasing polarization and reducing recombination time (a large current flows until equilibrium is reached). Consistent with this is the fact that a decrease in voltage gives an initial increase in current, indicating a reduction in the equilibrium number of electrons in traps.

It has been shown that the diamond detector has an under-response with increasing dose rate, as is predicted by the theory of radiation-induced conductivity in an insulator. The decrease in response is a consequence of a very short electron-hole recombination time, which decreases as dose rate increases (thus increasing the degree of incomplete charge collection). This behaviour is in contrast to the situation with an ionization chamber, where recombination in the time taken for charge collection is insignificant provided the bias voltage is sufficiently high. A similar dose rate dependence exists whether dose per pulse or pulse frequency is varied, indicating that the dependence is on the average, rather than the instantaneous, dose rate.

Of most importance is the fact that the diamond detector produces a depth dose curve which has a significantly shallower falloff than that obtained with an ionization chamber. This however only represents an over-estimate in percentage depth dose at 30 cm deep of approximately 1%, which is as good as the results with a diode, where percentage dose at 30 cm deep is under-estimated by 1%. Use of the *RFA-7* beam data acquisition system gives a larger difference between *RK* ionization chamber and

diamond depth dose curves than is the case when the Farmer or the Unidos electrometer is used: this is because the *RK* response, measured using the *RFA-7*, is steeper than that measured using the lectrometers.

In comparing the diamond detector to a diode, it is worth noting that because of the high atomic number of silicon, diodes are energy dependent as well as being dose rate dependent. This means that a shielded diode is required for photon beam measurements, necessitating two different diodes for photon and electron dosimetry. The energy dependence of a diode also adds uncertainty to its results, since any deviation from the ideal change in response as position is changed may be due to either non-linear dose rate response or a change in the proportion of scattered photons at the detector. The diamond detector on the other hand is only dose rate dependent, so a correction factor based on dose rate alone may be able to be applied to diamond readings. It has been shown by Rikner (1983) that a shielded diode (as used in photon beam dosimetry) has significantly greater directional dependence than an unshielded diode. Also it has been shown by Rustgi (1995) that the shielded diode detector has a directional dependence up to 27% (at 135°) for *Co-60* and 22% and 15% for 6 and 18 *MV x-ray* beams, respectively. The directional dependence of the diamond detector for above photon energies is mentioned to be better than 2% (Rustgi, 1995).

### **3.6. Evaluation of the diamond detector for electron beam measurements**

#### **3.6.1. Introduction**

Diamond detectors look attractive in electron beam dosimetry because of their tissue equivalence and their high spatial resolution. Figure 3.14 shows the collision mass stopping power ratios of water to air, carbon, silicon, and silver bromide as a function of energy (ICRU, 1984). As it is seen from this figure the ratios of collision mass stopping power water to silicon and silver bromide are not constant with electron energy, especially at energies below 5 *MeV*. This ratio for carbon remains approximately constant for energies higher than 1 *MeV*, which implies an advantage of diamond detectors over films and silicon diodes for electron dosimetry. Figure 3.14 also shows the decrease in the water/air stopping power ratio with energy caused by the density effect.

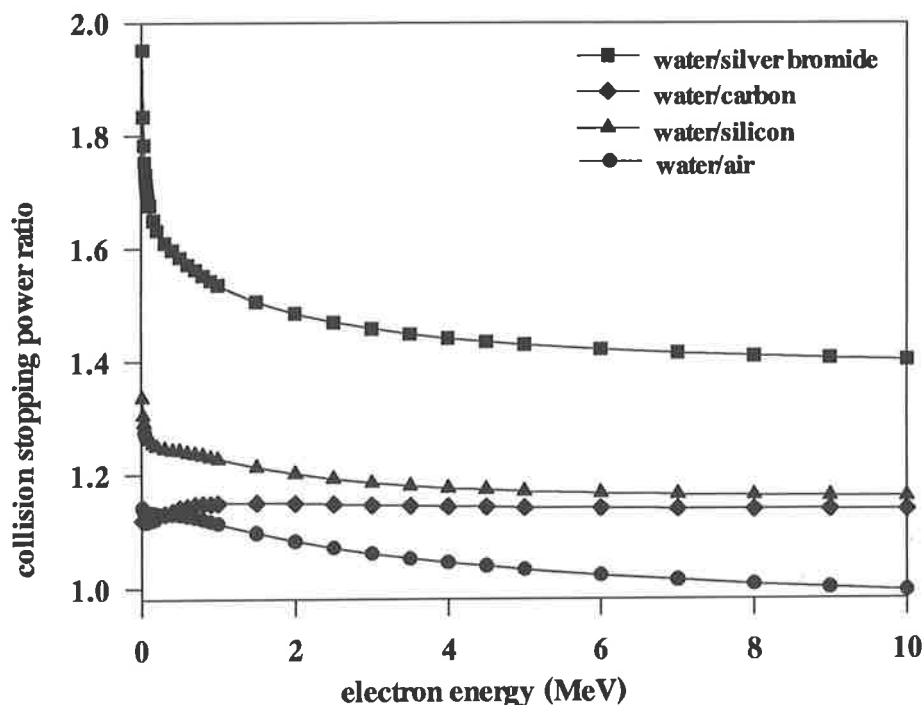


Figure 3.14. The collision mass stopping power ratios of water to air, carbon, silicon, and silver bromide as a function of energy (data from *ICRU*, 1984).

In this section, comparisons of the diamond detector response to 6 and 15 *MeV* electron beams are made with results obtained using a Scanditronix *p-Si* electron diode and the *RK* ionization chamber. Measurements were performed using the *RFA-7* beam data acquisition system and the Farmer electrometer, with the +100V bias being supplied to the diamond detector, using an external power supply. The directional response and spatial resolution for electron beams have been discussed as part of the diamond detector characteristics in sections 3.3.5 and 3.3.6, respectively. In here electron depth doses for 6 and 15 *MeV* electron beams produced by a Siemens Mevatron *KD-2* linear accelerator are measured with the diamond detector and compared with the corresponding results of other detectors.

### 3.6.2. Depth dose curves

Central-axis depth dose curves in water were measured for  $10 \times 10 \text{ cm}^2$ , 6 and 15 *MeV* electron beams, at 100 *cm FSD*. In Figure 3.15, a comparison between diamond, diode and ionization chamber results is shown for 6 *MeV*, where the diamond and diode were both orientated parallel to the beam. From the *IAEA* dosimetry protocol (*IAEA*, 1987),

the effective point of measurement of the ionization chamber is 1.0 mm proximal to the longitudinal axis of the chamber. The ionization chamber curve has been corrected for stopping power ratio variation (seen in Figure 3.14), using the protocol and is considered here to be the correct result. It can be seen that the diamond detector curve is in closer agreement than the diode with the ionization chamber curve. This is expected since the variation in water/silicon stopping power ratio is greater than that of the water/carbon stopping power ratio (see Figure 3.14). As mentioned by Rikner (1983), a stopping power ratio correction could be made to the diode result. Since the water/silicon stopping power ratio increases with a decrease in energy, such a correction would improve the agreement between diode and ionization chamber at depths greater than  $d_{max}$ , but worsen the agreement for depths less than  $d_{max}$ . Also, as mentioned in section 3.3.5, the directional response also has an influence on the measured depth dose curve. The initial increase in response with angle for both the diamond and diode detectors (see Figure 3.5a) would correspond to an increase in response with depth, due to increased obliqueness of the electron paths. This could be a contributing factor to the buildup region of the diode curve, and to a lesser extent the diamond curve, being too steep.

Depth dose curves for 15 MeV are shown in Figure 3.16, where it can be seen that the diode detector result is in closer agreement with the diamond and ionization chamber results than is the case for 6 MeV: this is because the water/silicon stopping power ratio becomes almost constant above 5 MeV (see Figure 3.14). Note that the depth scale in Figure 3.16 is smaller than that of Figure 3.15: any deviation from the ionization chamber curve is therefore more noticeable for the 6 MeV curve.

It can be concluded that the diamond detector is preferable to the diode for low energy electron beam depth dose measurements. The error in the diode results is small however, particularly when considered in terms of the depth corresponding to a particular dose level (because of the steepness of the falloff part of the depth dose curve). The diode detector under response for the 6 MeV case is about 1-2% and could be related to the diode dose rate dependence (Hoban et al, 1994).

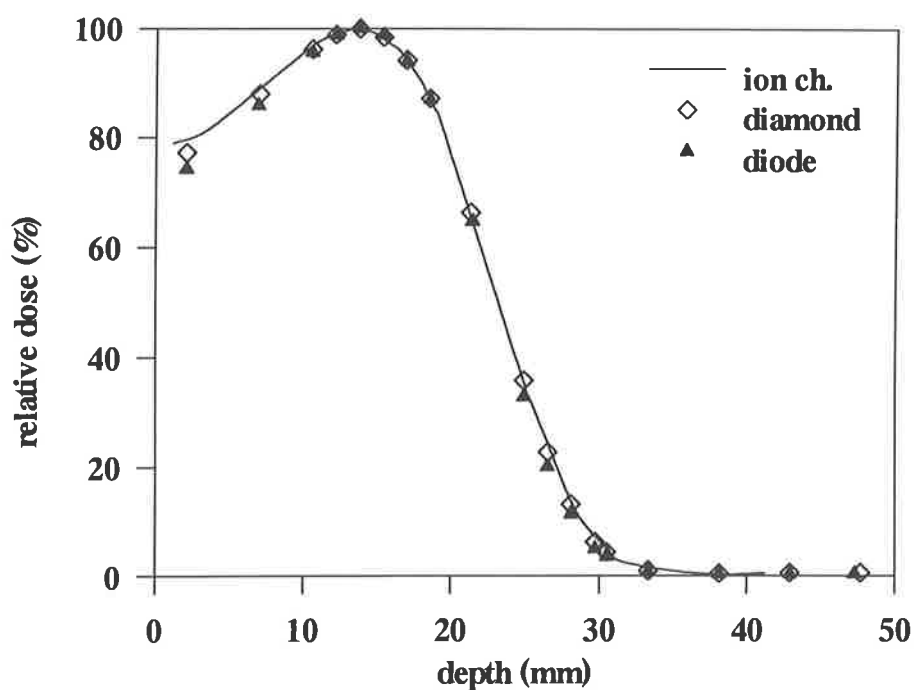


Figure 3.15. A comparison between diamond, diode and ionization chamber depth doses for 6 MeV electron beam, where the diamond and diode were both orientated parallel to the beam.

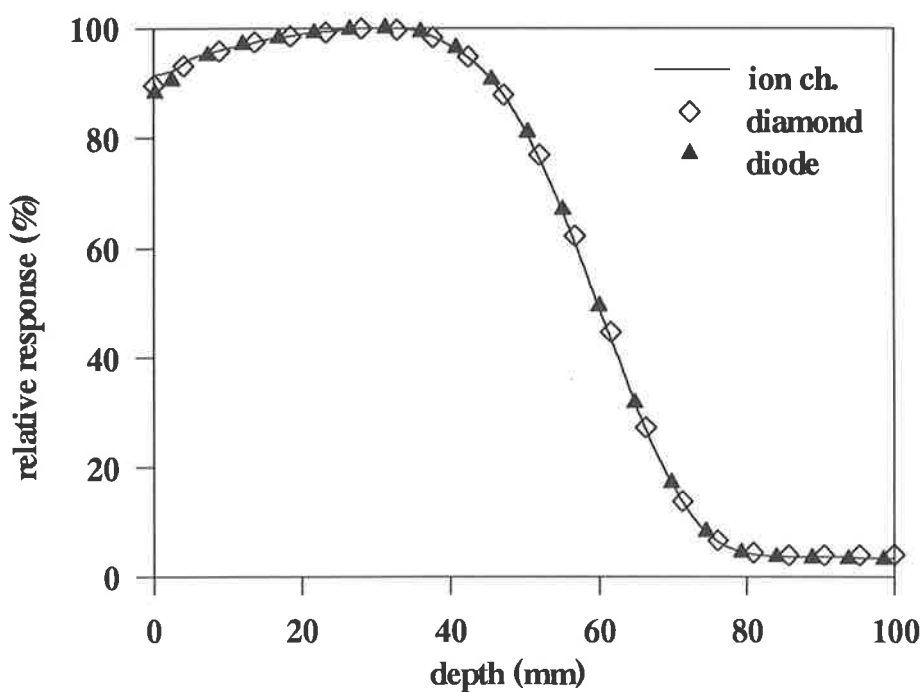


Figure 3.16. A comparison between diamond, diode and ionization chamber depth doses for 15 MeV electron beam, where the diamond and diode were both orientated parallel to the beam.

### 3.6.3. Summary and discussion

There are two main features of diamond detectors which make them attractive for electron dosimetry: (i) their small size and hence good spatial resolution; (ii) the near constancy of the water/carbon stopping power ratio with energy.

Comparison of profiles measured beneath a 2 mm slit using ionization chamber, diamond, and diode detectors, shows that resolution of the diamond detector is slightly less than that of the diode (with detector stems parallel to the beam axis) and considerably better than that of the ionization chamber. With the diamond and diode detectors orientated perpendicular to the beam, resolution is better than in the parallel orientation, with the diode again showing higher resolution. However, because of the reduced electron range and the worse directional response, it may not be advisable to use the diode detector in the perpendicular orientation. In term of directional response, the diamond detector has been shown by this group to have less directional dependence than an unshielded diode in electron beam dosimetry (Heydarian et al, 1993).

Depth dose curves at 6 and 15 MeV obtained using the diamond, diode and ionization chamber show no significant difference at 15 MeV, but at 6 MeV the diamond results are in closer agreement with energy-corrected ionization chamber results than are those of the diode detector. This is expected since the water/carbon stopping power ratio is almost constant for energies above 1 MeV, while the water/silicon stopping power ratio varies considerably up to approximately 5 MeV. The diamond detector is therefore preferable to the diode for obtaining low energy electron beam depth dose curves. Furthermore, curves measured with the diamond do not require an energy-dependent correction, as is required for ionization chamber measurements.

### 3.7. Dose rate correction

The dose rate dependence of the diamond detector was investigated in section 3.4. As was mentioned in that section, using the relationship of conductivity to dose rate (equation 1-3), the dose rate dependence of the diamond detector could be corrected. The value of  $\Delta$  was found to be 0.98 (Hoban et al, 1994) from the plot of  $\log(i_{norm})$  against  $\log(D_{norm})$  shown in Figure 3.9(b). Applying this  $\Delta$  value to the diamond

detector response for different experimental conditions, Zahmatkesh (1995) has shown that the diamond detector response could be successfully corrected. In this section the diamond detector depth dose curves for 6 MV photon beams of  $10 \times 10$  and  $3 \times 3$  cm<sup>2</sup> field sizes are corrected using above  $\Delta$  value. Results are compared to the corresponding depth dose curves, measured with the *RK* ionization chamber as a valid reference and is shown in Figures 3.17 and 3.18 for  $10 \times 10$  and  $3 \times 3$  cm<sup>2</sup> field sizes, respectively. In these figures the electrometer readings of the *RK* ionization chamber have been used for comparison with diamond measurements.

### 3.8. Conclusion

Diamond detectors are attractive for dosimetry of photon and electron beams, mainly because of their small size and tissue equivalence. It was shown that carbon (diamond) mass energy absorption relative to water is almost unity for energies above 0.1 MeV and has small variation for energies below that. In comparison, the corresponding values for silicon (diode) and silver bromide (film) show much more variation, especially for energies less than 0.2 MeV (Figure 3.11). As such diamond detector response to the conditions where the photon beam energy changes is more reliable than those of diode detector and film. Ionization chambers in this respect are very reliable, for conditions where lateral electronic equilibrium exist. On the other hand the presence of the relatively large air cavity ionization chamber in the absence of lateral electronic equilibrium will increase the degree of disequilibrium and lead to a reading which will underestimate the dose without the ionization chamber present. Dosimetry in the penumbral region, and indeed across the entire field for very small *SRS* beams are examples of conditions where lateral electronic equilibrium does not exist.

It was shown that collision mass stopping power ratio of carbon to water remains almost constant for a wide range of energies, while the corresponding ratio of air, silicon, and silver bromide vary with energy (Figure 3.14). Therefore, ionization chamber response to the conditions where electron energy changes has to be corrected for stopping power ratio variation. Such a correction is routinely performed in electron beam depth dose measurements. Also, it was shown that using an ionization chamber in dosimetry of small *SRS* beams (narrow beams), where lateral electronic disequilibrium exists is more complicated. In this case, because the average energy of the secondary electron at

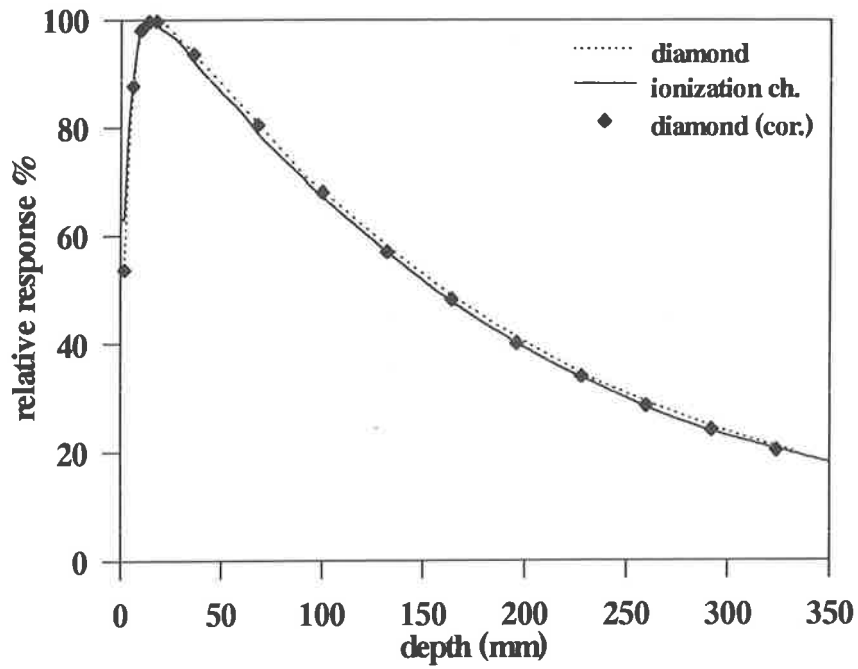


Figure 3.17. The diamond detector depth dose curves for a 6 MV photon beam,  $10 \times 10$   $cm^2$  field, before and after correction for dose rate dependence compared to RK ionization chamber.

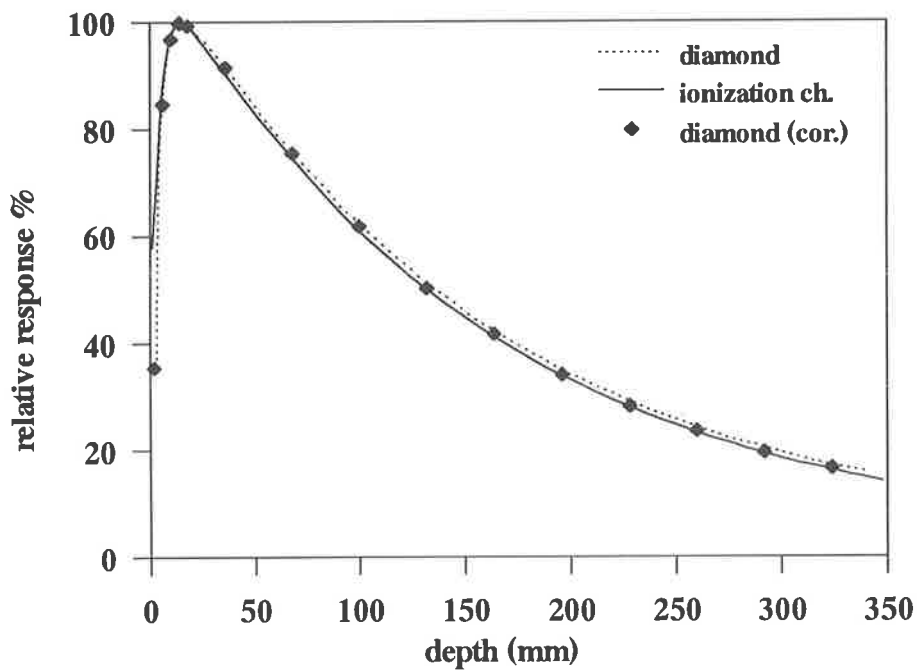


Figure 3.18. The diamond detector depth dose curves for a 6 MV photon beam,  $3 \times 3$   $cm^2$  field, before and after correction for dose rate dependence compared to RK ionization chamber.

the central axis is higher than in the case of electronic equilibrium, ionization chamber gives an over-estimation of the dose (see Figure 3.14). On the other hand the presence of the air cavity of ionization chamber will reduce the number of produced secondary electrons at the central axis. This will act against the previous case and cause some under-estimation of the dose. Diode detector shows almost the same over-estimation in this aspect, and film is worse. In addition, only one diamond detector is needed for both electron and photon measurements, whereas separate shielded and unshielded diodes are required for that purpose, respectively.

From measurements it appears that the diode detector has a spatial resolution higher than the diamond detector because of the smaller thickness of the sensitive volume, when both used perpendicular to the central axis. In this case the diode profile is skewed if it is shielded. Using both detectors parallel to the central axis the diode, although wider than the diamond, still gives higher spatial resolution. However, this is artificial and is due to the reduced electron range in the high electron density silicon diode and the housing.



# Chapter 4

## Monte Carlo Dose Calculation

### 4.1. Introduction

The Monte Carlo (*MC*) technique was first applied to electron-photon shower study by Wilson (1952). *MC* techniques then developed by Kahn (1954), Berger (1963) and others are mentioned in review articles by Raeside (1976), Turner (1985) and Rogers and Bielajew (1990). *MC* methods have found widespread use in radiation transport as well as particle physics, quantum chemistry, environmental engineering, mathematics, economics and many other fields. *MC* applications in medical radiation physics include nuclear medicine, diagnostic radiology, radiotherapy physics, radiation protection and applications based on microscopic techniques.

The most widely used *MC* codes in radiotherapy physics are *ETRAN* or *ITS* and *EGS*. *ETRAN* (Electron TRANsport) codes were originally developed at the National Bureau of Standard (*NBS*) by Berger and Seltzer in 1973 (Rogers and Bielajew, 1990). *ETRAN* then lead to the Integrated Tiger Series (*ITS*) codes developed at Sandia National Laboratories. *EGS3* (Electron Gamma Shower) was developed at the Stanford Linear Accelerator Centre (*SLAC*) by Ford and Nelson in 1978 to simulate electromagnetic cascades at energies up to a few thousand *GeV* and as low as 0.1 *MeV* and 1 *MeV* for photon and electron/positron transports, respectively (Nelson and Rogers, 1988). The need to extend the lower energy limits lead to development of the *EGS4* system which will be discussed later in section 4.5.

A Monte Carlo simulation code has four major components (Rogers and Bielajew, 1990):

- (i) physical data (such as cross sections) for all particles and processes being considered in the simulation.
- (ii) the algorithms used for particle transport.

- (iii) the methods used to specify the geometry of the problem and to determine the physical quantities of interest.
- (iv) the analysis of the information obtained during the simulation.

The underlying physics of the simulation is determined by the first two components, while the third ensures that the transport parameters used and quantities recorded are correct. Parameters can generally be specified which control the physical rigorosity of the simulation and the computation time.

In the last few years the use of Monte Carlo techniques in radiotherapy physics research has increased dramatically, largely due to the rapid developments in computer technology, in terms of speed and lower cost. One of the main reasons for using Monte Carlo technique in radiotherapy is to provide physically realistic dose distributions with which to compare other, less rigorous but faster, dose calculations. Furthermore, *MC* results can be used in place of experimental measurements when the simulations are known to give realistic results, particularly when accurate measurements are difficult or impossible. There are also quantities which can be obtained using *MC* which can not be measured experimentally, such as separate primary and scatter dose components, energy spectra and distributions of particle directions. All distributions resulting for particle transport, such as dose and particle energy, are the result of individual events in the "history" of each particle. Each history will be different, due to the (generally infinite) variation in each event. The aggregate effect of a very large number of particles is however reproducibility, where this effect is governed by the possibility distribution determining the outcome of individual events. The essence of a Monte Carlo simulation is summarised in Figure 4.1.

In radiation transport, using the probability relationships of the discrete events and a high-quality random number generator, the outcome of each event can be predicted. The track length between interaction points for each particle, the type of an interaction at each such point, the choice of energy and direction following a scattering interaction, and the possible products as the result of an interaction all can be determined by sampling a uniform random variable on the interval  $(0, 1)$ .

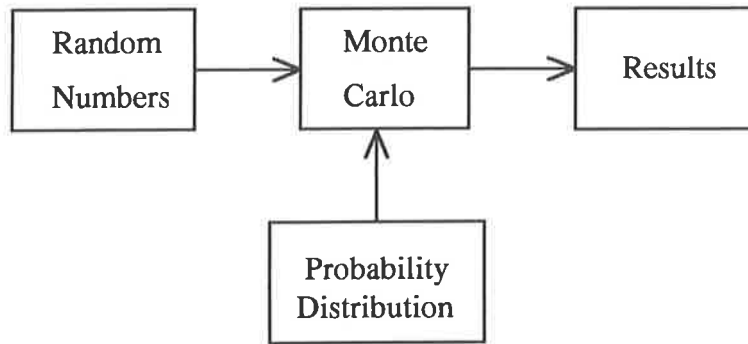


Figure 4.1. Flow diagram of the Monte Carlo technique (from Bielajew, 1992).

## 4.2. Sampling

The most common sampling method is direct sampling (also called the inversion method) using a probability distribution function (*PDF*), to describe the likelihood of a variable having a certain value. Two examples of quantities that are sampled using this method are (i) particle energy and (ii) distance to the next interaction site. In particle transport the normalised *PDF* of an interaction,  $f(x)$ , at the distance  $x$  is:

$$f(x) = \mu e^{-\mu x}, \quad (4-1)$$

where  $\mu$  is the linear attenuation coefficient. Correspondingly, there is a cumulative distribution function (*CDF*),  $F(x)$ , which is defined as:

$$F(x) = \int_0^x \mu e^{-\mu x'} dx' = 1 - e^{-\mu x}, \quad (4-2)$$

which is simply the probability of the interaction occurrence up to the distance  $x$ . Variation of the cumulative distribution function with  $x$  is shown in Figure 4.2. From this figure it is easily seen that  $F(0)=0$  and  $F(x)$  monotonically increases with  $x$  so that  $F(\infty)=1$ . Also it is seen that  $dF(x)$  is determined by the slope of the *PDF* which in turn is proportional to the value of  $f(x)$ . This is true for any interval with proper normalisation. Therefore by selecting a number  $R$ , randomly between 0 and 1 for  $F(x)$ , the distance  $x$  to the next interaction will be obtained from:

$$R = F(x) = 1 - e^{-\mu x} \quad (4-3)$$

$$x = F^{-1}(R) = -\frac{1}{\mu} \ln(1-R) \quad (4-4)$$

Both  $R$  and  $(1-R)$  are distributed in the same way, therefore:

$$x = -\frac{1}{\mu} \ln R = -\lambda \ln R \quad (4-5)$$

$\lambda = \frac{1}{\mu}$  is the mean free path, so the number of mean free paths to the next interaction site is:

$$N_\lambda = -\ln R \quad (4-6)$$

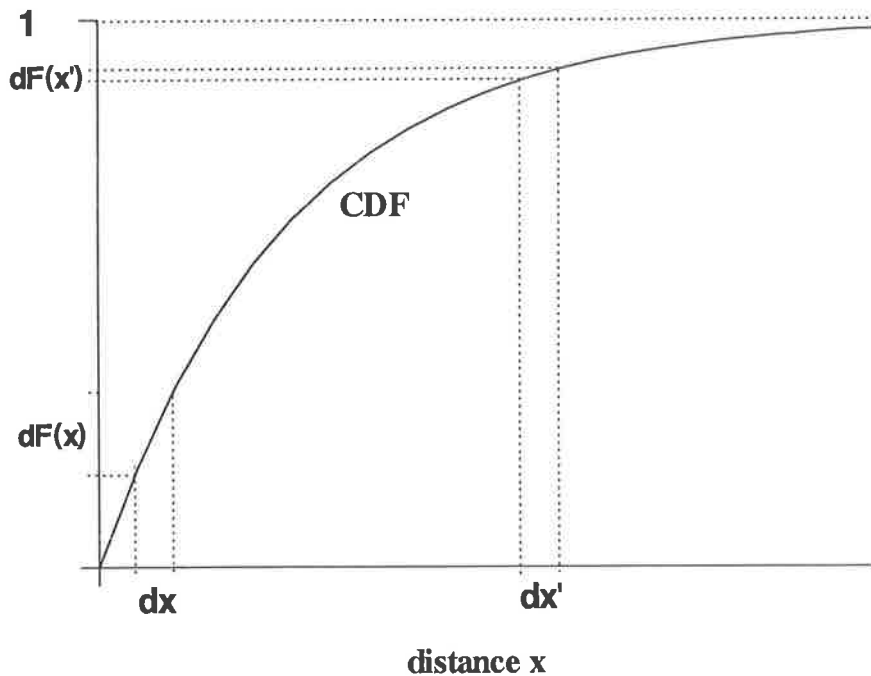


Figure 4.2. The cumulative probability distribution obtained by integrating the normalised  $PDF$  in formula (4-1).

In some cases when the  $PDF$  can not be integrated or  $x = F^{-1}(R)$  can not be solved, a rejection sampling is used. In this case using two random numbers on the  $x$  and  $y$  axes, a point on the normalised  $PDF$  graph is randomly selected. If this point lies outside the  $PDF$  then it is rejected and the process will be repeated, otherwise the  $x$  value is accepted (for more information see Bielajew, 1992 and Murray, 1990).

### 4.3. Random number generation

The random number generator (*RNG*) is the “soul” of a Monte Carlo calculation (Bielajew 1992). The random nature of a *MC* simulation depends on the *RNG*. The generation of a sequence of truly random numbers (ie. a random sequence of numbers that never repeats itself) is difficult, therefore pseudo random number generators are normally used for simulation. Good random number generators have large cycles. The cycle of a *RNG* is the number of generated numbers before repeating. Using normal *RNGs* coming with standard computing packages needs extreme caution, unless it is known to work well and is widely tested. New forms of random number generators based on lagged-Fibonacci sequences have been devised that have extremely long repeat sequences with up to  $2^{926}$  real numbers.

### 4.4. Monte Carlo particle transport

In order to model a real physical process using a *MC* technique, all relevant processes have to be simulated accurately. While explicit simulation of each interaction is possible for photon and neutron transports, there is serious time limitation in performing such an extensive simulation for electrons because of the great number of interactions involved. The problem for electron transport, however, is reduced using condensed-history technique in which the electron path is divided into a series of steps and the effect of the large number of interactions occurring in each step grouped together. In this case electron energy loss is calculated from stopping power {using the continuous slowing down approximation (*CSDA*) model}, instead of from discrete interactions. Grouping of angular deflections is performed using multiple scattering theory (such as that of Moliere) which accounts for deflections caused by elastic scattering.

*MC* codes are divided to class I and class II categories (Berger, 1963). In class I models, all energy losses and angular deflections of individual events are grouped together and the primary electron is not affected by the creation of individual secondary particles. In class II models, the energy and direction of the primary electron are affected by individual interactions when the energy loss is above a certain pre-

determined threshold (production threshold), otherwise interactions are grouped together as in class I.

#### 4.4.1. Photon transport

As a photon beam passes through a medium a number of interactions will occur. The type and probability of each interaction depend on the energy of the photon beam as well as the medium properties, such as atomic number and electron density. The mean free path of a photon,  $\lambda$ , is defined as the mean distance which the photon travels in a given medium between two successive interactions. As mentioned in section 4.2, the number of mean free paths to the next interaction site,  $N_\lambda = -\ln R$ , is determined by sampling a random variable,  $R$ , uniformly distributed between 0 and 1. Having found the interaction site, the type of photon interaction is determined again by a random variable and using the relative probabilities of all types of interactions for the current particle energy and current medium. Possible photon interactions include Compton (incoherent) scattering, the photoelectric effect, pair production, Thompson scattering and Rayleigh (coherent) scattering. The definition and the importance of each interaction for different energy and materials have been discussed in chapter 1.

Figure 4.3 presents a flow diagram for a *MC* simulation of photon transport (Rogers and Bielajew 1990). “*DETERMINE*” in this figure means that the quantities of interest are found by sampling from the relevant probability distribution, using one or more random numbers. Also the “stack” is used for storing the parameters of particles, whose histories are not complete, generated during simulation. Photon histories are terminated if the photon leaves the region of interest or its energy falls below a pre-determined cutoff value (*PCUT*). In the latter case the energy is deposited locally.

#### 4.4.2. Electron transport

In section 4.4, class I and class II models of electron transport are mentioned briefly. Class II algorithms are, in principle, more accurate than class I, because they include correlations between primary and secondary particles and introduce inherent randomness via the distribution of secondary particle energy (and other parameters).

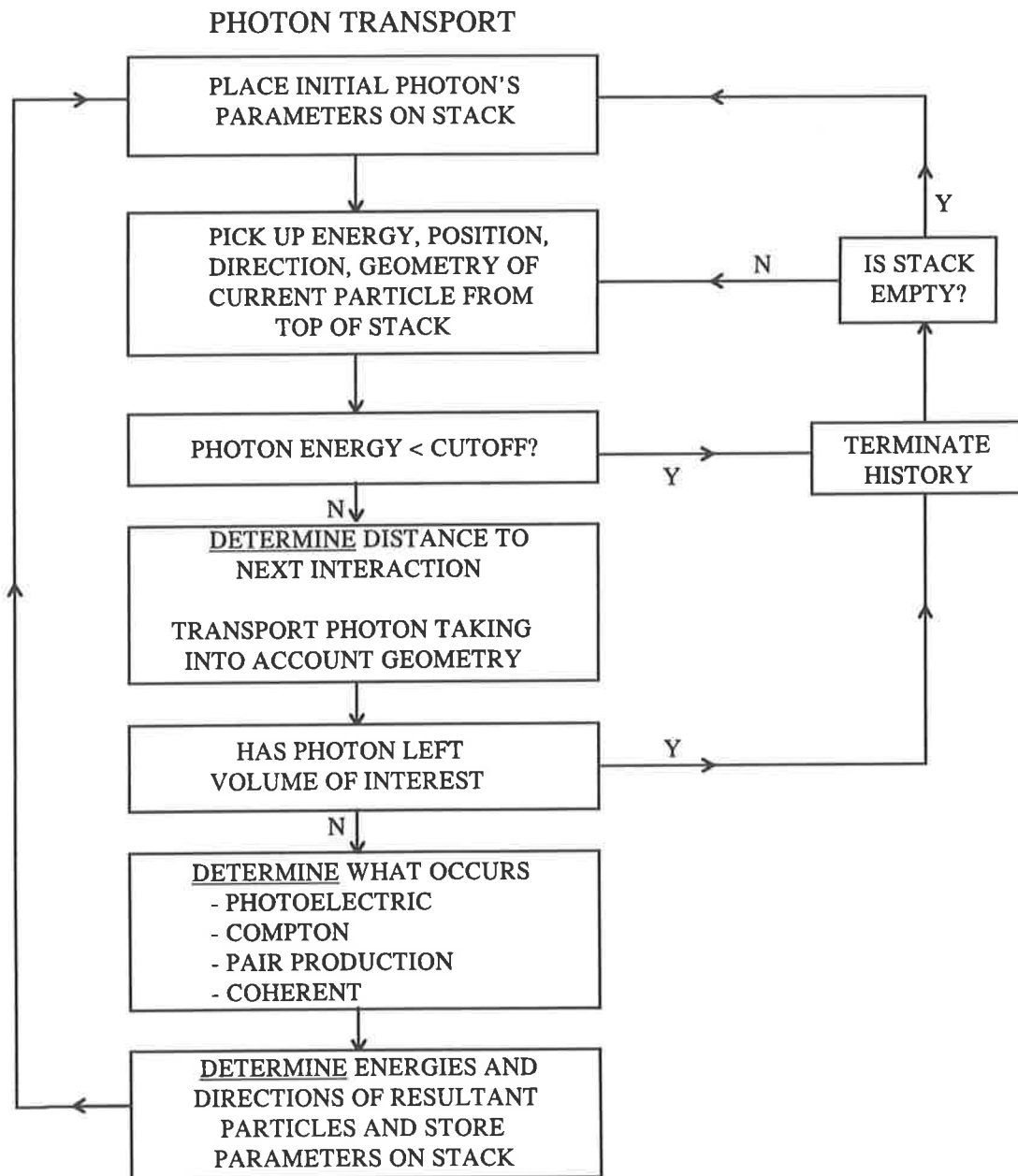


Figure 4.3. Logic flow of a Monte Carlo simulation of photon transport (Rogers and Bielajew 1990).

Both algorithms use energy cutoff below which energy deposited locally, whereas the production thresholds, in which secondary particles of energies higher than a certain threshold are treated individually, apply only to class II algorithms. Electron interactions in which energy loss is below this production threshold are grouped together as part of the continuous slowing down approximation. *CSDA* is modelled using restricted stopping power (defined in chapter 1), where the higher the secondary

particle production threshold, the closer the restricted stopping power approaches the total stopping power. Those relatively rare interactions which produce secondary particles with energies above the production thresholds are treated individually. These types of interactions are called “catastrophic” interactions. Figure 4.4 shows electron transport in a class II algorithm, in which the electron moves in short and straight steps along which the continuous energy loss is considered to occur. The deflection angle for each step is selected using multiple scattering theory. The model assumes that energy deposition by these low energy particles is on the path itself, although in reality the energy is deposited in the shaded area about the path by secondary particles with energies less than the production thresholds. In *EGS4*, the production thresholds for (i) delta rays (knock-on electrons) and (ii) bremsstrahlung photons are known as  $AE$  and  $AP$ , respectively. In a catastrophic interaction, a secondary particle with energy above  $AE$  or  $AP$  is produced, whose history will be followed.

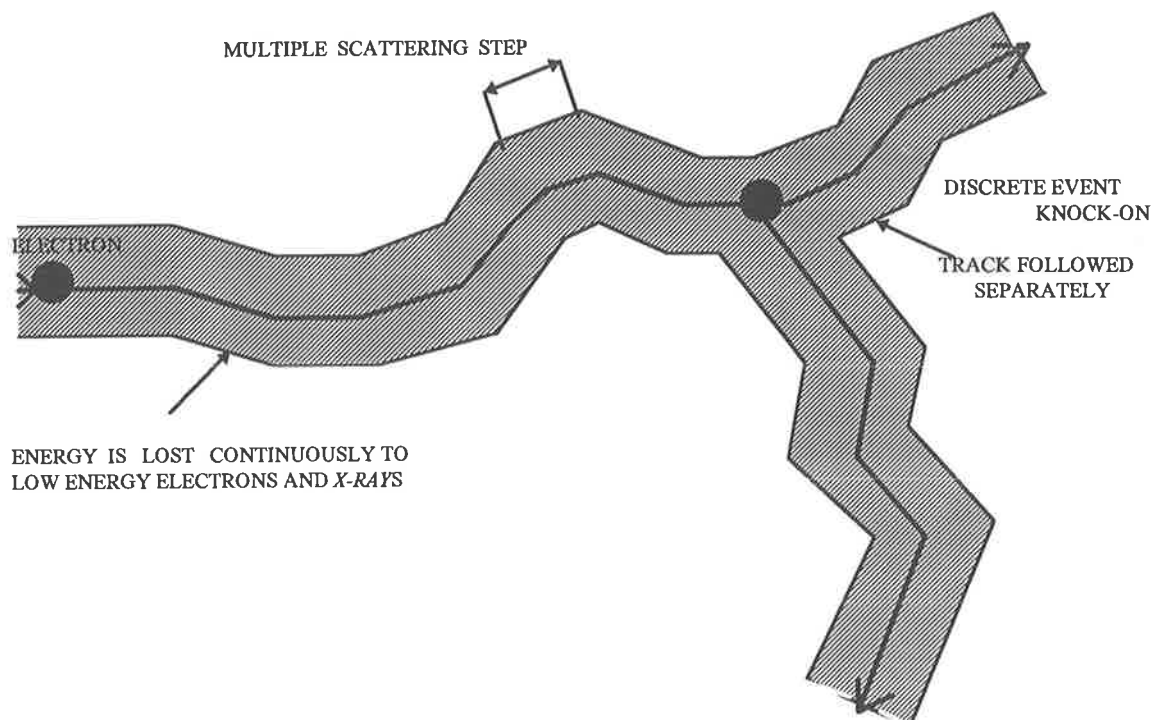


Figure 4.4. The class II algorithm in which discrete and continuous energy loss are combined together. Discrete interactions create knock-on electrons (delta-rays) or bremsstrahlung photons with energies above  $AE$  or  $AP$ , respectively (from Rogers and Bielajew, 1990).

Figure 4.5 shows effect of various approximations on calculation of electron depth dose distribution. Simulations are for a broad beam of 30 *MeV* electrons, perpendicularly incident on a semi-infinite water medium.

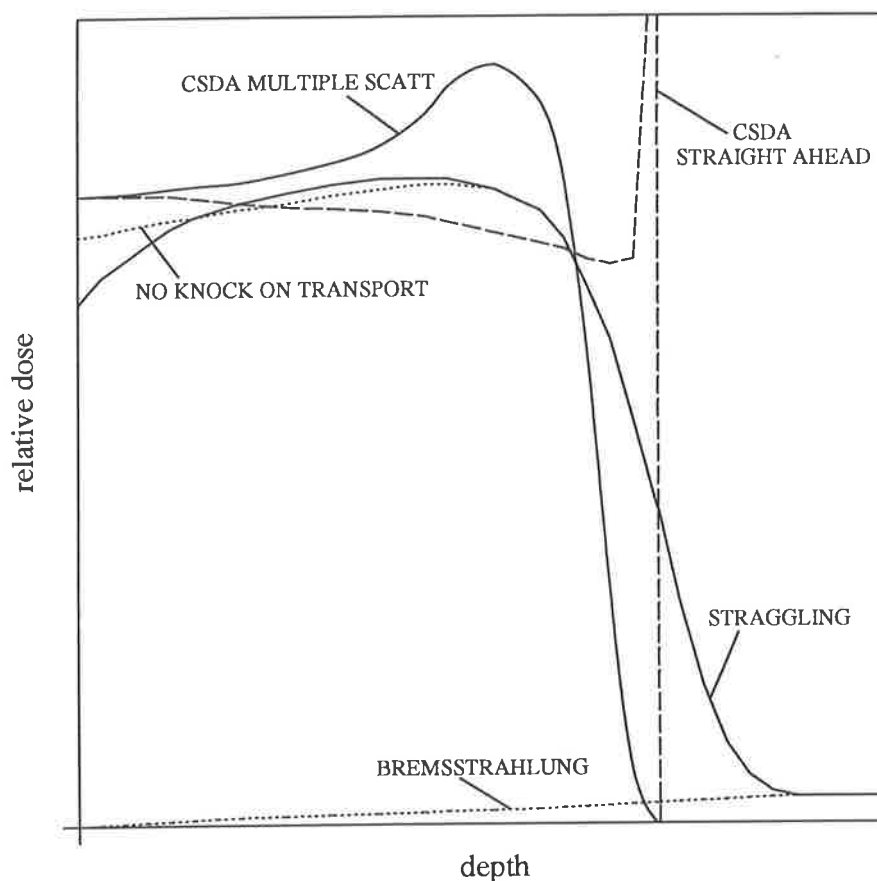


Figure 4.5. Depth dose curves of a broad 30 *MeV* electron beam in semi-infinite water medium, calculated using Monte Carlo, with different approximations (from Murray, 1991).

In the case of *CSDA* (straight ahead), because no scattering and delta-ray were modelled, all electrons reach the cutoff energy at the same depth, where their residual energy is deposited. In *CSDA* with electron multiple scattering included, the dose is deposited laterally as well, and so the depth dose is shallower. In a class II type simulation, energy loss straggling is taken into account and the result is much closer to the physical reality. The dotted-line on this is when straggling occurs but there is no knock-on transport (electrons undergo random large energy losses but no secondary electrons are created). When knock-on transport is included (straggling curve), the build-up part of the curve is affected by the transport of delta-rays (similar to photon

curve). A simplified logic-flow diagram for simulating electron transport, using class I and class II Monte Carlo algorithms is shown in Figure 4.6. "DETERMINE" has the same meaning as in Figure 4.3.

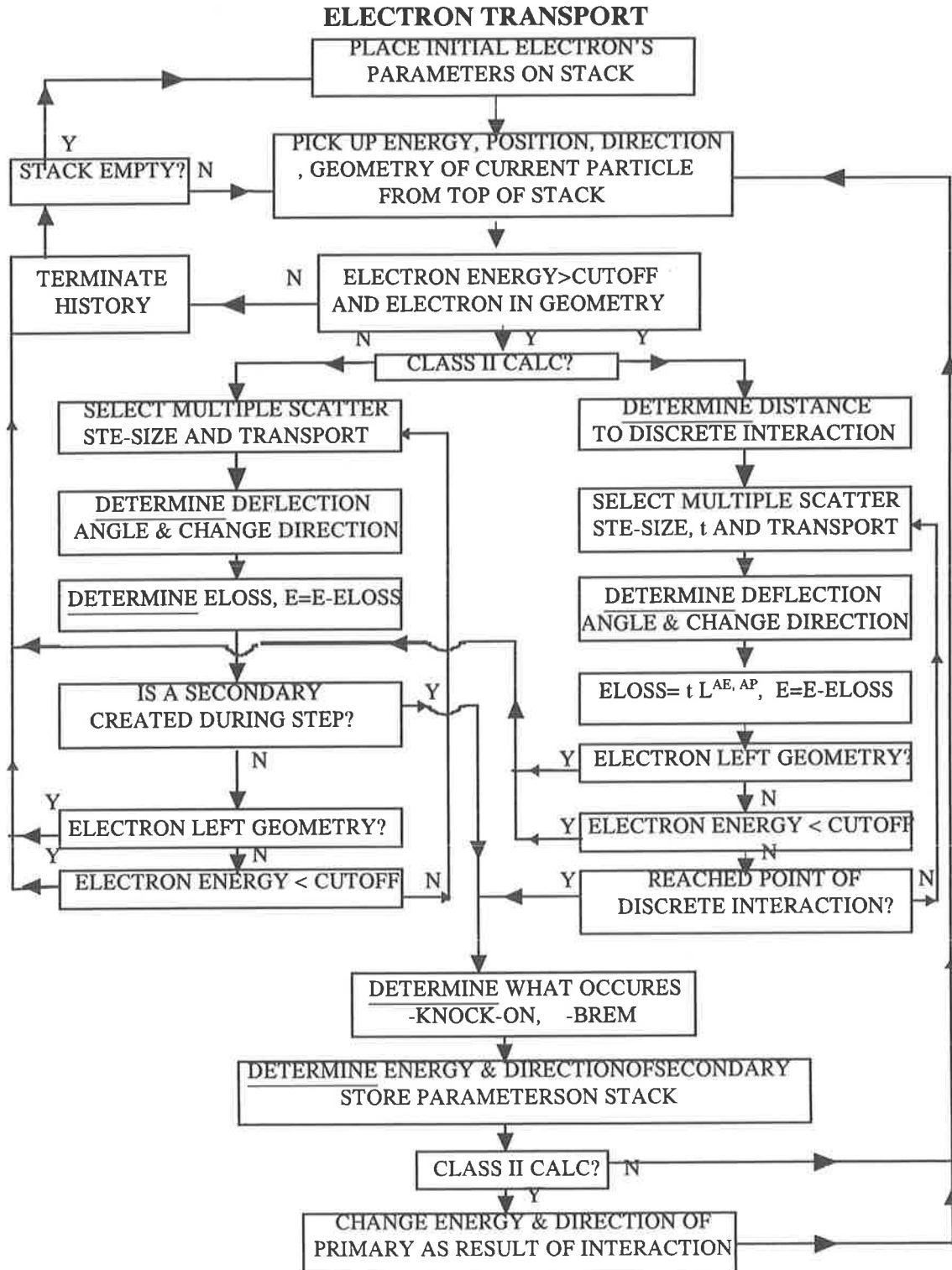


Figure 4.6. Logic flow of a Monte Carlo simulation of electron transport (Rogers and Bielajew 1990).

#### 4.5. The *EGS4* system

The current version of the *EGS* system, *EGS4*, was developed by Nelson, Hirayama and Rogers and is particularly suited to the energy and configurations in medical physics. *EGS4* has the advantage that actual physical processes are simulated as closely as possible. This makes simulations time consuming, but runs can be sped up by introducing variance reduction (not built-in) (Nelson et al, 1994). Also common geometries in radiotherapy are easily set up. The computational task of *EGS4* is divided into a preprocessor code, *PEGS4*, and the main *EGS4* code. *PEGS4*, which was created for efficiency reasons, uses theoretical and empirical formulae to compute the various physical quantities, such as cross sections, branching ratios, scattering coefficients, photon mean free path, electron stopping powers, etc. *PEGS4* prepares these data in a form for fast numerical evaluation by *EGS4*. This together with the user supplied data and routines are used for *EGS4* simulation. In fact *PEGS4* is created for efficiency and runs only once to generate data sets for each material used in the simulation. The following input file, for example, is used to generate data for water for energies between 10 keV and 25 MeV:

```

FILE NAME: water-25.pegs4
COMP
  &INP NE=2,RHO=1.0,PZ=2,1 &
WATER      H2O
H O
ENER
  &INP AE=0.521,UE=25.511,AP=0.010,UP=25.000 &
PWLF
  &INP &
DECK
  &INP &

```

The entire *EGS4* code system is written in a *FORTTRAN*-like language, called *MORTRAN3*, which has been developed by Cook and Shustek at *SLAC* (Murray, 1991). *MORTRAN3* contains macro-facility that is very useful and it is shorter and more readable than *FORTTRAN*. The general structure of the *EGS4* system is shown in Figure 4.7. This consists of the *EGS4* system code (below the dotted line) and the *EGS4* user written code. The user code calls two subroutines, *HATCH* and *SHOWER*, which are for retrieving *PEGS4* data and initiating each incident particle's history, respectively. The user code consists of *MAIN*, *HOWFAR* and *AUSGAB*. *MAIN* is a driving program

and initialises the media and particle parameters, cutoff energies and geometry of the simulation. *MAIN* then calls the *HATCH* to read-in media data, and calls *SHOWER* once for each incident particle to generate *EGS* history. *SHOWER* and its subroutines simulate the particle and its resultant beams until they leave the region of interest or fall below the cutoff energy. *HOWFAR* and *AUSGAB* are frequently called by *EGS4* system code to get information about the geometry and to record (score) quantities of interest, respectively.

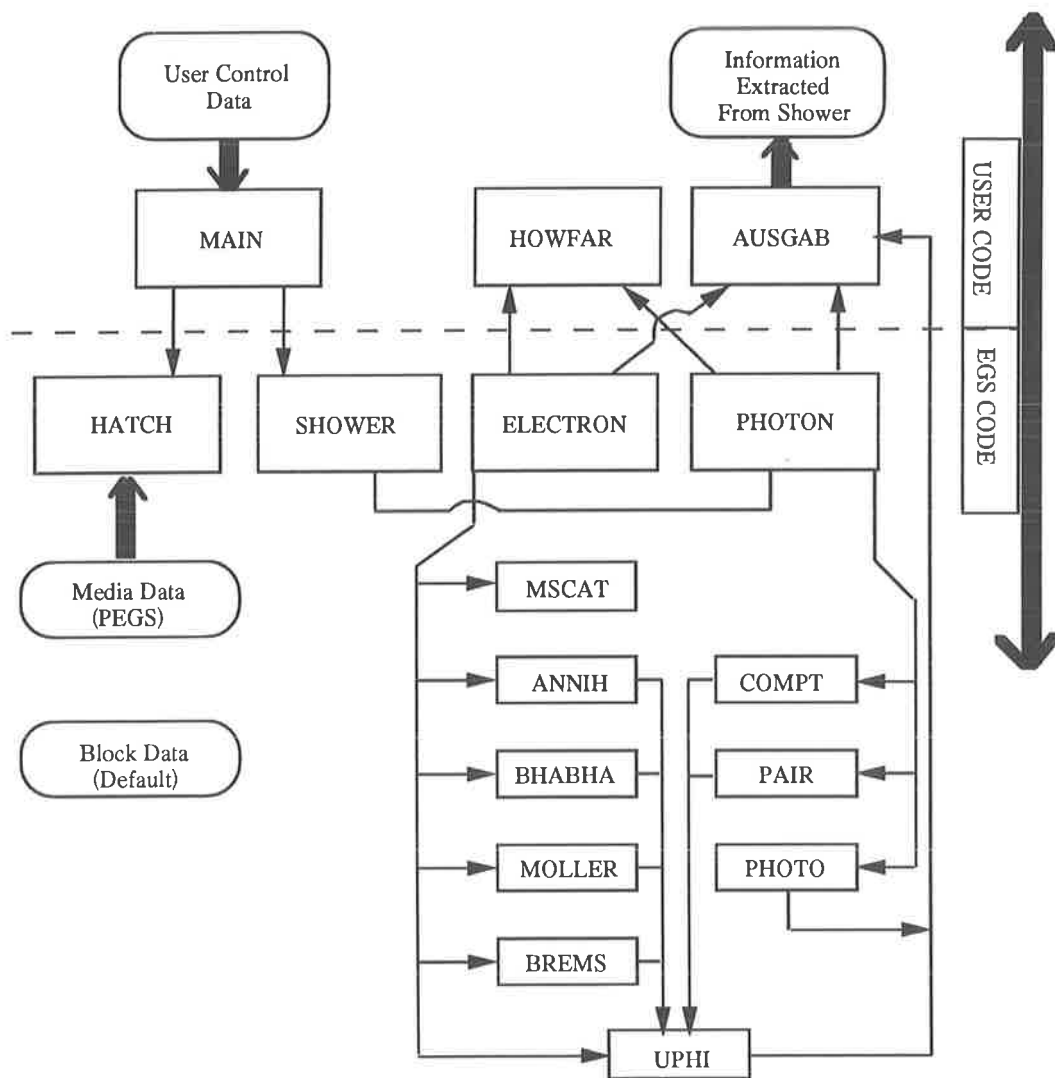


Figure 4.7. The general structure of the *EGS4* system. This consists of the *EGS4* code, the user code, and their various subroutines (from Bielajew, 1992).

#### 4.6. Dependence on electron step-size and energy cutoff parameters

Step-size selection can dramatically affect both the accuracy and the computation time in a simulation. *EGS4*, as mentioned before, is a class II model in which small collisions are grouped together, while large collisions are treated individually. The user can have some control and effect on simulation by selecting the simulation parameters. Definitions of user controlled parameters of energy cutoffs, production thresholds and *ESTEPE*, are summarised in Table 4.1. Energy cutoffs are used in both class I and class II, whereas the production thresholds apply only to class II algorithms. In this table *AE* is the threshold for delta ray production in which the collisional energy loss by the primary electron is relatively large. *AP* is the threshold for bremsstrahlung production.

Table 4.1. Definitions of the user control parameters in *EGS4* particle transport

Parameters	Symbol	Meaning
$e^-/e^+$ energy cutoff	<i>ECUT</i>	electron/positron energy is deposited locally below this
photon energy cutoff	<i>PCUT</i>	photon energy is deposited locally below this
$e^-/e^+$ production threshold	<i>AE</i>	low energy threshold for discrete electron/positron collision loss (delta-ray production)
photon production threshold	<i>AP</i>	low energy threshold for discrete electron/positron radiation loss (bremsstrahlung)
energy in electron step	<i>ESTEPE</i>	fractional energy loss per electron step

As mentioned above, electrons and photons produced as the results of electron energy losses above *AE* and *AP* thresholds will be treated by *EGS4* individually. Therefore the choice of these thresholds is important. If they are set too low the simulation time will increase unnecessarily, while if they are set too high it will lead to an inaccurate result. For most applications in medical physics a choice of 10 keV kinetic energy (10 keV and 511 keV for *AP* and *AE*, respectively) will produce satisfactory results. In this table also

*PCUT* and *ECUT* are photon and electron/positron cutoff energies, respectively, below which the energy is deposited locally.

In *PEGS4*, data is not produced for electrons of energy less than *AE* and for photons of energy less than *AP*. *ECUT* and *PCUT* must therefore be greater than or equal to *AE* and *AP*, respectively. *ECUT* and *PCUT* can be larger than *AE* and *AP* in which case, some discrete interactions will occur where there is no secondary particle transport.

In the condensed-history technique which is used by *EGS4*, the electron path is divided into a series of steps. The maximum fractional energy loss in each step is called *ESTEPE*. The smaller *ESTEPE* is set, the more realistic the electron track will be, however simulation time is increased. Since each electron step is a straight line, where in reality electron paths are very tortuous, choosing a large *ESTEPE* will cause an underestimation of the true electron path length per step distance. This causes the energy loss per step to be too small (this always occurs but the situation is worse for larger step sizes). To account for this, a pathlength correction factor (*PLC*) has to be applied to modify the straight-line step length to the curve's step length. This is an element of the *PRESTA* (see below).

$$PLC = \frac{t - s}{s} \quad (4-7)$$

In this equation, *t* is the average true pathlength for an electron step and *s* is the step distance in straight line.

#### 4.7. *PRESTA*

The occurrence of electron step-size artefacts, as mentioned above, are related to the change in the path length in electron transport, or to the abuse of the multiple-scattering theory in the vicinity of boundaries of the simulation media. Choosing the right value of *ESTEPE* for different simulations is difficult. The Parameter Reduced Electron-Step Transport Algorithm (*PRESTA*) has been developed by Bielajew and Rogers (1987) to address these problems. *PRESTA* dynamically selects a suitable step-size which provides accurate results as well as fast simulation. Basic features of *PRESTA* are as follows:

- (i) The path length correction (*PLC*), mentioned above, based on Moliere multiple-scattering theory. If the true curved path length in a step is  $t$ , then the straight line step length is  $s$  and the path length is reduced by  $(t-s)/s$ . *PLC* increases with increasing step-size (and so increasing energy loss per step), but decreases with electron kinetic energy.
- (ii) The lateral correction algorithm (*LCA*) to account for the lateral displacement which occurs in each step (only important for large steps).
- (iii) The boundary crossing algorithm (*BCA*). Using a large step-size near a boundary may mean that part of the step should be within a different medium. In this case the transportation is not accurate, the medium is different across the boundary. *PRESTA* uses a large step-size when electron is transported far from a boundary, but it reduces step-size near the boundary, such that the step length does not exceed the perpendicular distance to the boundary (Figure 4.8). When the distance to a boundary falls below a certain pre-defined minimum, this minimum is used as the step length.

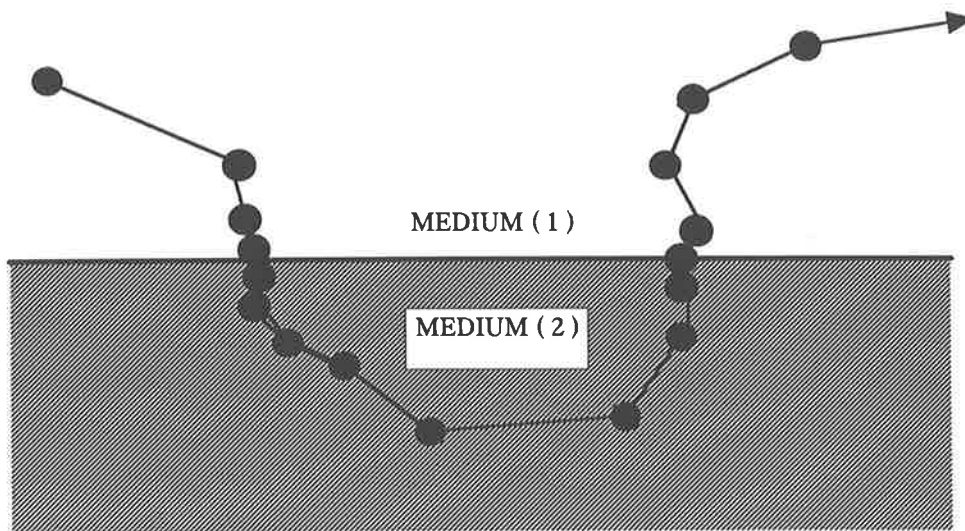


Figure 4.8. *PRESTA*'s boundary crossing algorithm (*BCA*) uses a large step-size when transports electron far away from a boundary, and a small step size when close to the boundary.

#### 4.8. Variance reduction techniques

Variance reduction techniques are those techniques which may be used to make calculations more efficient, that is to reduce the computation time for a given simulation and a statistical uncertainty. The efficiency of a calculational technique,  $\epsilon$ , is defined by:

$$\epsilon = \frac{1}{s^2 T}, \quad (4-8)$$

where  $T$  is the computing time (e.g., CPU seconds) and  $s^2$  is the variance of the result. This quantity is constant for a given simulation. For example, to reduce the uncertainty,  $s$ , by a factor of 2 the number of histories has to be increased by a factor of 4. Comparing equation (4-8) for different variance reduction methods gives a quantitative expression of the efficiency resulting from a specific technique.

There are different variance reduction techniques which can be employed for different conditions. These techniques have been discussed extensively by Bielajew and Rogers (1987). The new electron transport algorithm *PRESTA*, which was discussed in the previous section, is an example of these kind of techniques. *PRESTA*, using large electron steps only where needed, saves computing time and therefore is a variance-reduction technique. Photon interaction forcing, russian roulette, use of pre-computed results, use of geometry-symmetry, and geometry-equivalence or reciprocity are examples of variance-reduction techniques (Bielajew and Rogers, 1987). The effect of two different electron transport algorithms on the tracks is shown in Figure 4.9. In this figure two 10 *MeV* photon beams forced to interact at the origin of a water medium. Electron tracks are simulated (i) using the standard algorithm, *FIXTMS*, in which *ESTEPE* is set to a constant fraction (2% in here) of the current electron energy, and (ii) using the *PRESTA* algorithm. The simulation efficiency using *PRESTA* is 4.3 times more than the standard algorithm.

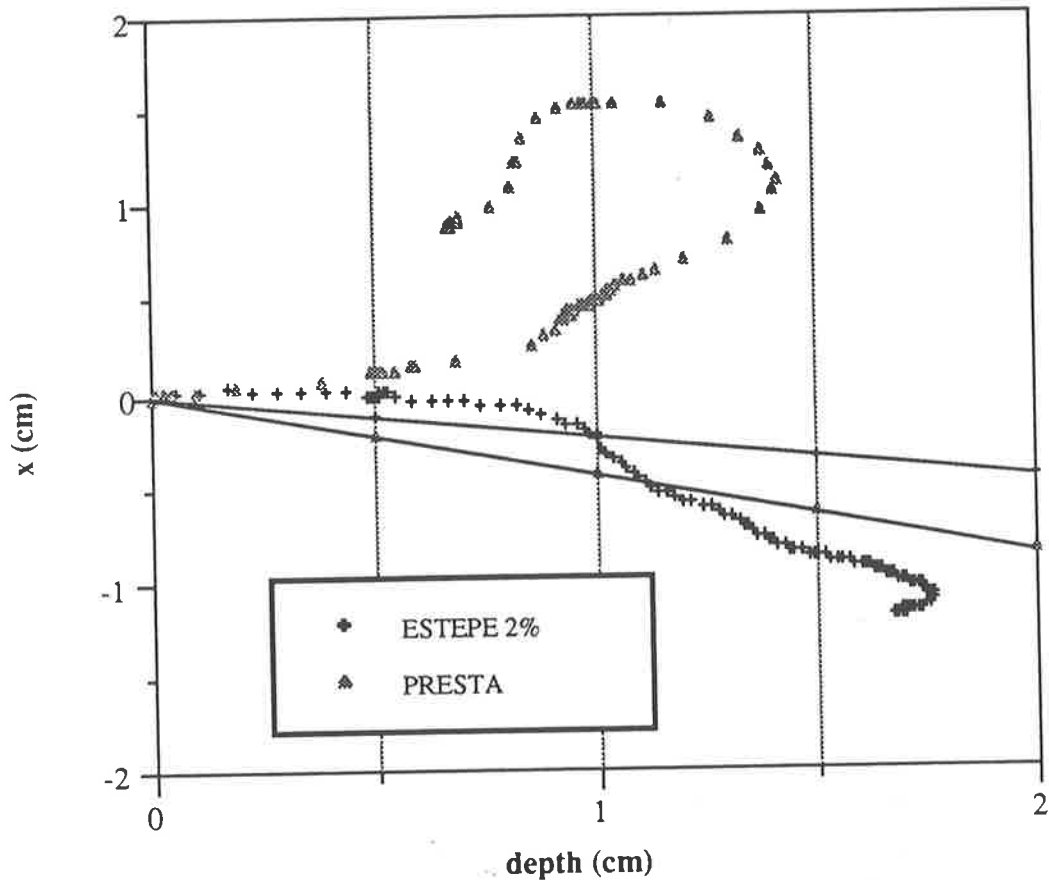


Figure 4.9. The effect of two different boundary crossing algorithms on the electron transport. Using *PRESTA* (upper track) is more efficient than the standard algorithm (lower track). The original photon beams with their straight tracks are also shown in this figure (from Murray, 1991).

#### 4.9. Reciprocity technique

Central axis depth dose calculation in the case of normal incidence of a circular beam on semi-infinite geometries, with or without semi-infinite inhomogeneities, can be performed more efficiently using a simple variance reduction technique, called “*geometry-equivalence*” or “*reciprocity*”.

In a full simulation to determine central axis depth doses for above conditions, a uniform photon beam across the beam boundaries enters the medium and the energy deposition is scored in small voxels in the central axis of the beam. In this case, of course, all interactions and trajectories of particles have to be calculated, even though only small part of them contribute to the dose deposition in central axis voxels.

Therefore, most of the computation time is wasted. Using the geometry-equivalence (reciprocity) technique, shown in Figure 4.10, a modified beam-detection voxel configuration was employed by Hoban (1991) to quantitatively evaluate the efficiency of this technique. In Figure 4.10(a) a circular photon beam with a uniform fluence,  $\phi$ , and a radius 1 cm enters perpendicularly to a medium.

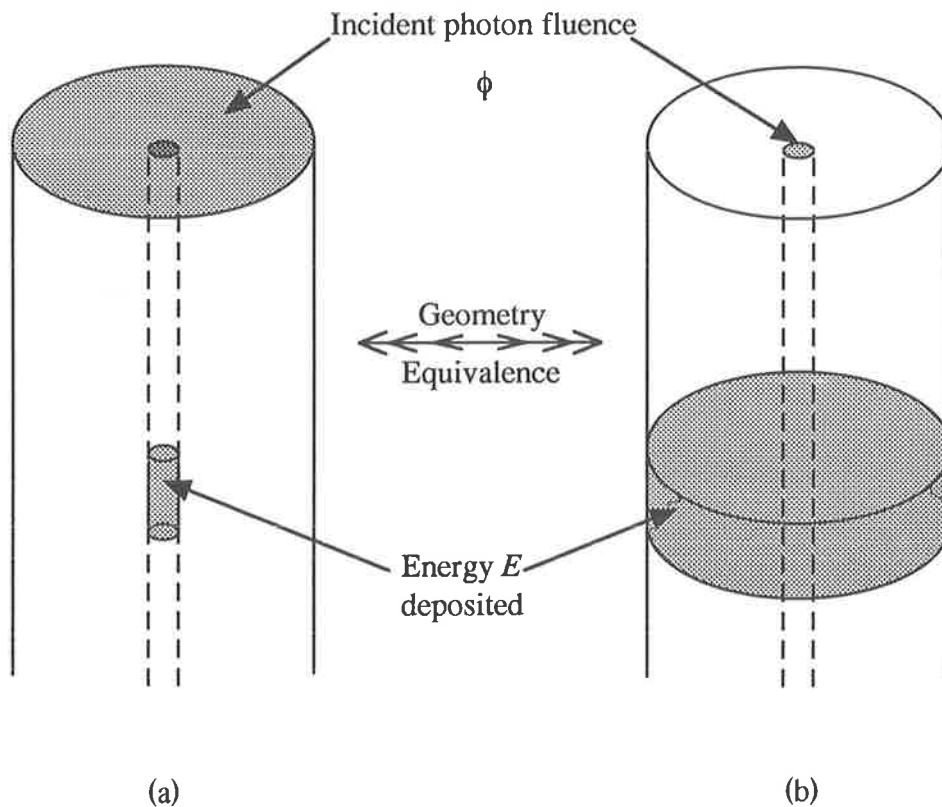


Figure 4.10. Energy deposition by a parallel photon beam of 1 cm diameter in a cylindrical voxel of 0.1 cm diameter (a) is the same as that of a parallel photon beam of 0.1 cm diameter in a cylindrical voxel of 1 cm diameter (b) (from Hoban, 1991).

According to the reciprocity theorem, the energy deposition in the scoring voxel of radius 0.1 cm and thickness 0.5 cm is the same as the energy deposition in the scoring voxel of radius 1 cm and thickness 0.5 cm in Figure 4.10(b) with the incident beam of the same fluence and 0.1 cm radius. The number of photons, in the second case is reduced by a factor of 100 (the ratio of areas). The efficiency gain can be calculated using equation (4-8) as follow:

$$\frac{\epsilon_2}{\epsilon_1} = \frac{s_1^2 T_1}{s_2^2 T_2} \quad (4-9)$$

The efficiency gained in above example would be 100 if the variance is the same for both cases. This is not necessarily true, because the number of particles contributed to the energy deposition voxels is not the same for the both cases. The variance ratio of the full simulation to that of the reciprocity technique for above example was found to be 0.52 (Hoban 1991) and hence the efficiency gain by using reciprocity technique and equation (4-9) is 52.

Using reciprocity technique is very efficient in central axis dose calculation of multiple beam diameters. This can be performed for several beam diameters in a single simulation, as it is shown in Figure 4.11. In this figure Tissue Maximum Ratios (*TMRs*) have been calculated using reciprocity technique, for circular beams of 3, 5, 10, 20, 30, 40 *cm* diameters. The related simulation input file, together with the introductory comments (on the right), is shown in Figure 4.12.

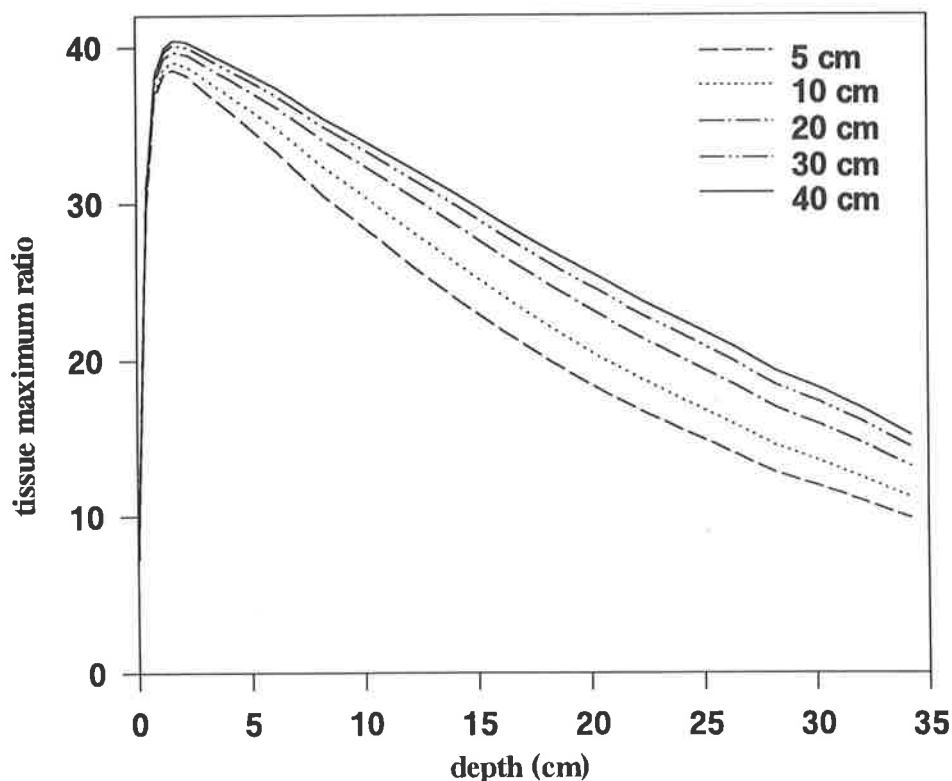


Figure 4.11. Tissue Maximum Ratios, calculated using *MC* reciprocity technique in a single simulation for circular beams of different diameters.

<b>6 MV Tissue Maximum Ratios</b>	<b>simulation title</b>
WATER	material 1
DUMMY	material 2 (not used)
DUMMY	material 3 (not used)
DUMMY	material 4 (not used)
35.0,-2,46	phantom thickness (cm), number of depth groups (- indicates groups follow), number of radial scoring regions
0.1,20,1,1.0,0.561,0.050	depth increment, number of depth regions in current group, material index, density, <i>ECUT</i> , <i>PCUT</i>
0.5,66,1,1.0,0.561,0.050	depth increment, number of depth regions in current group, material index, density, <i>ECUT</i> , <i>PCUT</i>
0.0	inner radius for the first radial region (cm)
2.5	inner radius for the second radial region (cm)
5.0	inner radius for other radial regions (cm)
10.0	“ “
15.0	“ “
20.0	“ “
-1,0,0,0,561,0.050	K.E. of incident particle (- indicates that spectrum followed), ANGSIGMA, global <i>ECUT</i> and <i>PCUT</i>
0.0	lower energy of 1st spectral bin
0.75,20.0	upper energy of 1st spectral bin, spectral weight
0.9,20.3	upper energy of 2nd spectral bin, spectral weight
1.125,41.0	3rd spectral bin
1.375,48.8	4th spectral bin
1.75,80.0	5th spectral bin
2.25,84.5	6th spectral bin
2.75,61.2	7th spectral bin
3.5,61.7	8th spectral bin
4.25,31.0	9th spectral bin
4.75,11.6	10th spectral bin
5.5,8.9	11th spectral bin
6.0,1.9	12th spectral bin
0.0	indicates end of spectrum
3	central axis depth dose curve for parallel finite radius beams
0.01	radius of the scoring region
4000000,0,0,6000000.0,0,123456113	number of histories, charge of incident beam, monitor routine off (normal output), CPU limit (hrs), histogram plot off, random number seed
35.0,0.2	depth limit (cm), survival probe of Russian roulette
0,0,0,0,0.0	for a default <i>PRESTA</i> run (IPLC, IBCA, ILCA, IOLDTM, BLCMIN turned on)
1,0,0,0,0,0,2,0	output options - total dose table, tables for primary dose, scattered dose and kerma, no region masses, no DOTPLOT, RAWDATA and IGETSPEC

Figure 4.12. The *EGS4* input file for generating *TMRs* shown in Figure 4.11. The simulation was performed in water for the pre-determined 6 *MV* photon beam spectrum.

#### 4.10. Benchmarking *EGS4*

Electron and photon transport includes extremely complicated physical processes and the Monte Carlo codes are also very complex. Therefore it is essential to evaluate these codes for different situations. The evaluation is performed by benchmarking *MC* calculations against high-quality experimental data. The comparison was made by Rogers and Bielajew (1990) for various simulations, including detector response functions, photon and electron depth dose curves, bremsstrahlung production and dose at an interface. From these comparisons, they have shown that *ETRAN* and *EGS4* codes are generally quite accurate. However, this does not mean that they can always be trusted. For example, even if a specific benchmark proves the accuracy of the code, the situation might change for different energy or material. This is because various components of the transport algorithm have different importance in different energy regions or materials. In the following section the *MC* calculation of depth doses is compared with the corresponding measured depth doses for 6 and 23 *MV* photon beams.

##### 4.10.1. Depth doses

Benchmarking *EGS4* calculation of depth doses against experimental results was performed for various clinical beams, along with (i) the known falloff rates for the corresponding depth dose curves and (ii) the falloff rates for the beams to be modelled. The effective 6 and 23 *MV* photon beam energy spectra, produced in a Siemens *KD-2* linear accelerator, have been determined by the author using the published effective energy spectra (Ahnesjo et al, 1992). For more information see chapter 5. Figures 4.13 and 4.14 show the energy spectra for above beams. The same spectra were used for both field sizes modelled here.

*EGS4* calculation of depth doses in water was performed for above spectra and  $10 \times 10$   $cm^2$  fields at  $FSD=100$   $cm$ . Comparisons have been made with the corresponding depth doses, measured with the *RK* ionization chamber and the Farmer electrometer. Results of these comparisons are shown in Figures 4.15 and 4.16 for 6 and 23 *MV* photon beams, respectively. As it is seen from these figures, *EGS4* calculated depth doses are

in very good agreement with the corresponding measured depth doses. This confirms the energy spectra and the validity of *EGS4* simulations.

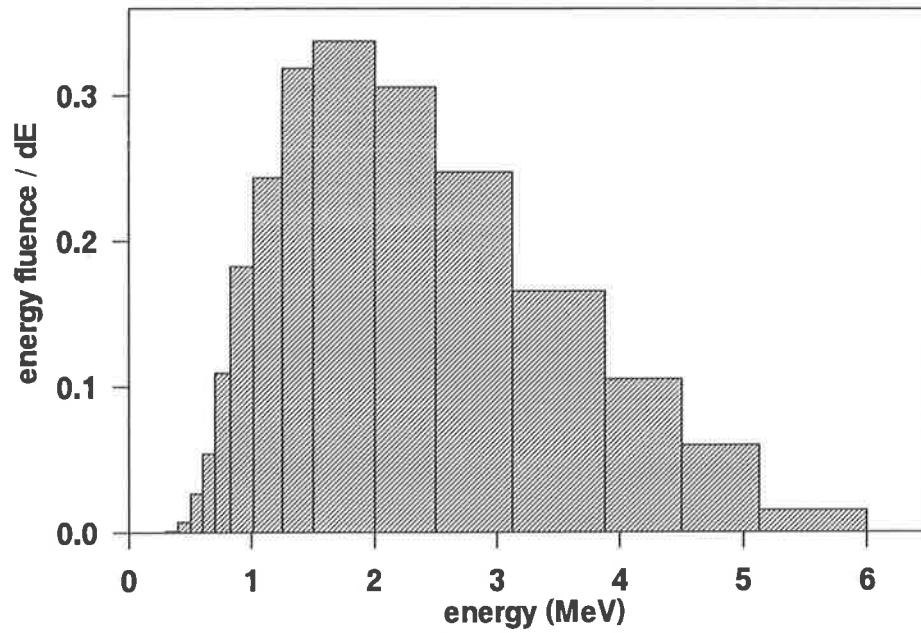


Figure 4.13. The effective 6 MV photon beam energy spectrum, produced in a Siemens *KD-2* linear accelerator.

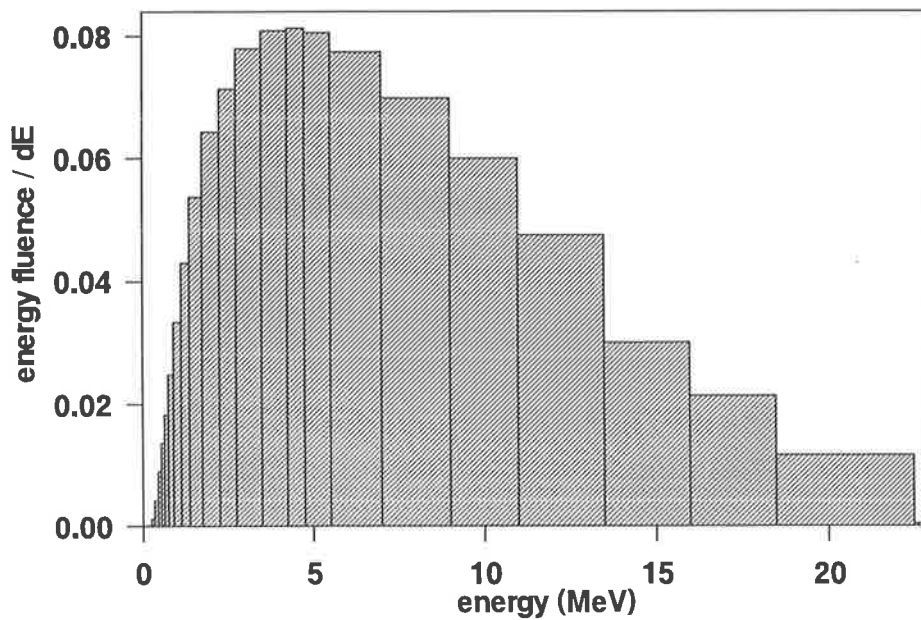


Figure 4.14. The effective 23 MV photon beam energy spectrum, produced in a Siemens *KD-2* linear accelerator.

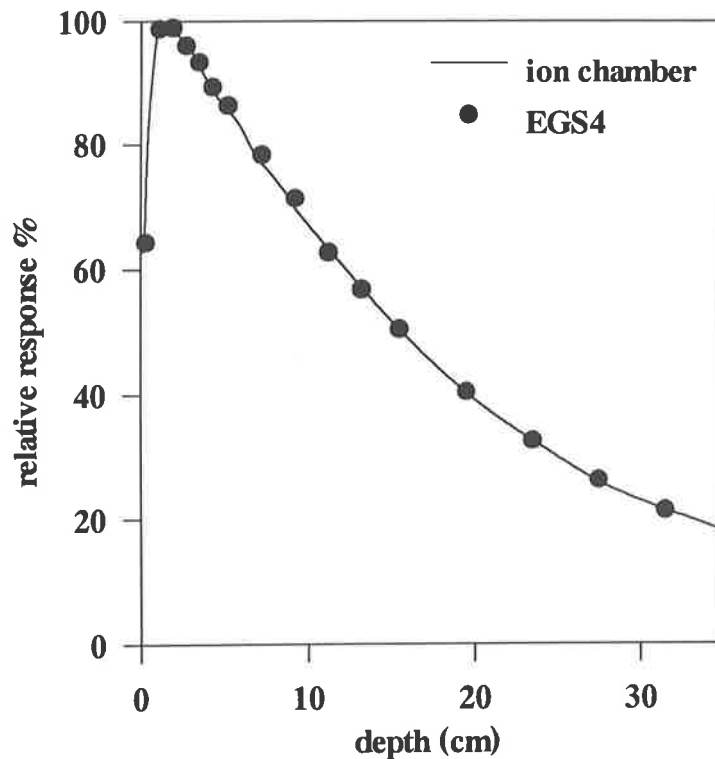


Figure 4.15. A comparison of the *EGS4* calculation and the *RK* ionization chamber measured depth doses in water for 6 MV photon beams,  $10 \times 10 \text{ cm}^2$  field at  $FSD=100 \text{ cm}$ . *EGS4* calculation was performed using the energy spectrum in Figure 3.13.

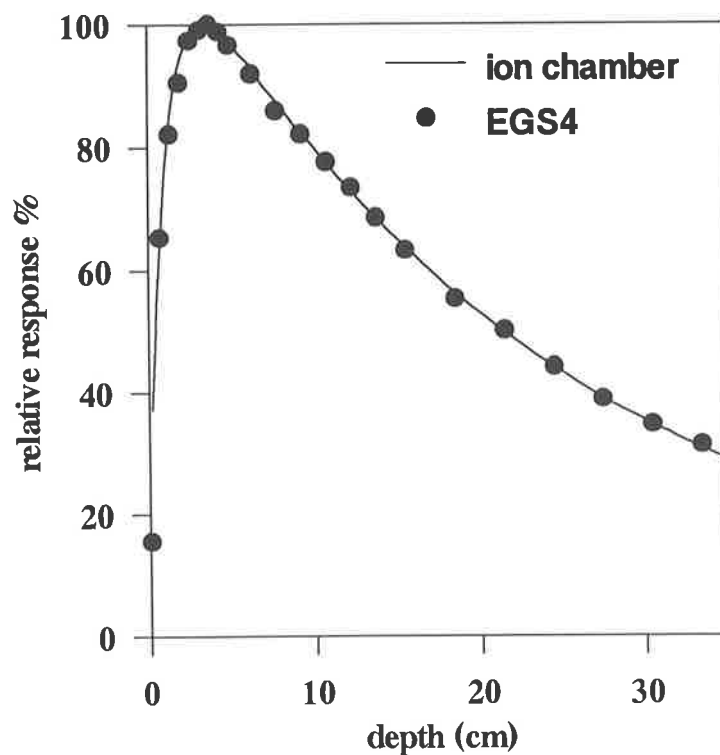


Figure 4.16. A comparison of the *EGS4* calculation and the *RK* ionization chamber measured depth doses in water for 23 MV photon beams,  $10 \times 10 \text{ cm}^2$  field at  $FSD=100 \text{ cm}$ . *EGS4* calculation was performed using the energy spectrum in Figure 3.14.

Having confirmed the energy spectra and *EGS4* simulations, they can be used as valid references for conditions where measurements are not possible and or are not reliable. For example, the dose distribution in a medium due to the primary and scattered photons can be scored separately using *MC* techniques. Figure 4.17 shows the relative contribution of primary and scattered photons to the total dose for different field sizes. The calculation was performed using the reciprocity technique in a single simulation for the 6 *MV* photon beam at  $d=14\text{ mm}$  in water. From this figure it can be seen that lateral electronic equilibrium for the 6 *MV* photon beam is not achieved for beams smaller than 3 *cm* in diameter. Therefore, ionization chamber-measured depth doses for very small fields such as those in stereotactic radiosurgery (*SRS*), where lateral electronic equilibrium does not exist- especially when beam is smaller than the detector, are not correct. This is shown for a  $0.5\times 0.5\text{ cm}^2$  field size, 6 *MV* photon beam in Figure 4.18. In this case the measured depth dose is much shallower than *EGS4* result, because of the large size of the ionization chamber and the fact that presence of the low density ionization chamber increases the degree of disequilibrium and further away from the Bragg-Gray theory.

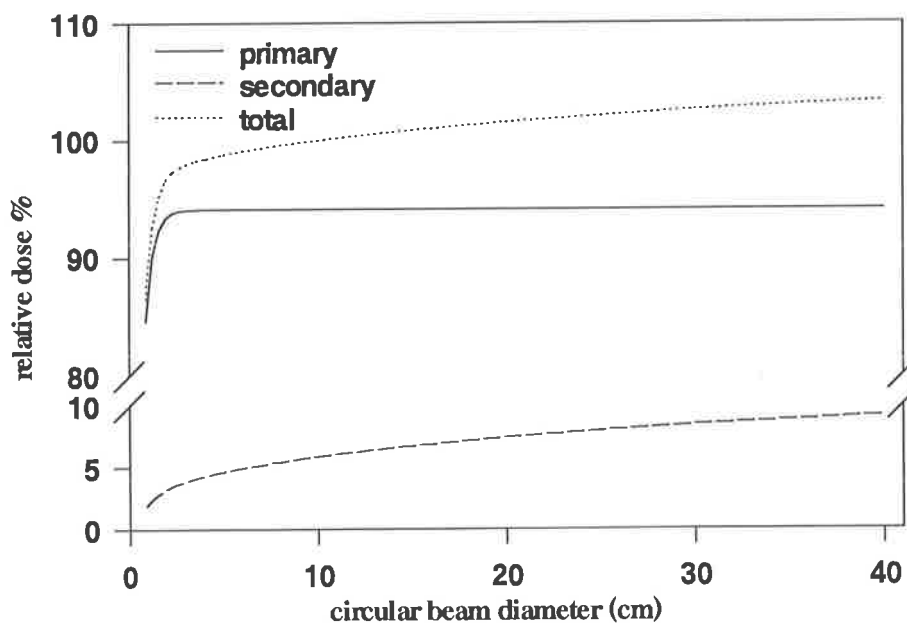


Figure 4.17. The relative contributions of primary and secondary photons to the total dose for different field sizes. The calculation was performed using the *EGS4* (reciprocity) technique for the 6 *MV* photon beam at  $d=14\text{ mm}$  in water.

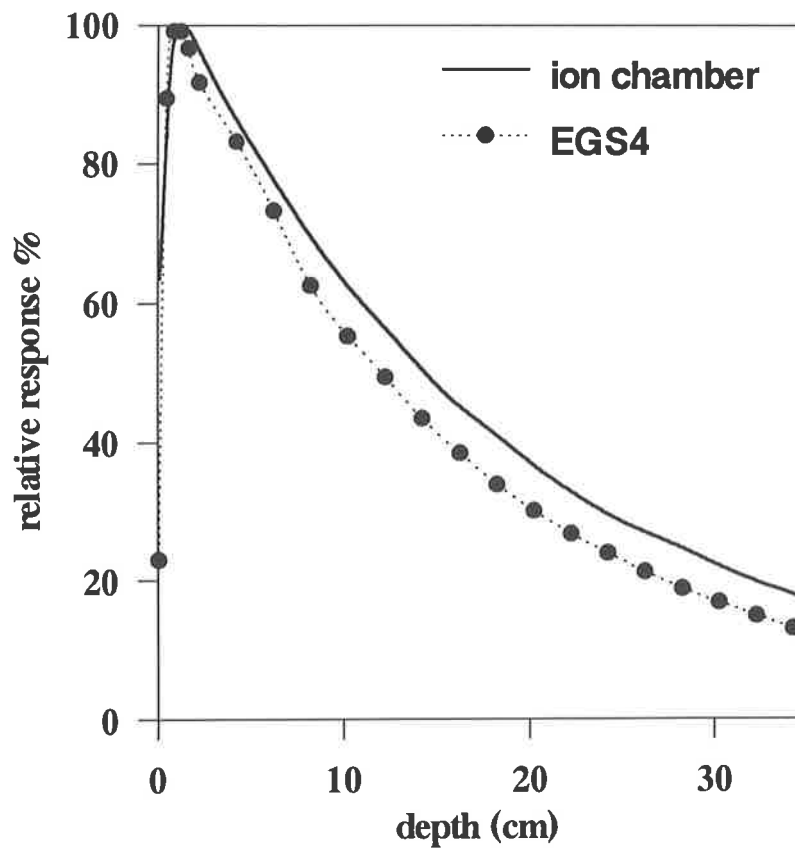


Figure 4.18. A comparison of the *EGS4* calculation and the *RK* ionization chamber measured depth doses in water for 6 *MV* photon beams,  $0.5 \times 0.5 \text{ cm}^2$  field at *FSD*=100 *cm*. *EGS4* calculation was performed using the energy spectrum in Figure 3.13.



## Chapter 5

# Evaluation of Dosimetry Techniques in Stereotactic Radiosurgery

### 5.1. Introduction

Radiosurgery in its routine role as single fraction treatment procedure is limited to lesions as large as a few *cm* in diameter and has most benefit in treating *AVMs*, due to their late-responding characteristics and the related radiobiological principles (Brenner et al, 1991 and Hall and Brenner, 1993). Also in past few years there has been increasing interest in fractionated-radiosurgery—that is stereotactic radiotherapy (*SRT*) for treating larger lesions and solitary malignant brain tumours or single metastases, using advantages of fractionation in sparing late-responding normal tissues and increasing the effectiveness of treating hypoxic tumours (Hariz et al, 1990; Dellannes et al, 1991 and Hall and Brenner, 1993).

In this department the Leibinger/Fischer stereotaxic system is used with a Siemens Mevatron *KD-2* linear accelerator with some minor modification to the linac. A 6 *MV* photon beam is used for this purpose, with an output of 200 cGy/min under calibration conditions (at  $d_{max}$  in water,  $10 \times 10 \text{ cm}^2$  field size and  $FSD=100 \text{ cm}$ ). The Fischer treatment planning requires Tissue Maximum Ratios (*TMRs*), Off Axis Factors (*OAFs*), and Collimator Output Factors (*OFs*) for different stereotactic collimators. These collimators provide *SRS* fields which are 8.8 to 41.0 *mm* in diameter at the isocentre ( $FAD=100 \text{ cm}$ ).

Accurate dosimetry of small field photon beams used in stereotactic radiosurgery can be made difficult because of the presence of lateral electronic disequilibrium and steep dose gradients. Detector response characteristics have an impact on dosimetry in these conditions and measuring penumbra (Metcalf et al, 1993). In the published literature most data acquisition in radiosurgery is based on diode, film, and partly thermoluminescent dosimetry (*TLD*) (Arcovito et al, 1985; Rice et al, 1987; Podgorsak

et al, 1988 and Beddar et al, 1994). However, these detectors are energy or dose rate dependent and the latter suffers from relatively high statistical uncertainty. There is little evidence of using *TLD* for dosimetry in the region of electronic disequilibrium (Podgorsak et al, 1988 and Kron et al, 1993). Ionization chambers on the other hand are especially inadequate for dosimetry of stereotactic radiosurgery (*SRS*) fields because of their relatively large dimensions and thus poor resolution in the penumbral region. Additionally, the presence of the large volume of air cavity will increase the degree of lateral electronic disequilibrium. In this case average electron fluence across the detector will be reduced so that it can not be used for absolute dosimetry or measuring the collimator output factors.

In measuring depth dose, when field size is smaller than sensitive volume of the detector, the problem is worse. In this case the detector will not show dose variations related to inverse square fall off, since a larger proportion of the detector is covered by the field as depth increases. However, in *SRS* in measuring *TMRs*, the problem related to the inverse square fall off does not exist and there is less deviation.

In recent years, state of the art diagnostic tools (*MRI*, *CT*, angiography, etc.), *3-D* treatment planning systems with very accurate dose calculation algorithms, and modern radiosurgery hardware have been employed to diagnose, plan, position, and treat a lesion to a geometric accuracy of better than 1 *mm*. Since field positions and sizes are chosen so that the high dose region closely matches the tumour volume, any inaccuracy in the calculated dose distribution will mean that the tumour coverage may not be adequate. Also, dose to normal tissues may be higher than it appears on the plan. This becomes very important when the lesion is close to a critical structure. Because of the above-mentioned dosimetry difficulties there are potential errors in measuring the required quantities, namely *OFs*, *TMRs*, and *OAFs*. The error in the *OAF* measurement particularly could have a large effect on the dose to the target volume as well as healthy tissue, because of the steep dose gradients encountered in *SRS* fields.

In this chapter small field dosimetry difficulties are pointed out, problems associated with detector non tissue-equivalency and detector finite size are discussed and quantified and their impacts on *3-D* dose calculations are investigated. Also *PTW* Riga diamond detectors, and Monte Carlo (*EGS4*) techniques have been added to the above

tools to measure and calculate treatment planning requirements in 3-D dose calculations and results are compared to each other. The validity of the energy spectrum used in the *EGS4* simulations has been confirmed by comparing *EGS4* depth doses to those obtained with an ionization chamber, where the field size is large enough for electronic equilibrium to be established at the central axis. The close match between ionization chamber and *EGS4* depth dose curves for above conditions indicates that the 6 MV photon energy spectrum used as input to the Monte Carlo simulations is correct. The *EGS4* generated *TMR* data for small *SRS* fields, where electronic equilibrium does not exist, can then be considered as valid reference.

Using *EGS4* calculations, the beam characteristics under the experimental conditions have also been quantified. The energy spectra of photons and secondary electrons at different depths and field sizes have been calculated and their impact on the responses of different detectors has been investigated. *EGS4* simulations were performed using cylindrical geometry. Energy cutoff parameters used were  $ECUT=AE=0.521\text{ MeV}$ ,  $PCUT=AP=0.01\text{ MeV}$ . The *PRESTA* algorithm was employed.

## 5.2. Small field dosimetry difficulties

The main problems associated with small field dosimetry are the lateral electronic disequilibrium, steep dose gradient and the related detector convolutions. The lateral electronic equilibrium will generally be achieved when the radiation field diameter is at least twice that of the maximum lateral range of the primary electrons which in turn is almost equal to the depth of the maximum ionization ( $d_{max}$ ). In the presence of electronic equilibrium there is an electron energy spectrum at the beam central axis which contains electron energies from zero to a maximum equal to the maximum photon energy. On the other hand for very small fields (narrow beams), when the lateral electronic equilibrium does not exist, there is lack of a lower energy electrons which otherwise could have reached the central axis from points at distances just smaller than the maximum electron range (Wu et al, 1993). In this case the electron energy spectrum at central axis will change in the favour of higher energy electrons and the average energy in the spectrum will increase. In this case the detector gives an incorrect response if it is not water equivalent and its restricted stopping power relative to water changes with energy. This will be discussed in the following sections.

### 5.2.1. Energy spectrum

Determination of the photon energy spectrum is important to quantify the energy dependence, when a photon detector is not water-equivalent (Miller and McLaughlin, 1982). In this case the ratio of the absorption coefficient of the detector to that of water will change with any change in the beam energy spectrum which naturally occurs by changing depth and field size. Also, determination of the electron energy spectrum, produced as a result of the photon interactions with the medium, is important for electron detectors when the restricted stopping power ratio of the detector relative to that of water varies with energy. This becomes more significant when lateral electronic equilibrium does not exist (as in the penumbra region) as any change in the degree of disequilibrium changes the spectrum.

Parallel polyenergetic photon beams with the determined effective energy spectrum were incident perpendicularly to a semi-infinite water medium. The energy spectra of both the photon beam and the resultant electrons will change with depth in different ways. Change in the energy spectrum with depth and the variation with field size will be explained in detail in the following sections. The energy spectra were recorded at central axis at different depths for circular beams of 1.25 and 4.1 cm in diameter (projections of the 7 and 23 mm SRS collimators at the isocentre, respectively) as well as for 0.5, 10 and 20 cm diameter beams. Because the detector response depends on the overall energy spectrum, the primary and scattered photons were scored together. The photon and electron energy spectra were scored at the surface,  $d_{max}$ , and every 5 cm up to 35 cm depth and their energy spectra were divided to 0.2 MeV segments.

Results of the MC (EGS4) calculated photon and electron mean kinetic energy and their variations with depth and field diameter at the isocentre are shown in Figures 5.1(a) and 5.1(b), respectively. In each case a 6 MV spectrum was used, with a mean energy of 2.11 MeV. Fluence was normalised to unity at each depth. In these figures it is shown that the photon and the resultant electron energy spectra for broad beams are softer than those of the narrow beams and have less variation with depth. This is the result of a large scatter contribution at depths beyond  $d_{max}$  to the total dose in the case of broad beam. The mean energy of narrow beams shows a larger increase with depth, as the result of the reduced scatter contribution (hardening of the primary beam dominates).

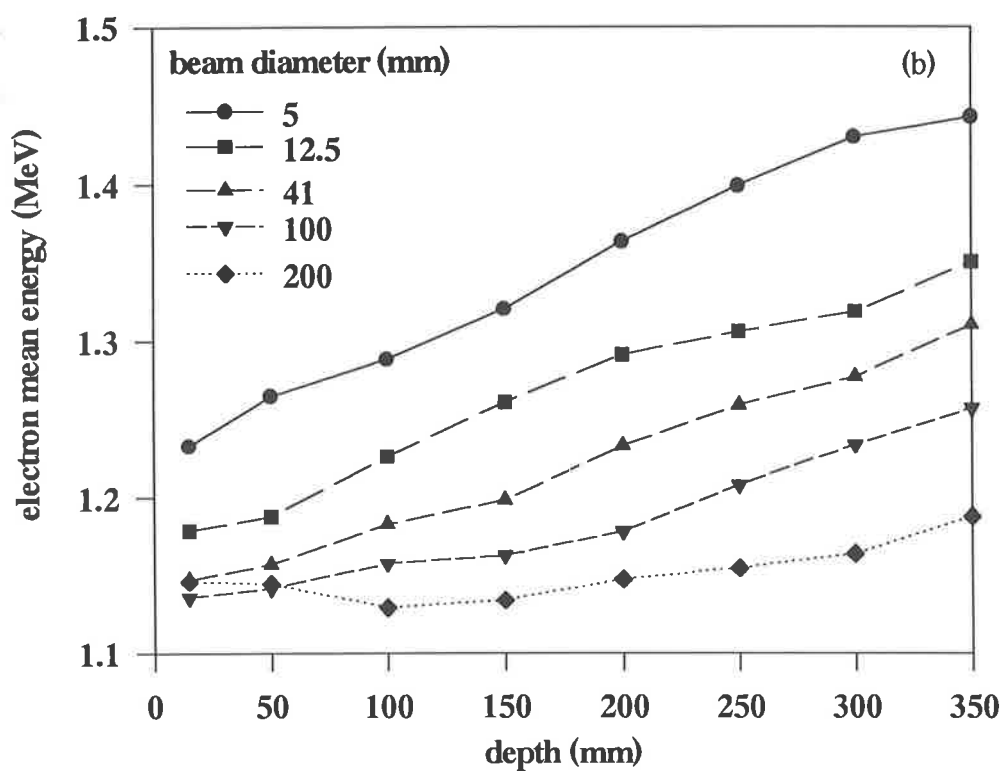
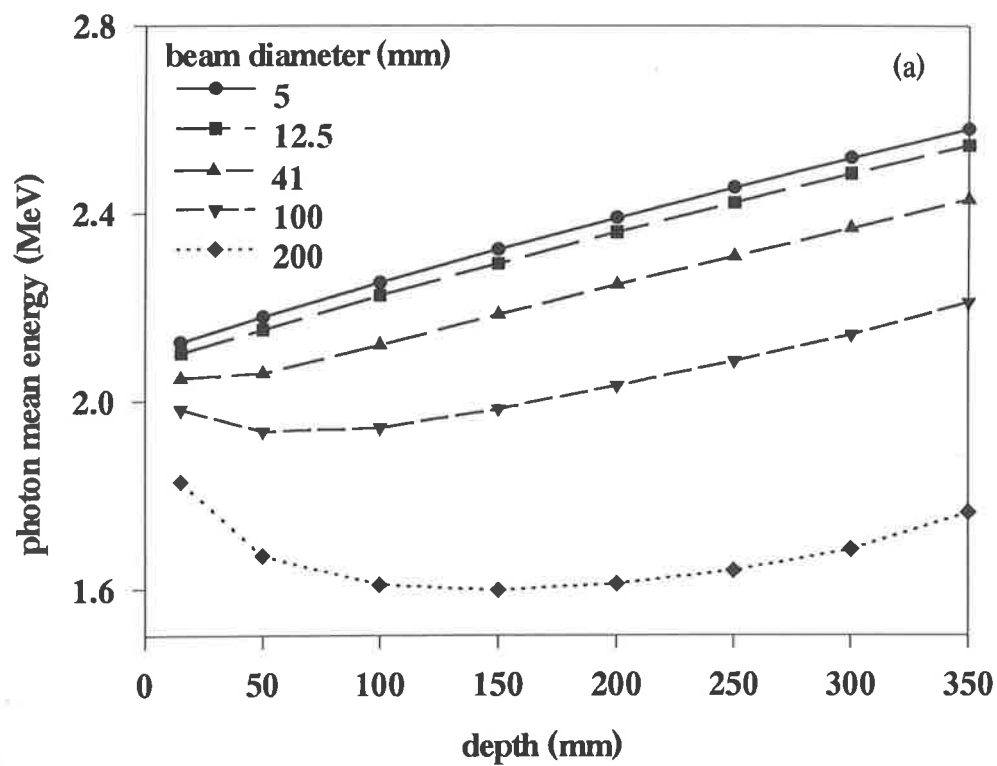


Figure 5.1. Variations of (a) photon and (b) electron (produced as the result of the photon interactions) mean kinetic energies with depth and field size at the isocentre, calculated using the MC (*EGS4*-reciprocity) technique.

Also, the electron energy spectra for 0.5 and 10 *cm* diameter photon beams at 20 *cm* deep are compared in Figure 5.2. From this figure it is obvious that the electron energy spectrum of the narrow beam is harder than that of the broad beam. This is due to the lack of lateral electronic equilibrium as well as a smaller low energy photon contribution (resulting in a smaller number of low energy secondary electrons). The same input photon energy spectrum with the average energy of 2.11 *MeV* was used for different field sizes. The energy spectrum was assumed to be uniform across the incident beam and the variation caused by the flattening filter was not included.

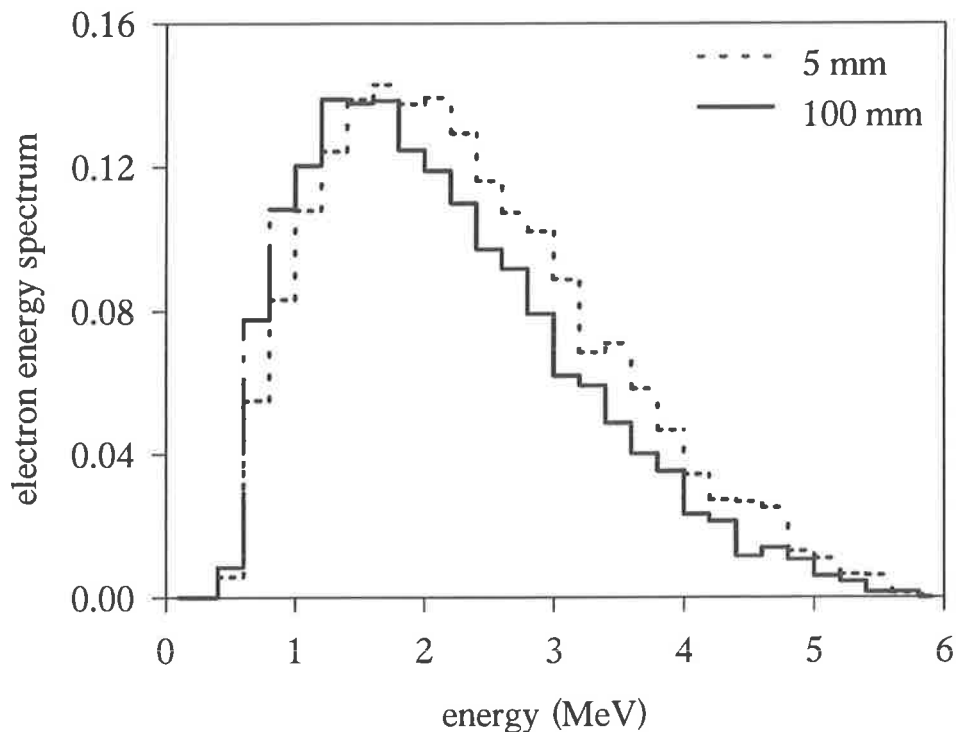


Figure 5.2. Normalized electron energy spectra at 20 *cm* deep in water, produced as the result of 0.5 and 10 *cm* diameter photon beam interactions using the *MC* (*EGS4*-reciprocity) technique.

### 5.2.2. Detector response to *SRS* fields

As the result of the change in electron energy spectrum, the ratio of the detector reading for narrow beam to that of the calibration beam does not necessarily give the exact absorbed dose ratio. That is, the ratio of detector response to absorbed dose in water

varies with any change in stopping power of the detector element relative to the medium (water). Under the conditions of the Bragg-Gray theory the dose to a point in water is related to the dose in the detector element at that point by the following equation:

$$\frac{D_w}{D_d} = \frac{(\bar{S}/\rho)_w}{(\bar{S}/\rho)_d} \quad (5-1)$$

where  $(\bar{S}/\rho)_w$  and  $(\bar{S}/\rho)_d$  are the average mass collision stopping power ratios for the medium and detector over the electron energy spectrum, respectively. In the case of an ionization chamber  $D_d = D_{air} = (Q/m)(W/e)$ . The above equation is approximately valid even in the case of electronic disequilibrium, if the cavity is small enough such that the change in the electron fluence is minimal and the correct electron energy spectrum is used in determining the average collision stopping powers.  $Q$  is the ionization produced in the air in coulombs,  $m$  is the air cavity mass in kg and  $w/e$  is the average energy required per unit charge of ionization. In this case  $D_{air}$  is in *joules/kg* or grays (Gy).

According to the adaptation of the IAEA International Code of Practice (IAEA Technical Reports Series No 277, 1987) the dose to water  $D_w$  at the effective point of measurement  $P_{eff}$  is determined as follows:

$$D_w(P_{eff}) = M_u N_D \left[ (\bar{S}/\rho)_{w,air} \right]_u P_u P_{cel}, \quad (5-2)$$

where  $M_u$  is the meter reading corrected for deviation from standard conditions of temperature, pressure, humidity, ionic recombination and polarity effect.  $N_D$  is the absorbed dose to air factor (per meter reading—traceable to a National Primary Standard Laboratory).  $\left[ (\bar{S}/\rho)_{w,air} \right]_u$  is the ratio of average mass stopping powers in water and air, and  $P_u P_{cel}$  is the product of the perturbation correction factor and the correction for the central electrode.

Using the above relationship, the ratio of absorbed doses for two different field sizes at  $d_{max}$  in the medium can be determined from the ion chamber readings at the same point and under the same conditions by the following formula:

$$\frac{D_w(n)}{D_w(c)} = \frac{M_u(n)}{M_u(c)} \times \frac{[(\bar{S}/\rho)_{w,air}]_n}{[(\bar{S}/\rho)_{w,air}]_c}, \quad (5-3)$$

where  $D_w(n)$  and  $D_w(c)$  are doses at  $d_{max}$  for a narrow beam and the calibration (broad) beam, respectively. The dose of the narrow beam,  $D_w(n)$ , is slightly overestimated by an ionization chamber because, as was shown in Figure 3.14, the  $[(\bar{S}/\rho)_{w,air}]_n$  averaged over the electron energy spectrum of a narrow beam is slightly less than the  $[(\bar{S}/\rho)_{w,air}]_c$  averaged over the spectrum of the calibration beam.

Using the Monte Carlo calculated mean electron energy spectrum for our 6 MV photon beam (see section 5.2.1), the ratio of the stopping powers water/air of the narrow beam (0.5 cm diameter) to that of the calibration beam was found to be 99.63 % at 8 cm deep. This is almost the same as the spectrum presented by Wu et al (1993). These authors using the published photon energy spectra for 6, 10, and 15 MV beams by Mohan et al (1985), have shown that the mean stopping power ratios water/air for a narrow beam at depth 8 cm in water would decrease to 99.7, 99.1, and 99.0 % of the corresponding values of a broad beam for these energies, respectively. The error is larger for higher energies because of the increased degree of lateral electronic disequilibrium. The error in ionization chamber reading of the dose at 8 cm deep is about 1 % for 15 MV x-rays. Also, referring to Figure 5.1(b) and also Figure 3.14, this error will be more significant in depth because of the decrease in stopping power ratio water/air with increasing depth. This decrease in stopping power ratio has two reasons. Firstly, because of beam hardening with depth and secondly, because of multiple scattering of low energy photons and the fact that these low energy beams predominantly scattered out of the central axis of small fields (Andreo and Brahme, 1986).

In cases of other detectors the absorbed dose in the medium (water) is calculated from equation (5-1). Similarly, the equation is approximately valid in the case of electronic disequilibrium, if electron fluence is not perturbed too much by the detector and the correct electron energy spectrum is used in determining the average collision stopping powers in equation (5-1). The ratio of absorbed dose in water for two different field

sizes and under the same conditions is calculated from the detector responses at those conditions by the following formula:

$$\frac{D_w(n)}{D_w(c)} = \frac{D_d(n)}{D_d(c)} \times \frac{\left[ (\bar{S}/\rho)_{w,d} \right]_n}{\left[ (\bar{S}/\rho)_{w,d} \right]_c} \quad (5-4)$$

Therefore, using this formula and refer to Figure 3.14 it is concluded that the dose in the case of narrow beam,  $D_w(n)$ , is also slightly overestimated by the diode detector and needs to be corrected by  $\left[ (\bar{S}/\rho)_{w,d} \right]_{n,c}$  using the correct energy spectrum. The diode overestimation is similar to that of the ionization chamber, due to the similar gradients in stopping power ratios of silicon and air to that of water. This is in addition to the diode detector dose rate dependence and diode density effect especially in the penumbral region which both will be discussed in the next section. On the other hand, again referring to Figure 3.14, it is seen that the collision stopping power ratio water/carbon is constant with  $E$ . Therefore the diamond detector response is independent of energy for a wide range of energy and does not need any correction in this respect. This is referred to the diamond detector tissue equivalence which is discussed more in the following sections. However, the diamond detector dose rate dependence still exists and has to be corrected using method discussed in chapter 3.

### 5.3. Small field dosimetry parameters and techniques

As it was mentioned above, the lateral electronic disequilibrium and steep dose gradients are characteristics of small *SRS* fields. Obviously ionization chambers, because of their large sensitive volumes compared to the very small beam diameters used in radiosurgery, are not suitable. Film dosimetry could be the preferred technique in dosimetry of these fields, but there exists film energy dependence and also variations in the film coating and film processing conditions which make it more difficult and sometimes unreliable.

Using radiochromic films in *SRS* can overcome some of the problems associated with conventional radiographic films. Better tissue equivalence, higher spatial resolution,

and non sensitivity to room light are the biggest advantages of radiochromic films (McLaughlin et al 1994). The main disadvantage of these films is nonlinearity of the response for doses in clinical range (Ramani et al and McLaughlin et al, 1994). To achieve acceptable precision ( $\pm 2\%$ ,  $1\sigma$ ), much higher doses are necessary (more than 100 Gy for conventional GafChromic™ *DM-1260* film and over 25 Gy for GafChromic™ *DM-55*), which in some cases is not desirable.

Silicon diodes, because of their small size of the sensitive volume (60  $\mu\text{m}$  thickness and 2.5 mm width), are the common choice in dosimetry of *SRS* beams (Rikner, 1983; Rice et al, 1987; Haworth and Perry 1993; Beddar et al, 1994). However diode detector energy, dose rate, and directional dependence of response are negative factors in this sort of application (Dawson et al, 1984; Beddar et al, 1994 and Wells et al, 1994). Also considered were two *PTW* Riga diamond detectors. Because of the near tissue equivalence of carbon, these could act as a suitable detector, although the dose rate dependence of diamond detectors (Fowler, 1966 and Hoban et al, 1994) could affect the result, if not corrected. In addition to the above methods, Monte Carlo (*EGS4*) techniques have been used to simulate *SRS* fields in calculating the dosimetry parameters. To examine the validity of the 6 MV photon energy spectrum used as input to Monte Carlo simulations and the *EGS4*-generated data and also to assess detectors performances in small field dosimetry in general, small field depth dose curves have been measured and calculated with these techniques and results compared. Detail of this comparison is discussed in the next section.

### 5.3.1. Depth doses

Depth dose curves have been measured in water using a Scanditronix *RFA-7* beam data acquisition system and a Farmer 2570 electrometer with (i) a Scanditronix *RK 83-05* ionization chamber, (ii) a *PTW* Riga diamond detector, and (iii) a Scanditronix p-type photon (shielded) silicon diode. Measurements were performed for 6 MV *x-rays*, *FSD*=100 cm and 10×10, 3×3 and 0.5×0.5 cm<sup>2</sup> fields. The diode and diamond measurements were performed with detector stems parallel to the beam central axis; the ionization chamber was in its normal position with the stem perpendicular to the central

axis. Also, *EGS4* depth doses for these fields have been calculated using the 6 MV photon energy spectrum obtained by comparison of an *RK* ionization chamber-measured depth dose for a  $10 \times 10 \text{ cm}^2$  field with the depth doses of the beams for which spectra have been calculated (Ahnesjo et al, 1992). Figure 5.3 shows comparisons of the results for above mentioned field sizes using above techniques. Depth dose for a  $10 \times 10 \text{ cm}^2$  field is shown in Figure 5.3a. As it can be seen from this figure there exists some over response with depth for the diamond detector, compared to the ionization chamber, which is referred to as the dose rate dependence of diamond detectors. In fact, this is an under-response of the diamond detector as dose rate increases, because of the reduction in recombination time with increasing dose rate (Hoban et al, 1994). Similarly, there is some under response with depth in the diode depth dose which is the result of diode supralinearity of response to higher dose rate in shallow depths (Rikner, 1983). The diamond and diode depth doses show the same magnitude of deviation from the *RK* ionization chamber depth dose, measured with the Farmer electrometer. This is in contrast with the fact that diode dose rate dependence has been shown to be twice as much as diamond (Hoban et al, 1994). The reason for this difference is that the diode under response with depth is partly compensated by the increased response due to scattered photons. Also, it can be seen from this figure that *EGS4* depth dose is in very good agreement with ionization chamber.

In Figure 5.3(b) is the same comparison for  $3 \times 3 \text{ cm}^2$  field using different techniques. The lateral electronic equilibrium still exists at this field size and thus the ionization chamber still gives a reliable result. It is especially important to notice that the Monte Carlo technique shows the same relative response as Figure 5.3(a) and agrees very well with ionization chamber. The achieved agreement between the Monte Carlo technique and ionization chamber will confirm the validity of the photon energy spectrum and *EGS4* simulation. This means that the Monte Carlo generated depth doses for small *SRS* fields, where lateral electronic equilibrium does not exist, can be used as reliable reference for dosimetry purposes. Figure 5.3(c) compares depth doses for a  $0.5 \times 0.5 \text{ cm}^2$  field and shows how unreliable the response of a big detector like an ionization chamber can be in measuring small fields. The main reason for this large ionization chamber deviation is that the beam does not cover the whole sensitive volume of the

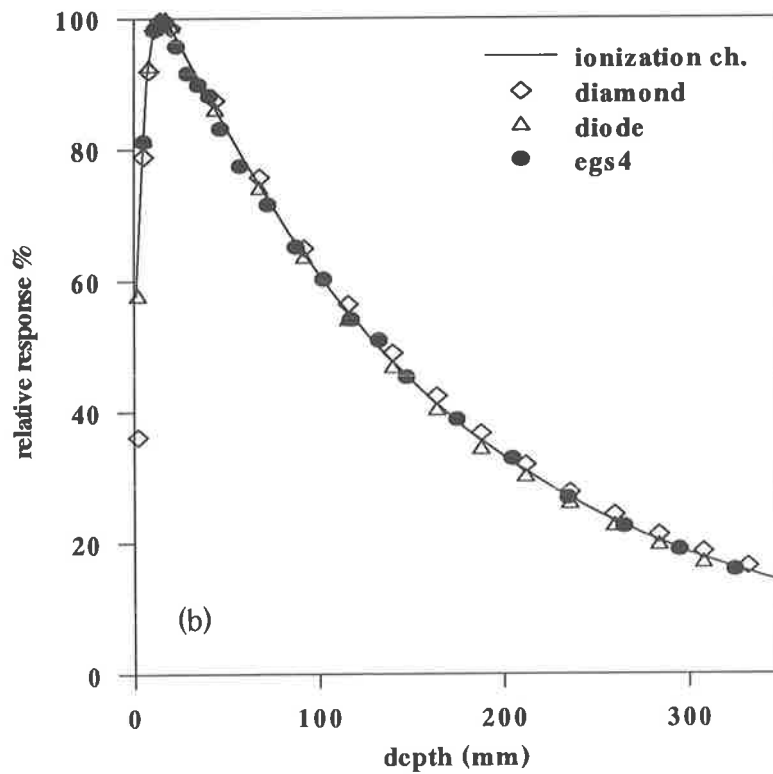
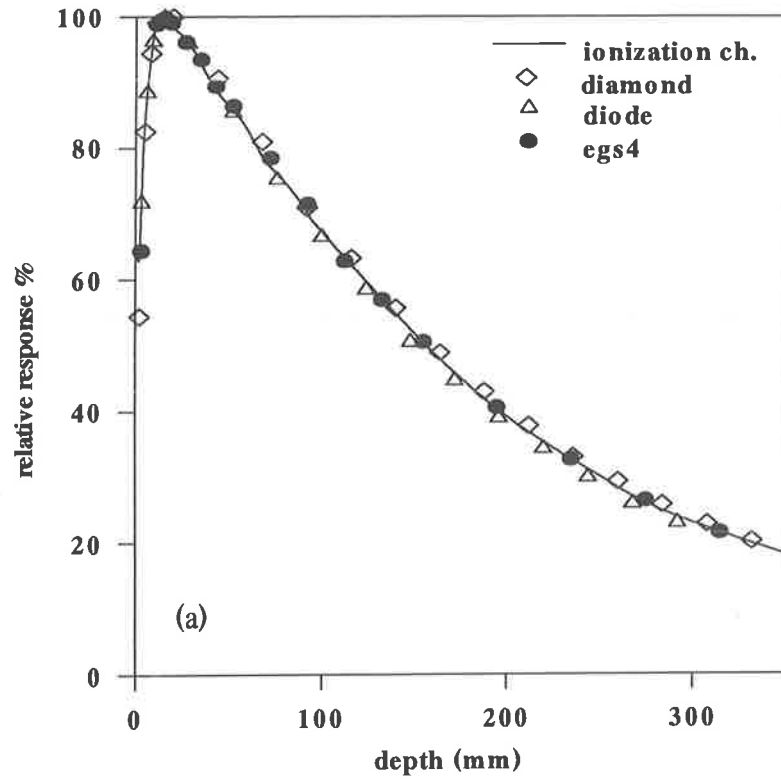


Figure 5.3. 6 MV photon beam percentage depth doses measured with ionization chamber, diamond and diode detectors and calculated using the MC (EGS4) for (a)  $10 \times 10 \text{ cm}^2$ , (b)  $3 \times 3 \text{ cm}^2$  and (c)  $0.5 \times 0.5 \text{ cm}^2$  field sizes at  $FSD=100 \text{ cm}$ .

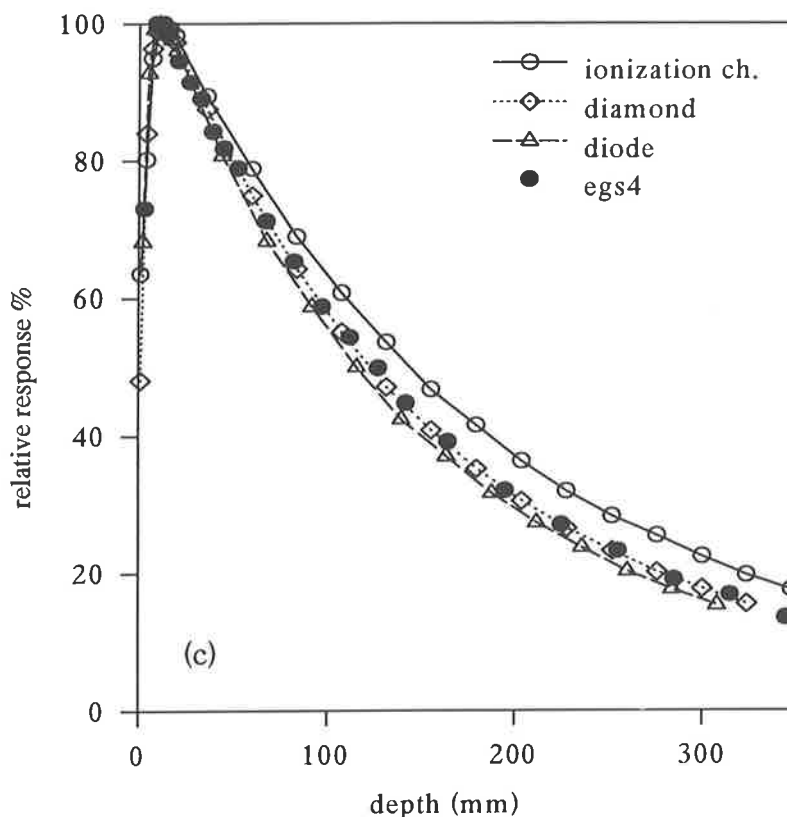


Figure 5.3. (Continued).

detector and a larger proportion of the chamber is irradiated at deeper points: the inverse square law will thus lose its effectiveness. It is important to notice that the relative position of the Monte Carlo depth dose compared to those of diamond and diode detectors is the same as for larger fields (where it agrees with ionization chamber) in Figures 5.3.(a) and 5.3.(b).

### 5.3.2. Tissue maximum ratios

Tissue maximum ratios for *SRS* collimators were measured in a water tank with diamond and diode detectors. Detectors were orientated parallel to the beam central axis and their sensitive point of measurement positioned at the isocentre, while the water level above detector was pumping out from 200 mm to 0 (*FSD* varied from 80 to 100 cm, respectively). The detector responses to the radiation have been recorded every 1 mm by means of the *RFA-7*'s *TMR* accessory (floating level detector). *TMR* measurements were also performed with X-Omat V Kodak film in *RMI* solid water slabs, while films were positioned at different depths at the isocentre with enough

backscatter material. The film exposure level was chosen in the linear range of the film characteristic curve and films were developed in an autoprocessor system (Protec *M45*). Film results have been analysed using a *PTW* film image processing system (*FIPS*) and Scanditronix RFA-3 film scanners. Also, *EGS4* calculation of *TMRs* for *SRS* collimators was performed in a single simulation using the reciprocity technique. Results are presented in Figure 5.4 for 7 and 23 mm collimators. As can be seen from this figure, *TMRs* measured with diamond and diode detectors reflect their dose rate dependence. Also, from this figure it is seen that film had a different response compared to other techniques. This could be due to the film energy dependence and also variations in the film coating and processing conditions.

### 5.3.3. Off axis factors

Off axis factors for *SRS* collimators have been measured at the isocentre at 6 cm deep in water with diamond and diode detectors and in the solid water with the film. Also, these profiles have been calculated using Monte Carlo (*EGS4*) simulations.

Diode measurements were performed with the detector stem parallel to the radiation beam. The shield at the base of the sensitive element would cause a skewed profile if the detector were used in the perpendicular orientation. Similar effect has been reported by Rikner (1983) as a practical problem associated with diode orientation when it is energy compensated (shielded). The diode profile measurement is affected by different factors. We divide these factors into two categories depending on their effect on the penumbra width: those factors which make the measured penumbra broaden and those which cause the measured penumbra to narrow.

Those factors contributing to the penumbral broadening are (i) the finite size of the detector, (ii) the detector directional dependence and (iii) the change in electron energy spectrum which occurs for small *SRS* fields (narrow beams). The penumbra broadening due to the finite size of the sensitive volume of detector (Dawson et al, 1984 and Beddar et al, 1994) at this orientation (2.5 mm wide) is the most important factor. In this case the penumbra broadens because the detector will average dose across its sensitive volume. The variation in detector directional response is another contributing factor (Wells et al, 1994). In profile measurements because the angular distribution of

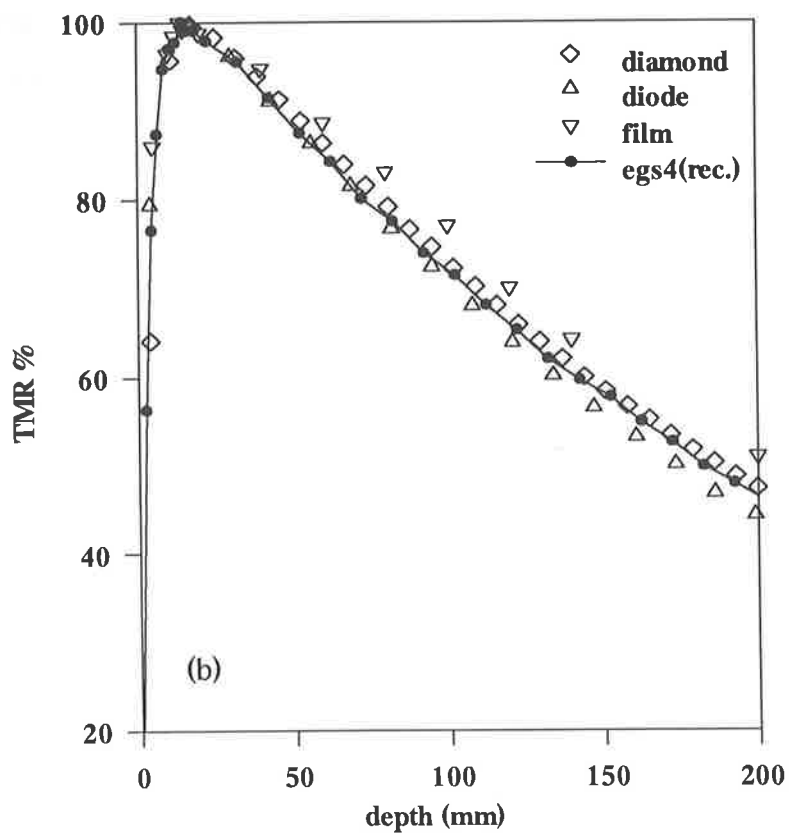
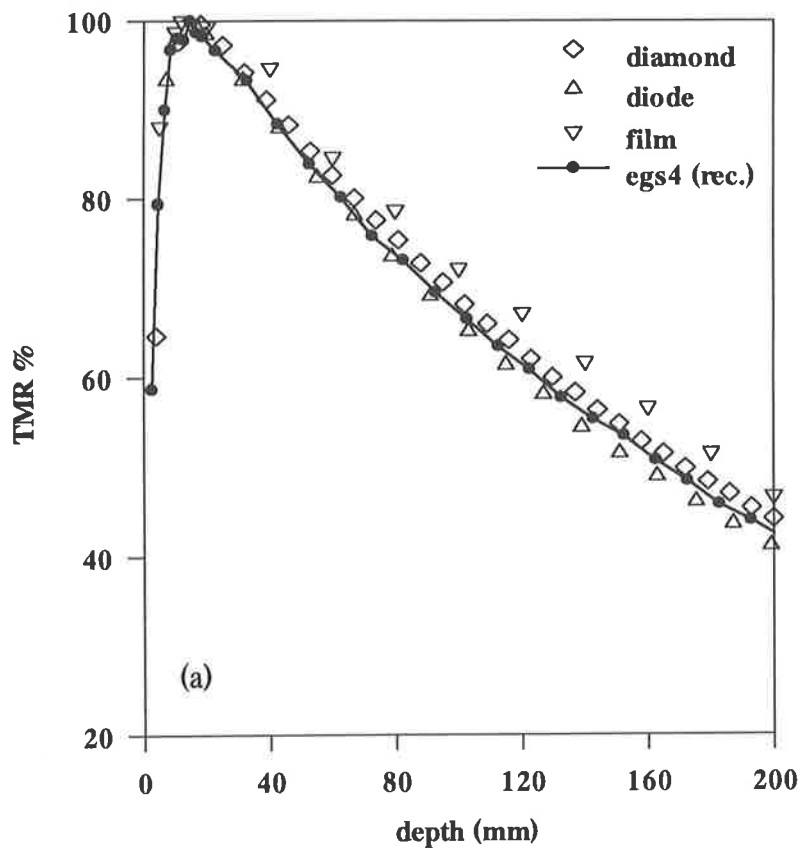


Figure 5.4. Tissue maximum ratios at the isocentre for (a) 7 mm and (b) 23 mm diameter SRS collimators, measured with diamond, diode and film and calculated using the MC (*EGS4-reciprocity*) technique.

scattered electrons varies across the beam, the directional response of the detector needs to be considered. The diode directional dependence has been reported to be 8% and 6% for angular orientations up to  $90^\circ$  and maximum 12% and 7% for  $105^\circ$  orientation for 6 and 15 MeV electron beams, respectively (Heydarian et al, 1993). The directional dependence of the diode for 18 MeV electrons has been reported to be about 5% for angular orientations up to  $90^\circ$  (Cygler et al, 1987). As a result of the diode directional dependence the detector response will drop too much toward the edge of the field, where angular distribution of electrons increases. The third factor which will contribute to the penumbra broadening comes from diode non-tissue equivalence and the fact that the electron energy spectrum will change for narrow beams (see section 5.2). In this case the average mass collision stopping power ratios for diode and the medium (water) varies across the profile with a larger response at the central axis. This will lead to the profile broadening for small SRS fields when it is measured with diode or ionization chamber.

Those factors which make the penumbra narrower are the dose rate dependence of diode detector and change in the electron transport in diode and the surrounding envelope. The diode detector dose rate dependence will cause an under response to lower dose rates. This, which is referred to the diode supralinearity of response, will force the profile to drop too much and as the result the penumbra width will decrease. Also, the silicon substrate is of a higher atomic number and density than water, the electron range in them is less than in water and so the lateral electron transport in penumbra region is reduced. This will lead to the sharpening the measured beam profile in a symmetrical fashion (Beddar et al, 1994).

The higher density of the silicon results in the detector acting more like a photon detector, since a larger proportion of the signal will be due to photons interacting in the silicon than is the case for a water-equivalent detector. Since the photon fluence profile is sharper than the dose profile, this will cause a narrowing of the measured penumbra compared to if the detector were water-equivalent. Other factors may override this effect however. The overall effect in measuring OAFs with diode at parallel orientation depends on the SRS field size and the penumbra definition. This will be discussed in details later in this chapter.

Profile measurement with a diamond detector was performed when the detector stem was perpendicular to the central axis of the beam. The diamond detector at this orientation gives a sharper penumbra due to the small thickness (0.25 mm) of the diamond chip. Diamond (carbon) is more tissue equivalent than silicon diode and so there is little change in electron transport. Meanwhile, the change of electron energy spectrum for the narrow beam will not affect the profile measurements with a diamond detector (see section 5.2). Also, the diamond detector has less directional dependence than a diode and so there is less penumbra broadening due to this phenomenon. The diamond detector directional dependence has been reported to be 6% and 3% for angular orientations up to  $90^\circ$  and maximum 8% and 4% for  $105^\circ$  orientation for 6 and 15 MeV electron beams, respectively (Heydarian et al, 1993). Film *OAF* measurements were performed at the isocentre at 6 cm deep with X-Omat V Kodak films in the solid water slabs. The film exposure level was chosen in the linear range of the film characteristic curve and films were developed in the autoprocesor system. The results were extracted using the RFA-3 and *FIPS* film scanners.

Monte Carlo (*EGS4*) calculation of profiles was performed using a finite source size, determined to be 1.8 mm by a pinhole camera method (Loewenthal et al, 1992). Figure 5.5 shows the comparison of the Monte Carlo and measured profiles for 7 and 23 mm *SRS* collimators. As is seen from this figure, *EGS4* and all measured profiles have almost the same width in terms of *FWHM* but different penumbra widths. Diode profiles have larger penumbra than those achieved with diamond and *EGS4*, due to the larger width of the sensitive volume. This is consistent for different *SRS* collimators, as is shown for 7 and 23 mm collimators in this figure. The profile parameters including *FWHM*, 80%-20% and 90%-10% penumbra widths are summarised in Table 5.1.

#### 5.3.4. Collimator output factors

Collimator output factor, or as sometimes referred to, total scatter correction factor, is the dose per monitor unit for that collimator (Holt et al, 1970). *OFs* for different *SRS* collimators were measured at  $d_{max}$  at the isocentre in water tank with diode and diamond detectors. *OFs* were determined by finding the ratio of the measured data  $R(r)$  for field

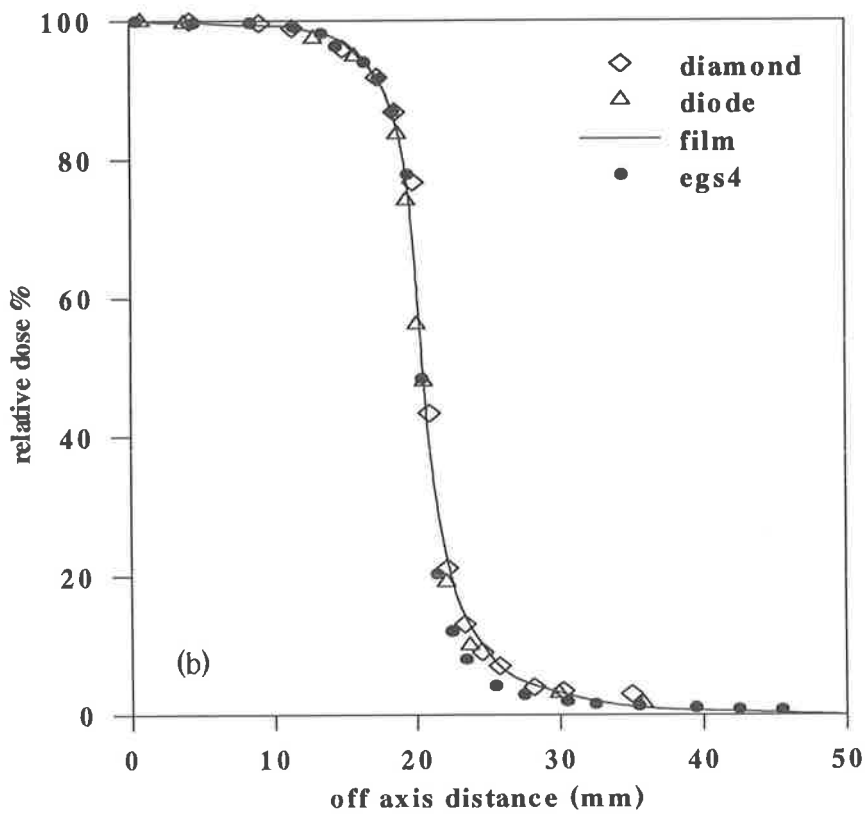
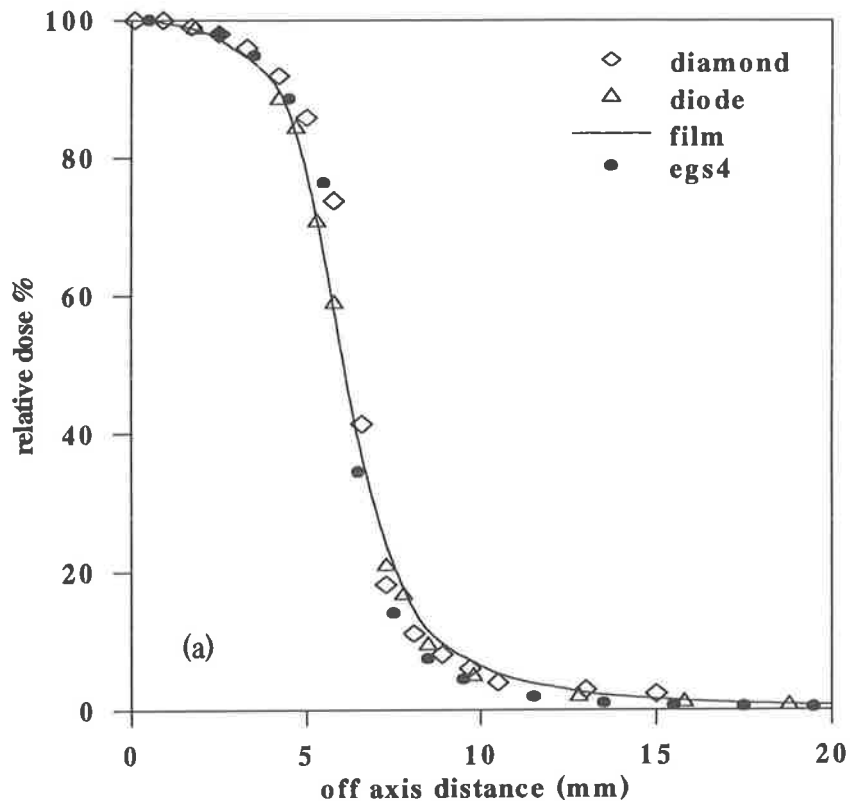


Figure 5.5. Off axis factors at the isocentre at 6 cm deep, measured with diamond, diode and film and calculated using the MC (EGS4), for (a) 7 mm and (b) 23 mm SRS collimators.

Table 5.1. *OAF* parameters for *SRS* fields, measured and calculated at the isocentre (*FAD*=100 *cm*) at 6 *cm* depth.

Collimator	7 mm collimator			23 mm collimator		
Detector	<i>FWHM</i> (mm)	Penumbra width (mm) (80-20%)	Penumbra width (mm) (90-10%)	<i>FWHM</i> (mm)	Penumbra width (mm) (80-20%)	Penumbra width (mm) (90-10%)
Diamond	12.5	1.85	4.10	41.3	2.7	6.23
Diode	12.3	2.45	4.27	40.9	3.5	5.86
Film	11.8	2.7	4.55	41.0	4.2	7.37
<i>EGS4</i>	12.35	2.01	2.84	41.0	2.23	5.15

sizes *r* to that of the calibration condition *R(c)* (10×10 *cm*<sup>2</sup> field at 100 *cm FSD*):

$$OF(r) = R(r) / R(c) \quad (5-6)$$

The collimator output factor, *OF*, can be separated to the collimator scatter factor, *CF*, and the phantom scatter factor, *PF*, by the following formula (Khan et al, 1980; Arcovito et al, 1985 and Haider and El-Khatib, 1994):

$$OF(r) = CF(r) \times PF(r) \quad (5-7)$$

*CF(r)* is the ratio of reading of the collimated beam to that of calibration condition, when measurement is performed in air with enough build up material to provide electronic equilibrium. *CF* represents the relative photon fluence output at each field size. *PF(r)* is the phantom scatter contribution at *d<sub>max</sub>* and represents the variation in scattered photon fluence with field size. The separation is important when blocked fields are used, since then the photon fluence depends on the beam jaw setting and photon scatter depends on the field size at the patient. We separated the *OF* here to use *MC*-generated *PF* values in the calculation of *OFs* for irregular field dosimetry (see also chapter 7).

*CFs* for different *SRS* collimators were measured using 1.7 *gr cm*<sup>-2</sup> thick brass build up cap with the *RK* ionization chamber, diamond and diode detectors at *FSD*=158 *cm*. This thickness of brass was enough to provide electronic equilibrium. The extended *FSD* was chosen so that the smallest *SRS* field could cover the whole build up cap.

Resulting *CFs* have been normalised to unity for the largest *SRS* collimator for relative comparison. As is seen from Figure 5.6, there is very good agreement between diamond and ionization chamber measurements.

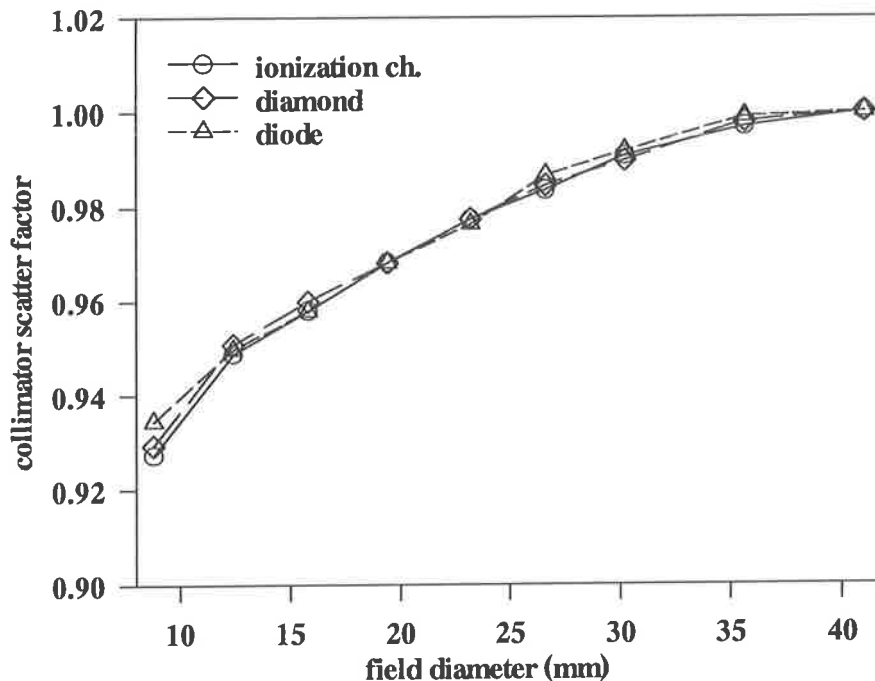


Figure 5.6. Collimator scatter factors (*CFs*) for different *SRS* collimators, measured with the *RK* ionization chamber, diamond and diode detectors using  $1.7 \text{ gr cm}^{-2}$  thick brass build up cap at  $FSD=158 \text{ cm}$ . Results are normalised to unity for the largest collimator.

The measured and calculated collimator output factors (*OFs*) are shown in Figure 5.7. The measured output factors are diode results in a water tank and calculated *OFs* are the result of Monte Carlo *PFs* multiplied by the corresponding measured diamond *CFs*. Again the result is normalised to unity for the largest collimator. Absolute values of *CFs* and *OFs* were established from their relative values and the corresponding measured values for the largest collimator at the isocentre, relative to the calibration conditions. The maximum deviation between measured and Monte Carlo generated *OFs* is about 2%. This deviation is reflected from the diode measured *OFs* (see the corresponding results in Figure 5.6).

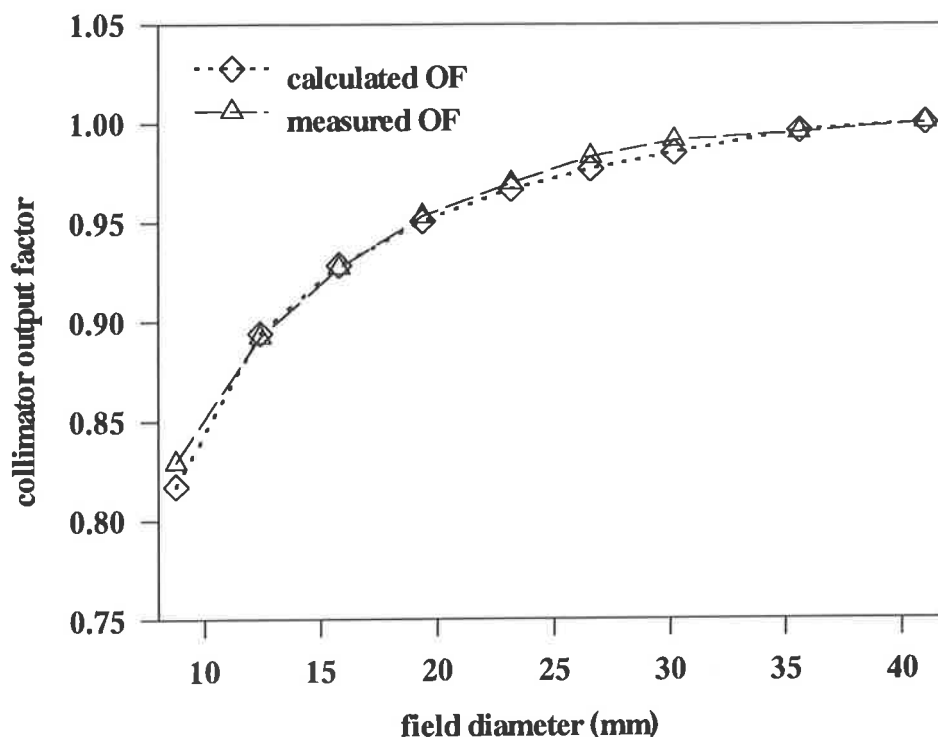


Figure 5.7. Measured and calculated collimator output factors (*OFs*) for different *SRS* collimators, normalised to unity for the largest collimator.

#### 5.4. Discussion

The findings of this study indicate that in the absence of lateral electronic equilibrium the detector response could cause errors in dose calculations. This will arise as the result of detector tissue non-equivalence, and will be worse as detector size increases. It was shown that, although the diode detector held perpendicular to the central axis has small thickness, it would under-estimate the penumbra width because of the reduced electron range in the diode and the housing. As a result, the actual volume within the 90% isodose would be over-estimated, if the diode in this orientation is used to measure *OAFs*. Additionally, skewness will appear when measuring profiles with a (photon) diode in this orientation. Here, the diode detector was held parallel to the central axis and did not show these problems. Moreover, the reduced penumbra width almost was cancelled out by the penumbra broadening due to the larger size of the diode in this orientation. Because of their large sensitive volumes, ionization chambers have the opposite effect and will under-estimate the actual treatment volume.

It was shown that Monte Carlo techniques can be used as reliable references for dosimetry of the *SRS* beams, especially where lateral electronic equilibrium does not exist. Diamond detectors have been shown by this group to have less directional and dose rate dependence than diodes (Heydarian et al, 1993 and Hoban et al, 1994). Using experimental results and the *MC* calculations of the energy spectra of the photon and resultant electrons, it was shown that diamond detectors, if corrected for dose rate dependence, produce better results than more commonly used diode and film dosimetry techniques.

## Chapter 6

# Advances in Stereotactic Radiosurgery/Radiotherapy Treatment Techniques

### 6.1. Review of the existing techniques

Stereotactic radiosurgery (*SRS*) is a precise technique for treating intracranial lesions. The most pronounced characteristics of this technique are geometric accuracy and steep dose gradient outside the target volume. For a spherical target volume the use of circular tertiary collimators is appropriate to conform the radiation dose to the shape of the target. However, target volumes encountered in radiosurgery often are not spherical and hence a significant volume of normal tissue will be included in the treatment volume, if the target is receiving a uniform dose. This is not radiobiologically acceptable, especially when the target volume is large or a critical structure is nearby.

Several treatment techniques, together with the appropriate software, have recently been developed to give more conformality of the dose to the shape of non spherical targets. This includes beam shaping techniques using circular collimators with customised gantry and couch rotations, using more than one collimator size for the target as well as using multileaf collimators and non coplanar irregular shaped fields, which conform the beam profile to the target cross-section in the “beam’s eye view”. Sophisticated conformal treatment planning and delivery systems, such as *Peacock* (Carol, 1996) and *Cyberknife* (Adler and Cox, 1996), have been introduced which significantly improve the conformality potential to the targets with very odd-shapes. Also, radiobiology of *SRS*, as a single fraction treatment technique, and dose response of benign lesions as well as malignancies are discussed. The rationale for stereotactic radiotherapy (*SRT*), as a fractionation technique, in treating lesions such as malignancies is discussed.

## 6.2. Dynamic stereotactic radiosurgery

The dynamic stereotactic radiosurgery (*DSRS*) technique was developed in 1986 at McGill University (Pike et al, 1987; Podgorsak et al, 1988 and Podgorsak, 1996). The characteristic of *DSRS* techniques is synchronised rotations of the linear accelerator gantry and treatment couch. As a result, there is a continuous beam path which enters the skull and converges at the target volume, as opposed to discrete arcs as in normal *SRS*. Figure 6.1 shows beam entry patterns on a patient's skull for various radiosurgical techniques, including multiple non coplanar arcs and *DSRS*. The beam entry trace on the skull in *DSRS* is a peculiar trace as is shown in this figure. A remote controlled motorised couch-rotation capability with a variable speed control and an angular position readout on the machine console are required for *DSRS*. The beam energy in the McGill *DSRS* system is 10 MV and the secondary collimators (jaws) are set to  $4 \times 4 \text{ cm}^2$ . The *SRS* (tertiary) collimators have cylindrical apertures with circular field diameters ranging from 0.5 cm to 3 cm (in 0.5 cm steps) at the isocentre (Podgorsak et al, 1988).

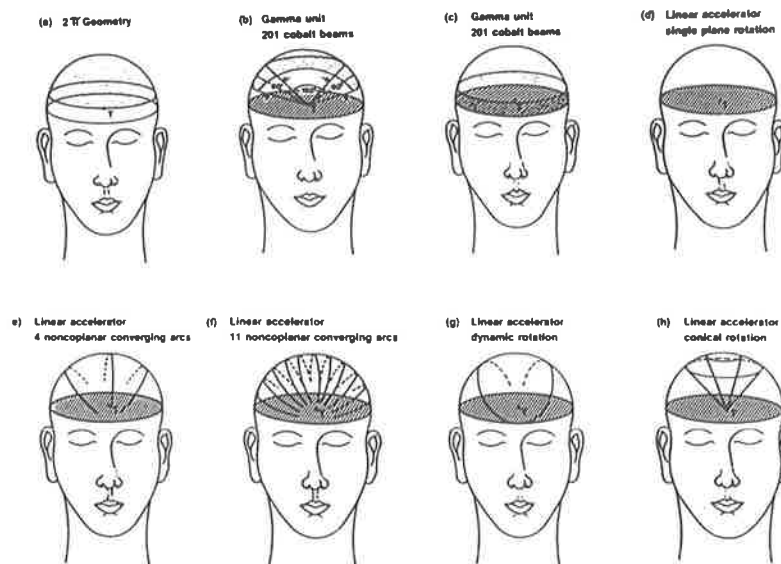


Figure 6.1. Beam entry patterns on a patient's skull for various radiosurgical techniques (From Schell et al, 1995).

In dynamic rotation all beam entry points are in the upper hemisphere of the skull. The gantry and couch angular ranges are  $300^\circ$  and  $150^\circ$ , from  $30^\circ$  to  $330^\circ$  and  $75^\circ$  to  $-75^\circ$  respectively, as is shown in Figure 6.2. As a result, there is no parallel-opposed beam to degrade the optimal steepness of the dose gradient outside the target volume. To

compare the dose profiles for different techniques, the dose distribution through a target volume and surrounding area were measured by the McGill group in a humanoid head phantom using *TLD* techniques. A 0.5 cm radius spheric target, which was assumed to be at the centre of the phantom, was irradiated with a 10 MV, 1 cm diameter circular field. Figure 6.3 shows the worst and best dose profiles obtained in a single plane and dynamic rotations. The worst and best cases are where the directions of profiles contain the entering beam and perpendicular to it, respectively. Dose profiles at any other direction through the centre of the target volume lie between the two extremes for the corresponding technique. This is shown for the dynamic rotation as the shaded area in this figure.

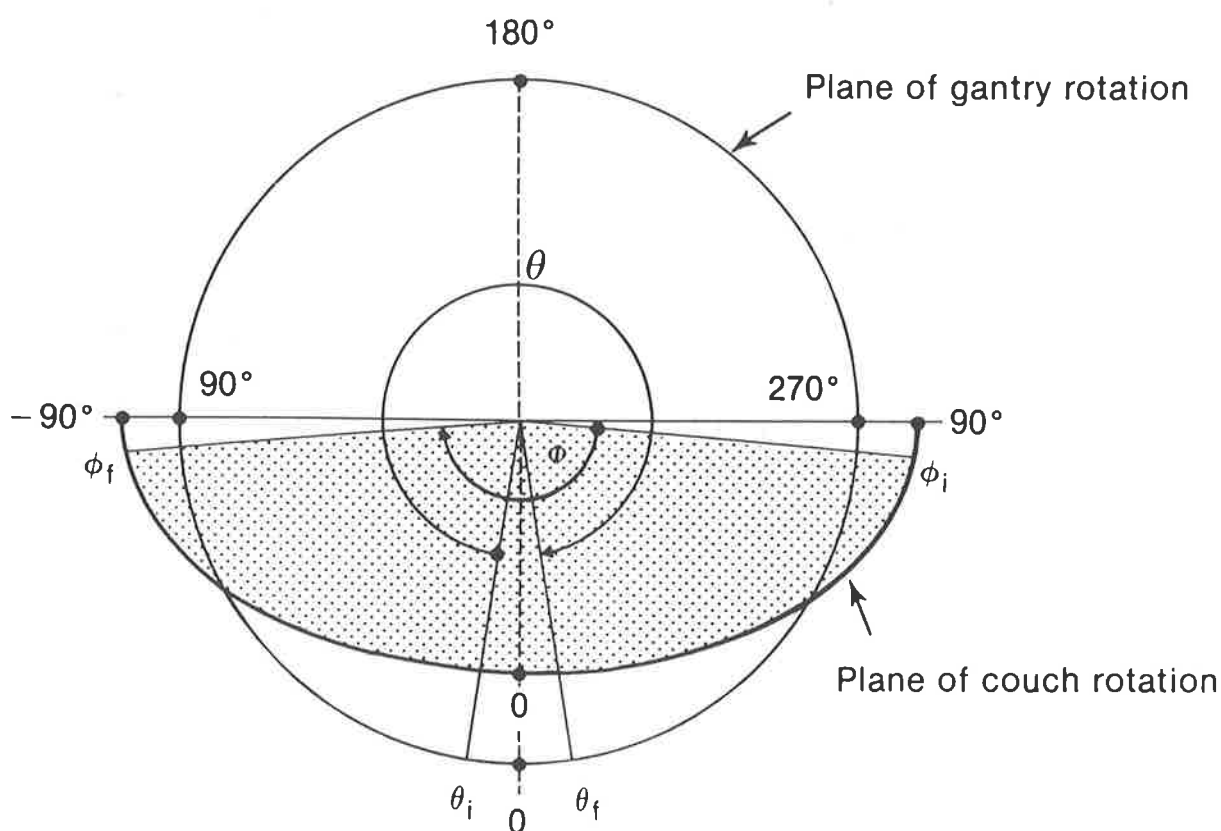


Figure 6.2. The gantry and couch motions for the single plane and dynamic rotation techniques. For the single plane technique the couch is stationary ( $\phi=0$ ) and the gantry rotates  $360^\circ$ . For the dynamic radiosurgery the gantry and couch angular ranges are  $300^\circ$  and  $150^\circ$ , from  $30^\circ$  to  $330^\circ$  and  $75^\circ$  to  $-75^\circ$ , respectively (From Podgorsak et al, 1988).

In Figure 6.4 the single plane rotation and the dynamic rotation dose profiles are compared for 1, 2, and 3 cm field diameters. The solid curves represent *TLD* measurements for the dynamic rotation in the head phantom in the direction of the in

coming beam. The dashed curves are calculated profiles in the rotation plane for the single plane rotation. As it is seen from this figure, the dose profiles in the single plane are much shallower than the dynamic rotation, because it is in the plane of rotation. However, the dose profile in a plane normal to the rotation plane is much sharper (see Figure 6.3). Consequently, the dose distribution outside the target volume is much more isotropic in the dynamic technique than in a single plane technique, as is expected, and is comparable with that of multiple noncoplanar arc technique.

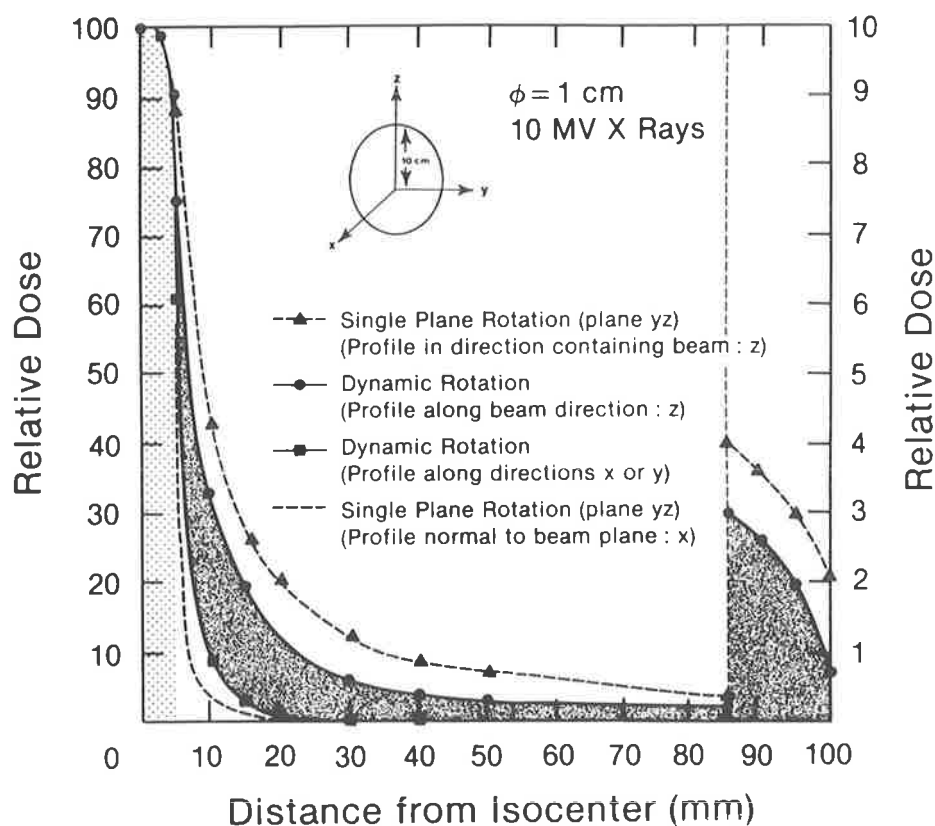


Figure 6.3. Measured dose profiles in several directions in a humanoid head phantom for single plane and dynamic rotations (From Podgorsak et al, 1988).

### 6.3. Conformal SRS

SRS is conventionally performed using circular collimators because of the high precision and stability of the collimation system as well as sharper penumbra. Use of circular collimators gives good conformation to the spherical targets. However, target volumes often are not spherical and treatment using circular collimators will frequently include normal tissue in the treatment volume. Because of the large single doses which are normally delivered to the macroscopic target volume, the potential radiation toxicity to the adjacent normal tissues and critical structures is high.

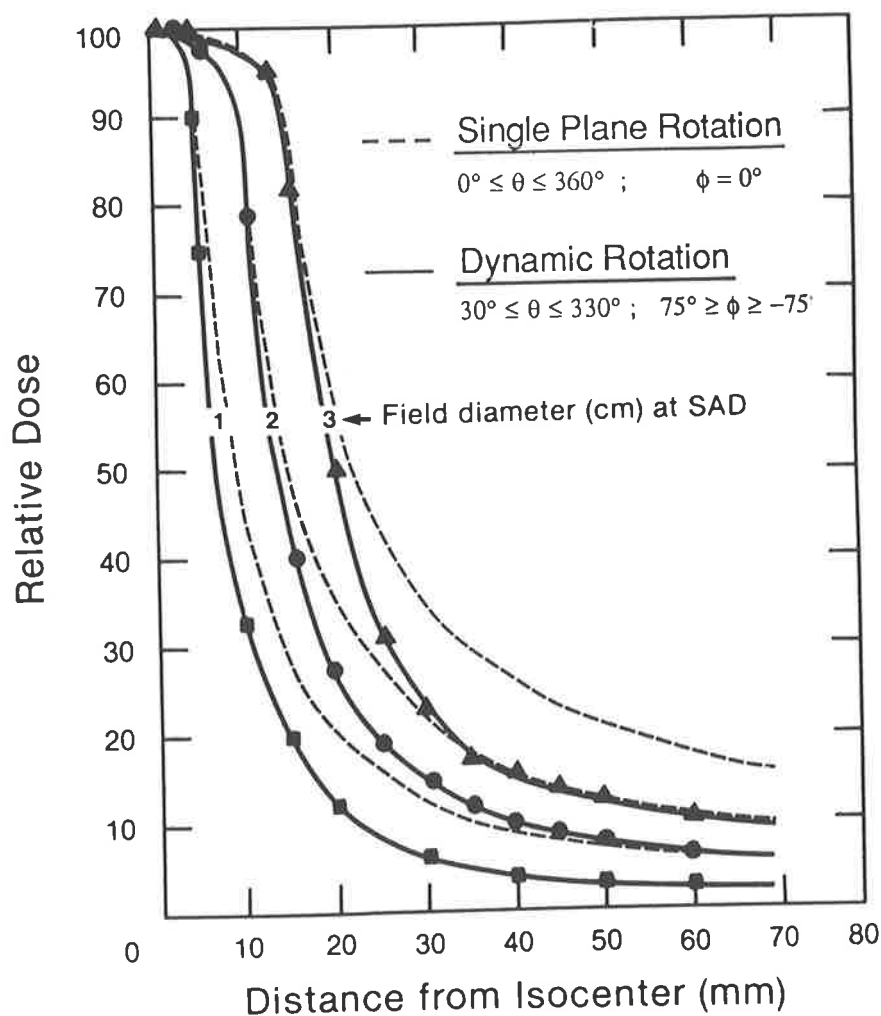


Figure 6.4. The single plane rotation and dynamic rotation dose profiles for 1, 2, and 3 cm field diameters. The solid curves represent TLD measurements in a head phantom in the direction of the incoming beam for the dynamic technique, while the dashed curves are the calculated profiles in the rotation plane of the single plane rotation (From Podgorsak et al, 1988).

The use of field shaping techniques is required to conform the beam to the target and reduce radiation toxicity. Using multiple isocentres in linear accelerator or Gamma-Knife units can be very effective in conforming the high dose to the target volume, especially for small non-spherical volumes. This will have some field shaping advantages and allows treatment of these lesions. The disadvantages of multiple isocentre techniques, however, are the wider penumbra of the combined field and nonuniformity of the dose distribution. Multiple isocentre treatment normally results in the generation of hot spots in the target volume. This is not considered to be a major problem when they occur within targets which do not contain functional brain (e.g., brain metastases and glioblastoma), whereas hot spots located in a target which contains

functioning brain tissue (e.g., low grade astrocytoma) are to be avoided. Moreover, due to the higher integral dose and the existing hot and cold spots, multiple isocentric treatment techniques cause more complications (Nedzi et al, 1993 and Ramani et al, 1995). This necessitates using better field shaping techniques for selected radiosurgical lesions with a maximum dimension greater than 3 cm (Kooy et al, 1996).

Conformal stereotactic radiosurgery (CSRS) refers to the techniques which conform the beam profile to the target cross-section in the "beam's eye view". CSRS would improve the dose delivery in approximately 40-70% of the SRS caseload (Schell et al, 1995). Using CSRS techniques it is possible to treat more extreme cases, such as large nonspherical targets in the vicinity of critical structures. Apart from a reduced integral dose, using CSRS techniques results in a reduction in the number of isocentres. In this way nonuniformity of dose distribution to the target volume is improved and also a lower dose outside the target is achieved. CSRS will permit an additional 25% reduction of normal tissue volume between the 80%-50% dose levels (Schell et al, 1995) and reduce treatment complications. The treatment time and also time required for patient set up (which is necessary for each isocentre) and for treatment planning, including determination of location of isocentres, field size and optimum arc geometry are reduced considerably using CSRS.

Several conformal therapy techniques have been proposed and considered, including: (i) single elliptical apertures; (ii) static field conformal SRS; (iii) set of two parallel independent jaws; (iv) set of rectangular independent jaws; and (v) set of four independent rotatable jaws. Using single elliptical apertures is suggested when it is necessary to encompass the maximum projection of the target volume throughout treatment. However, in many cases the projected cross-section of lesion changes even during a single arc, and therefore dynamic field shaping is necessary to have a good conformality.

Static irregular shaped field conformal SRS techniques has been shown to give a better dose uniformity across the target, especially if a large number of fields are used (Rhein et al, 1995 and Bourland and McCollough, 1993). The former group (from Heidelberg) uses 14 non coplanar irregular shaped fields, distributed in 5 separate planes (equivalent to the couch positions  $-15^\circ$ ,  $-52^\circ$ ,  $90^\circ$ ,  $52^\circ$ , and  $15^\circ$ ). Irregular shaped fields are

collimated with a micromultileaf collimator (*MMLC*). The high resolution of the leaves (1.5 mm width at the isocentre) makes it possible to form a curved beam outline and define arbitrary irregular fields of just a few mm in diameter. By comparison with the multiple isocentric technique, this group has shown that the maximum dose could be reduced from 160% (median) to 100% using this technique, in all 46 patients treated by them. Also, the dose concentration and the dose gradient outside the target volume is comparable to the 9 convergent non coplanar arcs.

In the four independent rotatable jaws (four vane collimator system), each jaw has an independent computer controlled translational motion (in-out) and circular rotation (around the target to isocentre axis). In this way part of the standard circular field, projected by the cylindrical collimator, is blocked by these jaws to trim and shape the beam more closely to the target (Leavill et al, 1991). Figure 6.5 shows the longitudinal and transverse cross sections of the collimating system in the four independent rotatable jaw system. Although this technique is suitable for many irregular shape tumours, it is unable to match the concave cross sections of some targets such as peanut shapes. In this case multi-vane collimators with a narrow vane projection (1.5-2 mm) will improve the conformality.

A recently-developed 3-D conformal treatment planning and delivery system (*PEACOCK*), uses beam intensity modulation with gantry rotation, through a dynamic ML collimator (Carol et al, 1996 and Mohan, 1996). This technique may allow radiosurgery to be applied to a wider range of targets in a greater number of locations than currently possible. Also, in a proposed method called *TOMOTHERAPY*, a linear accelerator configured similarly to a *CT* scanner is used, where the waveguide/target are mounted on a ring perpendicular to the patient axis (Mackie et al, 1993). The dose distribution would be conformed to the target using temporally-modulated collimators as the beam spirals along the axis of the patient. Before treatment delivery the machine would obtain a 3-D *CT* image (using a diagnostic *x-ray* tube) and determine the required beam intensity profile at each gantry angle via an optimisation technique (Holmes and Mackie, 1994).

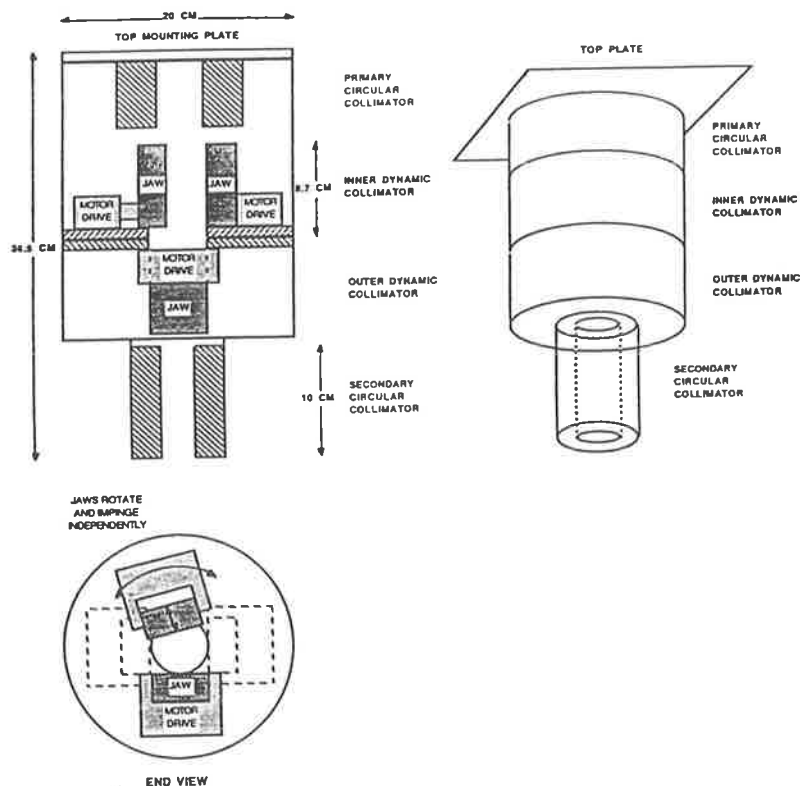


Figure 6.5. Longitudinal and transverse cross sections of the collimating system in the four independent rotatable jaw system (from Schell et al, 1995).

#### 6.4. Cyberknife: Image-guided SRS

In a novel treatment machine (*Neurotron 1000*) a mini-linac is mounted on a robotic arm and specially designed for frameless image-based radiosurgery (Cox et al, 1995 and Haneman et al, 1995). The machine provides 6 MV photon beams and an access to  $3\pi$  steradians about the head. The prototype system of this (see Figure 6.6) was installed at Stanford University Medical Centre in 1993. This system will be replaced by an improved model called *Cyberknife*.

One advantage of Cyberknife is that it does not require skeletal fixation. Instead, a real-time imaging system is used to direct the beam to any part of the target. The imaging system is shown in Figure 6.6(b) and includes two pairs of real-time diagnostic *x-ray* sources and digital *x-ray* cameras which are fixed at known positions in the treatment room. Assuming that the target position is fixed relative to the skull, the imaging system provides a stationary frame of reference for locating the skull and has a known relationship to the robot. Image correlation is used to determine the skull location with

respect to the *CT* coordinate system that is utilized in treatment planning. A specialised treatment planning system has been developed to take advantage of the Cyberknife radiation delivery. The target position is determined using the skull location in the camera coordinate system. In this system any movement of the patient can be detected by the imaging system and the target new coordinates are continuously recalculated and updated by looking at the treatment planned *CT* scan and sent to the robot.

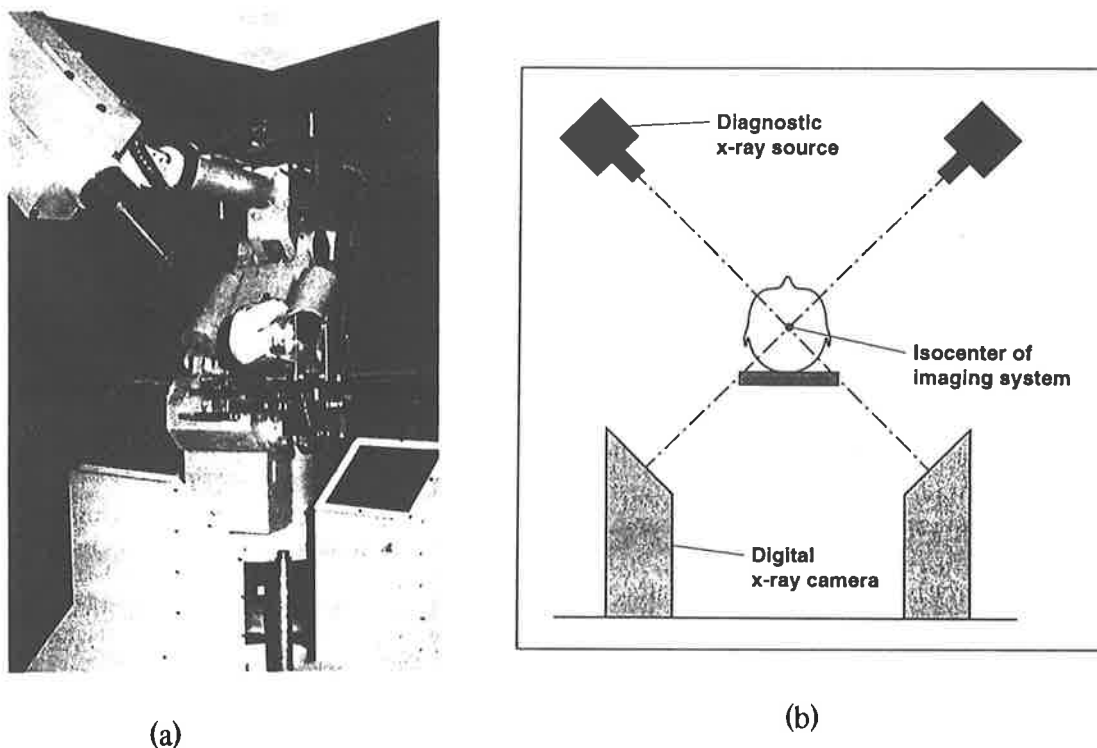


Figure 6.6. (a) A photograph of the “Neurotron 1000” system. The *LINAC*, robot, diagnostic *x-ray* cameras and the end of the couch are seen in this figure. (b) A schematic diagram of the imaging system (from Adler and Cox, 1996).

The *Cyberknife* uses a lightweight 6 *MV* linear accelerator which weighs just 135 *kg* (less than one-tenth of a conventional linear accelerator). The performance of the mini-linac is similar to conventional linear accelerators, despite its much lighter weight. A set of circular collimators are used to provide field diameters of 5 to 60 *mm* at 80 *cm* from the source. The dose rate of the system at this distance is 300 *cGy/min*. Also, the treatment time for a standard radiosurgical arcs takes less than 8 min. The system dose delivery precision is  $\pm 1\%$  (Adler and Cox, 1996).

The beam isocentre may travel within the treatment lesion and the *SAD* vary to change the field size. In this case some conformality is achieved by manipulating the beam,

rather than using complex collimation. The robot can rapidly direct the beam from some arbitrary points about the head to arbitrary points within the target, in delivering the prescribed dose. The pointing accuracy of the robot is better than 0.6 mm and the precision of localization is comparable to what can be achieved with stereotactic frame. Characteristic abilities of the system can be summarised as (Adler, 1995):

- (i) targeting precision comparable to SRS fixation frames.
- (ii) fractionated radiosurgery of larger tumours.
- (iii) improved dosimetry for complex irregular shaped tumours.
- (iv) radiosurgery of extracranial lesions including the spine.

### 6.5. Miniature *x-ray* radiosurgery

A miniature *x-ray* device has recently been developed, where 40 kV *x-rays* are produced at the tip of a 3 mm diameter, 10 cm long cylindrical probe. *X-rays* are generated by electrons accelerated along the probe, using a 9 V battery located in the control console. The output dose in this device is monitored using an internal scintillation detector whose output is proportional to the *x-ray* output, regardless of whether the probe is in air or any other medium. The output of the system has been shown to be stable within 2% at various current settings and within 2% of the response of a thin window parallel plate ionization chamber (Biggs et al, 1995). Dose rate varies almost inversely with the cube of the distance from the tip. The dose rate in water at 1 cm from the tip, for a 20  $\mu\text{A}$  current at 40 kV, was found to be 1.67 cGy/min. Also the equivalent energy of the beam in air and at 1 cm depth in water was found to be 10 keV and 20 keV, respectively. The background exposure of the system is minimal and therefore no special shielding is required (Cosgrove et al, 1995). The system behaves essentially as a point isotropic source, therefore it is suitable when only the minimum dose in the tumour is of consideration, as the dose at the probe tip will be many times higher than that at the tumour margin.

### 6.6. Body stereotactic radiosurgery

SRS techniques have been developed for treating intracranial lesions, because of the required high geometric accuracy. Also, the skull is a relatively easy part of the body to

immobilise and to attach a localizing frame. However, in past few years the extension of *SRS* techniques to other parts of the human body, including the spinal region has been investigated. Introducing advanced radiation delivery techniques such as *Cyberknife* (see section 6.4) and special stereotactic frames have played important roles in this innovation.

Hamilton et al (1995a) have developed a prototype device for linac-based *SRS* for spinal and paraspinal tumours. Eight patients with vertebral metastatic disease in different regions were already treated with spinal stereotactic radiosurgery. All patients in this trial had undergone standard surgical evaluation, where appropriate and had received standard regimes of external fractionated radiotherapy up to or close to the spinal cord tolerance. The tumours were treated generally with one isocentre and a median single fraction dose of 10 Gy. No unacceptable morbidity or radiosurgery-related complications have been noticed for this group, as the first clinical application of *SRS* in the spine. This demonstrates the technical feasibility of spinal radiosurgery (Hamilton et al, 1995a). Also, in a series of experiments, Hamilton et al (1995b) compared the localization ability for a segment of spine, using standard radiographic bony or implanted fiducial landmarks in the spine. This group has shown that fiducial markers will likely provide more than twice accuracy in localizing the spine, compared to the standard bony radiographic landmarks.

Also, a method for stereotactic high-dose radiotherapy of malignancies in the abdomen has been developed by Lax et al (1994). These authors used a specially designed stereotactic frame and fixation device for body *SRS*. This resulted in a reproducibility of liver and lung tumour positioning within 5-8 mm for 90% of the patient set-ups. In this technique eight non-coplanar individually shaped fields have been used for the treatments.

### **6.7. Radiobiology of radiosurgery**

*SRS* is a single fraction technique in which a high radiation dose is delivered to a small (less than 4 cm in diameter) intracranial lesion to treat the lesion. *SRS* has been used extensively, particularly for treatment of arteriovenous malformations (*AVMs*). In more recent years *SRS* has been adapted for the treatment of small primary malignancies or

metastases in the brain. This is despite the fact that different radiobiological principles apply to the treatment of *AVMs* and malignancies (Hall and Brenner, 1993).

*SRS* should cause sufficient cellular damage to the vasculature of *AVMs*, such that after months the nidus will disappear and the deformity is corrected. However, the use of *SRS*, as a single fraction technique, for treating malignancies is contrary to the radiobiological principles for optimising effect (Hall and Brenner, 1993).

### 6.7.1. Radiobiological principles

Two well-established radiobiological principles in radiation therapy are as follows. Malignant tumours, even with a limited size, usually contain a proportion of hypoxic cells which are relatively radioresistant. Therefore, the treatment schedule should allow for tumour reoxygenation. This is one advantage of fractionation. Second, there is a difference in the dose response characteristics of early-responding tissues and tumours to that of late responding tissues (Hall and Brenner, 1993). This difference is derived from the linear-quadratic relation, in which the surviving fraction,  $SF$ , of cells from an acute irradiation of dose,  $D$ , is calculated from:

$$SF = \exp(-\alpha \cdot D - \beta \cdot D^2) \quad (6-1)$$

This equation describes cell killing as a result of the interaction of two sublethally damaged sites (*DNA* double strand breaks). The linear and quadratic terms in this equation describe the damage produced by the same radiation track or by two different tracks, respectively (Brenner et al, 1991). The ratio  $\alpha/\beta$  is the dose at which the contribution to cell kill is equal for the linear and quadratic terms. For a fractionated course of  $n$  fractions, a dose per fraction  $d$  and assuming complete repair of sublethal damage between fractions, the  $SF$  is derived from:

$$SF = \exp[-n(\alpha \cdot d + \beta \cdot d^2)] \quad (6-2)$$

The  $\alpha/\beta$  ratio is approximately 3 for late-responding tissues such as *AVMs* and normal tissues, 5 for meningioma and acoustic neuroma and 10 for early-responding tissues such as metastasis and glioblastoma (Larson, 1996). Late-responding tissues are more sensitive to fractionation changes than early-responding tissues. That is the same dose

in many small fractions, instead of a single irradiation, gives a much higher cell survival for late responding tissue. For early responding tissue there is little difference. Consequently, a fractionated regime spares late-responding normal tissue, while not reducing, and or even increasing (due to reoxygenation) the killing of tumour cells (Hall and Brenner, 1993). The therapeutic ratio (effect of irradiation on tumour divided by that on normal tissue) can be quantified using the biologically effective dose (*BED*) as a method of assessment of different fractionation schemes. The negative exponent in equation (6-2),  $n(\alpha.d + \beta.d^2)$ , can be referred as the effectiveness of radiation cell killing (Lee et al, 1995)—from that *BED* can be defined so that:

$$BED(n) = \frac{n(\alpha.d + \beta.d^2)}{\alpha} = nd \left( 1 + \frac{d}{\alpha/\beta} \right) \quad (6-3)$$

From this equation,  $BED_{target}(n)$  which is related to local control and  $BED_{normal}(n)$  which is related to complications can be calculated (Larson, 1996). The therapeutic ratio is then achieved from  $TR(n) = BED_{target}(n) / BED_{normal}(n)$ .

The effect of fractionation is shown in Figure 6.7 for different kind of tissues. Figure 6.7(a) shows how total dose increases with number of fractions for nonproliferating targets, to give the same *BED* as a single radiosurgery dose of 20 Gy. These targets contain both target cells and normal cells. Noncompact *AVMs*, acoustic neuromas and infiltrating astrocytomas are examples of this kind. In *SRS* of these targets any complications are assumed to arise from damage to normal tissue within the target volume, since the dose to normal tissue is equal to that of the lesion. On the other hand, target volumes such as compact *AVMs* and most metastases contain little functional normal tissue. Any complications in these targets is due to the damage to normal tissue within a rim of tissue surrounding the target volume. For late responding tissue ( $\alpha/\beta=3$ ), the total dose increases because of sparing due to small dose per fraction. For early responding tissue ( $\alpha/\beta=10$ ), dose required to give the same *BED* increases less because a small dose per fraction does not produce much sparing.

Figure 6.7(b) shows the variation of  $BED_{normal}$ , related to the complication rate, with the number of fractions for cases where complications arise only from damage to normal tissues within the target volume. Figure 6.7(c) shows the same relationship, for cases where complications arise only from damage to normal tissue beyond the target

volume. From Figures 6.7(b) and (c) it is seen that for late responding tumours (low  $\alpha/\beta$  values), where no normal tissue resides in the target volume, *SRS* is preferred to a fractionated scheme. Also, it is seen that in fractionation treatment of early responding tumours (high  $\alpha/\beta$  values) normal tissues are spared. The rate of a reduced complication with fractionation is more for those targets which contain normal tissue. Also, fractionation is better for medium responding lesions ( $\alpha/\beta=5$ ) if they include normal tissue. The benefits of fractionation in sparing late responding normal tissue are somewhat lost when the volume of normal tissue irradiated is increased due to uncertainty in repositioning. Remembering that *BED* varies with dose per fraction (as well as the number of fractions) and the biological parameters (e.g.,  $\alpha$  and  $\beta$  values in the *LQ* model) related to the structure in question. Therefore, using a subscript is recommended to make such a distinction (Lee et al, 1995). For example in Figure 6.7,  $Gy_3$  is for *BED* based on  $\alpha/\beta$  of 3 *Gy*.

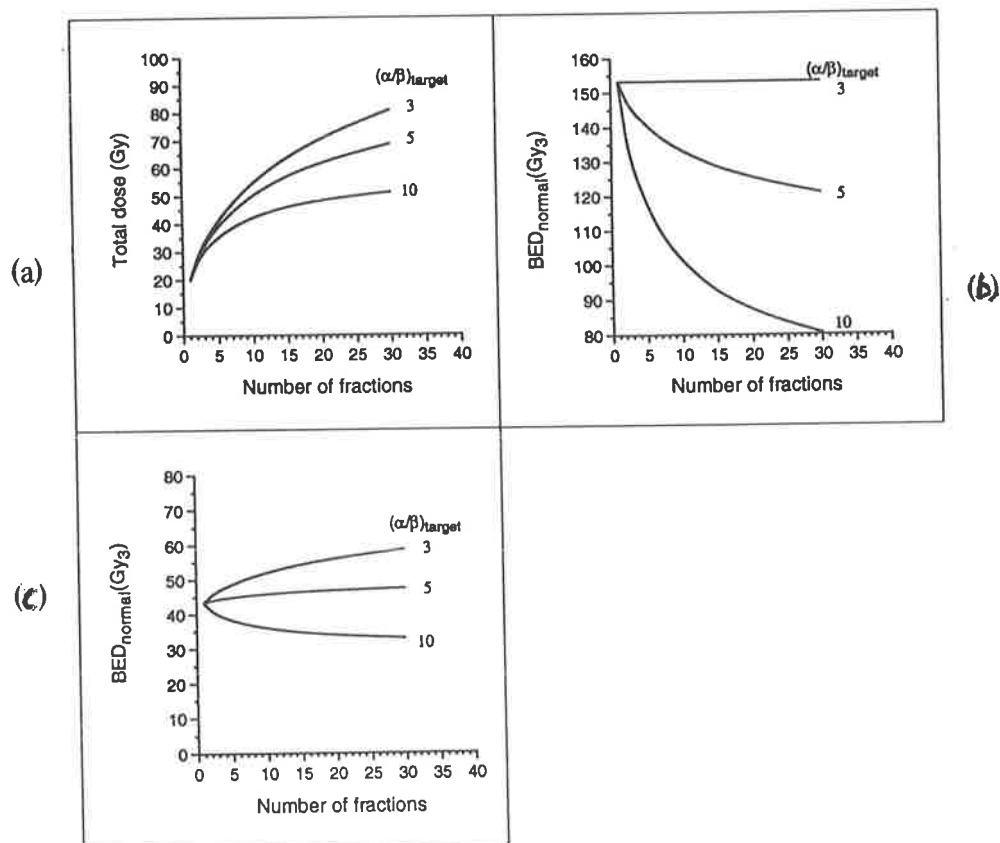


Figure 6.7. (a) The total dose as a function of number of fractions for a constant local control.  $BED_{\text{normal}}(n)$ , which is related to complications, as a function of number of fractions for different  $\alpha/\beta$  values and with the normal tissue effects confined to the target volume (b) and to a rim beyond the target volume (c) (from Larson, 1996).

In calculating the biologically effective dose the following equation has been used (Larson et al, 1993c):

$$\begin{aligned} BED &= RS_D \times [1 + RS_D / (\alpha/\beta)] \\ &= TF_D \times [1 + d / (\alpha/\beta)] - n \times 0.693 / \alpha, \end{aligned} \quad (6-4)$$

where  $RS_D$ ,  $d$ , and  $TF_D$  are radiosurgery dose, dose per fraction, and total fractionated dose respectively and  $n$  is number of cell doublings. In plotting this figure it was assumed that the last term of the above equation was negligible, otherwise the total fractionated dose, corresponding to a given radiosurgery dose, would be somewhat larger.

Radiosurgery, as a single fraction scheme, is limited to the target sizes smaller than a few *cm*, as mentioned earlier. This is due to the large volume of normal tissue receiving significant radiation dose and so a large integral dose. Despite the steep dose gradient of *SRS* fields, a significant dose is delivered to a thin rim of normal tissues just beyond the target periphery. The volume of this rim is proportional to the square of the target radius. Also, in radiosurgery of targets embedded in normal tissue (such as in case of malignancies), a significant additional dose is delivered to the normal tissue residing within the target volume. This volume is proportional to the cube of the target radius. Therefore, the volume of the normal tissue receiving a significant dose rapidly increases with the target size. This causes the “*volume effect*” which is a prohibiting factor for *SRS* of the larger lesions, so that for the larger tumours, the prescribed dose has to be reduced. The *NTCP* could be kept constant by decreasing the dose as the volume irradiated is increased (Fowler, 1993). Therefore, larger targets should be treated using fractionated techniques.

### 6.7.2. Dose response of *AVM* and benign lesions

*AVM* histology was briefly discussed in section 2.2. In treating *AVMs* an inflammatory reaction is intended in the vessel walls of the lesion, by irradiating the constituent epithelial cells (Hall and Brenner, 1993). This is a late response (low value of  $\alpha/\beta \leq 3$ ) which occurs weeks to months after the irradiation. The complete response rate following *SRS* for small *AVMs* is usually greater than 75% at 2 years, depending on *AVM* size, with permanent neurologic complication rate of about 5% (Larson et al,

1993c). *AVM* haemorrhage risk after *SRS* is the major risk. However, Pollock et al (1995) in a study on 314 *AVM* patients, before and after *SRS*, have shown that *SRS* did not significantly increase the annual risk of haemorrhage which existed before *SRS* (2.4%) and no gain was achieved before complete nidus obliteration. However, no haemorrhage has occurred after a confirmed obliteration. Normal tissues consist mostly of late-responding tissues (glial cells, for example), therefore, have almost the same radiobiological response as *AVMs*. Consequently, in treating *AVMs*, there is nothing to be gained by fractionation of the dose. Moreover, because the *AVM* nidus does not provide nourishment to the embedded adjacent tissues, it is probable that some glial cells within and near *AVM* are in a hypoxic condition which favours their radioresistivity. Therefore, there is a strong rationale for radiosurgery of *AVMs*.

Stereotactic radiosurgery is used in treating a variety of benign intracranial tumours, including pituitary adenoma, acoustic neuroma and meningioma. With the same principles as for *AVMs*, it is unlikely that a therapeutic gain would be achieved by fractionation in treatment of benign brain lesions, due to their late-responding characteristics. In fact where  $\alpha/\beta$  is small the opposite would be true and the cell kill will be reduced due to recovery. This is an example of a late-responding lesion surrounded by late-responding normal tissue, which considering the steep dose gradient of *SRS* fields, can receive much higher dose than the surrounding normal tissue and so could have a high therapeutic ratio. Acoustic neuromas account for 8 to 10% of primary intracranial tumours and a preservation of useful hearing can be accomplished in a significant proportion of the patients using *SRS* (Foote et al, 1995).

The total obliteration in *SRS* of small *AVMs* (< 5 cc) with a peripheral dose > 20 Gy, has been reported to be 40% in the first year (Friedman, 1995) and about 86% within two years after treatment (Friedman, 1995 and Hirai et al, 1995). There is much less success in treating larger *AVMs* (> 6 cc), especially where the peripheral dose is less than 18 Gy. In this case 81.8% of the *AVMs* became smaller but obliteration of the nidus was uncommon within two years following the treatment (Hirai et al, 1995). Schwartz et al (1995) have defined an obliteration prediction index (*OPI*) by dividing the peripheral dose (in Gy) by the lesion diameter (in cm) to estimate the treatment outcome. They have shown that all *AVMs* with a mean *OPI* of 10.6 were obliterated in two years, whereas those with a mean *OPI* of 7.6 did not disappear completely. *SRS*

treatments with an *OPI* between these two have certain success probabilities of obliteration.

### 6.7.3. Dose response of malignancies

Malignant tumours are early-responding tissues ( $\alpha/\beta = 10$ ) containing hypoxic cells, whereas the normal brain is a late-responding tissue ( $\alpha/\beta \leq 3$ ) which is composed entirely of well oxygenated cells. Therefore, fractionation increases the damage to the tumour because of the reoxygenation. At the same time fractionation reduces the damage to late-responding normal tissues because of the difference in shape of the survival curve and their greater sensitivity to changes in fractionation. This is especially pronounced for cases which the early-responding target is embedded within normal tissue. Low grade astrocytoma is an example of this kind of tumour. A big gain in therapeutic ratio is expected when *SRT* is used in this case.

There is another category, in which the early-responding tissue is surrounded by normal tissue and the target volume contains mainly malignant cells. Glioblastoma and metastases are examples of this kind of tumour. In this case *SRT* does not give such a large increase in therapeutic ratio (see Figure 6.7c). However, there are indications of an improved control rate with the combined fractionated radiotherapy with *SRS* (Larson et al, 1993c and Gannett et al, 1995).

Flickinger et al (1994) in a multi-institutional experience have shown that *SRS* is effective in treating solitary brain metastases with a low morbidity. In that work they have reviewed 116 patients with solitary brain metastases who underwent Gamma Knife *SRS* at five institutions. The primary tumour histology distribution for these patients is shown in Table 6.1. Minimum tumour doses were 8-30 Gy (mean 17.5 Gy). Median survival was 11 months after radiosurgery and 20 months after diagnosis. Follow up documented local tumour control in 99 patients (85%), tumour recurrence in 17 (15%) and one radiation necrosis (1%). Also, Loeffler et al (1995) in a report of 672 metastatic tumours in 381 patients who underwent *SRS* in the Joint Center in Boston, have stated that radiosurgery is an effective treatment for small intracranial metastases and provides local control rates equivalent to those of surgical series and is an attractive treatment option for patients with surgically inaccessible lesions, or with histology

resistant to the conventional radiotherapy. They used whole brain radiotherapy in adjunct to *SRS* for all the patients.

Table 6.1. Histology of solitary brain metastases (from Flickinger et al, 1994).

Primary histology	No.	(%)
Lung, non-small cell	41	(35)
Malignant melanoma	28	(24)
Renal cell carcinoma	14	(12)
Breast cancer	13	(11)
Unknown primary	7	(6)
Colorectal cancer	6	(5)
Other miscellaneous tumours	7	(6)
Total	116	(100)

### 6.8. Dose to the critical organs

The dose distribution in *SRS* spares normal tissues, compared to other radiotherapy techniques, for an acceptable dose distribution across the target volume. Normal tissues can be spared more using greater degree of arcing. Also, critical organs can be avoided by changing the arc geometry. In a typical *SRS* using a linear accelerator or Gamma units, the surface dose is generally less than 1% of the dose at the isocentre. The leakage dose to the eye lens is about 0.1%, but if the beam passes through the lens the dose increases to about 2.5% of the dose at the isocentre, which is still well below the cataract formation threshold (Podgorsak et al, 1990). Gamma Knife and linac-based *SRS* systems have very similar scatter and leakage dose. A summary of the total amount of scatter plus leakage dose to critical organs, using the measured data by Chiarego et al (1989) and Podgorsak et al (1990), is shown in Table 6.2. All values are almost insignificant.

### 6.9. *SRS* limitations

The steep dose gradients characteristic of *SRS* fields make the treatment of lesions close to the critical organs possible. The treatment is limited to a maximum lesion size of a

few *cm* (3-4 *cm*). This is based on the clinical evidence that radiosurgery complications are much more strongly associated with the target size than dose (Larson et al, 1993c). This is known as the “volume effect” and is related to the volume of normal tissue receiving significant radiation dose (see section 6.7.1 for more detail).

Table 6.2. *SRS* scatter and leakage dose to critical organs.

Position	Dose% (relative to isocentre)
Thyroid	0.17
Neck	0.14
Spinal cord	0.11
Eye lens	0.08
Eye surface	0.09
Gonades	0.02
Breast	0.06

The other limitation in *SRS* is the tolerance of the adjacent critical organs. Tishler et al (1993) have investigated the tolerance of cranial nerves of the cavernous sinus to radiosurgery. The study was performed for 62 patients treated for lesions within or near the cavernous sinus. They have shown that a single dose up to 40 *Gy* is a safe technique and *SRS* should be considered a viable alternative to the surgery or radiotherapy for cavernous sinus lesions, when the optic apparatus is located in a sufficient distance (>5 *mm*) from the target volume. They also recommend that the dose to the optic structures should be limited to less than 8 *Gy*, whenever possible.

Also, Nedzi et al (1991) have studied variables associated with the development of complications from radiosurgery of 64 intracranial tumours in 60 patients. They have shown that maximum dose and dose inhomogeneity within tumours treated with radiosurgery are important variables associated with complications. Also, they pointed out that 8/11 (72%) of the patients with tumour volumes >10 *cc* treated to maximum tumour dose >25 *Gy* developed complications. They concluded that *SRS* of intracranial tumours has a low risk of complications for lesions <10 *cc*, maximum tumour dose <25 *Gy* and a tumour dose inhomogeneity <10 *Gy*. The last two factors cause a significant dose to the normal tissue within the target volume.

The required dose homogeneity within the target necessitates a prescribed dose to the 90-95% isodose contour. This is more achievable with linear accelerators with a larger range of collimator sizes available, which is an advantage of linac-based *SRS* over Gamma Knife units.

#### **6.10. Stereotactic radiotherapy (*SRT*)**

It is now well established that *SRS*, as a single fraction technique, represents a suboptimal treatment technique in treating malignant tumours, compared with the fractionated techniques. Fractionation decreases the level of damage to normal tissue for a given tumour local control. This occurs for several reasons related to the radiobiological principles (Larson, 1996): First, the rate of repair of radiation damage in normal tissue (inter fraction repair of sublethal damage) is greater than for target cells. Second, reoxygenation of the hypoxic cells which exist in some lesions. Third, reassortment of cells into more sensitive phases of cell cycle. Moreover, a fractionated scheme is recommended for larger lesions or where a critical structure is nearby, since critical location and volume are two of the most important parameters associated with *SRS* complications (Loeffler et al, 1996). Using *SRT* has become practical in the last few years with development of relocatable head frames (Brenner and Hall, 1994a and Loeffler et al, 1995). *SRT* is a fractionated technique which combines geometric accuracy and dose distribution characteristics of *SRS* with the radiobiological advantages of fractionation.

There are different arguments related to the optimal number of fractions in *SRT*. Logically, referring to the previous discussion, any multifractionation scheme (with an appropriately chosen dose) would be expected to be superior to *SRS* in treating malignancies. This is because apart from sparing late-responding normal tissue, if a tumour contains hypoxic cells, it is most unlikely that it could be sterilised by a single dose irradiation (Brenner and Hall, 1994a).

When critical structures (such as optic nerve) are likely to receive a large dose, large fraction numbers are advisable in treating malignant tumours. However, when critical structures are not at risk an accelerated fractionation regime could be the treatment of choice to avoid tumour repopulation (Brenner and Hall, 1994a). Brenner and Hall

(1994b) suggested that an optimal stereotactic protocol for a large intracranial tumour reasonably could involve as many as 20 fractions in two weeks, although reports of 33 fractions for *SRT* of malignant tumours (Loeffler et al, 1995) might be a more conservative approach. It is important to mention that the majority of benefit occurs over 5 to 10 first fractions in treating tumours with  $\alpha/\beta = 5$  and in 2 to 5 first fractions in treating tumours with  $\alpha/\beta = 10$ . The complications become worse with fractionation for lesions with  $\alpha/\beta \leq 3$ , since a high total dose is necessary.

#### **6.10.1. Patient repositioning techniques**

*SRT* requires a precise relocatable technique with a minimal degradation of patient positioning accuracy as well as minimal personal time. Different relocatable techniques, including mask systems, relocatable frames, magnetic field sensor and computer controlled relocation (using radiographic markers embedded into the scalp) are commercially available (Gill et al, 1991; Schell et al, 1995 and Kooy et al, 1996). The accuracy and long term stability of mask system and relocatable frames for fractionated *SRT* have been confirmed (Engenhart et al, 1995 and Vanden berg et al, 1995) and shown to have a mean and maximum displacements of 0.4 and 0.7 mm, respectively (Gill et al, 1991). Also, a system consisting of a bite plate and a separate head support and restrain has shown a reproducibility of 0.5 mm with a standard deviation of 0.1 mm (Bova et al, 1995).

In another patient repositioning technique, three gold radiographic markers are embedded into the skull and during the first patient set-up radiographs locate the three markers in space. The set-up for other fraction sessions is performed by taking similar set of radiographs and using a computer program to determine the required movements to get to the original set-up (Schell et al, 1995). In another technique a special low-frequency magnetic field in the linac gantry and a field-sensor as an integral part of the stereotactic head ring are used to digitise the patient's spatial coordinates (Schell et al, 1995).

## 6.16. Discussion and conclusion

Stereotactic radiosurgery is a precise treatment technique with a steep dose gradient outside the target volume. This is a double sided characteristic with a very attractive outlook, in terms of quick dose fall off outside the target volume and hence sparing normal tissue. Meanwhile, this could be very dangerous due to the possible errors in dosimetry and spatial positioning (which in this case is more critical, due to the small field and a single fraction high dose), and dose calculation procedures. Because of various reasons, which have been explained throughout the thesis, the treatment volume could be easily over- or under-estimated — both result in a reduced therapeutic ratio and a poor treatment outcome. The current developments on conformal treatment planning and dose delivery systems together with their features have been discussed with the general idea of conforming the dose to the shape of the target. Also, advanced treatment techniques, such as *Tomotherapy* and *Cyberknife* have been introduced.

Using the radiobiological principles it was shown that *SRS*, as a single fraction technique, is appropriate for treating *AVMs* and most benign lesions. Also, it was shown that *SRS* is a sub-optimal technique for treating early-responding tissues and malignancies, whereas stereotactic radiotherapy (as a fractionation scheme) is highly recommended. Fractionation increases the damage to the tumour due to the reoxygenation and reduces the damage to late-responding normal tissues due to the difference in shape of the survival curve and their greater sensitivity to changes in fractionation. Different patient repositioning techniques were also discussed.

## Chapter 7

# ***SRS Treatment Planning and MC Dosimetry of Irregular Fields***

### **7.1. Introduction**

Treatment planning for stereotactic radiosurgery and stereotactic radiotherapy normally involves (i) importation of *CT*, *MRI* and angiographic images (*CT* at a minimum); (ii) registration of fiducial markers to transfer image coordinates to the frame of the stereotactic system; (iii) outlining of the skull, target and critical structures to form 3-D structures (iv) selection of beam diameter, couch angles and gantry arc limits for each treatment isocentre; (v) dose calculation and plan evaluation. The latter two stages are performed iteratively to ensure that the best treatment configuration is chosen, in terms of target volume coverage and avoidance of normal tissue (in particular critical structures such as the brain stem)(see Figure 7.15).

In *SRS*, as a high technology treatment technique, many assumptions have been made to speed the dose calculation process. Included in these assumptions are tissue homogeneity, assumptions related to the body contour, and an invariant dose profile for different depths. In this chapter the validity of these assumptions are investigated using measurements and Monte Carlo simulations, and the effect of any deviation will be quantified.

A method of calculating beam data using sector-integration of Monte Carlo-generated pencil beam kernels is presented, which can be used both for circular and irregular fields. Also, bioeffect planning as a new means for assessment of the treatment plans is introduced. Using this modality, the effect of dose and fractionation regime on the tumour and normal tissue can be shown by isoeffect lines, based on radiobiological models such as the linear quadratic model. In this way treatment plans are assessed according to the bioeffect distribution rather than a physical dose distribution. This is a useful tool for evaluating treatment plans and deciding between the rival plans.

## 7.2. The validity of SRS treatment planning assumptions

### 7.2.1. The effect of tissue heterogeneity on SRS dose calculation

Currently, dose calculation in stereotactic radiosurgery is performed with no inhomogeneity correction. While this assumption seems to be valid in treating most of the brain tumours, it may produce undesirable consequences when the approach is applied outside the brain in regions such as the sinus and nasopharynx (Solberg et al, 1995).

Lateral electronic disequilibrium, which can extend to the central axis for small SRS fields, increases drastically in presence of air cavities. Monte Carlo simulations were performed as part of this project to show the effect of air gaps on absorbed dose for these conditions. *TMRs* were calculated at the isocentre for semi-infinite layers of water-air-water. Air gap layers of 5, 10, and 20 mm thick were positioned at 26 mm deep, after  $d_{max}$  for our 6 MV photon beam spectrum. Remembering that the  $d_{max}$  for this configuration is more than the original value, due to the presence of air gaps and the lack of back scatter contribution. Calculated *TMRs* for above configuration are shown in Figure 7.1 for 7 and 23 mm SRS collimators, with 12.4 and 41.0 mm beam diameters at the isocentre, respectively. Also, the corresponding *TMRs* in water are shown for comparison.

As it is seen from this figure, compared to a homogenous medium, the *TMR* drops just before the air gap and after passing a minimum gradually builds-up again until reaches a maximum in a few mm after the air layer. This “secondary build-up” is due to the re-establishment of electronic equilibrium after the air gap. Depth dose afterward stays higher than the depth dose in the homogenous medium due to the reduced attenuation in the air layer. As is seen from this figure, the drop in depth dose depends on the field size and the thickness of air cavity. This drop depends on the degree of electronic disequilibrium and therefore is more for smaller field size and larger air cavity. Calculated *TMRs* for the above configurations showed that depth doses immediately beyond the cavity dropped by 45%, 65% and 75%, respectively for 7 mm collimator and 19%, 30% and 45% for 23 mm collimator, relative to the homogeneous medium. *TMRs* after the second build-up stay approximately 2.5%, 3.5% and 7% higher than those for the homogenous medium for the 7 mm collimator and 2%, 3.5% and 6% higher for

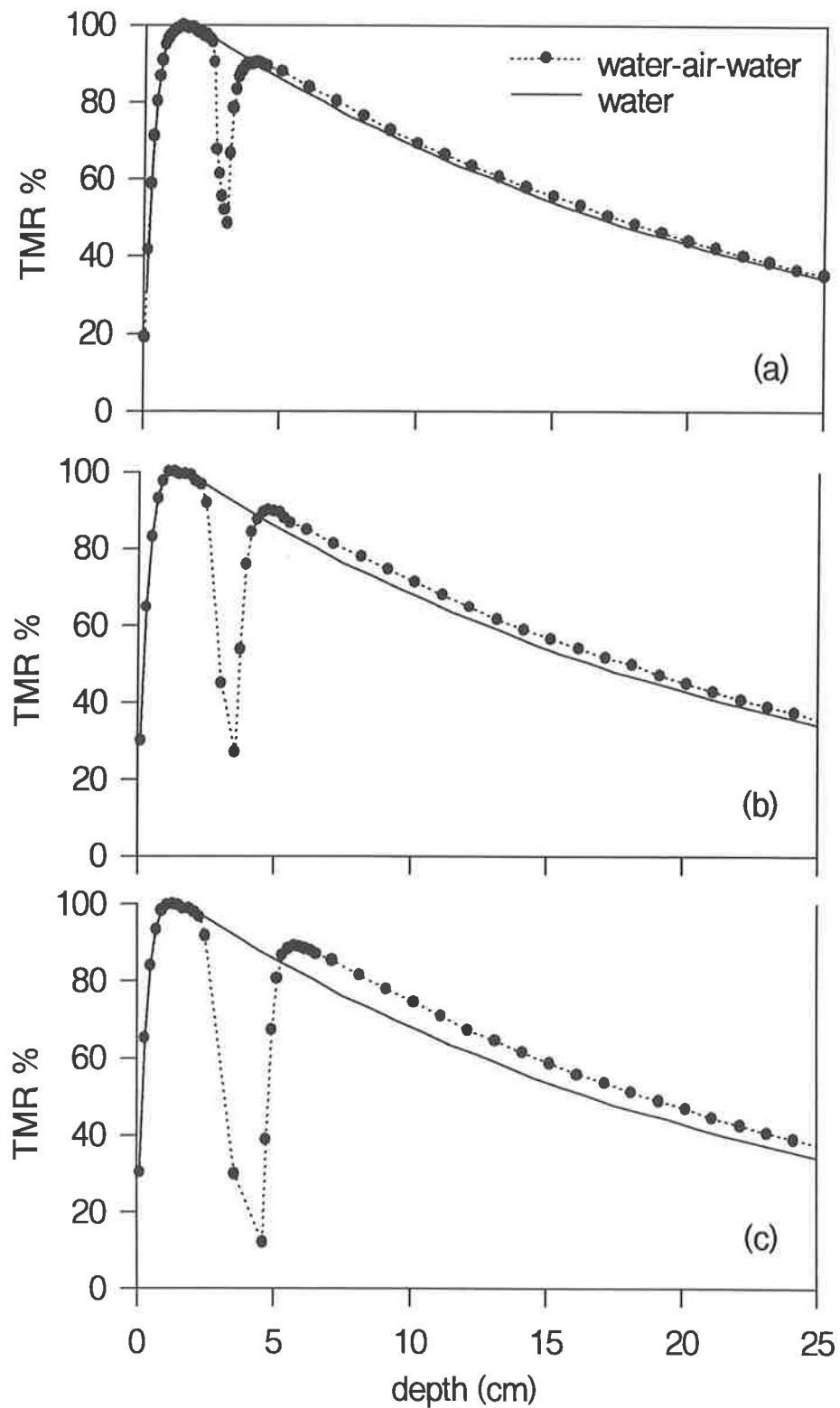


Figure 7.1. (a) to (c) Tissue maximum ratios in water and water-air-water for 7 mm SRS collimator, with 5, 10 and 20 mm thickness of air gaps, respectively. The air gaps were positioned after  $d_{max}$ , at 26 mm depth.

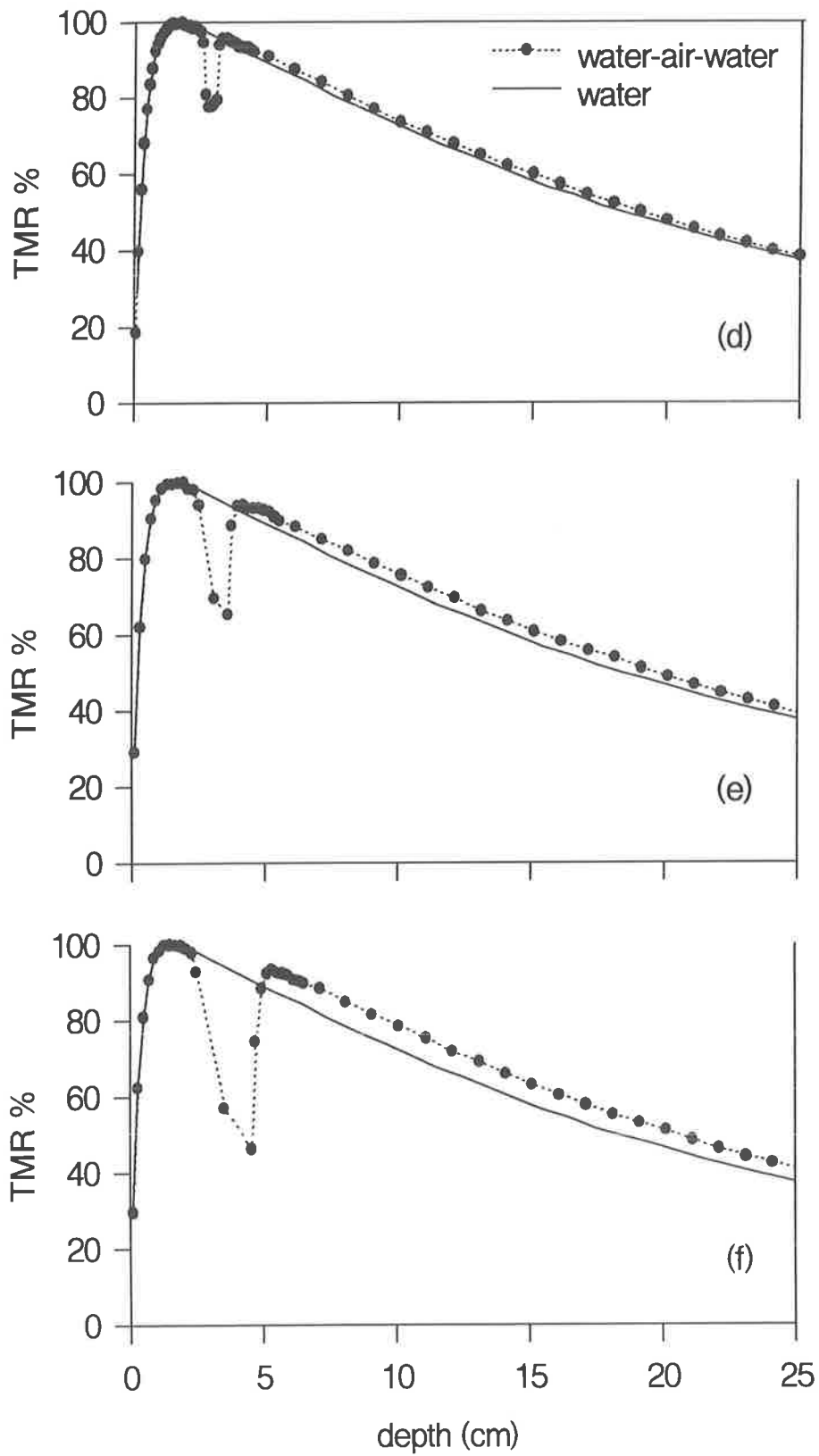


Figure 7.1. (d) to (f) Tissue maximum ratios in water and water-air-water for 23 mm SRS collimator, with 5, 10 and 20 mm thickness of air gaps, respectively. The air gaps were positioned after  $d_{max}$ , at 26 mm depth.

the 23 mm collimator, for 5, 10 and 20 mm thickness of air gaps, respectively.

Apart from changes in the central axis depth dose, the dose profiles also vary due to the increased lateral spread of secondary electrons. MC simulations were performed to calculate dose profiles at the isocentre at 6 cm depth in water, where a 5 mm air gap was positioned after 54 mm depth in water. The result is shown in Figures 7.2 and 7.3 for 7 and 23 mm SRS collimators, respectively. Note that the dose was scored in water just 1 mm after the air gap and in an electronic disequilibrium region, therefore dose is relatively less compared to the homogeneous medium, as is shown in Figure 7.2(a) for 7 mm collimator. The other reason for dose reduction in the central axis is that in presence of the air cavity electrons have more lateral spread, due to their increased range in air. This is clearly seen from Figures 7.2(b) and 7.3, where the relative percentages of the dose profiles are compared. The increased penumbral width due to the presence of the air gap is shown in Table 7.1. As a result, the dose spread beyond the cavity would be under-estimated if a homogeneous medium is assumed.

The presence of an air cavity will cause an under-dose to a target located just after the cavity and an over-dose to the normal tissue adjacent to the target volume. The deviation is greater for smaller fields and larger air cavities. Of course using multiple non-coplanar arc techniques, as in normal SRS/SRT, will reduce the importance of the effect. However, the effect will be significant when a few (irregular) static fields are used to conform the beam to the target shape in the “beam’s eye view”. This is of particular importance when a critical structure is adjacent to the air cavity.

### 7.2.2. Assumptions related to the body contour

In SRS dose calculation, a normal incidence of the beam on the body surface is assumed. This is a valid approximation due to the small field sizes encountered in this technique. Also in calculating the number of monitor units (MUs) per arc, the average depth of the beam entries is used to obtain a TMR value. This value is found from the TMR input files which are already measured at the isocentre for different depths. The resulting TMR value will be very close to the average TMR value, since the TMR curve has an almost linear falloff. Ideally, the average TMR for an infinite number of beams

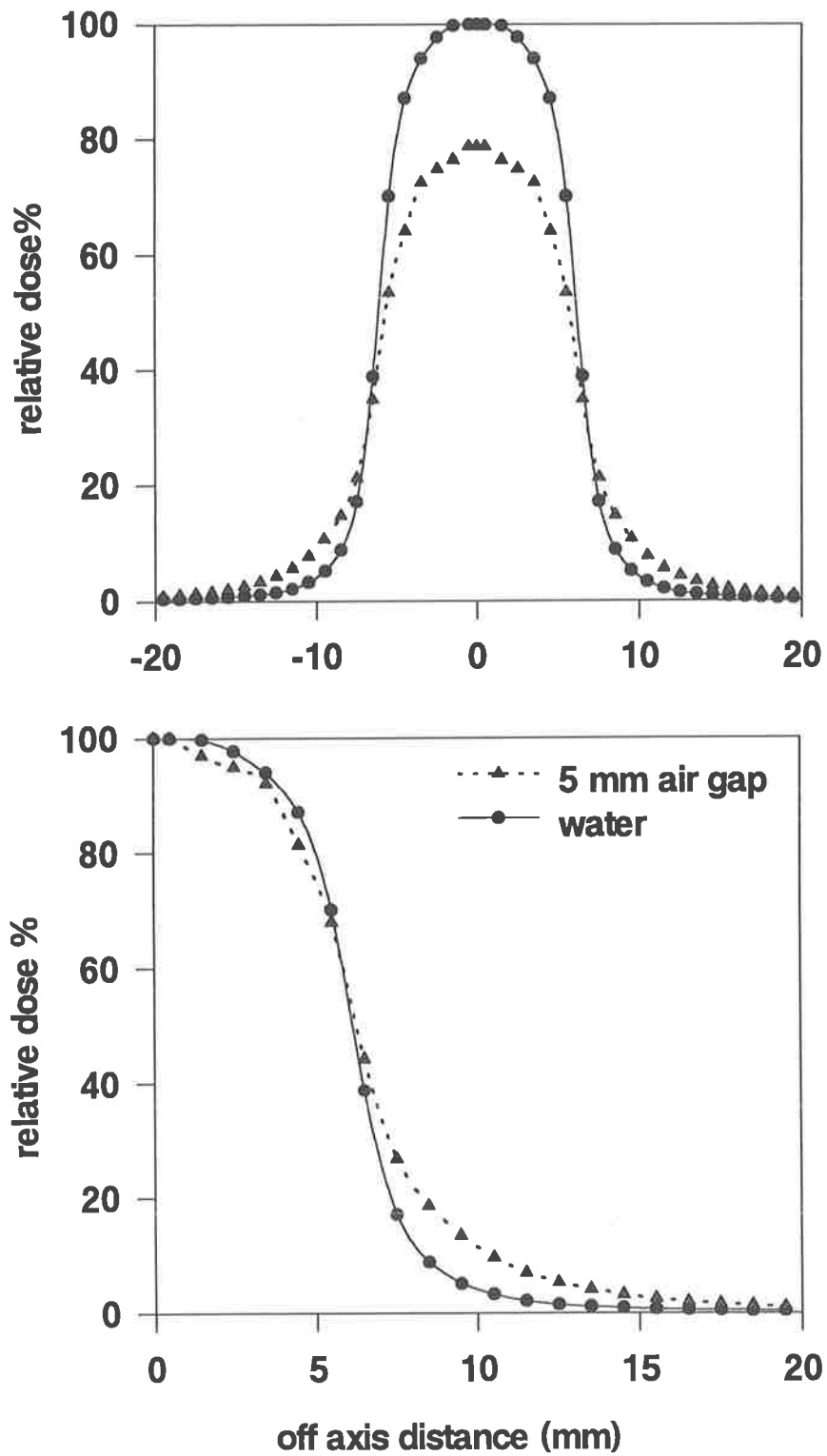


Figure 7.2. Comparison of dose profiles for the 7 mm collimator at the isocentre at 6 cm deep in water and when a 5 mm air gap is placed just 1 mm before the isocentre (a) as the relative dose and (b) when both normalised to 100% at the central axis. This was performed using the MC (EGS4) simulations.

Table 7.1. The increased 90%-50%, 90%-20% and 90%-10% penumbra widths at the isocentre for the 7 and 23 mm collimators, due to the presence of 5 mm air gap just 1 mm before the scoring region, calculated by the *Monte Carlo (EGS4)* technique.

SRS collimator	Increased penumbra width (mm) due to the presence of the air cavity		
	90%-50%	90%-20%	90%-10%
7 mm	0.5	1.4	2.5
23 mm	3.3	4.8	5.9

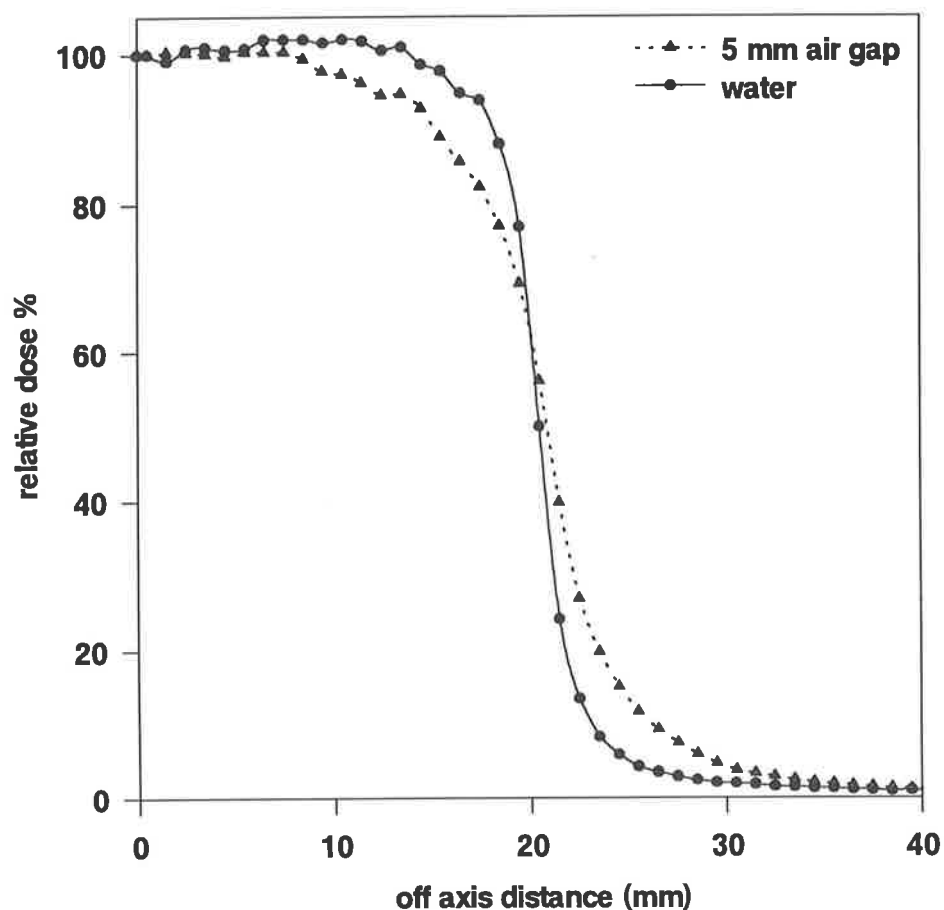


Figure 7.3. Comparison of dose profiles for the 23 mm collimator in water and when a 5 mm air gap is placed just 1 mm before the isocentre. Profiles normalised to 100% at the central axis. This was performed at the isocentre at 6 cm depth using *MC (EGS4)* simulations.

would be used. In the Leibinger (Fischer) treatment planning system, instead of using infinite beam entries (the reality) for each arc, a finite number (eight) of the beam entry points to the surface is assumed, to speed the dose calculation process. The validity of this assumption was investigated for three patients with different tumour locations by increasing the number of entry points by a factor of 4 (32 entry points). The maximum difference in the average *TMRs* was found to be 0.3%, which is insignificant.

### 7.2.3. Invariant dose profile with depth

As mentioned before, the Leibinger treatment planning system requires a beam profile measured at the isocentre in an average tumour depth which was assumed to be 6 *cm*. However, in a real clinical case the tumour depth could vary from a few *cm* to more than 15 *cm*. Strictly speaking, the dose fall off (profile shape and penumbra) is not the same for all depths. The penumbral shape is due to a geometric and a physical penumbra. The former is constant in this case but the latter increases with depth. This is a result of the increased proportion of dose due to scattered photons. To quantify the change in profile characteristics with depth, profiles for 7 and 23 *mm* *SRS* collimators were measured at the isocentre at 2, 6 and 15 *cm* depths in solid water, using Kodak X-Omat V films. The measured dose profiles for the above conditions are shown in Figures 7.4(a) and (b) for 7 and 23 *mm* collimators, respectively. Also the dose profiles were calculated using *MC* simulations with an 1.8 *mm* effective radiation source size (see chapter 5 for more information). The *MC* calculated dose profiles showed good agreement with the measured profiles.

Also, the measured 90%-50%, 90%-20% and 90%-10% penumbra widths are shown in Table 7.2. As seen from this table, the penumbra width increases with depth as well as field size, due to the increased scattered photon contribution in both cases. Consequently, in treating lesions at different depths, the volume within a high isodose surface will be under- or over-estimated if the lesion site is shallower or deeper than 6 *cm*, respectively. As with any source of error in the true penumbral shape, this may lead to incorrect choice of collimator size or prescription dose at the planning stage. If so, then the dose to the critical structures such as the brain stem will be different compared to what is seen in the plan, and similarly for the target volume. This would affect

the tumour control probability (*TCP*) as well as normal tissue complication probability (*NTCP*) and is more important in treating larger lesions, relating to the volume effect.

Volumes receiving 90%-50%, 90%-20% and 90%-10% of the dose at the isocentre will increase with the target depth. Figure 7.5 shows the increased proportion of the volumes within above isodose surfaces, due to the change in the penumbra width with depth, for 7 and 23 mm collimators. As is seen from this figure, the volume within a certain isodose surface increases with depth.

### 7.3. Treatment planning verification

The overall accuracy of the treatment planning dose calculation was investigated by simulating the whole *SRS* process which is normally performed in a real clinical case. A humanoid head phantom was used for this purpose. The *SRS* head ring was fixed to the rando head with *TLD* capsules at different positions within the phantom, including the centre of an imaginary target. A complete set of *CT* scans was taken from below the target to the top of scalp with a 2 mm slice distance, while the *CT* fiducials were attached. After determining the stereotactic coordinates of the target, the treatment planning was performed using the routine 6 arcs technique, the 23 mm collimator (41 mm at the isocentre) and 1000 cGy dose to the centre of target. The rando head was fixed to the treatment couch and the target was positioned at the isocentre, using the treatment protocol and the target positioning frame. To verify the treatment set-up, *x-ray* fiducial plates were attached and two double exposure films (*AP* and lateral) were taken, each of which once with the 23 mm collimator attached and once with an open-large field (e.g., 35×35 cm). After development, the fiducial markers and the centre of the target were digitised on the digitiser laptop and showed an accuracy of better than 0.5 mm. After this the treatment proceeded using the treatment protocol.

The target *TLD* showed an averaged dose which was almost 4% more than the prescribed dose. It should be noted that the dose calculation in this case was performed in the routine way, that is using the data which has been measured by a diode detector. The treatment planning dose calculation was exactly repeated with the diamond detector data file, after they corrected for dose rate dependence (see chapter 3 and 5 for more detail). The number of the monitor units was required in this case was 3.4% less than that of the

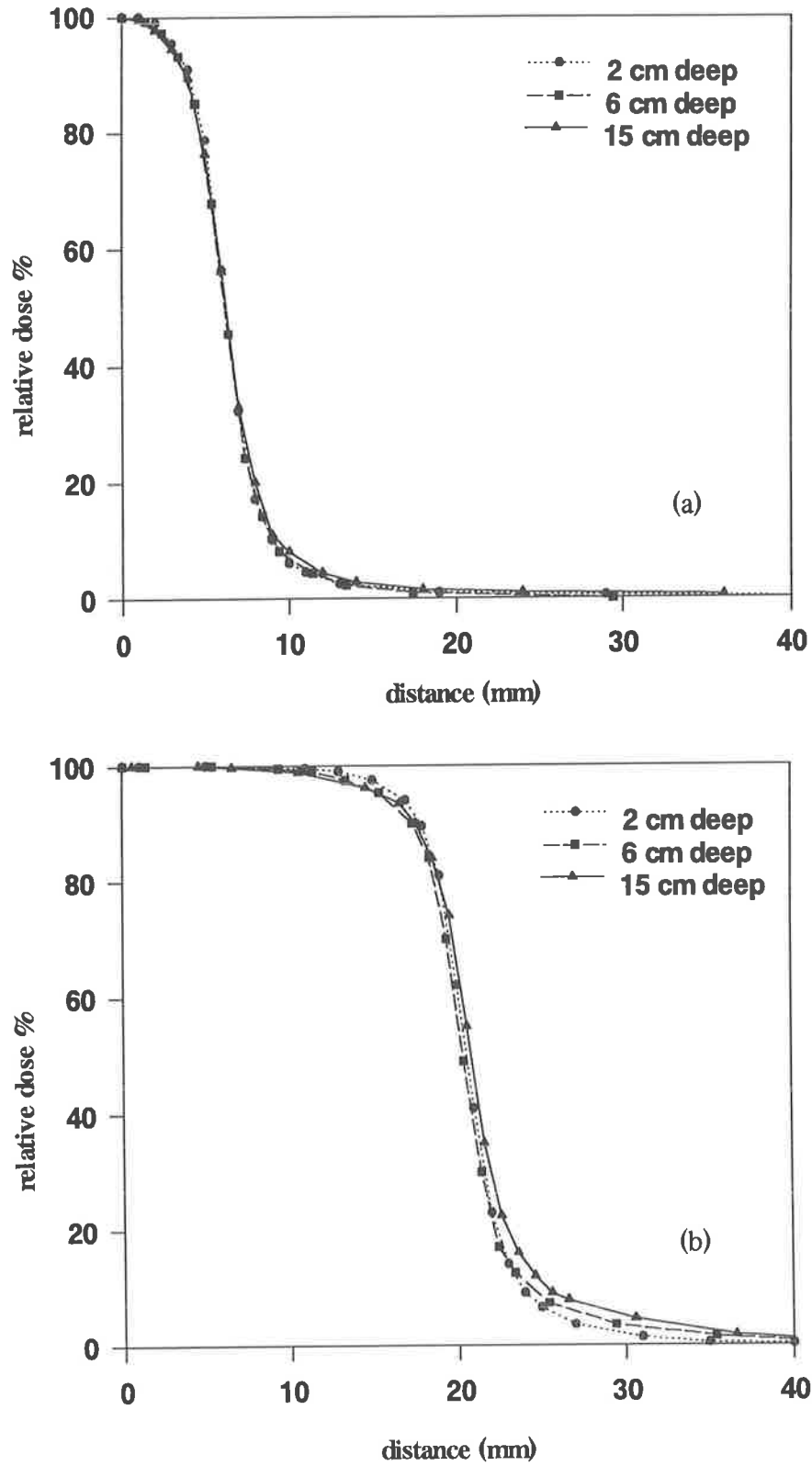


Figure 7.4. Dose profiles at the isocentre at 2, 6 and 15 cm depths, measured using films in the solid water for (a) 7 and (b) 23 mm collimators.

Table 7.2. Measured 90%-50%, 90%-20% and 90%-10% penumbra widths for 7 and 23 mm SRS collimators at the isocentre at 2, 6 and 15 cm depths in solid water.

Depth (mm)	Penumbra (mm) for 7 mm collimator			Penumbra (mm) for 23 mm collimator		
	90%-50%	90%-20%	90%-10%	90%-50%	90%-20%	90%-10%
20	2.1	2.9	5.0	2.7	3.3	5.9
60	2.3	3.1	5.2	3.0	3.4	7.1
150	2.4	3.3	5.4	3.3	4.0	7.8

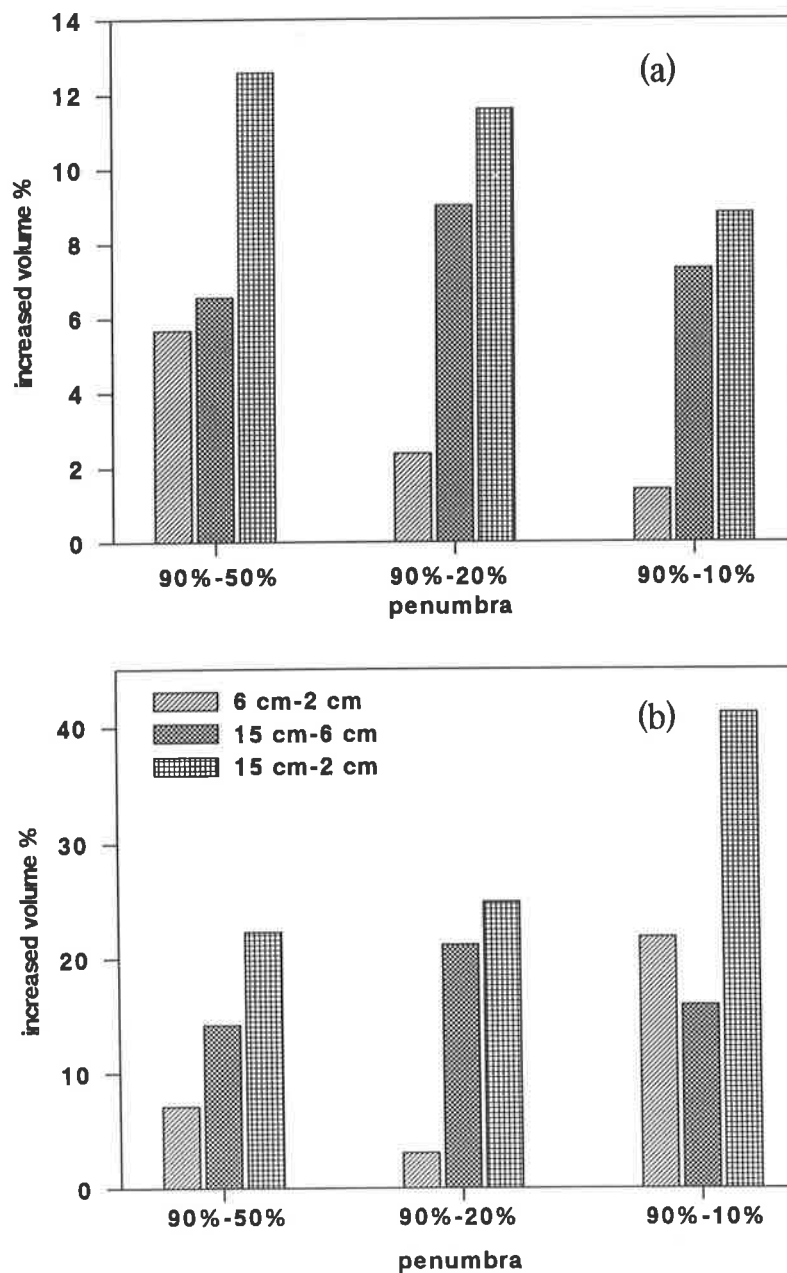


Figure 7.5. The increased volume (%) due to the change of the penumbra width with depth, for (a) 7 and (b) 23 mm SRS collimators.

previous case (using diode data file), which is in a better agreement with the released dose at the isocentre (measured by *TLD*). This can be attributed to the diode detector under response with depth in measuring *TMRs* which was discussed in chapter 5.

In a different approach, to validate the treatment planning calculation of the dose distribution, comparisons were made with the corresponding measured dose distributions for a *SRS* 6 arcs technique. This was performed for the 7 and 23 *mm* collimators. For each collimator a piece of Kodac X-omat V film was cut and fit between two layers of the rando humanoid head phantom. Each time the target was marked with a small pin hole on the film and the head was covered with a dark tape to prevent the film exposure to the light. The whole *SRS* process, from *CT* scan to the treatment, was repeated as above. However, to keep the film exposure in the linear range of the film response, a 7.2 *mm* thick lead block was placed just before the tertiary collimator. In this case the exposure was reduced to approximately 2.6%. After the irradiation, films were developed and scanned using the *RFA-3* film scanner and results were compared with those of the treatment planning calculation.

Figures 7.6 and 7.7 show the comparisons of the dose profiles on the sagittal and coronal directions, in a transverse plane which contains the target centre for 7 and 23 *mm* collimators, respectively. As is seen from these figures, the calculated dose profiles are generally wider, with a greater difference is the coronal section for this combination of arcs. The treatment planning calculated dose distribution was performed under the same conditions of the film irradiation in the phantom — by accounting for the lead block effects on the radiation (e.g., the increased scattering and beam hardening). To do this, the *TMRs* and profiles were measured with films as required for the treatment planning data file (see chapters 2 and 5) but with the lead block mounted before the tertiary collimators. Films were scanned using *RFA-3* and the data have been loaded into the treatment planning system for the dose calculation.

To quantify and compare the calculated and measured dose distributions, the half widths of the profiles at different dose levels were measured and summarised in Table 7.3. As mentioned before, the calculated dose profiles are somehow wider than those measured. In this case the treatment volume would be over-estimated by the treatment planning system. The over-estimation volume in *cc* as well as its ratio to the volume of

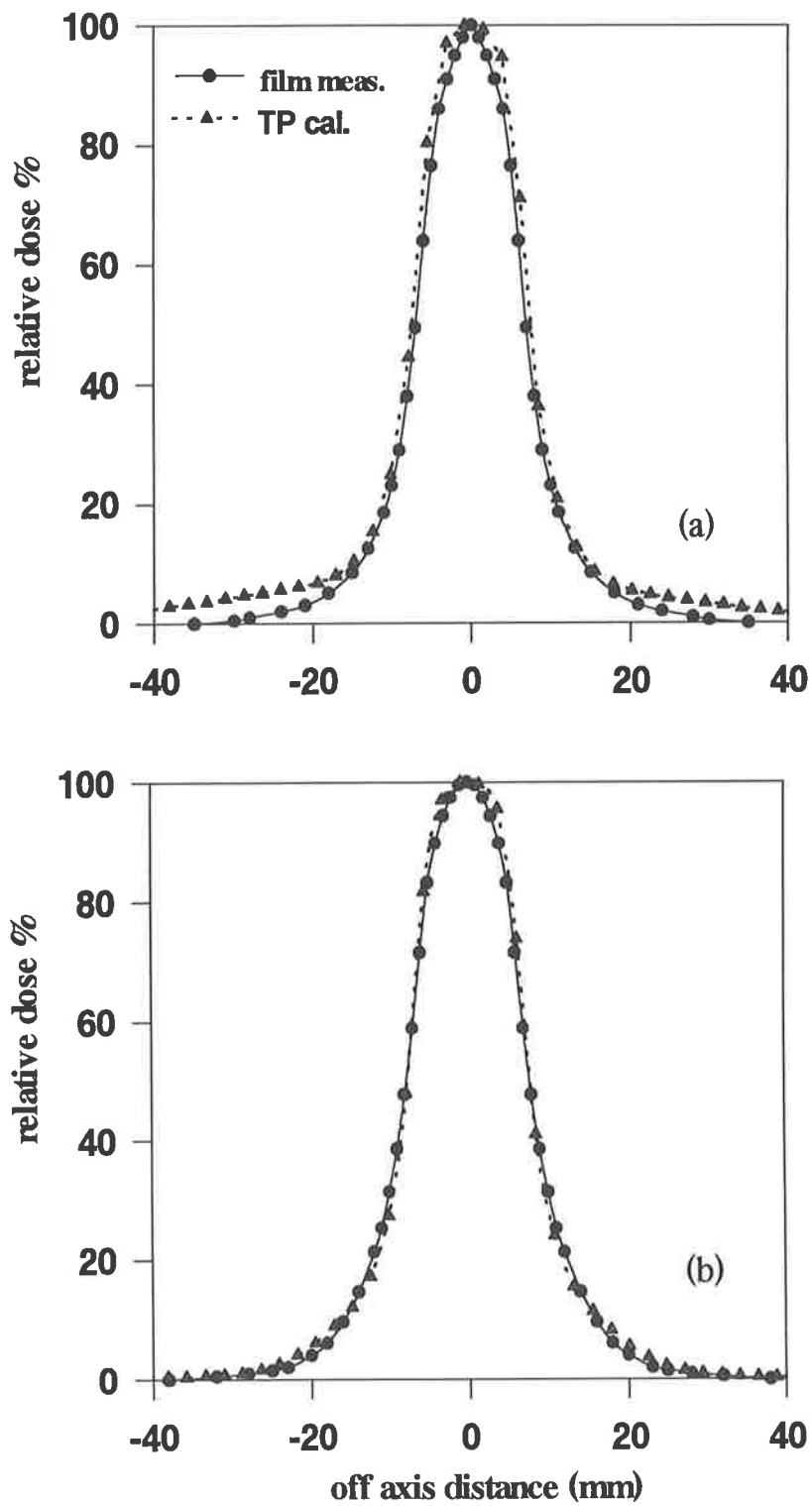


Figure 7.6. (a) Coronal and (b) sagittal dose profiles for 7 mm SRS collimator and the routine 6 arcs technique, calculated by the treatment planning and measured by film in the head phantom.

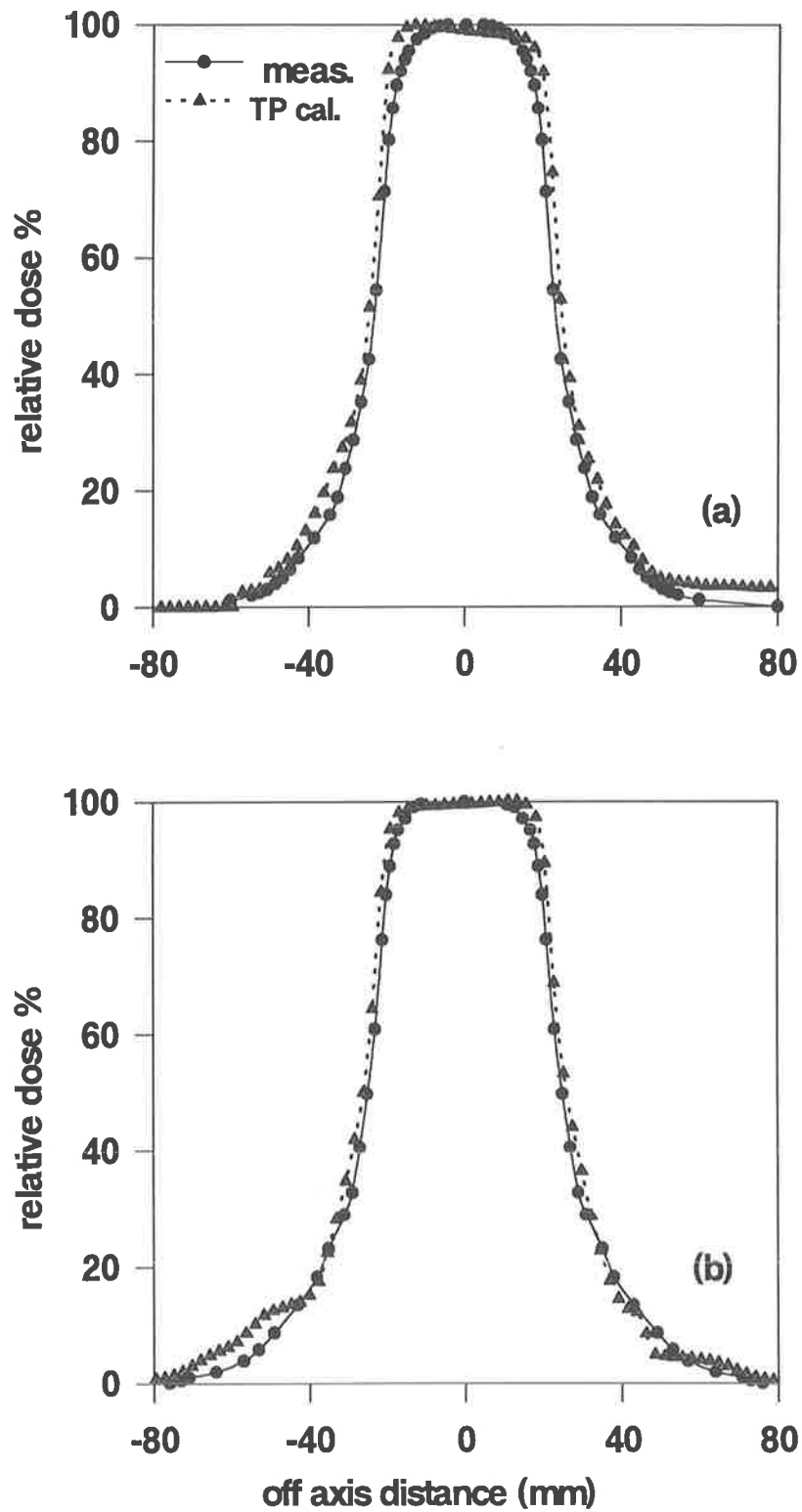


Figure 7.7. (a) Coronal and (b) sagittal dose profiles for 23 mm *SRS* collimator and the routine 6 arcs technique, calculated by the treatment planning and measured by film in the head phantom.

the target (encompassed by 90% isodose surface) is shown in Table 7.3. As seen from this table, there is a big difference between the target volume (calculated 90%) and the treated volume (measured 90%). This means that a large proportion of the target volume does not received the prescribed dose. Taking into account the number of clonogens which exists in this portion will show the danger of this underdose. To account for this over-estimation, the safety margin around the tumour has to be increased. The difference between the lower isodose levels is more. This could indirectly affect the choice of the collimator and the dose to the target volume, regarding the maximum permissible dose to the critical structures.

Table 7.3. The treatment planning calculated and film measured dose profile characteristics in the coronal plane for a routine *SRS* 6 arcs technique, as the half widths (mm) of dose profiles at 90%, 80%, 50%, 20% and 10% of the maximum dose, for 7 and 23 mm *SRS* collimators.

	7 mm <i>SRS</i> collimator					23 mm <i>SRS</i> collimator				
	90%	80%	50%	20%	10%	90%	80%	50%	20%	10%
Calculated	4.4	5.6	7.8	11.3	15.1	20.3	21.6	24.8	34.7	43.3
Measured	3.2	4.6	7.0	10.6	14.1	17.6	19.6	23.2	32.0	40.6
Over-estimation volume (cc)	0.22	0.33	0.55	1.06	2.68	12.21	10.67	11.59	37.76	59.73
Ratio of over-estimation to the target volume	0.61	0.92	1.54	2.96	7.51	0.35	0.30	0.33	1.08	1.70

#### 7.4. Optimum number of arcs

To investigate the optimum dose distribution in our *SRS* system, different techniques with different numbers of arcs were employed in treating an average midbrain tumour (23 mm in diameter). The tumour was encompassed by the 90% isodose, while 100% dose was selected at the isocentre. The aim of this investigation was to spare normal tissue by providing a reasonably uniform and low dose outside the target volume, with minimum dose calculation and treatment times. In this work parallel-opposed fields were avoided and the table angles were chosen to give maximum practical dose spread around the target. The number of employed arcs in different techniques were 3, 4, 6, 9 and 12. The gantry and table angles and also the average *CTMR* (calibrated tissue

maximum ratio—see chapters 2 and 5 for more detail) corresponding to each technique are shown in Table 7.4. As is seen from this table, different techniques resulted in almost the same *CTMR* values, confirming that the table angles were uniformly chosen to give as much dose spread around the target as possible for these techniques.

To show the dose distribution around the targets, the maximum and minimum distances for the dose to fall off from 90% (at the edge of the target) to 50%, 20% and 10% were measured in three transverse, coronal and sagittal planes and the results are shown in Table 7.5. Generally, the closer the minimum and maximum values the better dose distribution and so the better sparing normal tissues.

Table 7.4. The treatment couch and gantry angles for different *SRS* arc techniques and the resultant average *CTMR* for each technique.

Technique	Table	Gantry arc from to	Average depth (mm)	Average <i>CTMR</i> %
3 arcs	-60.0	-20 20	73.5	76.2
	0.0	20 160	77.3	
	60.0	20 160	70.1	
4 arcs	-70.0	-20 -160	71.6	76.3
	-23.3	-20 -160	78.4	
	23.3	20 160	72.8	
	70.0	20 160	70.0	
6 arcs	-60.0	-20 -160	73.5	76.3
	-30.0	-20 -160	77.6	
	0.0	20 160	77.3	
	30.0	20 160	71.6	
	60.0	20 160	70.1	
	90.0	20 160	69.4	
9 arcs	-80.0	-20 -160	70.4	76.2
	-60.0	-20 -160	73.5	
	-40.0	-20 -160	77.0	
	-20.0	-20 -160	79.5	
	0.0	20 160	77.3	
	20.0	20 160	73.6	
	40.0	20 160	71.4	
	60.0	20 160	70.1	
	80.0	20 160	69.0	
12 arcs	-84.0	-20 -160	69.6	76.2
	-68.7	-20 -160	71.6	
	-53.5	-20 -160	74.6	
	-38.2	-20 -160	77.1	
	-22.9	-20 -160	78.4	
	-7.6	-20 -160	81.8	
	7.6	20 160	75.7	
	22.9	20 160	73.0	
	38.2	20 160	71.7	
	53.5	20 160	70.7	
	68.7	20 160	70.0	
	84.0	20 160	69.3	

The dose distributions are also shown in Figure 7.8. As seen from this figure, the 90%-50% distance is almost the same for different techniques, however the 90%-20% and 90%-10% distances are more different. Significant improvement in the dose distribution

Table 7.5. The maximum and minimum distances for the dose to fall off from 90% at the edge of a 23 mm diameter target to 50%, 20% and 10%, in different techniques.

Technique	Minimum distance (mm)			Maximum distance (mm)		
	90%-50%	90%-20%	90%-10%	90%-50%	90%-20%	90%-10%
3 arcs	4.0	10.6	15.4	4.7	15.0	38.7
4 arcs	3.8	10.2	17.8	4.7	13.6	33.5
6 arcs	4.0	11.6	17.4	4.6	13.3	26.7
9 arcs	3.7	11.0	18.8	4.7	12.7	25.1
12 arcs	4.0	11.2	19.0	4.7	12.9	25.3

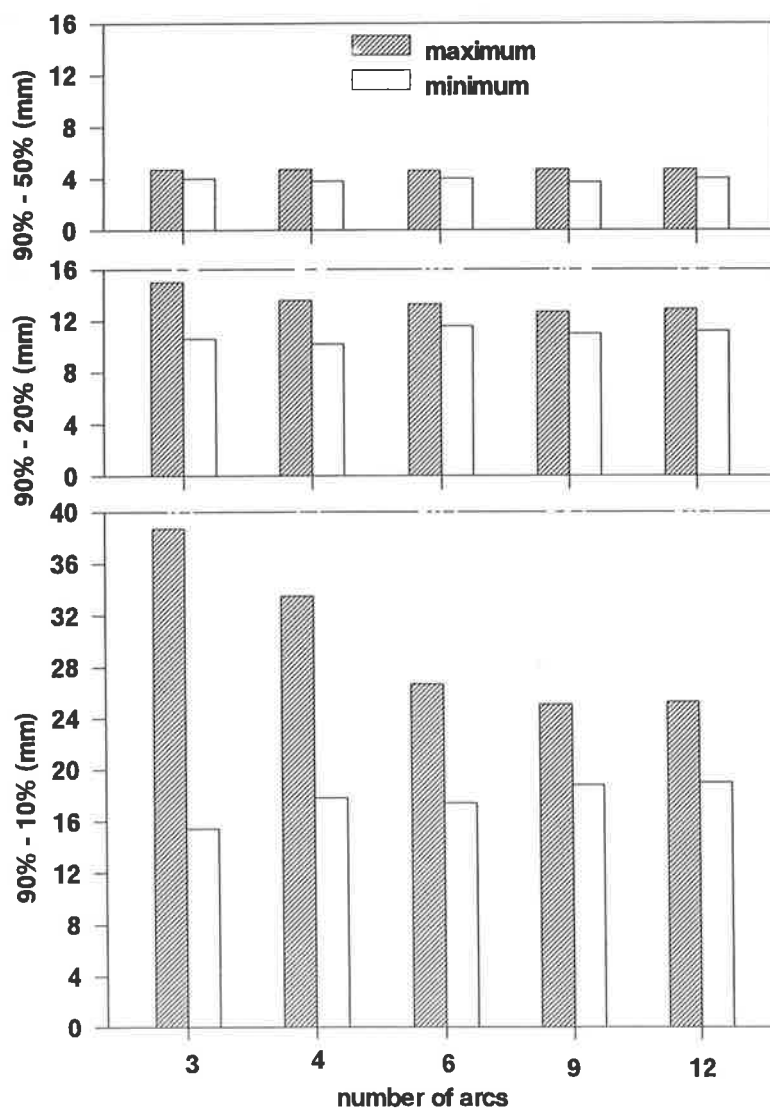
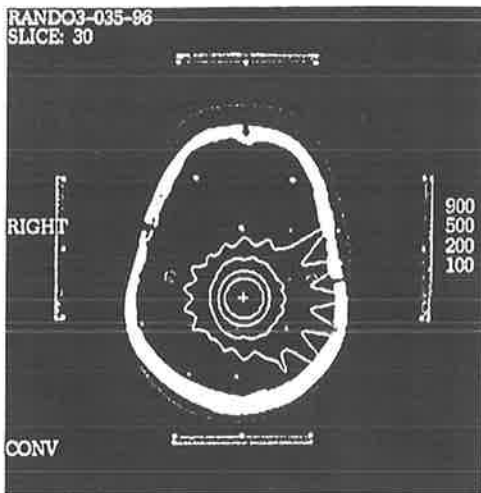
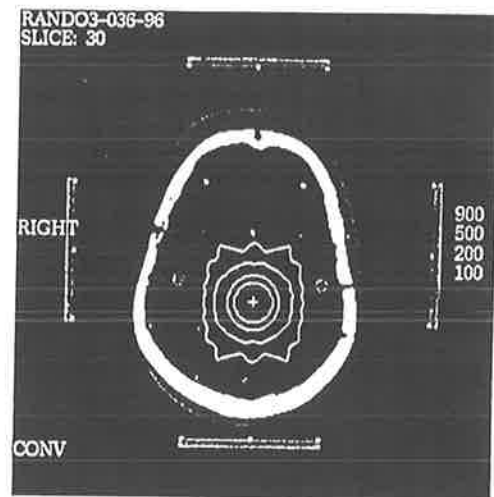


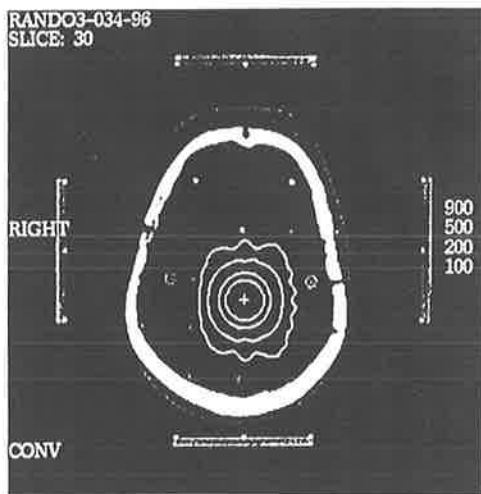
Figure 7.8. The maximum and minimum distances for the dose to fall off from 90% (at the edge of the target) to 50%, 20% and 10%. Distances were measured in three transverse, coronal and sagittal planes, in the treatment planning system.



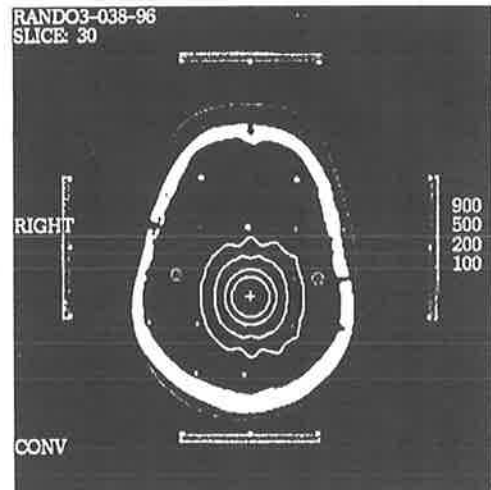
(a)



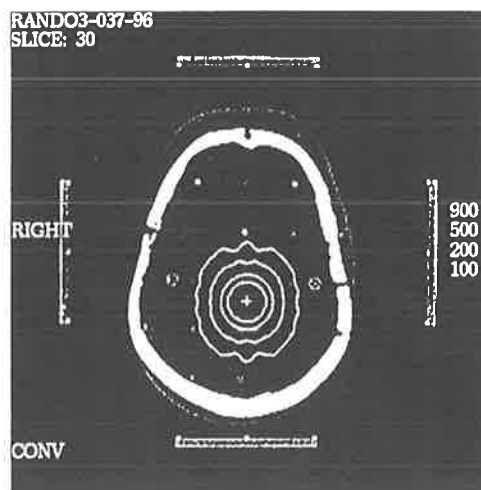
(b)



(c)



(d)



(e)

Figure 7.9. Isodose distribution in a CT transverse plane in treating an average midbrain tumour (23 mm in diameter) using 3, 4, 6, 9 and 12 noncoplanar uniformly distributed arcs (a) to (e), respectively. The tumour is encompassed by 90% isodose lines, while 100% dose was selected at the isocentre. 90%, 50%, 20% and 10% isodose lines are shown for comparison.

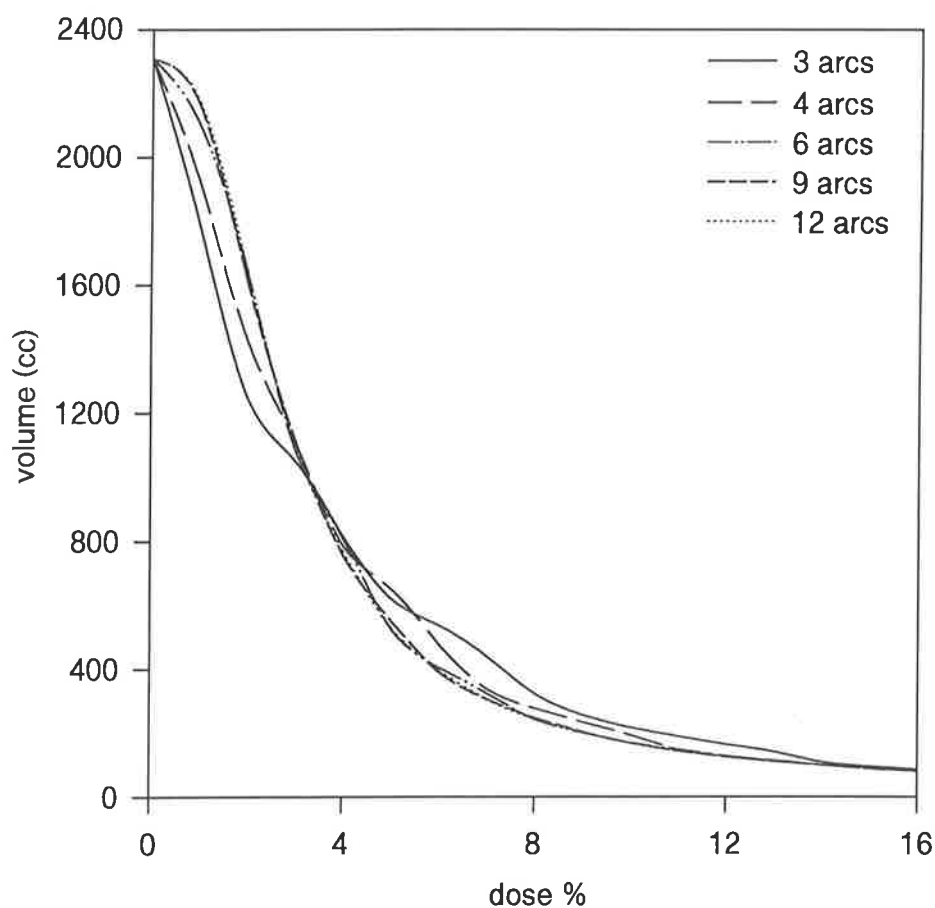


Figure 7.10. Dose volume histograms corresponding to different arc techniques.

is achieved by increasing the number of arcs up to 6, but as is seen, there is not much more improvement afterwards.

The dose distribution can also be considered using isodose charts. Figure 7.9 shows 90%, 50%, 20% and 10% isodose lines for above techniques, when 1000 cGy was given to the isocentre. Dose volume histograms corresponding to the above treatment techniques are shown in Figure 7.10, in order to compare the integral dose. Again improvement is achieved by increasing the number of arcs, but considering the required treatment time, there is not much advantage in increasing the number of arcs to more than 6. As is seen from this figure, a significant volume is receiving a dose of 5-14% of the maximum dose in 3 arcs technique compared to when more arcs are used.

## 7.5. Monte Carlo dosimetry of irregular field stereotactic radiosurgery

### 7.5.1. Introduction

For standard circular-field *SRS* dose calculation, measured beam data is stored for each available collimator, where the required information is (i) an output factor (*OF*) relative to a calibration field; (ii) a tissue-maximum ratio (*TMR*) curve; (iii) an off-axis factor (*OAF*) curve at a single depth, measured in the plane of the isocentre. Beam data is usually measured in a water-phantom using a high resolution detector. A high resolution detector ensures that (i) the penumbra of the dose profile is measured accurately, and (ii) output factor measurements are not erroneous due to the presence of electronic disequilibrium (which exists when very small fields are used).

A system based on a Monte Carlo pencil beam kernel is proposed here to calculate *TMRs* and *OAFs*. Since *OFs* depend on incident photon fluence, these require some measured data unless a full Monte Carlo simulation of the treatment head is carried out. Monte Carlo-based dosimetry has the advantage that finite detector size and lack of a tissue-equivalent detector are not issues. Most importantly, if the shape of treatment fields is determined during planning, based on the “*beam’s eye view*” of the target from various portals, then pre-measured beam data does not in general provide the dose distribution for the chosen beams. In this case, either (i) measured beam data must be corrected to account for the irregular field edge, or (ii) basic sets of computer-generated data must be used to construct the dose distributions, such as when a convolution method is used. Convolution calculations have previously been used in stereotactic radiosurgery, both using 3-*D* kernels (Kubsad et al, 1990) and 2-*D* pencil beam kernels (Treuer et al, 1993).

### 7.5.2. Method

An alternative to normal convolution calculations is to use a sector-integration based method, where dose at a point is calculated using a Monte Carlo-generated pencil-beam kernel  $H(z,r)$  (a function of depth and radius) and a set of sectors radiating out from the calculation point. At each depth, the kernel contains cumulative energy deposited within each radius. The computational task is to find the distances  $r_i$  along the bisector of each sector from the calculation point to the beam boundaries and then to obtain the

kernel value for the current depth and radius  $r_i$ . The dose is integrated by summing over each sector, where the dose contribution from the sector is divided by the number of sectors. This is analogous to the Clarkson's sector integration method (Johns and Cunningham, 1983), where the kernel takes the place of the tissue-air ratio table. Sector integration is in principle faster than pencil-beam convolution, since the number of iterations to find the dose at each point is equal to the number of sectors, rather than the large number of elemental pencil beams incident on the surface. Furthermore, the number of sectors is constant with beam size, whereas in convolution calculations the number of elementary kernels increases with beam area (2-D convolution) or irradiated volume (3-D convolution).

For a field of arbitrary shape, the outline is defined by a set of line segments, where each has an associated equation defined by a y-intercept and a gradient. Intersection points of sector bisectors with the outline are found algebraically. There may be more than one intersection for each sector and, as with Clarkson's method, kernel values are added or subtracted to give an aggregate kernel value depending on whether the bisector approaches the intersection from inside or outside the field respectively. Mathematically, the summation is as follows, where  $D(x,y,z)$  is a dose per incident fluence (later to be renormalised) and  $K_n$  is the aggregate kernel value for sector  $n$ .

$$D(x, y, z) = \frac{1}{N} \sum_{n=1}^N K_n(x, y, z), \quad (7-1)$$

where:

$$K_n(x, y, z) = \sum_{m=1}^M C_m H(z, r_{x,y,m}) \quad (7-2)$$

$M$  is the number of intersections for sector  $n$  at  $x,y$  and  $C_m$  is equal to 1 or -1 for intersections from inside or outside the field, respectively.

For a circular beam, the method involves initially finding a non-diverging 3-D dose distribution where the values are normalised to incident photon fluence. From this can be extracted a central-axis depth dose curve (infinite *FSD*) and a dose profile at each depth. When normalised to its maximum, the depth dose curve in this case is a *TMR* curve and the maximum value represents the phantom scatter factor (*PF*). The *PF* can be normalised to a calibration field size. To give the *OF*, the *PF* must be multiplied by

a collimator scatter factor ( $CF$ ) to account for the variation in photon fluence incident on the surface. The  $CF$  can be measured by a diamond detector or a small ionization chamber, encapsulated in a dense (brass in this case) build-up cap at an extended  $FSD$  (so that electronic equilibrium is established at the detector—see chapter 5 for more detail).

For irregular fields, sector integration using Monte Carlo kernels was used to obtain relative dose distributions as for circular fields, except that at each depth dose must be calculated for points in a plane instead of a line. The field is initially considered to be non-diverging so that bisector-outline intersection points for a calculation point  $x,y,z$  are independent of  $z$ —this greatly reduces computation time as intersection points need only be found once for each  $x,y$  and sector number. Dose at each depth is later transformed radially according to beam divergence. To find output factors for irregular fields, some measured data is required to reflect the variation in  $CF$ , however measurement in the irregular fields themselves is not an option since field shape is decided just prior to treatment. Here, the measured  $OF$ s for circular fields were used in a sector integration—the circular field  $OF$ s replaced the Monte Carlo kernel data in the summation. This assumes that the contribution to dose on the beam axis due to a sector in an irregular field is equal to that from a sector of a circular beam whose radius is that of the sector.

### 7.5.3. Results

For circular fields,  $TMR$ ,  $OAF$  and  $OF$  data were calculated and compared with measurement. The  $TMR$  curves agree well with results obtained with a  $PTW$  diamond detector, after corrected for dose rate dependence (see chapters 3 and 5 for more detail). This indicates that the correct spectrum was used in the formulation of the Monte Carlo kernels (see chapters 4 and 5).  $OAF$ s also agreed well with experiment, but it was found that the projection of the measured effective radiation source with a Gaussian shape with  $FWHM = 1.8\text{ mm}$  (see chapter 5 for more information) had to be convolved with the calculated results to slightly broaden the penumbra, so as to improve agreement with experiment. The most interesting results of the circular beam calculations is the output factor determination. In Figure 7.11,  $EGS4$  calculated  $PF$ s, diamond detector measured  $CF$ s and the resulting calculated  $OF$ s are shown along with diode measured  $OF$ s. The calculated  $OF$ s are the result of the Monte Carlo  $PF$ s multiplied by the corresponding

measured diamond *CFs*. These results are for the Fischer collimators at the *RAH* and are plotted versus physical hole diameter. Measured and calculated output factors are very close as can be seen. All curves are normalised to the value for the largest *SRS* collimator (23 mm drill diameter).

Irregular collimators in the shape of a *cross*, *zed* and *dumbbell* were manufactured from a lead composite (*LMA*) at Prince of Wales Hospital, Sydney. Four sizes were made for each shape, where the field area at isocentre is equal to that for circular fields of diameter at isocentre of 20, 25, 30 and 35 mm. Output factors were determined by sector integration of circular field output factors as described above. The results are shown in Figure 7.12 along with the measured values, for comparison. The measured values for circular fields are also shown. In this figure, both calculated and measured collimator output factors are the values relative to the calibration conditions and are in relatively good agreement.

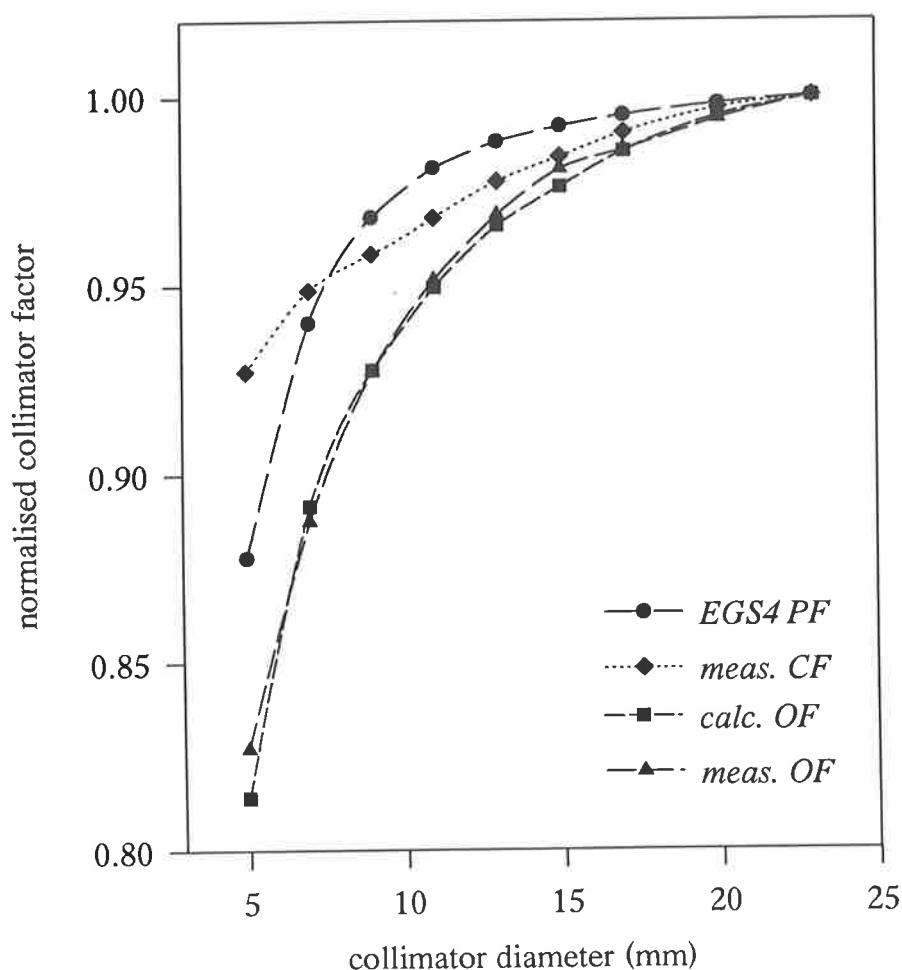


Figure 7.11. Variations of the *EGS4* calculated *PFs*, diamond detector measured *CFs* and the calculated as well as measured *OFs* for different *SRS* collimators. Results are normalised to the value for the largest *SRS* collimator.

Finally, as the calculated dose profile, a surface plot of the dose distribution at 5 cm deep for 20 mm equivalent diameter *cross* is shown in Figure 7.13, where the Monte Carlo kernels were used in the sector integration.

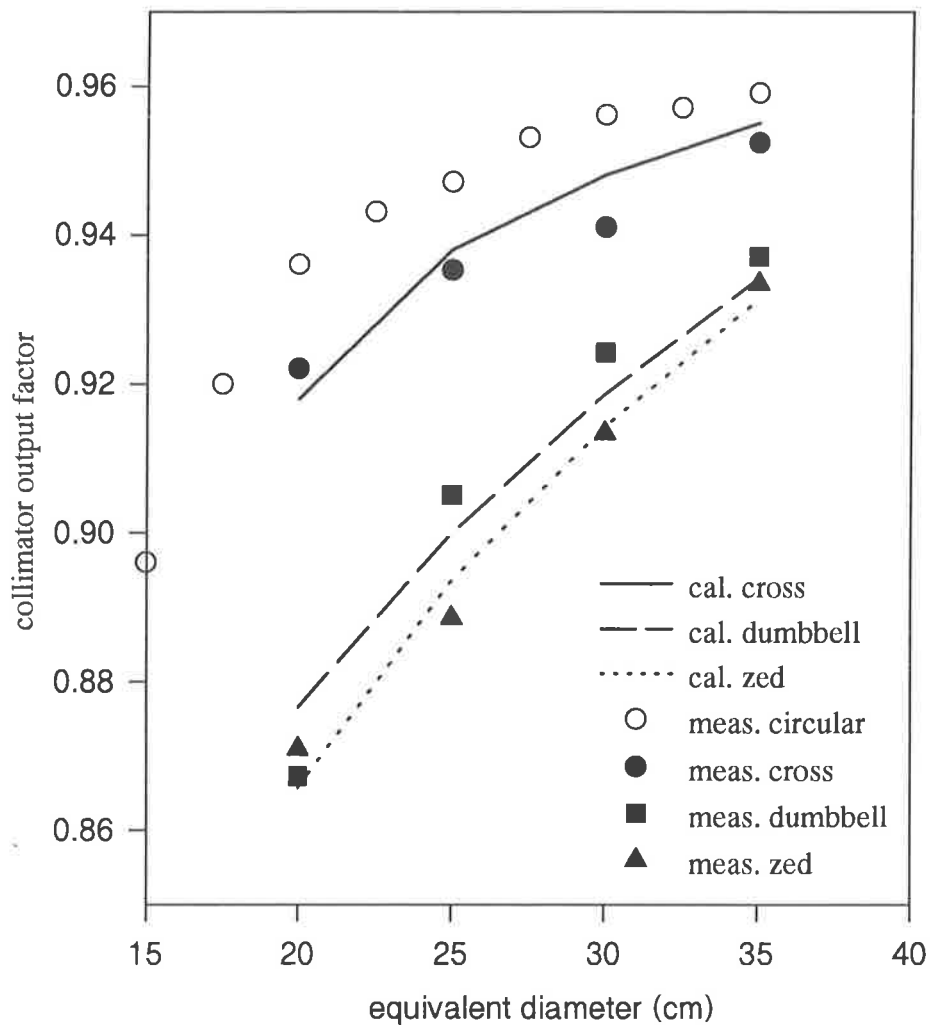


Figure 7.12. Sector integration calculated and also measured output factors for circular-, cross-, dumbbell- and zed-shaped fields.

## 7.6. Image registration and correlation

Accurate localization of tumour volume and critical structures, and also precise placement of the radiation fields to the target volume are of the paramount importance in radiotherapy and in SRS, specifically. Magnetic resonance imaging is superior to CT and other modalities for diagnostic neuroanatomical imaging and treatment planning, due to its excellent soft tissue contrast resolution and ability to scan in any plane

orientation (Moerland et al, 1995). *MRI* as a valuable imaging modality is often the only appropriate technique for visualising many brain tumours, especially those which do not enhance with contrast. *MRI* and magnetic resonance angiography (*MRA*) have resolutions in tissue better than 1 mm, however their spatial accuracy is unacceptable for

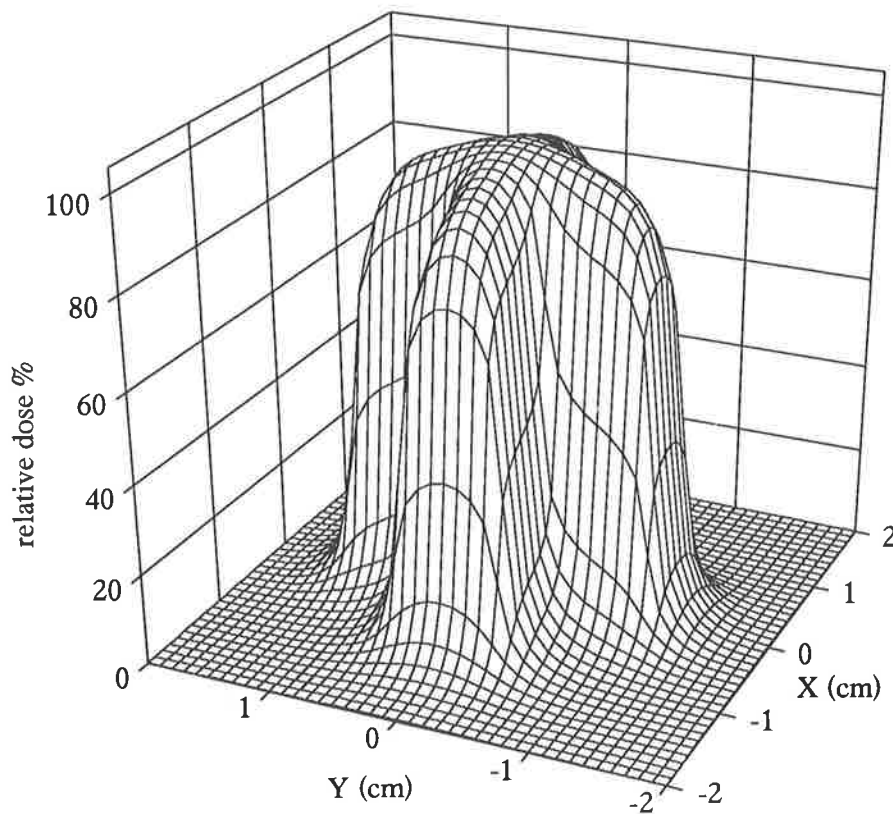


Figure 7.13. Relative dose distribution in a plane normal to the central axis, at 5 cm deep for 20 mm equivalent diameter cross.

*SRS* because of the image distortions. *MR* image distortions are caused by the static magnetic field inhomogeneity and non-linearity of the field gradients. An additional source of field inhomogeneity is the imaging object itself. The magnetic properties of the object induce the chemical shift and susceptibility artefacts. Susceptibility distortions are caused by the presence of a patient in the *MRI* scanner. This is due to magnetic field perturbations as a result of the difference in susceptibility between the patient's body and the surrounding air as well as within the body. The effect is pronounced at bone-tissue and tissue-air interfaces (Kooy et al, 1994). The spatial distortions should be measured and corrected before stereotactic localization.

Different dewarping techniques have been developed to correct the image distortions (Schad et al, 1992; Kessler and Carson, 1992 and Beckham, 1994). In these techniques generally two- or three-dimensional phantoms are scanned and the distortion quantified. Error in position can be assessed using such phantoms (Figure 7.14). The geometrical distortions within the imaging plane can be measured using the 2-D phantom, while the 3-D phantom measures displacement, warp and tilt of the image plane itself. The correction can be made by dewarping the image or adjusting the gradient-shimming currents of the magnetic field until the image shows the exact geometry of the phantom structure. Above dewarping techniques can correct for magnetic field inhomogeneity, but not for the chemical shift and susceptibility.

A more accurate technique has been presented by Kooy et al (1994), which utilises an automated method for image fusion of *MRI* and *CT*. Generally, image fusion is a technique which combines information from separate imaging studies into a single image.

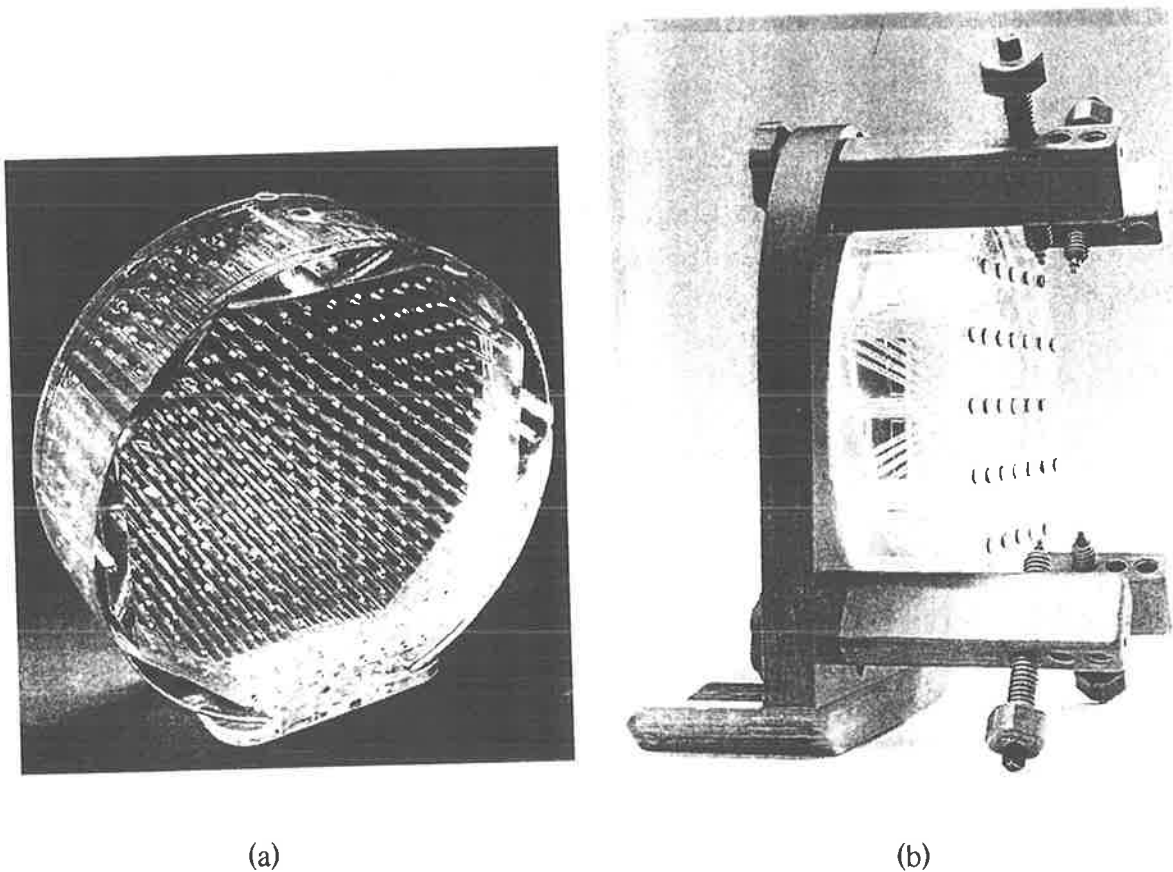


Figure 7.14. (a) Two- and (b) three-dimensional phantoms to measure geometrical distortions within the imaging plane. The 3-D phantom contains rectangular as well as oblique water-filled boreholes (From Hartmann, 1995).

For example the combination of *MRI* with *SPECT* or *PET* will give a direct comparison of anatomy and metabolic activities. The image fusion can be performed using fiducial markers/ or landmarks (which in the case of *MRI* are both of course distorted). Kooy et al (1994 and 1996) have used the chamfer match technique, in which individual sets of points belonging to the same anatomical structures (on each imaging technique) are automatically used for the fusion. This technique corrects the *MR* image for the susceptibility and magnetic field inhomogeneities as well as the chemical shift, so that the bony edges line up with the *CT* bony edges. In this way the *CT* fiducial markers are used for stereotactic localization together with the superior *MR* image to plan and treat the lesion. This technique allows that *MRI* data (without using fiducial and fixation device) to be used for *SRS* by the fusion with a *CT*, obtained with the stereotactic head ring and fiducial markers attached.

Figure 7.15 shows a treatment plan for a spherical target in the midbrain position, using a *LINAC* 6 arcs technique. In this figure the brain stem, eye balls and optic nerves are outlined as critical structures, as well as the target (in dark red). By rotating the 3-D graphic picture on the treatment planning computer, the couch and gantry angles are chosen so that the beam fans (shown in red) avoid the critical structures, while uniformly covering the target volume. The fusion result is shown in Figure 7.16. The left picture is the split slice display with *CT* image in the upper part and *MR* image in the lower part. The intersection can be slide up or down to check the fusion perfection. The right picture is the slice overlay with *CT* in red and *MR* in green.

### 7.7. Bioeffect planning

Treatment planning is conventionally performed by evaluating the dose distribution both across the target volume and normal tissue. The clinical decision on the required dose is normally based on the tumour histology and the clinical data as well as the size of the tumour, observation of the isodoses regarding the dose to the normal tissue and critical structures, and the patient's general condition. Valuable information is achieved, however, by incorporating the tumour control probability (*TCP*) and the normal tissue complication probability (*NTCP*). The *TCP* is the probability of eradicating all tumour cells and *NTCP* is the probability of inducing a particular complication (e.g., a functional disorder/ or producing necrosis) in normal organ.



Figure 7.15. A treatment plan for treating a midbrain tumour. In this picture, the critical structures such as the brain stem (yellow), eyes (green) and optic nerves (lemon) are outlined to be avoided. Also, the beam fans and the *CT* fiducials are seen in this figure (Picture from *X-Knife3* treatment planning system, Prince of Wales Hospital, Sydney).

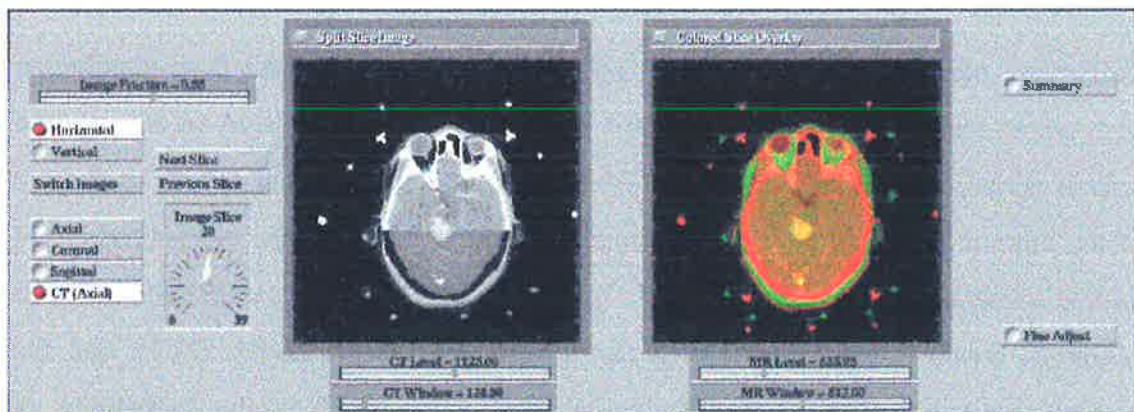


Figure 7.16. Image fusion result. The left picture is split slice display and on the right is the slice overlay with *CT* in red and *MR* in green (Picture from *X-Knife3* treatment planning system, Prince of Wales Hospital, Sydney).

Therefore, uncomplicated tumour control probability, that is tumour control with no complications, is given by:  $UTCP = TCP (1 - NTCP)$ .  $UTCP$  has a maximum at a certain dose and increases as the ratio of the dose to the target to the dose to the normal tissue increases. This is the aim of the conformal therapy techniques which were discussed in section 6.3.

Both  $TCP$  and  $NTCP$  are functions of dose and increase with dose in specific rates which depend on many factors. These factors include the clonogen cell density and sensitivity to radiation, organ histology and architecture, fractionation scheme and the involved volume. In other words, it is a complex process to convert the physical dose distribution to biological effect under various conditions.  $TCP$  and  $NTCP$  and their variation with dose have been discussed in more details elsewhere (Johns and Cunningham, 1983; Khan, 1994 and Hall, 1994).

Attempts have been made for a number of years to assess treatment plans according to bioeffect rather than just a physical dose distribution (Wigg and Wilson, 1981; Wigg and Nicholls, 1984; Flickinger et al, 1990; Webb, 1993b; Lee et al, 1995 and Clark et al, 1996). Biologically effective dose was defined in section 6.7.1 as

$BED(n) = nd \left( 1 + \frac{d}{\alpha/\beta} \right)$ —from which  $BED_{target}(n)$ ,  $BED_{normal}(n)$  and therefore the

therapeutic ratio, which can be defined as  $TR(n) = BED_{target}(n) / BED_{normal}(n)$ , can be calculated (Larson, 1996). The  $BED$  can be displayed in conjunction with anatomical structures using isoeffect lines, in the same way as normal isodoses. This is the basis of bioeffect planning and a useful tool to see the different effect of dose on tumour and normal tissue and comparing rival plans.

The  $NTCP$  can be derived from the differential dose volume histograms ( $DVHs$ ). Suppose  $NTCP(1, D)$  is the  $NTCP$  when the whole organ is irradiated to dose  $D$ . Using differential  $DVH$  and the  $NTCP_i$  for a fractional volume  $v_i$ , in which dose  $D_i$  is assumed to be uniform, the  $NTCP$  for an inhomogeneous irradiation is calculated using the following equation (Webb, 1993b):

$$NTCP_{inhom} = 1 - \prod_{i=1}^M [1 - NTCP(1, D_i)]^{v_i}, \quad (7-3)$$

where  $M$  is the number of subvolumes in the differential  $DVH$ . The product of terms is the probability of no complications in the whole organ, where each term is the probability of no complications in element  $i$ . The volume exponent represents the decrease in probability of no complications with volume irradiated.

The above equation represents a critical element architecture, where the probability of no complications is the probability that no sub-volume will be damaged. The brain stem is an example of such a structure, consisting functional subunits ( $FSUs$ ) which are arranged in series. In this case the integrity of each intermediate or final structure is critical to the function (Colombo et al, 1995) and any damage to a  $FSU$  has an effect on the whole organ (e.g., the spinal cord). On the other hand "silent" brain area (e.g., frontal lobe) are arranged in parallel and should be considered as an organ with an integral response. In this case the complication occurs only when a substantial fraction of the  $FSU$  is damaged (Colombo et al, 1995).

The question raised is whether bioeffect planning is adequate to predict the treatment outcome. The conversion of  $DVH$  data into the biological response is still controversial with little data available and questionable radiobiological modelling.

## 7.8. Discussion and conclusion

To evaluate the  $RAH$ 's treatment planning dose calculation accuracy and the validity of its existent assumptions, different experiments as well as Monte Carlo dose simulations were performed. It has been shown that, although the assumption of a homogeneous medium for the brain is valid in most cases, in some conditions this could cause significant errors (such as in using small number of static fields). Also, it was shown that the constancy of the dose profile with depth is not a good assumption, especially when the target volume is close to a critical organ. This may lead to incorrect choice of collimator size or prescription dose and will reduce the therapeutic ratio. In the  $SRS$  system in the  $RAH$ , treating a target using the 23 mm collimator could cause up to 14% and 21% differences in the irradiated volumes between the 90%-50% and 90%-20% isodose lines respectively, due to this assumption. The corresponding errors for the 7 mm collimator are 6.5% and 9%. This effect will be less in multiple arc techniques, and varies with the target depth.

A method based on Monte Carlo pencil beam kernels has been proposed to calculate the treatment planning parameters. This method can be used both for circular and irregular fields. However, this technique is more useful in calculating dosimetry parameters for irregular fields, where the shape of treatment fields is determined during planning (based on the “*beam’s eye view*” of the tumour) and pre-measured beam data does not in general provide the dose distribution for the chosen beams.

To appreciate the biological response and the treatment outcome a method based on bioeffect planning, rather than conventional planning techniques using the physical dose distribution, has been presented. This is a useful tool to visualise the effect of the dose on the tumour and normal tissue and to compare the rival plans by looking at the isoeffect lines.



# Chapter 8

## Discussion and Future Developments

### 8.1. Introduction

As many as 50% of all cancer patients develop brain metastases (Flickinger et al, 1994). This is in addition to other intracranial lesions such as primary tumours, arteriovenous malformations, acoustic neuromas and functional disorders. Due to the great number of the patients involved as well as the complexity of the brain structures, maximum efforts have to be made to have an optimal dose distribution and an increased therapeutic ratio. This is achieved by sparing normal tissue, while an appropriate dose is released across the target volume, and is especially important where the lesion is in the vicinity of critical structures such as the brain stem, optic chiasma or optic nerves. Additionally, limitations in diagnosis, dose calculation, dose delivery, etc. have to be realistically considered to ensure that geometrical accuracy, as the most important requirement in *SRS*, is maintained. A multidisciplinary quality assurance program is necessary not only for radiation oncology but also for radiology and neurosurgery. A team consisting of a neurosurgeon, radiation oncologist and physicist should be involved in this program to ensure that diagnosis, dosimetry, treatment planning and the dose delivery is performed satisfactorily.

### 8.2. Dosimetry of *SRS* fields

Dosimetry of radiosurgery fields has special difficulties arising from the steep dose gradient and electronic disequilibrium, which could extend to the central axis of the beam. Therefore, a high resolution detector has to be used for this purpose. A tissue-equivalent detector is always preferred in radiotherapy dosimetry, and especially in *SRS*, since the presence of a non-tissue-equivalent detector will change the degree of the lateral electronic disequilibrium. Additionally, the response of such a detector to a constant dose varies with the field size, since (i) the secondary electron energy spectrum

changes with the degree of electronic disequilibrium, as discussed in chapter 5 and (ii) the proportion of dose due to scattered photons increases with field size.

Monte Carlo techniques have been shown in chapters 4 and 5 to be reliable references for dosimetry of *SRS* fields, providing that radiation transport is modelled adequately. This is due to the fact that *MC* modelling is a direct dose calculation technique which uses explicit radiation transport to simulate the physical situation. Therefore, Monte Carlo-based dosimetry has the advantage that finite detector size and lack of a tissue-equivalent detector are not issues.

Diamond detectors are potentially attractive due to their small size and tissue equivalence. It is shown that (i) the mass energy absorption of diamond (carbon) relative to that of water is almost unity and (ii) mass collision stopping power ratio of carbon to that of water remains almost constant with energy. The above ratios vary significantly with energy for film and diode detectors, while for the ionization chamber only the ratio of the mass collision stopping power varies with energy. Also, while diamond and diode detectors are both dose rate dependent (Hoban et al, 1994), the former's response can be corrected readily for this effect to give accurate results. This has been confirmed in chapter 3 by comparing the diamond response after correction with the corresponding responses of the ionization chamber (for large fields) and Monte Carlo (for small fields). Applying such a correction for the diode detector is not so easy since silicon suffers from energy dependence as well, so that the detector response varies for different conditions of field size, depth and off axis distance. Using experimental results and the *MC* calculations of the energy spectra of the photon and resultant electrons, it has been shown that diamond detectors are potentially ideal for *SRS* and yield more accurate results than more commonly used diode and film dosimetry techniques, especially if they are corrected for dose rate dependence.

### **8.3. Treatment planning**

Stereotactic radiosurgery treatment planning dose calculation is a 3-dimensional method, as discussed in chapter 2. The patient localization is performed using a stereotactic head ring and a stereotactic coordinate system, which relates anatomical information achieved by one or more imaging modalities to the coordinates of the

stereotactic localiser device. The patient is then positioned so that the coordinates of the tumour centre correspond to the machine isocentre. Stereotactic methods enable highly conformal delivery of dose to a well-defined target volume with maximal sparing of adjacent normal tissue. An interactive treatment planning system is required to efficiently utilise the available capabilities and to conform the beam to the shape of the target. Treatment planning features like “*beam’s eye view*”, automatic beam shaping and 3-D visualisation of the target, critical structures and beam fans within the skull are most desirable.

In SRS, as a high technology treatment technique, many assumptions have been made to speed the dose calculation process. The validity of these assumptions have been considered in chapter 7. It was shown that although assumption of a homogeneous medium for the brain is valid in most of the cases, in some conditions this could cause significant errors. Treating lesions adjacent to the sinuses, especially using small number of static fields is an example of this kind. Also, it was shown that the constancy of the dose profile with depth is not a good assumption. This becomes very important when the target volume is close to a critical organ. The effect is up to 14% and 21% differences in the irradiated volumes between the 90%-50% and 90%-20% isodose lines respectively, in treating a target using the 23 mm collimator. This effect will be less in multiple arc techniques and varies with the target depth, however as with any source of error in the true penumbral shape, this may lead to incorrect choice of collimator size or prescription dose at the planning stage. Therefore, it is suggested that the dose profiles be measured for different number of depths (e.g., five), as a requirement to ensure that the treated volume is the same the target volume.

A method based on Monte Carlo pencil beam kernels has been proposed to calculate the treatment planning parameters. This method is especially useful in calculating dosimetry parameters for irregular fields, where the shape of treatment fields is determined during planning and pre-measured beam data does not in general provide the required information. To include the biological response and the treatment outcome, a method based on bioeffect planning has been presented. In this case by looking at the isoeffect lines, the effect of the dose on the tumour and normal tissue can be visualised and the rival plans compared. This needs more research, based on the relevant biological parameters and appropriate radiobiological modelling.

#### 8.4. Dose delivery

The most important requirement for stereotactic radiosurgery is geometric accuracy. This has to be maintained throughout the whole process of diagnostic, dosimetry, planning and the dose delivery and needs to be checked regularly, as part of the quality assurance program. Any uncertainty and movements such as the isocentre movement during the rotations should be added to the safety margin around the target. The overall accuracy of the dose delivery and treatment planning dose calculation was investigated using a humanoid head phantom, by performing the whole *SRS* process which is normally performed in a real clinical case.

The current developments such as image guided *SRS* system (*CYBERKNIFE*), beam intensity modulation with gantry rotation and a dynamic multileaf collimator (*PEACOCK* system), and *TOMOTHERAPY* provide good conformality of the dose to the shape of non spherical targets, with maximal sparing of adjacent normal structures. Using the radiobiological principles it has been shown that *SRS* is appropriate for treating *AVMs* and most benign lesions, however it is a sub-optimal technique for treating early-responding malignancies. Stereotactic radiotherapy (a fractionated scheme) is highly recommended for these lesions, or where the target is too big or too close to a critical structure. In the last case it should be investigated to see if the fractionation scheme gives benefit to the patient, regarding the cumulative uncertainties on the patient repositioning and the dose delivery.

## **Appendix**

### **Publications**

This is a reprint of the published papers which the author has been involved during the course of this project.



Heydarian, M., Hoban, P.W. & Beddoe, A.H. (1996) A comparison of dosimetry techniques in stereotactic radiosurgery.

*Physics in Medicine and Biology*, v. 41(1), pp. 93-110

NOTE:

This publication is included on pages 217-234 in the print copy of the thesis held in the University of Adelaide Library.

It is also available online to authorised users at:

<http://doi.org/10.1088/0031-9155/41/1/008>

Hoban, P.W., Heydarian, M., Beckham, W.A. & Beddoe, A.H. (1994) Dose rate dependence of a PTW diamond detector in the dosimetry of a 6 MV photon beam.  
*Physics in Medicine and Biology*, v. 39(8), pp. 1219-1229

NOTE:

This publication is included on pages 235-245 in the print copy of the thesis held in the University of Adelaide Library.

It is also available online to authorised users at:

<http://doi.org/10.1088/0031-9155/39/8/003>



Heydarian, M., Hoban, P.W., Beckham, W.A. & Beddoe, A.H., Borchardt, I.M. (1993) Evaluation of a PTW diamond detector for electron beam measurements.  
*Physics in Medicine and Biology*, v. 38(8), pp. 1035-1042

NOTE:

This publication is included on pages 247-254 in the print copy of the thesis held in the University of Adelaide Library.

It is also available online to authorised users at:

<http://doi.org/10.1088/0031-9155/38/8/002>

## References

Adler J R 1995 Preliminary clinical experience with frameless image-based radiosurgery: The CYBERKNIFE. 2ND Congress of International Stereotactic Radiosurgery Society, Boston.

Adler J R and Cox R S 1996 Preliminary clinical experience with the Cyberknife: Image-guided stereotactic radiosurgery. Radiosurgery 1995 Ed. Kondziolka D (Pittsburgh: Karger).

Ahnesjo A 1989 Collapsed cone convolution of radiant energy for photon dose calculation in heterogeneous media. Med. Phys. **16** 577-92.

Ahnesjo A and Andreo P 1989 Determination of effective bremsstrahlung spectra and electron contamination for photon dose calculations. Phys. Med. Biol. **34** 1451-64.

Ahnesjo A, Andreo P and Brahma A 1987 Calculation and application of point spread functions for treatment planning with high energy photon beams. Acta Oncol. **26** 49-55.

Ahnesjo A, Saxner M and Trepp A 1992 A pencil beam model for photon dose calculation Med. Phys. **19** 263-73.

Ahnesjo A, Saxner M and Trepp A 1992 A pencil beam model for photon dose calculation Med. Phys. **19** 263-73.

Alexander E, Kooy H M, Herk M V, et al. 1995 Magnetic resonance image-directed stereotactic neurosurgery: use of image fusion with computerized tomography to enhance spatial accuracy. J. Neurosurg. **83** 271-76.

American Association of Physicists in Medicine (AAPM) 1995 Stereotactic radiosurgery. Report of Task Group 42 (New York: AAPM).

Andreo P 1991 Monte Carlo techniques in medical radiation physics. Phys. Med. Biol. **36** 861-920.

Andreo P and Brahme A 1986 Stopping power data for high-energy photon beams Phys. Med. Biol. **31** 839-58.

Arcavito G, Piermattei A, D'Abramo G and Bassi F A 1985 Dose measurements and calculations of small radiation fields for 9 MV x rays Med. Phys. **12** 779-84.

Ballinger C T 1992 Comments on A macro Monte Carlo method for electron beam dose calculation. Phys. Med. Biol. **37**.1611-13.

Barish R J and Barish S V 1988 A new stereotactic x-ray knife. Int. J. Radiat. Oncol. Biol. Phys **14** 1295-98.

- Batho H F 1964 Lung corrections in cobalt 60 beam therapy J Can. Assn. Radiol. **15** 79.
- Beatty J, Biggs P J, Gall K, et al. 1996 A new miniature *x-ray* device for interstitial radiosurgery: Dosimetry. Med. Phys. **23** 53-62.
- Beckham 1994 MRI distortion correction. EPSM'94 Conference, Perth, Australia.
- Beddar A S, Mason D J and O'Brien P F 1994 Absorbed dose perturbation caused by diodes for small field photon dosimetry Med. Phys. **21** 1075-79.
- Begnozzi L, Gentile F P, Chiatti L, et al. 1993 Study on the reference dose level in radiotherapy treatment planning. Int. J. Radiat. Oncol. Biol. Phys. **28** 515-22.
- Berger M J 1963 Monte Carlo calculations of the penetration and diffusion of fast charged particles Methods in Computational Phys. Vol 1 Ed. Alder B, Fernbach S, and Rotenberg M, (New York: Academic).
- Betti O O and Derechinsky V E 1984 Hyperselective encephalic irradiation with linear accelerator. Acta Neurochirurgica, Suppl. **33** 385.
- Bielajew A F 1992 EGS4 Monte Carlo teaching course APSEM/BECON'92 conference, Gold Coast, Australia.
- Bielajew A F and Rogers D W O 1987 Monte Carlo transport of electrons and photons. Ed. Jenkins T M, Nelson W R, and Rindi A (New York: Plenum).
- Bielajew A F and Rogers D W O 1988 Variance reduction techniques in Monte Carlo transport of electrons and photons Ettore Majorana international science series **38** (New York: Plenum).
- Biggs P J, Beatty J, Gall K, et al. 1995 Acceptance testing, commissioning and use of a new model miniature *x-ray* tube for stereotactic radiosurgery of small intracranial lesions. 2ND Congress of International Stereotactic Radiosurgery Society, Boston.
- Bjarngard B E, Vadash P and Zhu T 1995 Doses near the surface in high-energy *x-ray* beams. Med. Phys. **22** 465-68.
- Blais Noel and Podgorsak E B 1992 The mass angular scattering power method for determining the kinetic energies of clinical electron beams. Phys.Med.Biol. **37** 1931-42.
- Bortfeld Th, Burkelbach J, Boesecke R and Schlegel W 1990 Methods of image reconstruction from projections applied to conformation radiotherapy. Phys. Med. Biol. **35** 1423-34.
- Bourland J. D. and Chaney E L 1992 A finite-size pencil beam model for photon dose calculations in three dimensions. Med. Phys. **19** 1401-12.
- Bourland J. D. and McCollough 1993 Static field conformal stereotactic radiosurgery: Physical techniques. Int. J. Radiat. Oncol. Biol. Phys. **28** 471-79.
- Bova F J and Friedman W A 1991 Stereotactic angiography: an inadequate database for radiosurgery? Int. J. Radiat. Oncol. Biol. Phys. **20** 891-95.

Bova F J, Friedman W A, Buatti J M and Mendenhall W M 1995 System for fractionated stereotactic radiation therapy. 2ND Congress of International Stereotactic Radiosurgery Society, Boston.

Boyer A and Mok E C 1985 A photon dose distribution model employing convolution calculations *Med. Phys.* **12** 169-77.

Boyer A and Mok E C 1986 Calculation of photon dose distributions in an inhomogeneous medium using convolutions *Med. Phys.* **13** 503-9.

Brahme A 1988 Optimisation of stationary and moving beam radiation therapy techniques *Radiother. Oncol.* **12** 129-40.

Brenner D J and Hall E J 1994a Correspondence: One, 10, 20, or 30 Fractions in stereotactic radiotherapy for brain malignancies? *Int. J. Radiat. Oncol. Biol. Phys.* **30** 501.

Brenner D J and Hall E J 1994b Stereotactic radiotherapy of intracranial tumors-an ideal candidate for accelerated treatment. *Int. J. Radiat. Oncol. Biol. Phys.* **28** 1039-41.

Brenner D J, Martel M K and Hall E J 1991 Fractionated regimens for stereotactic radiotherapy of recurrent tumors in the brain *Int. J. Radiat. Oncol. Biol. Phys.* **21** 819-24.

Buatti J M, Friedman W A, Bova F J, et al. 1995 Treatment selection factors for stereotactic radiosurgery of intracranial metastases. *Int. J. Radiat. Oncol. Biol. Phys.* **32** 891-895.

Burgemeister E A 1981 Dosimetry with a diamond detector acting as a resistor. *Phys. Med. Biol.* **26** 269-75.

Burlin T E, Sidwell J M and Wheatley B M 1973 Applications of Monte Carlo methods in medical radiology *B. J. Radiol.* **46** 398-9.

Canali C, Gatti E, Kozlov S F, et al. 1979 Electrical properties and performances of natural diamond nuclear radiation detectors. *Nucl. Instrum. Meth.* **160** 73-7.

Carol M 1992 An automatic 3-D treatment planning and implementation system for optimized conformal therapy by the NOMOS Corporation. 34 Annul. Meet. ASTRO, San Diego.

Carol M, Grossman R, Selker R, et al. 1996 Preliminary clinical experience with the Peacock intensity modulation 3-D conformal radiation therapy system. *Radiosurgery 1995* Ed. Kondziolka D (Pittsburgh: Karger).

Chaney E L, Cullip T J and Gabriel T A 1994 A Monte Carlo study of accelerator head scatter. *Med. Phys.* **21** 1383-90.

Chierego G, Marchetti C, Avanzo R C, et al. 1989 Dosimetric considerations on multiple arc stereotaxic radiotherapy. *Radioth. and oncol.* **12** 141-52.

Clark B G, Souhami L, Pla C, et al. 1996 The calculation of an integral biologically effective dose in fractionated stereotactic radiotherapy. *Radiosurgery 1995* Ed. Kondziolka D (Pittsburgh: Karger).

- Colombo F, Francescon P, Cora S, et al. 1995 Evaluation of linear accelerator radiosurgical techniques using biophysical parameters (NTCP and TCP). *Int. J. Radiat. Oncol. Biol. Phys.* **31** 617-28.
- Cosgrove G R, Valensuela R, Biggs P, et al. 1995 Interstitial photon radiosurgery for intracranial tumours. 2<sup>ND</sup> Congress of International Stereotactic Radiosurgery Society, Boston.
- Cox R, Haneman W P and Brain S W 1993 Dose distributions produced by a robot-mounted linac (abstract). *Med. Phys.* **20** 889.
- Cunningham J R 1972 Scatter-air ratios *Phys. Med. Biol.* **17** 42-51.
- Cunningham J. R. 1989 Dose calculations for high energy electron and photon beams *Comp. Med. Imag. Graph.* **13**.241-50.
- Cygler J, Battista J J, Scrimger J W, et al. 1987 Electron dose distributions in experimental phantoms: a comparison with 2D pencil beam calculations *Phys. Med. Biol.* **32** 1073-86.
- Dawson D J, Harper J M and Akinradewo A C 1984 Analysis of physical parameters associated with the measurement of high energy *x-ray* penumbra *Med. Phys.* **11** 491-97.
- Dawson D J, Schroeder N J and Hoya J D 1986 Penumbra measurements in water for high energy x rays *Med Phys* **13** 101-4.
- De Salles A A F, Vassilev G, Vassilev V, et al. 1995 Radiation necrosis in patients treated radiosurgically for brain metastasis. 2<sup>ND</sup> Congress of International Stereotactic Radiosurgery Society, Boston.
- Dean R D 1980 A scattering kernel for use in true three-dimensional dose calculations. *Med. Phys.* **7** 429.
- Delannes M, Daly N J, Bonnet J, et al. 1991 Fractionated radiotherapy of small inoperable lesions of the brain using a non-invasive stereotactic frame *Int. J. Radiat. Oncol. Biol. Phys.* **21** 749-55.
- Ding G X, Rogers D W O and Mackie T R 1995 Calculation of stopping power ratios using realistic clinical electron beams *Med. Phys.* **22** 489-501.
- Dinsmore M, Harte K J, Sliski A P, et al. 1996 A new miniature *x-ray* source for interstitial radiosurgery: device description. *Med. Phys.* **23** 45-52.
- Drzymala R E, Klein E E, Simpson J R, et al. 1994 Assurance of high quality linac-based stereotactic radiosurgery. *Int. J. Radiat. Oncol. Biol. Phys.* **30** 459-72.
- Dupont S and Rosenwald J C 1994 Convolution calculations of dose in buildup regions for high energy photon beams obliquely incident. *Med. Phys.* **21** 1391-400.
- Engenhart R, Debus J, Rudat V, et al. 1995 Accuracy and long term stability of a mask system for fractionated stereotactic radiosurgery. 2<sup>ND</sup> Congress of International Stereotactic Radiosurgery Society, Boston.

Faddegon B A, Ross C K and Rogers D W O 1992 Measurement of collision stopping powers of graphite, aluminium and copper for 10 and 20 MeV electrons. *Phys. Med. Biol.* **37** 1561-71.

Flickinger J C, Kondziolka D, Lunsford L D et al. 1994 A multi-institutional experience with stereotactic radiosurgery for solitary brain metastasis. *Int. J. Radiat. Oncol. Biol. Phys.* **28** 797-802.

Flickinger J C, Lunsford L D, Kondziolka D and Maitz A A 1993 Potential human error in setting stereotactic coordinates for radiosurgery: Implications for quality assurance. *Int. J. Radiat. Oncol. Biol. Phys.* **27** 397-401.

Flickinger J C, Schell M C and Larson D A 1990 Estimation of complication for linear accelerator radiosurgery with the integrated logistic formula. *Int. J. Radiat. Oncol. Biol. Phys.* **19** 143-48.

Foote R L, Coffey R J, Swanson J W, et al. 1995 Stereotactic radiosurgery using the Gamma Knife for acoustic neuromas. *Int. J. Radiat. Oncol. Biol. Phys.* **32** 1153-60.

Ford R L and Nelson W R 1978 The EGS code system: Computer programs for the Monte Carlo simulation of electromagnetic cascade shower (version 3). Stanford Linear Accelerator Centre Report SLAC-210.

Fowler J F 1966 Solid state electrical conductivity dosimeters Radiation dosimetry Ed. F H Attix and W C Roesch (New York: Academic).

Fowler J F 1993 The volume effect in radiotherapy. *J. Jpn. Soc. Ther. Radiol.* **5** 75-87.

Friedman W A and Bova F J. Stereotactic radiosurgery: Report of Task Group 42, Radiation Therapy Committee. *AAPM*, 1995 (New York: AIP).

Fuller B G, Kaplan I D, Adler J, et al. 1992 Stereotactic radiosurgery for brain metastases: the importance of adjacent whole brain irradiation. *Int. J. Radiat. Oncol. Biol. Phys.* **23** 413-18.

Gannet D, Stea B, Lulu B, et al. 1995 Stereotactic radiosurgery as an adjunct to surgery and external beam radiotherapy in the treatment of patients with malignant gliomas. *Int. J. Radiat. Oncol. Biol. Phys.* **33** 461-68.

Gill S S, F R C S, Thomas D G T, et al. 1991 Relocatable frame for stereotactic external beam radiotherapy. *Int. J. Radiat. Oncol. Biol. Phys.* **20** 599-603.

Graham J D, Nahum A E and Brada M 1991 A comparison of techniques for stereotactic radiotherapy by linear accelerator based on 3-dimensional dose distributions. *Radioth. and oncol.* **22** 29-35.

Grusell E and Rikner G 1983 Radiation damage induced dose rate nonlinearity in an n-type silicon detector Silicon diodes as detectors in relative dosimetry of photon, electron and proton radiation fields Ed. G Rikner (Sweden: Uppsala).

Guan T Y, Almond P R, Park H C, et al. 1993 Imaging of radiation dose for stereotactic radiosurgery. *Med. Dosimet.* **18** 135-42.

Gustafsson A, Lind B K and Brahme A 1994 A generalized pencil beam algorithm for optimization of radiation therapy. *Med. Phys.* **21** 343-56.

Gustafsson A, Lind B K, Svensson R and Brahme A 1995 Simultaneous optimization of dynamic multileaf collimation and scanning patterns or compensation filters using a generalized pencil beam algorithm. *Med. Phys.* **22** 1141-56.

Haider T K and El-Khatib E E 1994 Measurements of phantom scatter factors for small field sizes in high energy x rays *Med. Phys.* **21** 663-66.

Haider T K and El-Khatib E E 1995 Differential scatter integration in regions of electronic non-equilibrium *Phys. Med. Biol.* **40** 31-43.

Hall E J and Brenner D J 1993 The radiobiology of radiosurgery: Rationale for different treatment regimes for AVMs and malignancies *Int. J. Radiat. Oncol. Biol. Phys.* **25** 381-85.

Halperin E C, Bentel G, Heinz E R, et al. 1989 Radiation therapy treatment planning in supratentorial glioblastoma multiforme. *Int. J. Radiat. Oncol. Biol. Phys.* **17** 1347-50.

Hamilton A J, Fosemire H, Lulu B A and Gossett L 1995a Phase I trial of LINAC-based stereotactic radiosurgery for spinal metastatic disease. 2<sup>ND</sup> Congress of International Stereotactic Radiosurgery Society, Boston.

Hamilton A J, Orozco J and Lulu B A 1995b Spina stereotactic relocation. which is better: Radiographic landmarks or fiducial markers? 2<sup>ND</sup> Congress of International Stereotactic Radiosurgery Society, Boston.

Haneman W P, Cox R S and Brain S W 1993 Treatment planning for a multi-degree-of-freedom robotic linear accelerator (abstract). *Med. Phys.* **20** 889.

Hariz M I, Henriksson R, Loforth P O, et al. 1990 A non-invasive method for fractionated stereotactic irradiation of brain tumors with linear accelerator *Radioth. and oncol.* **17** 57-72.

Hartman G H 1995 Quality assurance program on stereotactic radiosurgery. (Berlin: Springer).

Hartmann G H, Bauer-kirpes B, Serago C F and Lorenz W J 1992 Precision and accuracy of stereotactic convergent beam irradiations from a linear accelerator. *Int. J. Radiat. Oncol. Biol. Phys.* **28** 481-92.

Hartmann G H, Schlegel W, Sturm V, et al. 1985 Cerebral radiation surgery using moving field irradiation at a linear accelerator facility. *Int. J. Radiat. Oncol. Biol. Phys.* **11** 1185-92.

Haworth A and Perry A M 1993 Data acquisition for linac based stereotactic radiosurgery *Australasian Physical & Engineering Sciences in Medicine* **13** 49-56.

Heydarian M, Hoban P W and Beddoe A H 1996 A comparison of dosimetry techniques in stereotactic radiosurgery. *Phys. Med. Biol.* **41** 93-110.

- Heydarian M, Hoban P W, Beckham W A, et al. 1993 Evaluation of a PTW diamond detector for electron beam measurements. *Phys. Med. Biol.* **38** 1035-42.
- Higgins P D, Sibata C H, Siskind L and Sohn J W 1995 Deconvolution of detector size effect for small field measurement. *Med. Phys.* **22** 1663-66.
- Hirai T, Moriki A, Takizawa T, et al. 1995 The effectiveness and limitations of the Gamma Knife treatment of AVM. 2<sup>ND</sup> Congress of International Stereotactic Radiosurgery Society, Boston.
- Ho A K, Podgorsak M B, Sibata C H and Shin K H 1995 Application of the bioeffect algorithm of a treatment planning system. *Med. Dosimet.* **20** 139-41.
- Hoban P W 1991 Lateral electron disequilibrium in radiotherapy treatment planning. Ph.D. thesis, University of Waikato.
- Hoban P W, Heydarian M, Beckham W A and Beddoe A H 1994 Dose rate dependence of a PTW diamond detector in the dosimetry of a 6 MV photon beam *Phys. Med. Biol.* **39** 1219-29.
- Hoban P W, Murray D C and Round W H 1994 Photon beam convolution using polyenergetic energy deposition kernels *Phys. Med. Biol.* **39** 669-85.
- Hogstrom K R, Mills M D and Almond P R 1981 Electron beam dose calculations *Phys. Med. Biol.* **26** 445-59.
- Holmes T W and Mackie T R 1994 A comparison of three inverse treatment planning algorithms *Phys. Med. Biol.* **39** 91-106.
- Holmes T W, Mackie T R and Reckwerdt 1995 An iterative filtered backprojection inverse treatment planning algorithm for tomotherapy. *Int. J. Radiat. Oncol. Biol. Phys.* **32** 1215-25.
- Holt G, Laughlin J and Moroney J 1970 The extension of the concept of tissue-air ratios (TAR) to high energy *x-ray* beams *Radiology* **96** 437-46.
- Houdek P V, Fayos J V, Van Buren J M and Ginsberg M S 1985 Stereotaxic radiotherapy technique for small intracranial lesions. *Med. Phys.* **12** 469-72.
- Hubbell J H 1982 Photon mass attenuation and energy-absorption coefficients from 1 keV to 20 MeV *Int. J. Appl. Radiat. Isot.* **33** 1269-90.
- IAEA 1987 International Atomic Energy Agency: Absorbed dose determination in photon and electron beams. An international code of practice Technical Report Series No 277 (Vienna: IAEA).
- ICRP 1991 International Commission on Radiological Protection: Recommendations Report No. 60 (New York: Pergamon).
- ICRU 1972 International Commission on Radiation Units and Measurements: Radiation dosimetry- Electrons with initial energies between 1 and 50 MeV Technical Report Series No 21 (Maryland: ICRU).

ICRU 1980 International Commission on Radiation Units and Measurements: Radiation quantities and units. Report No. 33 (Washington, DC: ICRU).

ICRU 1980 International Commission on Radiation Units and Measurements: Radiation quantities and units Technical Report Series No 33 (Washington, DC: ICRU).

ICRU 1984 International Commission on Radiation Units and Measurements: Radiation dosimetry- Electron beams with energies between 1 and 50 *MeV*. Report No. 35 (Maryland: ICRU).

ICRU 1984 International Commission on Radiation Units and Measurements: Stopping powers for electrons and positrons. Report No. 37 (Maryland: ICRU).

ICRU 1984 International Commission on Radiation Units and Measurements: Radiation dosimetry- Electron beams with energies between 1 and 50 *MeV* Technical Report Series No 35 (Maryland: ICRU).

ICRU 1984 International Commission on Radiation Units and Measurements: Stopping powers for electrons and positrons Technical Report Series No 37 (Maryland: ICRU).

Johns H E and Cunningham J R 1983 The physics of radiology. Fourth Edition, (Springfield: Charles C Thomas).

Johnson C R, Thames H D, Huang D T and Schmidt-Ullrich R K 1995 The tumor volume and clonogen number relationship: Tumor control prediction based upon tumor volume estimates derived from computed tomography. *Int. J. Radiat. Oncol. Biol. Phys.* **33** 281-87.

Kahn H 1954 Applications of Monte Carlo. USAEC Report AECU-3259 62.

Kalend A M, Wu A, Yoder V and Maitz A 1990 separation of dose-gradient effect from beam hardening effect on wedge factors in photon fields *Med. Phys.* **17** 701-4.

Keall P and Hoban P W 1995 Accounting for primary electron scatter in *x-ray* beam convolution calculations *Med. Phys.* **22** 1413-18.

Kessler M L and Carson P L 1992 Test object design and performance simulation for 3-D imaging systems: spiral rod image distortion phantom. Annual Meeting of the Radiological Society of North America (abstract).

Kessler M L, Pitluck S, Petti P et al. 1991 Integration of multimodality imaging data for radiotherapy treatment planning. *Int. J. Radiat. Oncol. Biol. Phys.* **21** 1653-67.

Khan F M 1994 The physics of radiation therapy. Second Edition, Ed. Passano III W M (Maryland: Williams & Wilkins).

Khan F, Swechand W, Lee J and Williamson J 1980 Revision of tissue maximum ratios and scatter maximum ratio concepts for cobalt 60 and higher energy *x-ray* beams *Med. Phys.* **7** 230-37.

Khrunov B S, Martynov S S, Marchenko N P, et al. 1988 Diamond detectors for detection of ionizing radiation in biological medicine *Izmeritelnaya Technika* **6** 47-9.

Khrunov B S, Martynov S S, Vatrinsky S M, et al. 1990 Diamond detectors in relative dosimetry of photon, electron and proton radiation fields Radiation Protection Dosimetry **33** 155-7.

Killoran J H, Kooy H M, Bellerive M R, et al. 1996 Treatment planning support for dynamic LINAC stereotactic delivery. Radiosurgery 1995 Ed. Kondziolka D (Pittsburgh: Karger).

Kjellberg R N, Davis K R, Lyons S, et al. 1983 Bragg peak proton peak therapy for arteriovenous malformation of the brain. Clin. Neurosurg. **31** 248.

Kjellberg R N, Shintani A, Frantz A G and Kliman B 1968 Proton beam therapy in acromegaly. N. Engl. J. Med. **278** 689.

Knoos T, Ahnesjo A, Nilsson P and Weber L 1995 Limitations of a pencil beam approach to photon dose calculations in lung tissue Phys. Med. Biol. **40** 1411-20.

Knoos T, Ceberg C, Weber L and Nilsson P 1994 The dosimetric verification of a pencil beam based treatment planning system. Phys. Med. Biol. **39** 1609-28.

Konorova E A, Kozlov S F, and Vavilov V S 1966 Sov. Phys.-Solid State **8** 1-5.

Kooy H M, Bellerive M R and Loeffler J S 1996 Stereotactic Radiotherapy. Proceedings of the 1996 AAPM Summer School. Teletherapy: Present and Future Eds. Mackie T R and Palta J R (Wisconsin: Advanced Med. Publishing).

Kooy H M, Cosman E R, Harlan R B et al. 1996b A dynamic collimator system for conformal stereotactic radiosurgery and radiotherapy. Radiosurgery 1995 Ed. Kondziolka D (Pittsburgh: Karger).

Kooy H M, Herk M V, Barnes P D, et al. 1994 Image fusion for stereotactic radiotherapy and radiosurgery treatment planning. Int. J. Radiat. Oncol. Biol. Phys. **28** 1229-34.

Kozlov S F, Konorova E A, Kuznetsov Y A, et al. 1977 Diamond detector for *x-ray* and gamma-radiation. IEEE Trans. Nucl. Sci. **NS-24** 235-37.

Kozlov S F, Stuck R, Hage-Ali M and Siffert P 1975 Preparation and characteristics of natural diamond nuclear radiation detectors. IEEE Trans. Nucl. Sci. **NS-22** 160-70.

Kron T, Elliott A and Metcalfe P 1993 The penumbra of a 6 MV *x-ray* beam as measured by thermoluminescent dosimetry and evaluated using an inverse square root function. Med. Phys. **20** 1429-38.

Kubsad S S, Mackie T R, Gehring M A, et al. 1990 Monte Carlo and convolution dosimetry for stereotactic radiosurgery. Int. J. Radiat. Oncol. Biol. Phys. **19** 1027-35.

Kurup R G, Hogstrom K R, Otte V A, et al. 1992 Dosimetric evaluation of a two-dimensional, arc electron, pencil-beam algorithm in water and PMMA. Phys. Med. Biol. **37** 127-44.

Lam C F, Zhu J G, Fenn J O and Jenrette J M 1995 Treatment planning optimization for multiple arcs stereotactic radiosurgery using a linear accelerator. *Int. J. Radiat. Oncol. Biol. Phys.* **3** 647-57.

Larson D A 1994 Linac and Gamma Knife radiosurgery *Physica Medica* **2** 67-71.

Larson D A 1996 Radiosurgery and fractionation. *Radiosurgery 1995* Ed. Kondziolka D (Pittsburgh: Karger).

Larson D A, Bova F, Eisert D, et al. 1993(a) Consensus statement on stereotactic radiosurgery quality improvement. *Int. J. Radiat. Oncol. Biol. Phys.* **28** 527-30.

Larson D A, Bova F, Eisert D, et al. 1993(b) Current radiosurgery practice: Results of an ASTRO survey. *Int. J. Radiat. Oncol. Biol. Phys.* **28** 523-26.

Larson D A, Flickinger J C and Loeffler J S 1993c The radiobiology of radiosurgery. *Int. J. Radiat. Oncol. Biol. Phys.* **25** 557-61.

Larsson B, Leksell L, Rexed B, et al. 1958 The high energy proton beam as a neurosurgical tool. *Nature* **182** 1222.

Larsson B, Linden K and Sarby B 1974 Irradiation of small structures through the intact skull. *Acta Radiologica. Ther. Phys. Biol.* **13** 512.

Laughlin J S, Mohan R and Kutcher G J 1986 Choice of optimum megavoltage for accelerators for photon beam treatment *Int. J. Radiat. Oncol. Biol. Phys.* **12** 1551-57.

Lawrence J H, Tobias C A, Born J L, et al. 1962 Heavy-particle irradiation in neoplastic and neurologic disease. *J. Neurosurg.* **19** 717.

Lax I, Blomgren H, Naslund I and Svanstorm 1994 Stereotactic radiotherapy of malignancies in the abdomen. *Acta Oncol.* **6** 677-83.

Leavitt D D, Gibbs F A, Heilbrun M P, et al. 1991 Dynamic field shaping to optimize radiosurgery. *Int. J. Radiat. Oncol. Biol. Phys.* **21** 1247-55.

Leavitt D D, Martin M, Moeler J H and Lee W L 1990 Dynamic wedge field techniques through computer-controlled collimator motion and dose delivery *Med. Phys.* **17** 87-91.

Lee S P, Leu M Y, Smathers J B, et al. 1995 Biologically effective dose distribution based on the Linear Quadratic model and its clinical relevance. *Int. J. Radiat. Oncol. Biol. Phys.* **2** 375-89.

Leibel S A, Ling C C, Kutcher G J, et al. 1991 The biological basis for conformal three-dimensional radiation therapy. *Int. J. Radiat. Oncol. Biol. Phys.* **21** 805-10.

Leksell L 1968 Cerebral radiosurgery I: Gammathalamotomy in two cases of intractable pain. *Acta Chir. Scand.* **134** 585-95.

Levy R P, Steinberg G K, Schulte R W M, et al. 1995 A multi-institutional interactive network for stereotactic proton irradiation of intracranial AVMs: Design, implementation and initial experience. 2ND Congress of International Stereotactic Radiosurgery Society, Boston.

Li X A and Rogers D W O 1995 Electron mass scattering powers: Monte Carlo and analytical calculations *Med. Phys.* **22** 531-41.

Li X A, Soubra M, Szanto J and Gerig L H 1995 Lateral electron equilibrium and electron contamination in measurements of head-scatter factors using miniphantoms and brass caps *Med. Phys.* **22** 1167-70.

Loeffler J S, Shrieve D C, Alexander III E, et al. 1996 Stereotactic radiosurgery for meningiomas. *Radiosurgery 1995* Ed. Kondziolka D (Pittsburgh: Karger).

Loeffler J S, Shrieve D C, Mlack P M, et al. 1995 Results of fractionated stereotactic radiotherapy for meningiomas. 2<sup>ND</sup> Congress of International Stereotactic Radiosurgery Society, Boston.

Loewenthal E, Loewinger E, Bar-Avraham E and Barnea G 1992 Measurement of the source size of a 6 and 18 *MV* radiotherapy linac *Med. Phys.* **19** 687-90.

Luts W, Winston K R and Maleki N 1988 A system for stereotactic radiosurgery with a linear accelerator. *Int. J. Radiat. Oncol. Biol. Phys.* **14** 373-81.

Luxton G, Jozsef G and Astrahan M A 1991 Algorithm for dosimetry of multi arc linear accelerator stereotactic radiosurgery. *Med. Phys.* **18** 1211-21.

Lyman J T, Kanstein L, Yeater F, et al. 1986 A helium-ion beam for stereotactic radiosurgery of central nervous system disorders. *Med. Phys.* **13** 695-99.

Lyman J T, Phillips M K, Frankel K A and Fabrikant J I 1989 Stereotactic frame for neuroradiology and charged particle Bragg peak radiosurgery of intracranial disorders. *Int. J. Radiat. Oncol. Biol. Phys.* **16** 1615-21.

Mackie T R 1990 Applications of Monte Carlo method in radiotherapy: The dosimetry of ionizing radiation vol III Ed. K R Kase, B E Bjarngard and F H Attix (New York: Academic).

Mackie T R, Reckwerdt P J, Swerdloff S, et al. 1993 Tomotherapy: a proposal for optimized dose delivery of radiotherapy. *Abstract. Med. Phys.* **20** 875.

Mackie T R, Scrimger J W and Battista J J 1985 A convolution method of calculating dose for 15 *MV* x rays. *Med. Phys.* **12** 188-96.

Maleki N 1989 Parameter specification for two-isocenter-technique in radiosurgery. *AAPM Anual Meeting Program*.

McLaughlin W L, Soares C G, Sayeg J A, et al. 1994 The use of a radiochromic detector for the determination of stereotactic radiosurgery dose characteristics *Med. Phys.* **21** 379-88.

McLellan J, Papiez L, Sandison G A, et al. 1992 A numerical method for electron transport calculations *Phys. Med. Biol.* **37** 1109-25.

McLellan J, Sawchuk S, Battista J J, et al. 1994 A method for the calculation of electron energy-straggling spectra *Med. Phys.* **21** 367-78.

- Metcalf P E, Hoban P W, Murray D C and Round W H 1990 Beam hardening of 10 MV radiotherapy *x-rays*: analysis using a convolution/superposition method *Phys. Med. Biol.* **35** 1533-49.
- Metcalf P E, Wong T P Y and Hoban P W 1993 Radiotherapy *x-ray* beam inhomogeneity corrections: the problem of lateral electronic disequilibrium in lung *Aust. Phys. Eng. Sc. Med.* **16** 155-67.
- Metcalf P, Kron T, Elliott A, et al. 1993 Dosimetry of 6 MV *x-ray* beam penumbra. *Med. Phys.* **20** 1439-45.
- Miller A and McLaughlin W L 1982 Calculation of the energy dependence of dosimeter response to ionizing photons *Int. J. Appl. Radiat. Isot.* **33** 1299-310.
- Moerland M A, Beersma R, Bhagwandien R et al. 1995 Analysis and correction of geometric distortions in 1.5 T magnetic resonance images for use in radiotherapy treatment planning. *Phys. Med. Biol.* **40** 1651-64.
- Mohan R 1996 Intensity Modulation in Radiotherapy. Proceedings of the 1996 AAPM Summer School. Teletherapy: Present and Future Eds. Mackie T R and Palta J R (Wisconsin: Advanced Med. Publishing).
- Mohan R, Chui C and Lidofsky L 1985 Energy and angular distributions of photons from medical linear accelerators *Med. Phys.* **12** 592-97.
- Mohan R, Chui C and Lidofsky L 1986 Differential pencil beam dose computation model for photons. *Med. Phys.* **13** 64-73.
- Mohan R, Mageras G S, Baldwin B, et al. 1992 Clinically relevant optimization of 3-D conformal treatments. *Med. Phys.* **19** 933-44.
- Mohan R, Wang X, Jackson A, et al. 1994 The potential and limitations of the inverse radiotherapy technique. *Radioth. and oncol.* **32** 232-48.
- Morin R L 1988 Monte Carlo simulation in the radiological sciences. Ed. Morin R L (Florida: CRC).
- Murray D C 1990 Using EGS4 Monte Carlo in medical radiation physics *APESM J.* **13** 132-47.
- Murray D C 1991 The application of parallel processing to radiotherapy dose computation. Ph.D. thesis, University of Waikato.
- Nath R, Biggs P J, Bova F J, et al. 1994 *AAPM* code of practice for radiotherapy accelerators: Report of *AAPM* radiation therapy task group No. 45. *Med. Phys.* **21** 1093-121.
- Nedzi L A, Kooy H M, Alexander III E, et al. 1991 Variables associated with the development of complications from radiosurgery of intracranial tumors. *Int. J. Radiat. Oncol. Biol. Phys.* **21** 591-99.

Nedzi L A, Kooy H M, Alexander III E, et al. 1993 Dynamic field shaping for stereotactic radiosurgery: A modelling study. *Int. J. Radiat. Oncol. Biol. Phys.* **25** 859-69.

Nelson W R and Rogers D W O 1988 Structure and operation of the EGS4 code system. In *Monte Carlo transport of electrons and photons*. Ed. Jenkins T M (New York: Plenum).

Nelson W R, Bielajew A F, Rogers D W O and Hirayama H 1994 "EGS4 in '94 A decade of enhancements". World Congress on Medical Physics and Biomedical Engineering, Rio de Janeiro, Brazil.

Neuenschwander H and Born E J 1992 macro Monte Carlo method for electron beam dose calculation. *Phys. Med. Biol.* **37** 107-25.

Noyes W R, Auchter R M, Craig B, et al. 1996 Cost analysis of radiosurgery versus resection for single brain metastases. *Radiosurgery 1995* Ed. Kondziolka D (Pittsburgh: Karger).

O'Brien P F, Gillies B A, Schwartz M, et al. 1991 Radiosurgery with unflattened 6 MV photon beams. *Med. Phys.* **18** 519-21.

O'Connor J E 1957 The variation of scattered *x-rays* with density of an irradiated body. *Phys. Med. Biol.* **1** 352-69.

Otto-Oelschlagel S, Schlegel W and Lorenz W 1994 Different collimators in convergent beam irradiation of irregularly shaped intracranial target volumes. *Radioth. and oncol.* **30** 175-79.

Papanikolaou N, Mackie T R, Meger-wells C, et al. 1993 Investigation of the convolution method for polyenergetic spectra *Med. Phys.* **20** 1327-36.

Paul J M, Koch R F, Khan F R and Devi B S 1983 Characteristics of Mevatron 77 15 MV photon beam. *Med. Phys.* **10** 237-42.

Pike B, Podgorsak E B, Peters T M and Pla C 1987 Dose distributions in dynamic stereotactic radiosurgery *Med. Phys.* **14** 780-89.

Pike G B, Podgorsak E B, Peters T M, et al. 1990 Dose distribution in radiosurgery. *Med. Phys.* **17** 296-304.

Planskoy B 1980 Evaluation of diamond radiation detectors. *Phys. Med. Biol.* **25** 519-32.

Podgorsak E B 1996 Linac-Based Stereotactic Radiosurgery. Proceedings of the 1996 AAPM Summer School. Teletherapy: Present and Future Eds. Mackie T R and Palta J R (Wisconsin: Advanced Med. Publishing).

Podgorsak E B, Oliver A, Pla M, et al. 1988 Dynamic stereotactic radiosurgery *Int. J. Radiat. Oncol.* **14** 115-26.

Podgorsak E B, Pike G B, Pla M, et al. 1990 Radiosurgery with photon beams: physical aspects and adequacy of linear accelerators. *Radioth. and oncol.* **17** 349-58.

Pollock B E, Flikinger J C, Lunsford L D, et al. 1995 Hemorrhage risk after stereotactic radiosurgery of arteriovenous malformations. 2<sup>ND</sup> Congress of International Stereotactic Radiosurgery Society, Boston.

Raeside D E 1976 Monte Carlo principles and applications Phys. Med. Biol. **21** 181-97.

Ramani R, Lightstone A W, Mason D L D and O'Brien P F 1994 The use of radiochromic film in treatment verification of stereotactic radiosurgery Med. Phys. **21** 389-92.

Ramani R, O'Brien P F, Davey P, et al. 1995 Implementation of multiple isocentre treatment for dynamic radiosurgery. Br. J. Radiol. **68** 731-35.

Rhein B, Debus J, Pastyr O, et al. 1995 Optimization of dose distribution of irregular shaped lesions of the brain. 2<sup>ND</sup> Congress of International Stereotactic Radiosurgery Society, Boston.

Rice R K, Hansen J L, Svensson G K and Siddon R L 1987 Measurements of dose distributions in small beams of 6 MV x-rays Phys. Med. Biol. **32** 1087-99.

Rice R K, Hansen L J, Chin L M, et al. 1988 The influence of ionization chamber and phantom design on the measurement of lung dose in photon beams. Med. Phys. **15** 884-90.

Rikner G 1983 Characteristics of a p-Si detector in high energy electron fields Acta Radiologica Oncology **24** 71-4.

Rogers D W O and Bielajew A F 1990 Monte Carlo techniques of electron and photon transport for radiation dosimetry: The dosimetry of ionizing radiation vol III Ed. K R Kase, B E Bjarngard and F H Attix (New York: Academic).

Rogers D W O and Bielajew A F 1990 Monte Carlo techniques of electron and photon transport for radiation dosimetry The dosimetry of ionizing radiation vol III Ed. K R Kase, B E Bjarngard and F H Attix (New York: Academic).

Rustgi S N 1995 Evaluation of the dosimetric characteristics of a diamond detector for photon beam measurements Med. Phys. **22** 567-70.

Rustgi S N, and Working K R 1992 Dosimetry of small field electron beams. Med. dosimetry **17** 107-10.

Rutigliano M H, Lunsford L D, Kondziolka D, et al. 1995 The cost effectiveness of stereotactic radiosurgery versus surgical resection in the treatment of solitary metastatic brain tumors. 2<sup>ND</sup> Congress of International Stereotactic Radiosurgery Society, Boston.

Scanditronix Dosimetry Products Guide. Scanditronix Medical Instruments.

Schad L R, Boesecke R, schlegel W, et al. 1987 Three-dimensional image correlation of CT, MR, and PET studies in radiotherapy treatment planning of brain tumours. J. CAT **11** 948-54.

Schad L R, Ehrlicke H, Wowra B, et al. 1992 Correction of spatial distortion in magnetic resonance angiography for radiosurgical treatment planning of cerebral arteriovenous malformations. *Magnetic Resonance Imaging*. **10** 9.

Schell M C and Kooy H 1994 Stereotactic radiosurgery quality improvement: Interdepartmental collaboration. *Int. J. Radiat. Oncol. Biol. Phys.* **28** 551-52.

Schell M C, Bova F J, Larson D A, et al. 1995 Stereotactic radiosurgery: Report of Task Group 42, Radiation Therapy Committee. *AAPM* (New York: AIP).

Schwartz M L, Sixel K E, Young C S and O'Brien P F 1995 Prediction of obliteration of AVMs after radiosurgery: The obliteration prediction index (OPI). 2<sup>ND</sup> Congress of International Stereotactic Radiosurgery Society, Boston.

Seltzer S M and Berger M J 1982 Procedure for calculating the radiation stopping power for electrons *Int. J. Appl. Radiat. Isot.* **33** 1219-26.

Serago C F, Houdek P V, Bauer-Kirpes, et al. 1992 Stereotactic radiosurgery: Dose volume analysis of linear accelerator techniques. *Med. Phys.* **19** 181-85.

Sixel K E and Faddegon B A 1995 Calculation of *x-ray* spectra for radiosurgical beams. *Med. Phys.* **22** 1657-61.

Sixel K E and Podgorsak E B 1993 Buildup region of high-energy *x-ray* beams in radiosurgery *Med. Phys.* **20** 761-64.

Sixel K E and Podgorsak E B 1994 Buildup region and depth of dose maximum of megavoltage *x-ray* beams *Med. Phys.* **21** 411-16.

Sneed P K, Albright N W, Wara W M, et al. 1995 Fetal dose estimates for radiotherapy of brain tumors during pregnancy. *Int. J. Radiat. Oncol. Biol. Phys.* **32** 823-30.

Solberg T D, Holly F E, De Salles A A F, et al. 1995 Implications of tissue heterogeneity for radiosurgery in head and neck tumors *Int. J. Radiat. Oncol. Biol. Phys.* **32** 235-39.

Sontag M R and Cunningham J R 1977 Corrections to absorbed dose calculations for tissue inhomogeneities. *Med. Phys.* **4** 431-36.

Sontag M R and Cunningham J R 1978 The equivalent tissue-air ratio method for making absorbed dose calculations in a heterogeneous medium. *Radiology* **129** 789-94.

Souhami L, Oliver A, F R C S, et al. 1990 Radiosurgery of cerebral arteriovenous malformations with the dynamic stereotactic irradiation. *Int. J. Radiat. Oncol. Biol. Phys.* **19** 775-82.

Sperduto P W and Hall W A. 1995 The cost effectiveness of alternative treatments for a single brain metastasis. 2<sup>ND</sup> Congress of International Stereotactic Radiosurgery Society, Boston.

STP manual 1992 Fischer stereotactic radiosurgery treatment planning system.

Sumanaweera T S, Alder J R, Napel S and Glover G H 1994 Characterization of spatial distortion in magnetic resonance imaging and its implications for stereotactic radiosurgery. *Neurosurgery* **35** 696-704.

Takahashi S, Kitabatake T, Morita K et al 1961 Conformation radiotherapy applied to cancer of uterus *Nippon Acta Radiol.* **20** 2746-53.

Target treatment planning system physics manual 1993 IGE Medical Systems Ltd.

Thomas S J 1994 Factors affecting penumbral shape and 3D dose distributions in stereotactic radiotherapy. *Phys. Med. Biol.* **39** 761-71.

Thomas S J and Foster K R 1995 Radiotherapy treatment planning with dynamic wedges-an algorithm for generating wedge factors and beam data *Phys. Med. Biol.* **40** 1421-33.

Thwaites D I, Burns D, Klevenhagen S C, et al. 1992 Addendum to the code of practice for electron beam dosimetry in radiotherapy (1985): interim additional recommendations. *Phys. Med. Biol.* **37** 1477-83.

Tishler R B, Loeffler J S, Lunsford L D, et al. 1993 Tolerance of cranial nerves of the cavernous sinus to radiosurgery. *Int. J. Radiat. Oncol. Biol. Phys.* **27** 215-21.

Treuer H, Bocsecke R, Schlegel W, et al 1993 The source-density function: determination from measured lateral dose distributions and use for convolution dosimetry. *Phys. Med. Biol.* **38** 1895-909.

Tsai J, Buck B A, Svensson G K, et al. 1991 Quality assurance in stereotactic radiosurgery using a standard linear accelerator. *Int. J. Radiat. Oncol. Biol. Phys.* **21** 73748.

Turner J E, Wright H A, and Hamm R N 1985 Review article: A Monte Carlo primer for health physicists. *Health Phys.* **48** 717.

Van den Berge D L, Marc C, Herregodts P, et al. 1995 A stereotactic reference frame for fractionated radiotherapy in the head and neck region. 2ND Congress of International Stereotactic Radiosurgery Society, Boston.

Vatnitsky S and Järvinen H 1993 Application of a natural diamond detector for the measurement of relative dose distributions in radiotherapy *Phys. Med. Biol.* **38** 173-84.

Vatnitsky S, Miller D, Siebers J and Moyers M 1995 Application of solid state detectors for dosimetry of therapeutic proton beams. *Med. Phys.* **22** 469-73.

Weaver K A, Albright N, Pickett B and Stuart A 1994 Applicability of standard irregular field calculations for high-energy photon beams. *Med. Dosimetry* **19** 125-33.

Webb S 1989 Optimisation of conformal radiotherapy dose distributions by simulated annealing *Phys. Med. Biol.* **34** 1349-69.

Webb S 1993a The effect on tumour control probability of varying the setting of a multileaf collimator with respect to the planning target volume. *Phys. Med. Biol.* **38** 1923-36.

- Webb S 1993b The physics of three-dimensional radiation therapy. (Bristol: IOP).
- Webb S 1994 Optimizing the planning of intensity-modulated radiotherapy. *Phys. Med. Biol.* **39** 2229-46.
- Webb S 1994 Optimum parameters in a model for tumour control probability including interpatient heterogeneity. *Phys. Med. Biol.* **39** 1895-914.
- Webb S and Nahum 1993 A model for calculating tumour control probability in radiotherapy including the effects of inhomogeneous distributions of dose and clonogenic cell density. *Phys. Med. Biol.* **38** 653-66.
- Wells C M M, Mackie T R, Podgorsak M B, et al. 1994 Measurements of the electron dose distribution near inhomogeneities using a plastic scintillation detector *Int. J. Radiat. Oncol.* **29** 1157-65.
- Wigg D R and Nicholls R L 1984 In optimization of cancer radiotherapy. Proceedings of the 2nd international conference on dose, time and fractionation Ed. Paliwal B R (New York: AIOP).
- Wigg D R and Wilson B C 1981 Isodose versus isoeffect in radiotherapy planning as applied to parallel opposed fields *Aust. Radiol.* **25** 205-12.
- Williamson J F 1989 Radiation transport calculations in treatment planning. *Comput. Med. Imag. and Graphics* **13** 251-68.
- Wilson R R 1952 Monte Carlo study of shower production *Phys. Rev.* **86** 261.
- Woo M K 1994 Analysis of photon beam exit dose using photon point kernels. *Phys. Med. Biol.* **39** 687-702.
- Woo M K and Cunningham J R 1990 The validity of the density scaling method in primary electron transport for photon and electron beams *Med. Phys.* **17** 187-94.
- Woo M K, Cunningham J R and Jezioranski 1990 Extending the concept of primary and scatter separation to the condition of electronic disequilibrium *Med. Phys.* **17** 588-95.
- Wu A, Lindner G, Maitz A H, et al. 1990 Physics of Gamma Knife approach on convergent beams in stereotactic radiosurgery. *Int. J. Radiat. Oncol. Biol. Phys.* **18** 941-49.
- Wu A, Zwicker R D, Kalend A M and Zheng Z 1993 Comments on dose measurements for a narrow beam in radiosurgery *Med. Phys.* **20** 777-79.
- Yacoot A, Moore M and Makepeace A 1990 *X-ray* studies of synthetic radiation-counting diamonds. *Phys. Med. Biol.* **35** 1409-22.
- Yeung D, Palta J, Fontanesi J and Kun L 1993 Systematic analysis of errors in target localization and treatment delivery in stereotactic radiosurgery (SRS). *Int. J. Radiat. Oncol. Biol. Phys.* **28** 493-98.
- Yin F F 1995 Physical penumbra change of beam profile due to film digitization. *Med. Phys.* **22** 803-5.

Young R F, Vermeulen S S, Posewitz A, et al. 1996 Functional neurosurgery with the Leksell Gamma Knife. Radiosurgery 1995 Ed. Kondziolka D (Pittsburgh: Karger).

Yu C X 1995 Intensity-modulated arc therapy with dynamic multileaf collimation: An alternative to tomotherapy. Phys. Med. Biol. **40** 1435-49.

Yu C X, Mackie T R and Wong J W 1995 Photon dose calculation incorporating explicit electron transport **22** 1157-65.

Zahmatkesh M H 1995 Diamond detector dose rate correction factors for megavoltage photon beams. M.Sc. thesis, The University of Adelaide.



